

<http://researchcommons.waikato.ac.nz/>

## Research Commons at the University of Waikato

### Copyright Statement:

The digital copy of this thesis is protected by the Copyright Act 1994 (New Zealand).

The thesis may be consulted by you, provided you comply with the provisions of the Act and the following conditions of use:

- Any use you make of these documents or images must be for research or private study purposes only, and you may not make them available to any other person.
- Authors control the copyright of their thesis. You will recognise the author's right to be identified as the author of the thesis, and due acknowledgement will be made to the author where appropriate.
- You will obtain the author's permission before publishing any material from the thesis.

**Modelling of low- and high-frequency sea level variability and their  
drivers around the southern African coast**

A thesis  
submitted in fulfilment  
of the requirements for the degree  
of  
**Doctor of Philosophy in Earth Sciences**  
at  
**The University of Waikato**  
by  
**CHRISTO RAUTENBACH**



2020

# Abstract

---

Recent surveys indicate that marine operational forecasting is becoming increasingly important due the pressure to manage impacts associated with our changing climate. The methods with which forecasts are being produced are also changing as computational power is becoming more accessible. Nevertheless, understanding and improving the incorporation of oceanographic dynamics, underpinning hind- and forecasting models, will remain fundamental to the accurate prediction of physical ocean and coastal dynamics. Numerous recent studies have investigated current and possible future Southern Ocean dynamics. However, these dynamics are under studied in the continental shelf areas of southern Africa. The present study aims to address this knowledge gap and reports results of a methodical exploration of water level and wave dynamics in these waters. The structure of the thesis is based on the operational marine forecasting platform developed at the South African Weather Service (SAWS). As part of this thesis, I conceptualized and co-developed the operational platform presented here. The complete platform incorporates a coupled ocean model driven with atmospheric pressure and winds (simulated in the downscaled Unified Model (UM)). The oceanographic model consists of tidal, storm surge and wave dynamics. The coupled system was developed in a depth-averaged Delft3D FLOW model and Simulating Waves in the Nearshore (SWAN, a.k.a. Delft3d WAVE) spectral wave model.

The study is divided into six chapters, each aligned with the physical description of a phenomenon. The hindcast development, assumptions, calibration, validation and operational deployment strategies are also presented. First the tidal characteristics of South Africa are fully investigated and mapped. *In situ* validation was performed with the main tidal constituents compared against those extracted from total water level signals observed at nine coastal measurement locations. Mapping of regional tidal characteristics was also performed for each constituent and compared with other regional tidal predictions (e.g. the TPXO 7.2 and 8 African computational nests). Coastal semi-diurnal tidal resonance is identified and quantified over the broad continental shelf areas (e.g. the Agulhas and Namaqua Banks). This model formed the bases of all the other models developed in the SAWS Wave and Storm Surge (SWaSS) operational platform.

The storm surge dynamics around the southern African coastline were investigated in the next chapter. Model validation was performed at six coastal *in situ* measurement locations. The atmospheric dynamics for South Africa are summarised and independently validated. The UM and Wave Watch 3 (WW3) boundary forcing models were developed outside of the scope of the present study and thus only employed as forcing. The coupled, depth-averaged storm surge model was calibrated and validated. The validated model was used to quantify the various contributions of the drivers of storm surge. It was found that wave set-up contributed approximately 20% of the total surge signal in the southwest, while wind set-up contributed approximately 55%.

Wave validation and sensitivity analysis was investigated next. The wave component of the SWaSS system was coupled online with the storm surge hydrodynamic model. This implied that the wave simulations responded to fluctuations in the changing water levels and the wave model contributed to the water level set-up in the hydrodynamic model. Reconstruction methods for spectral wave model boundary condition reconstruction methods were investigated and quantified. Both *in situ* (eight stations) and remotely sensed altimetry measurements were used for model validation. The accuracy of the SWaSS wave model component was also investigated with regards to whitecapping formulations. It was found that the Van der Westhuysen (2007) whitecapping formulation performed best together with fully spectral boundary conditions obtained from a global WW3 model. The results using the boundary reconstruction methods were performed adequate. Consideration must be given to each coastal location though as the combination of most appropriate models did vary depending on the dynamics of the mixed sea state (swell and wind seas).

These studies are followed by a practical chapter investigating the computational efficiencies associated with deploying one of the most widely used spectral wave modelling software, Simulating Waves in the Nearshore (SWAN). The model extent and configuration were based on SWaSS. It was found that the most efficient SWAN simulation (for southern Africa and the Van der Westhuysen whitecapping formulation) is executed on six computational threads.

Initial results and recommendations for future thorough investigations are made in the final chapter. Here the first results of using the new ST06, SWAN model physics are presented with a few permutations of the underlying parametrised physical models. The resulting accuracies, as compared with satellite altimetry measurements are also given.



# Acknowledgements

---

When I pray,  
Coincidences happen;  
When I don't,  
They don't.

*-William Temple, former archbishop of Canterbury*

First, I would like to acknowledge and thank my God (the God of Abraham, Isaac, and Jacob), who through His insight and companionship has led me through meandering life paths. Thank you, אבא (Abba, meaning the Father), for never leaving me.

My family (Fanie, Susan and Ess-Jee Rautenbach), for always supporting me in whatever I choose. They are the ones who taught me how to love unconditionally and how to see the good in life even when everything around me was dark.

My friends, old and new, for putting a spring in my step with humour, laughter and love.

Lastly, I want to acknowledge and thank both the University of Cape Town and Waikato University for allowing me to complete this extraordinary achievement. I also like to thank all my co-authors for making this study possible and for co-developing this marine forecasting platform for South Africa. I also like to thank Dr. Lara van Niekerk for giving me the idea to pursue a second PhD.

# Table of Contents

---

Abstract.....	i
Acknowledgements .....	iii
Table of Contents .....	iv
List of Figures.....	v
List of Tables .....	vi
Chapter 1: <i>Introduction</i> .....	1
1.1 Setting the scene.....	2
1.2 Thesis aim and structure.....	6
Chapter 2: <i>A new era for marine forecasting in South Africa</i> .....	9
2.1 Abstract .....	9
2.2 Publication details .....	9
2.3 Author contributions .....	9
Chapter 3: <i>Tidal characteristics of South Africa</i> .....	12
3.1 Abstract .....	13
3.2 Publication details .....	13
3.3 Author contributions .....	13
Chapter 4: <i>A coupled wave, tide and storm surge operational forecasting system for South Africa – validation and physical description</i> .....	34
4.1 Abstract .....	35
4.2 Publication details .....	35
4.3 Author contributions (as appeared in paper) .....	35
4.4 Errata .....	36
Chapter 5: <i>Southern African wave model sensitivities and accuracies</i> .....	70
5.1 Abstract .....	71
5.2 Publication details .....	71
5.3 Author contributions (as appeared in paper) .....	71
Chapter 6: <i>Parallel computing efficiency of SWAN</i> .....	95
6.1 Abstract .....	96
6.2 Publication details .....	96
6.3 Author contributions (as appeared in paper) .....	96
Chapter 7: <i>Future studies</i> .....	107
Chapter 8: <i>Conclusions</i> .....	113
References .....	117

# List of Figures

---

Figure 1-1: An original linoleum print made during the course of the present study. The image is a self-portrait portraying the deeper questions in life that ultimately shape who we are. The quoted text comes from the book by Rainer Rilke, “Letters to a young poet”, 1964.....	1
Figure 1-2: Flow diagram of the operational marine forecasting platform developed during the course of the present study. The operational platform may be found at <a href="http://marine.weathersa.co.za/">www. http://marine.weathersa.co.za/</a> . ....	6
Figure 1-3: Logical flow of chapters and their relationship with the operational flow depicted in Figure 1-2. All these components together illustrate the developments in the present study. Boundary conditions were extracted from various sources as described in each chapter and Figure 1-2. ....	8
Figure 3-1: This image was featured as the cover of Deep Sea Research 1: Oceanographic Research Papers, Volume 150, August 2019, 103092, <a href="https://doi.org/10.1016/S0967-0637(19)30237-7">https://doi.org/10.1016/S0967-0637(19)30237-7</a> . Southwestern Africa’s M2 tidal constituent ellipses and phases (Rautenbach, Barnes, & de Vos, (2019)). ....	12
Figure 4-1: An original linoleum print made during the course of the present study. This artwork was inspired but the atmosphere-ocean interactions described in the present chapter. In the distance a coastline can also be seen, highlighting the importance of this study to coastal vulnerability considerations. ....	34
Figure 4-2: {Fig. 8} Final model calibration results for Cape Town. Each upper panel indicates the modelled and measured water levels on the left axis, after the tidal signals have been filtered out. On the right-hand axis, the prevailing atmospheric pressure close to the coastal city of interest is provided. Each lower panel indicates the associated near shore UM wind speeds together with their directions as magenta, True North arrows. ....	36
Figure 5-1: A linoleum print inspired by the physical wave dynamics described in the present study. To everything in nature, and life, these must be balance: push and pull, cause and effect, fasting and the feast. This is also known as spiritual symmetry and presented here as the tides and waves. ....	70
Figure 6-1: Another original linoleum print made during the course of the present study. This print was inspired by the freedom and hope that a new day and season brings. It also highlights the importance that the Sun has on all Earth-system dynamics.....	95
Figure 7-1: Basic statistical performance of SWAN compared with co-located Altimetry measurements for 2016. (a) Bias for the ST6 01 configuration (refer to Table 7-1), (b) Root-Mean-Square-Difference (RMSD) for the ST6 01 configuration, (c) Bias for the ST6 02 configuration, (d) RMSD for the ST6 02 configuration, (e) Bias for the ST6 04 configuration, (f) RMSD for the ST6 04 configuration. ....	110

# List of Tables

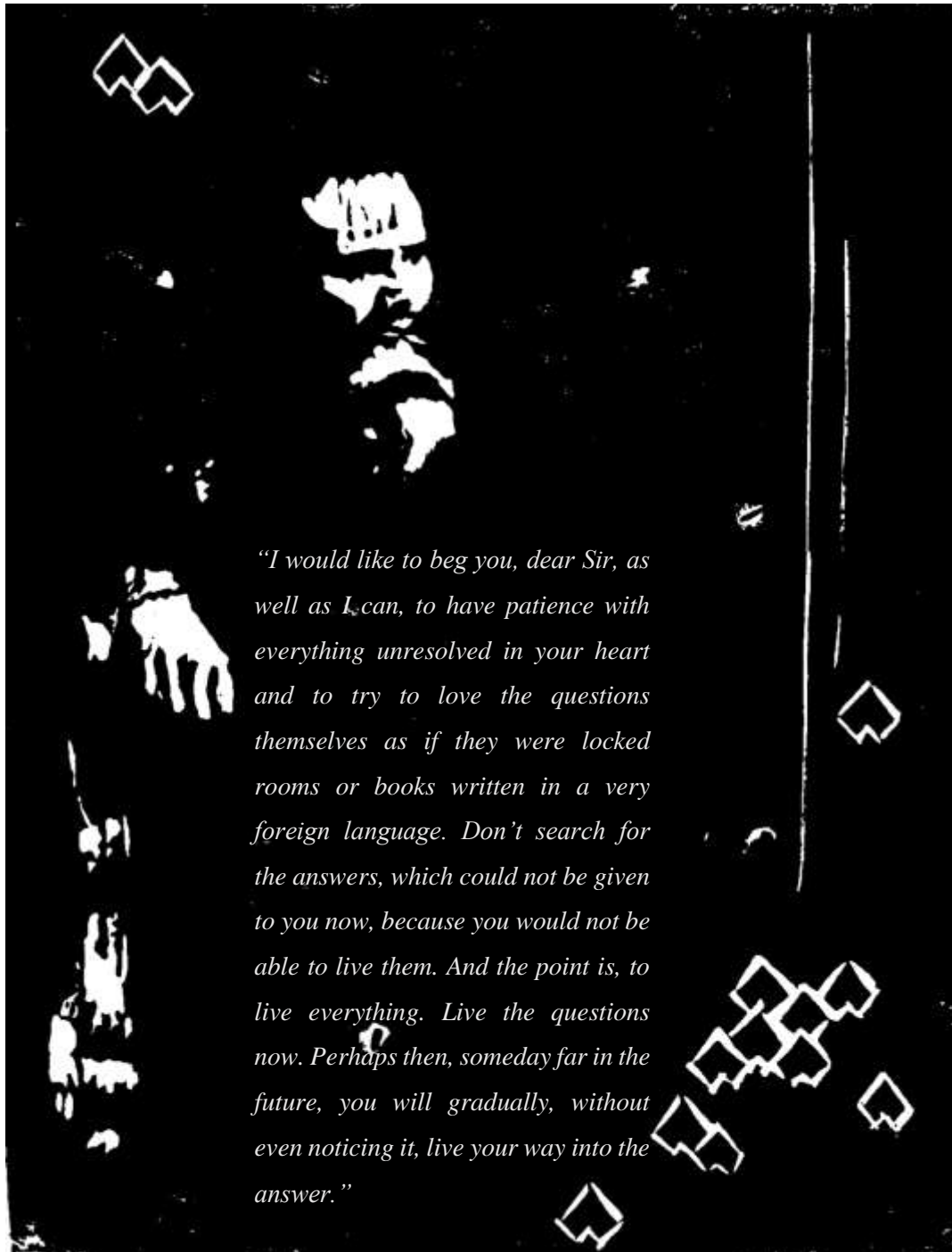
---

Table 7-1: ST6 parameter sensitivity testing scenarios. ....	111
Table 7-2: Regionally averaged, basic statistical summary. ....	112

# Chapter 1

## *Introduction*

---



**Figure 1-1:** An original linoleum print made during the course of the present study. The image is a self-portrait portraying the deeper questions in life that ultimately shape who we are. The quoted text comes from the book by Rainer Rilke, "Letters to a young poet", 1964.

## 1.1 Setting the scene

The importance of Earth system forecasting is well known for most communities. Meteorological forecasts appearing on the news, newspapers and forecasting applications have given the public a thorough insight into one of the Earth-systems forecasting realms. Marine operational forecasting involves the prediction of various ocean dynamic parameters, and these nowcasts and forecasts are used in various applications ranging from coastal disaster management, search and rescue operations and governing safety of life at sea.

Hindcasts are also important, as these are usually used to calibrate and validated numerical and statistical models, ultimately deployed in forecasting applications. The scope of the present study will focus on two main ocean dynamical parameters: water levels (tides and storm surge) and waves. Although these parameters can also have significant impacts on ecosystems, the remainder of the present study will focus on the abiotic coastal effects (e.g. coastal infrastructure protection).

Cavaleri et al., (2018) recently presented an extensive overview of their perspective on what the future for wave modelling is for coastal and inner seas. Within their review they list some well-known and large operational, Earth-system, forecasting agencies. These include the European Centre for Medium-Range Weather Forecasts (ECMWF) in the United Kingdom and the National Center for Environmental Prediction (NCEP) in the United States of America. These agencies produce both atmospheric and oceanographic forecasts with various prediction horizons (now-casts to seasonal predictions). Similarly, SAWS, in South Africa, now produce both atmospheric and marine forecasts and the present study represents the first steps in the marine forecasting abilities. Even though SWaSS is the initialisation of a forecasting division, it still addressed numerous aspects addressed by Cavaleri et al., (2018). These include the methodologies employed and physical parameterizations investigated.

Usually the accuracy of the forecast becomes more uncertain the further away the prediction horizon is (Cavaleri et al., 2018). Both atmospheric and oceanographic forecasting have multiple challenges in improving accuracy. These challenges are approached in a variety of different ways. Some researchers are considering machine learnt (ML) statistical methods as the path to improved forecast reliability. These methods could either be during the post-processing phase of a typical numerical prediction

(Niehuser, et al., 2018) or the entire prediction could be based on statistical methods (Tadesse, et al., 2020). Numerous studies are exploring different methodologies of using both numerical models and ML to optimize predation accuracy. The strength of the numerical models lay in solving (or approximating) the underlying physics through parametrizations. This approach allows the prediction to take unexpected and new climate scenarios into account. One of the weaknesses of the ML techniques are that they can only base their prediction on events that has been part of the training phase of model development.

For medium range forecast, the solution appears to be fully coupled Earth-system models. E.g. in these models the atmosphere influences the ocean and vice versa (e.g. Harris, (2018)). The various forecasting timescale are climate scales (10 to 100+ years), decadal scales (1 to 20 years), seasonal (3 to 12 months) and short to medium range (1 to 2 weeks) (Harris, 2018). The present study is currently only used for short range forecasting and according to Harris, (2018) short to medium range forecasting is still the least mature and is an area of active research.

The most complex model is not necessarily the best model for a desired outcome. For example, it is necessary to incorporate wave-current interaction in nearshore models, but in the open ocean far away from strong boundary currents, such effects are negligible. For southern Africa, very limited effort has gone into marine forecasting. Before the establishment of SWaSS there has only been some local wave forecasts freely available. During a workshop between the South African Weather Service and Disaster Management in 2018, the clear need for an operational wave and storm surge forecasting system was articulated. Being cognizant of the state-of-the-art technologies, the present study aimed to establish a baseline forecast with a widely acceptable standard in marine, abiotic forecasting. Thus, a coupled numerical modelling system was developed which each component of the operational platform calibrated and validated. These methodologies and associated physical dynamics are thus elucidated in this thesis. Beyond the scope of this thesis the model prediction accuracies are being improved through ML post-processing corrections. The effects of wave-current interaction of the Agulhas Current has already been investigated and published outside the scope of the present study (Barnes & Rautenbach, 2020). This increased accuracy is now also operationally available.

Limited to no open research has been done on the tidal, storm surge and wave dynamics around South Africa. Most tidal and surge research for southern Africa has been conducted in the 1980s and 1990s. The few studies that do exist focused on the signal analysis of measured data. No numerical investigation has been attempted to elucidate the physical dynamics associated with the southern African tide and storm surge. The first two technical chapters will thus primarily focus on these phenomena. Numerous novel contributions may be found within these chapters. Of particular interest is the description and quantification of the semi-diurnal tidal resonance found on the Agulhas Bank, the largest extent of South Africa's continental shelf. Within the second chapter the relative contribution of the drivers of storm surge are quantified. In both chapters a thorough introduction to southern African atmospheric and oceanographic dynamics are presented. These results were presented in two peer reviewed publications. The tidal dynamics paper was also featured on the cover of Volume 150 of Deep Sea Research 1, as illustrated on the cover of Chapter 3. This was the first time in history that an African scientist was featured as a cover page for this journal and illustrates the scientific relevance of this study.

Another component of the motivation for the present research was the need for an operational marine forecasting system for South Africa and the operational model was thus developed as part of the thesis. I built all the models and conceptualized the coupled operational system. The models were developed for the purpose of establishing the first operational marine forecasting platform for South Africa. While building the models, I was employed by the South African Weather Service (SAWS) to establish and conceptualize the science methodology for the marine research division. Although operational in intent, from the beginning of the project, I decided to use the new models to understand the dynamics of the coastline, and so worked to develop them into publications in international journals. I believed that this approach was essential because it provided the international scientific audience with confidence in the quality of the newly developed products. The approach also assures the end users that the models are sound and reliable and based on international norms and accepted practices (even though it is likely that the public might not understand the scientific details). While the models were developed, I involved others in my group as collaborators or through mentorship roles. This mentorship was successful and resulted in two employees currently pursuing their own PhDs with myself as main supervisor (I have a PhD (obtained 2012) in Process-, Energy and Environmental Engineering), which has eventuated in further co-authored



publications. For example, some of these studies took the developments of the present thesis even further, e.g. including wave-current interaction in the operational system (Barnes & Rautenbach, 2020) and exploring the connection between search and rescue incidents with metocean conditions (de Vos & Rautenbach, 2017). The present study thus represents the work that I did during the establishment of the SWAS marine operational forecasting platform. My ultimate aim in presenting this work as a PhD thesis is to firmly establish myself as a Physical Oceanographer.

The research presented here thus illustrates how these numerical components were implemented in the first operational marine forecasting platform for South Africa. Chapter 2 presents a paper that introduced this new era for African based marine forecasting. The system is currently housed within SAWS. As described in this study, the system provides twice daily, hourly forecasts of tidal, storm surge and wave dynamics. The latter being provided at a  $1/48^{\text{th}}$  degree resolution while the other dynamics are provided at  $1/16^{\text{th}}$  degree resolution. These models are all dynamically coupled and forced with a 4 km resolution, regional atmospheric model. The full details of the operational workflow are provided in Chapter 4 and Figure 1-2. The atmospheric model was deployed in the Unified Model (UM) while the oceanographic model was developed in the numerical code Delft3D and Simulation Waves in the Nearshore (SWAN). The UM was not developed by Dr. Rautenbach but rather only used as forcing. All other water level and wave models were developed by the author during the present thesis.

Chapter 5 and 6 focused on waves dynamics around southern Africa. The spectral wave models SWAN and WaveWatch 3 (WW3) were employed for these studies. The WW3 model was not developed during the course of the present study but only used as boundary condition forcing for the SWAN model. Model validation and description is dealt with in Chapter 5. The sensitivities with regards to various boundary conditions are also investigated. More specifically, the effect of regional boundary wave parameterization and reconstruction assumptions are elucidated. Here validation is performed via *in situ* and remotely sensed measurements. The physics associated with wave energy dissipation is also considered. The final chapter then investigated some of the practical limitation of deploying numerical models operationally. Within this chapter a thorough investigation of the computational scalability of SWAN is presented. These experiments were performed on the computing cluster of MetOcean (a division of the Meteorological service of New Zealand). This chapter concludes with a clear recommendation of the

optimal amount of computational resources required to deploy a typical operational or hindcast model. The remaining chapter also use the same operational domain.

## 1.2 Thesis aim and structure

The thesis follows the component structure of the SAWS Wave and Storm Surge (SWaSS) operational set-up. In Figure 1-2 the coupled model, operational low chart is given. The overarching aim of the study was to validate each component of the SWASS model to provide users with confidence in the individual and coupled model performance.

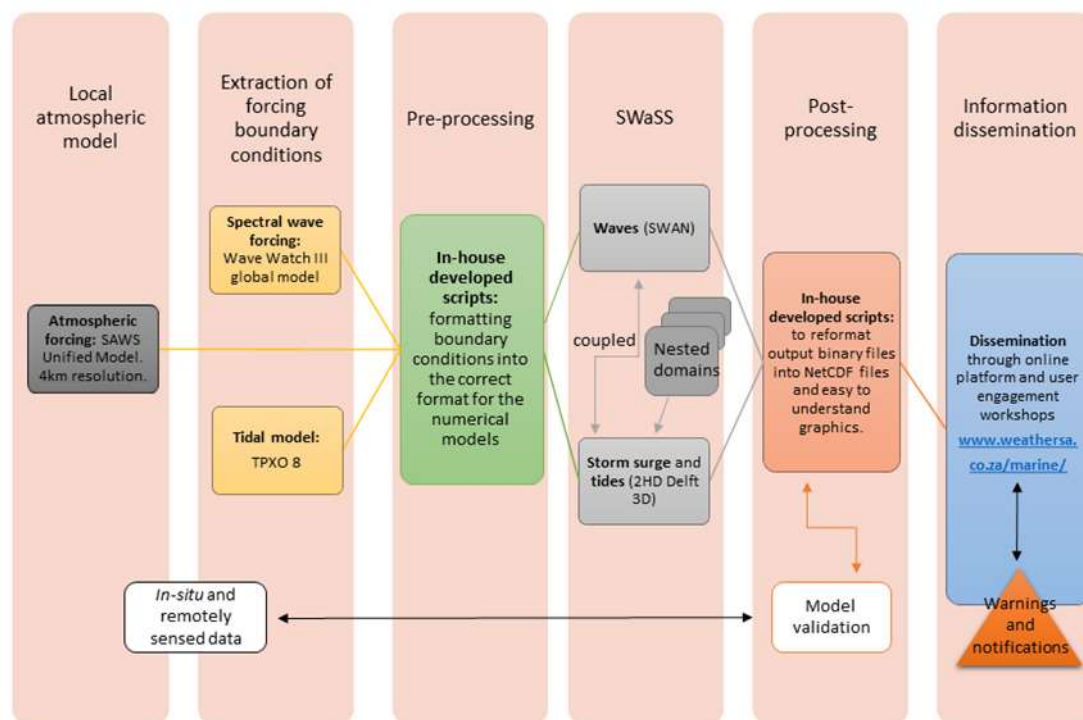


**Figure 1-2: Flow diagram of the operational marine forecasting platform developed during the course of the present study. The operational platform may be found at [www. http://marine.weathersa.co.za/](http://marine.weathersa.co.za/).**

Each chapter thus focused on one aspect of the coupled numerical model that needed to be calibrated and validated. Since so little research has been done with regards to southern African abiotic drivers of coastal vulnerability, each chapter also investigated the appropriate physical dynamics.

Chapter 2 is a short introduction to why this platform was developed and why this study is relevant to both local users and international science. From the establishment of the SAWS marine division in 2018, the decision was made that all the products and services,

that emanates from the group, will be based on robust science and will be made available through peer reviewed literature. This will also help the users to cultivate a perception of trust in the marine forecasts provided.

Next, the tidal validation was performed in Chapter 3. Nine *in situ*, long term, measured water level recording were used for this purpose. Together with the validation of the numerical model deployed in SWaSS, a full description of the South African tidal characteristics was also done. Semi-diurnal, coastal resonance was identified and quantified for the first time. A numerical experiment was included to prove this resonance phenomenon and was used to explain the “higher than normal” tides experienced on the west and south coast of South Africa (adjacent to the broadest extents of the continental shelves). Various two-dimensional comparisons were also made with the TPXO 7.2 and 8, African nested, tidal model. Full tidal characterization was done by means of the Form Factor, tidal ellipse eccentricity and dominant constituent amplitudes and phase lags. This tidal validation and characterisation form the first component of SWaSS in Figure 1-3.

The increased complexity of adding atmospheric and wave dynamics to the water level variations were considered in Chapter 4. Six *in situ* water level stations were used for validation purposes. The calibrated tidal model from Chapter 3 were used as the underpinning tidal fluctuations in the rest of the numerical investigations and operational models. The aim of Chapter 4 was to validate the full, coupled storm surge model. Atmospheric pressure, winds and waves were coupled for these simulations. The depth-averaged model was online coupled with waves (SWAN) while all the atmospheric were only used as drivers and developed outside the scope of the present study. A short description of southern African atmospheric dynamics is included in this chapter. Using the numerical model configuration, the individual contributions of the main drivers of storm surge was investigated. Chapter 4 is conceptualized in Figure 1-3 and leads to the next logical validation of the waves model.

In Chapter 5 the waves component was validated using eight *in situ* wave measurement locations. Seven of these were Datawell wave rider buoys while one was a wave radar system. The latter was the farthest offshore *in situ* measurement location, situated on an oil and gas platform (FH Platform). The regional model was also validated using co-located satellite, altimetry measurements.

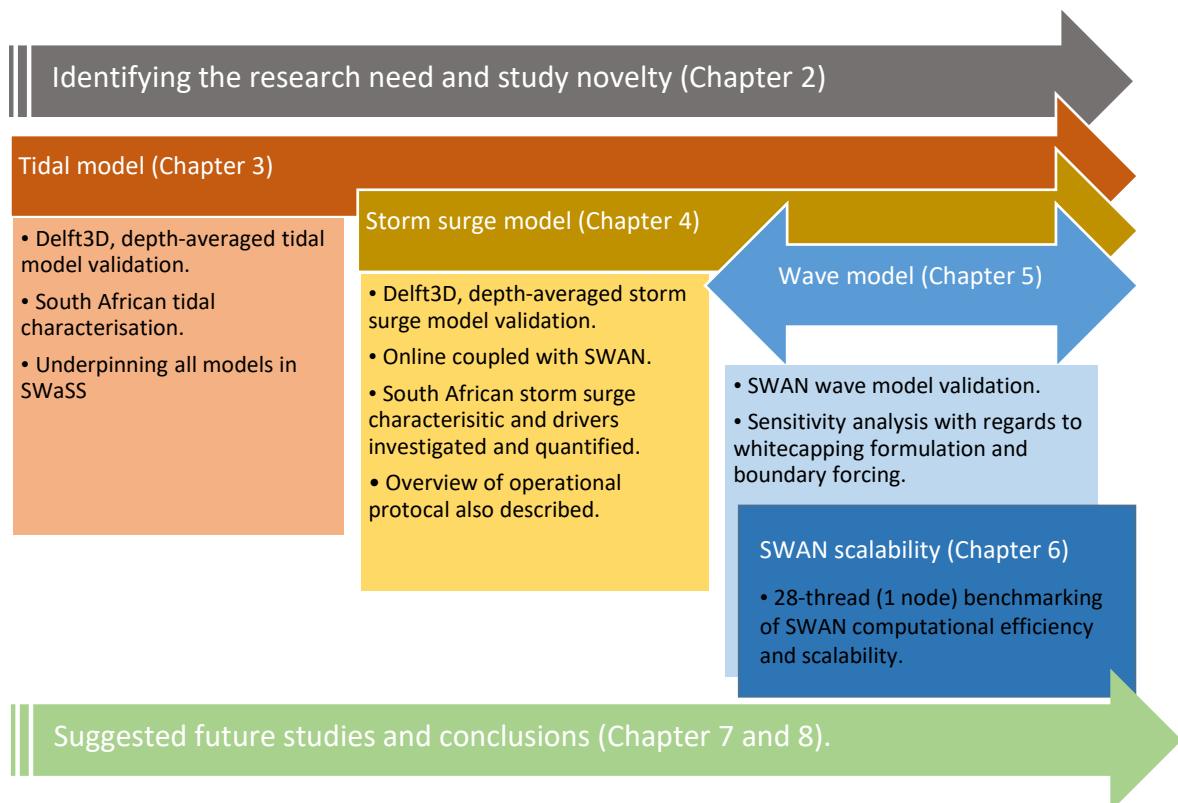


**Figure 1-3: Logical flow of chapters and their relationship with the operational flow depicted in Figure 1-2. All these components together illustrate the developments in the present study. Boundary conditions were extracted from various sources as described in each chapter and Figure 1-2.**

This model component also contained nested computational domains, with local refinement in areas of *in situ* measurements. Beyond the validation of the coupled wave model (e.g. the waves responded to changing storm-tidal levels), the best model configuration was also investigated. Various wave model boundary conditions were tested, including full spectral boundary conditions obtained from a global WW3 model and two different methods of commonly reconstructing spectral boundary conditions. The two most well-known and widely used whitecapping formulations were also used in these sensitivity investigations. In this chapter a full South African wave climatology was also added. In Figure 1-3, Chapter 5 contains another sub-chapter. It was placed within this schematical depiction of Chapter 5 as Chapter 6 focused on benchmarking the wave modelling aspect of the operational system.

Chapter 6 then wraps up the logical flow by exploring some of the practical constraints with developing a new operational service. Only with adequate computational infrastructure can a useful and effective service be established. The scalability of SWAN is investigated by means of the speed-up ratio, efficiency and time-saving ratio. All experiments were performed on a single node with 28-threads. All comparisons were made with regards to the performance change relative to a single thread computation.

## Chapter 2

### *A new era for marine forecasting in South Africa*

---

#### **2.1 Abstract**

This paper focused on science communication. The ocean and coastal societies of South Africa were not accustomed to locally developed, high resolution marine forecasts. This communication was thus one of the marketing attempts to inform both the scientific and recreational users of the new scientific platform available for public use. This paper was accompanied by nationwide information sharing and training workshops to selected key stakeholders.

#### **2.2 Publication details**

Morris, T., Rautenbach, C., & Stander, J. (2019). A new era for marine forecasting in South Africa. *South African Journal of Science*, 115(5/6), 5–6.  
<https://doi.org/10.17159/sajs.2019/6170>

#### **2.3 Author contributions**

T. Morris wrote the publication. C. Rautenbach lead the scientific development of the SAWS Marine research group. He also formulated the suggested overview and focus of the paper. J. Stander was the group director and provided insights and review. The figures were extracted from the operational platform developed by the whole SAWS Marine research group.



#### AUTHORS:

Tamaryn Morris<sup>1</sup>   
Christo Rautenbach<sup>1,2</sup>   
Johan Stander<sup>1</sup>

#### AFFILIATIONS:

<sup>1</sup>Marine Unit, South African Weather Service, Cape Town, South Africa

<sup>2</sup>Department of Oceanography and Marine Research Institute, University of Cape Town, Cape Town, South Africa

#### CORRESPONDENCE TO:

Tamaryn Morris

#### EMAIL:

tamaryn.morris@weathersa.co.za

#### HOW TO CITE:

Morris T, Rautenbach C, Stander J. A new era for marine forecasting in South Africa. *S Afr J Sci*. 2019;115(5/6), Art. #6170, 2 pages. <https://doi.org/10.17159/sajs.2019/6170>

#### ARTICLE INCLUDES:

- ☐ Peer review
- ☐ Supplementary material

#### KEYWORDS:

waves; storm surge; tides; disaster management; weather

#### PUBLISHED:

29 May 2019

# A new era for marine forecasting in South Africa

The International Convention for the Safety of Life at Sea (SOLAS) was established in 1914 as a consequence of the sinking of the RMS *Titanic* in 1912, one of the deadliest peacetime marine disasters and which resulted in the loss of more than 1500 lives. However, the International Meteorological Organisation, born as a direct result of an international maritime conference in 1853, had already initiated weather information for shipping safety, but this was information that the RMS *Titanic* did not believe it needed to heed. In 1950, the World Meteorological Organization (WMO) took on the role of the International Meteorological Organisation, enhancing SOLAS, and establishing METAREAs (geographical oceanic regions in which meteorological information is transmitted to ships) with global responsibilities.

South Africa is responsible for providing marine weather-related information and warnings for the world's second largest METAREA (METAREA VII), which extends from 6°S to the Antarctic continent and from 20°W to 80°E (note from 55°E to 80°E, only south of 30°S falls within the South African METAREA). SOLAS products related to extreme and potentially life-threatening events are disseminated through the Global Marine Distress and Safety Service (GMDSS) and this dissemination is a key objective of the South African Weather Service (SAWS).

Moreover, the SAWS helps neighbouring coastal African countries to assist the ever-growing number of non-SOLAS vessels (i.e. vessels that do not typically undertake international voyages, but must adhere to safety standards according to their size, type and operations). The rapidly increasing coastal populations around the world that are at risk from marine hazards are also an emerging priority. An example is the recent, and devastating, Cyclone Idai, which tore through the port city of Beira in Mozambique. But are we at SAWS doing the very best we can? We believe that the Marine Unit and our novel forecasting system is innovative and extremely helpful.

The oceans are extensively used for commerce and recreation. Shipping is by far the dominant method for global trade and trillions of US dollars pass through the world's harbours annually. The oceans also provide mineral resources such as gas and oil, while precious minerals such as diamonds are mined on the seafloor. Through recreational activities (e.g. ocean liners and sailing yachts, surfers, kite-surfers and beach-goers), the coasts of many countries receive millions of visitors every year – an industry which supports local communities and economies. And, it should be noted, in most countries that have a coastline, much of the population typically lives on the coast.

To manage these issues of safety, an efficient and dynamic marine service is needed – one that can provide essential information that ranges from daily forecasts of passing weather systems and that might impact on safe shipping, to the more extreme and potentially life-threatening events. The latter might include storm surge and destructive wave activity along the coast, hazardous seas in the METAREA, or Marginal Ice Zone navigation and warnings in the Antarctic region.

Marine services not only contribute to shipping information and safety, but also provide information to coastal engineers and environmental managers about best practices of ensuring coastal longevity. Population trends and changing climate conditions have increased the vulnerability of coastal populations and infrastructure, and these are amplified by the effects of weather and conditions in the ocean. Technology has also changed rapidly in the last decade, vastly improving the services historically provided. In addition, effective access, dissemination and alerting systems are critically important for a national meteorological service. For no matter how accurate products are, they must be used wisely in decision-making processes. The ability to facilitate reliable, timely access to information is critical to ensuring that products and services are relevant.

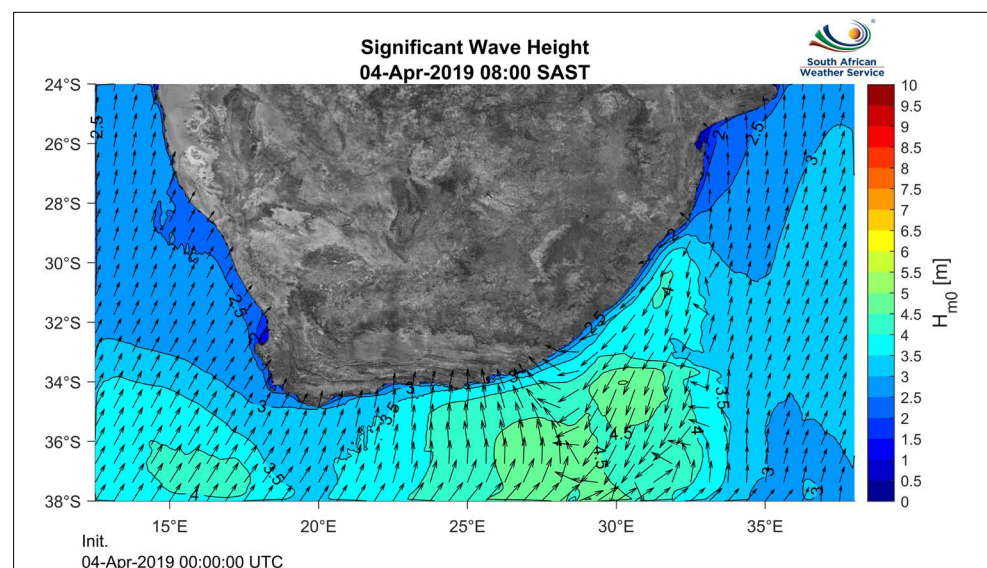


**Figure 1:** Significant wave height forecast for the entire coast of South Africa.

The Marine Unit of the SAWS has developed a dynamic marine forecasting website for all coastal and marine users. The website is primarily used to disseminate operational high-resolution wave, storm surge and tidal forecasts (72 hours), and additional products are planned as the Unit and its website develop. Figure 1 illustrates the regional wave forecast with a high-resolution snapshot of the Cape Peninsula (Figure 2). This forecast allows coastal and



offshore ocean users, disaster management structures and municipal authorities to prepare for potentially damaging situations in real-time. Our forecasts will also assist small-scale commercial fishermen and recreational ocean users, such as surfers, kayakers and long-distance swimmers, to plan their marine activities in the short term. In addition, the website showcases the research that underpins the Marine Unit's products and services. Projects range from those related to infrastructure and observations (such as ocean surface drifters, Argo floats and sea-ice drifters and observations) to the high-resolution numerical prediction of water levels and waves.

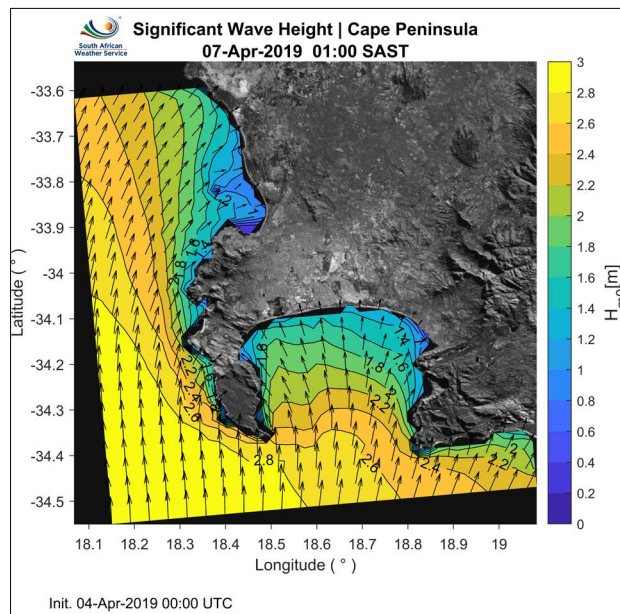


**Figure 2:** High-resolution significant wave height forecast for the Cape Peninsula.

The Marine Unit is a young and energetic team, comprising an applied mathematician, physical oceanographers and marine meteorologists, with technical support. The Marine Master Plan that explains the Unit's objectives and deliverables is new, having been approved by the Executive Board of SAWS little more than a year ago. Yet already the Unit has doubled in capacity and has exceeded expectations within the first year. In addition, the Unit, working under the technical guidance of the WMO and the International Oceanographic Commission, has been requested to develop a marine services implementation plan that is coherent with the implementation plan of the WMO Strategy for Service Delivery and considers practices from the Global Data Processing and Forecasting System.

Users are finding ways to gather and display information in a manner that meets their own needs, regardless of the SAWS's original intention. The way in which products and services are delivered has to change to accommodate risk-based products that are linked to the capacity of users to interpret information. To improve service delivery to users, marine meteorological and climate observations and research must precede the rollout of any new or improved operational products. Rigorous testing of predictive models must occur prior to the use of the product in an operational setting, once their configurations have been improved. Thus, ongoing research should be seen as integral to the service delivery process.

Strong operational and academic collaborations underpin the Marine Unit's success and range from universities and research councils and academic institutions, to environmental consultancy groups, local and national government departments, and coastal engineering companies. The Unit is keen for all users of met-ocean information to peruse the website at [www.weathersa.co.za/marine/](http://www.weathersa.co.za/marine/). A formal survey of different user communities will be initiated shortly to determine the usability and general perception of the portal. Through the survey we hope to make improvements as needed, and our ideal is to service as large a met-ocean community as possible. Informally, marine users have already commented favourably on having 'old-school' synoptic charts and SOLAS communications available under the 'Observations' tab because many seafarers still rely on these systems for their work, particularly further out from the coastline. Other users have been pleased with the coastal automatic weather station map available under the 'Products and Services' tab (observational data), which assists students, engineering teams and coastal users. Through the development of a map and with relevant feedback from stakeholders, the Marine Unit is also able to motivate for additional automatic weather stations in key areas, such as False Bay, where currently only one station, at Strand, is available. The Unit has also begun work on sea-ice observations and, in July 2019, will be deploying sea-ice drifters to understand how sea-ice drifts in the Antarctic region directly south of South Africa may help us to forecast sea-ice movement in the future. Finally, the Unit aims eventually, through the portal, to make available for all users daily, a Forecaster's Synopsis which will summarise what is forecast through the wave, storm surge and tidal forecasts, coupled with information from coastal observations and meteorological forecasts. During extreme events such as storm surges during which flooding of terrestrial regions, potential loss of life and damage to infrastructure may become a possibility, these forecasts will be updated more regularly to assist in informing disaster management and similar organisations.

Should you be keen to participate in our surveys, or would just like to provide feedback, please contact the Marine Coordinator, Tamaryn Morris at [tamaryn.morris@weathersa.co.za](mailto:tamaryn.morris@weathersa.co.za). We look forward to continued and enhanced engagements with our coastal and ocean user communities.

## Chapter 3

### *Tidal characteristics of South Africa*

---

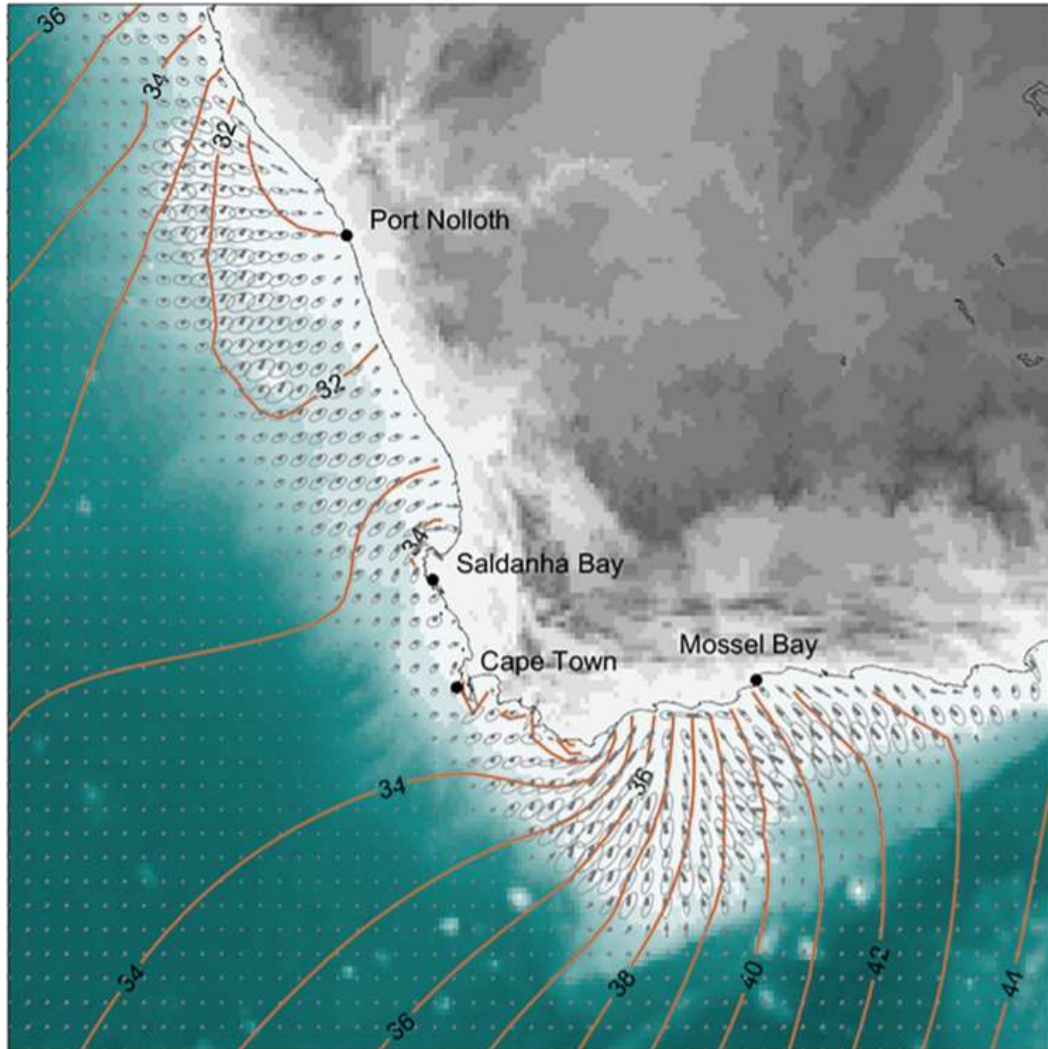


**Figure 3-1:** This image was featured as the cover of *Deep Sea Research 1: Oceanographic Research Papers*, Volume 150, August 2019, 103092, [https://doi.org/10.1016/S0967-0637\(19\)30237-7](https://doi.org/10.1016/S0967-0637(19)30237-7). Southwestern Africa's M2 tidal constituent ellipses and phases (Rautenbach, Barnes, & de Vos, (2019)).



### **3.1 Abstract**

The tidal characteristics of South Africa are explored in the present study by means of a calibrated and validated regional numerical model. The coastal tidal characteristics and semi-diurnal resonance of the South African coastline have yet to be accurately quantified. Model development was conducted in the numerical code Delft 3D for a two-year simulation period. A horizontal model resolution of 1/16th geographical degree was employed. The results were calibrated against long-term measured water levels provided by the South African Navy Hydrographic Office. Model validation was performed for each major constituent's amplitude and phase lag at nine coastal locations around the South African coastline. Regional, two-dimensional comparisons were also made between this study's model results and those of the data assimilative TPXO 8 African regional model. The tide was characterized in terms of constituent amplitude and phase lag, Form Factor and tidal ellipse eccentricity, regional map plots. The model was particularly sensitive to bathymetry-related friction and model resolution. Accurate model results were obtained, providing the first identification and quantification of the semi-diurnal coastal resonance around South Africa. The phase lag associated with the shallower shelf areas is also clearly observed with Form Factor calculations confirming the semi-diurnal dominance of the South African coastline. The intermediate and shallow water friction-induced phase lag of the mixed progressive and standing tidal wave is also mapped, together with the tidal current phase lags.

### **3.2 Publication details**

Rautenbach, C., Barnes, M. A., & de Vos, M. (2019). Tidal characteristics of South Africa. *Deep Sea Research Part I: Oceanographic Research Papers*, 150, 103079. <https://doi.org/10.1016/j.dsr.2019.103079>.

### **3.3 Author contributions**

Dr. C. Rautenbach wrote the manuscript. He also conceptualized the study and paper structure. The underpinning model was developed by Dr. C. Rautenbach as well as the majority of the analysis and scientific insights. Mr. M. Barnes processed some of the tidal signals and assisted in creating the plots. Mr. M. de Vos formatted the raw data into digital formats that could then readily be used for the present study. All authors reviewed the manuscript several times.



## Tidal characteristics of South Africa

Christo Rautenbach<sup>a,b,\*</sup>, Michael A. Barnes<sup>a</sup>, Marc de Vos<sup>a,b,c</sup><sup>a</sup> Marine Research Unit, South African Weather Service, Cape Town, South Africa<sup>b</sup> Department of Oceanography and Marine Research Institute, University of Cape Town, South Africa<sup>c</sup> National Sea Rescue Institute, Cape Town, South Africa

## ARTICLE INFO

## Keywords:

Tide  
Harmonic analysis  
Tidal resonance  
Tidal constituents  
Water level  
Form Factor  
Tidal currents

## ABSTRACT

The tidal characteristics of South Africa are explored in the present study by means of a calibrated and validated regional numerical model. The coastal tidal characteristics and semi-diurnal resonance of the South African coastline have yet to be accurately quantified. Model development was conducted in the numerical code Delft 3D for a two year simulation period. A horizontal model resolution of 1/16th geographical degree was employed. The results were calibrated against long-term measured water levels provided by the South African Navy Hydrographic Office. Model validation was performed for each major constituent's amplitude and phase lag at nine coastal locations around the South African coastline. Regional, two-dimensional comparisons were also made between this study's model results and those of the data assimilative TPXO 8 African regional model. The tide was characterized in terms of constituent amplitude and phase lag, Form Factor and tidal ellipse eccentricity regional by means of map plots. The model was particularly sensitive to bathymetry-related friction and model resolution. Accurate model results were obtained, providing the first identification and quantification of the semi-diurnal coastal resonance around South Africa. The phase lag associated with the shallower shelf areas is also clearly observed with Form Factor calculations confirming the semi-diurnal dominance of the South African coastline. The intermediate and shallow water friction-induced phase lag of the mixed progressive and standing tidal wave is also mapped, together with the tidal current phase lags.

## 1. Introduction

Tides and their effects on coastal and estuarine water levels are one of the most well-known ocean phenomena amongst coastal societies. Nevertheless, important complexities of tidal phenomena can easily be overlooked or misunderstood by coastal scientists and engineers due to the apparent predictability of the tide. Astronomical tides are one of the most predictable forces in the oceans due to our in-depth understanding of the motion of the sun, earth and our moon (Schumann and Perrins, 1982). However, simulating or forecasting the localized tide is not necessarily trivial, as local bathymetry (and associated substrate friction) plays an important role in determining tidal dynamics around coastal and estuarine landmasses. A tide is basically a combination of various long period waves (Holthuijsen, 2007). The result is that the seabed will influence the tides far further offshore than it would shorter waves, such as swell. This is especially true on shallower continental shelves and estuaries, where the tidal and inertial currents are most clearly observed (Jithin et al., 2017; Schumann and Perrins, 1982). According to Canhanga and Dias (2005), characterizing the local tidal behaviour (in terms of tidal heights and currents) is necessary to be able

to understand the complex coastal zone dynamics (both biotic and abiotic). Moreover, initial investigation by Devlin et al. (2017) suggests that changing relative sea levels might even change the characteristics of global tidal behaviour. Zaron and Jay (2014) found supporting results looking at trends in the Pacific Ocean M2 amplitude. Regional changes in tidal characteristics observed in North America have not yet been diagnosed in other parts of the world like Europe, Australasia and Asia (Woodworth, 2010) and few to no studies have been done in southern African waters (Mawdsley et al., 2015). Tidal trends such as those dealt with for the Pacific by Devlin et al. (2017) were investigated for Europe by Devlin et al. (2019). Even though the focus of this study is not to investigate changes in the major tidal constituents around southern Africa, the developing need to understand changes in this regard underscores the importance of a baseline characterization of existing tidal behaviour.

The coastal relevance of tides ranges from human activities and infrastructure (naval and maritime operations, protection of coastal key points and infrastructure) to ecological health and biodiversity. Numerous studies have indicated the importance of tidal variations to nutrient movement (e.g. Yincan et al., 2017), which has a direct effect

\* Corresponding author. Marine Research Unit, South African Weather Service, Cape Town International Airport, 7525, Cape Town, South Africa.

E-mail address: [christo.rautenbach@weathersa.co.za](mailto:christo.rautenbach@weathersa.co.za) (C. Rautenbach).

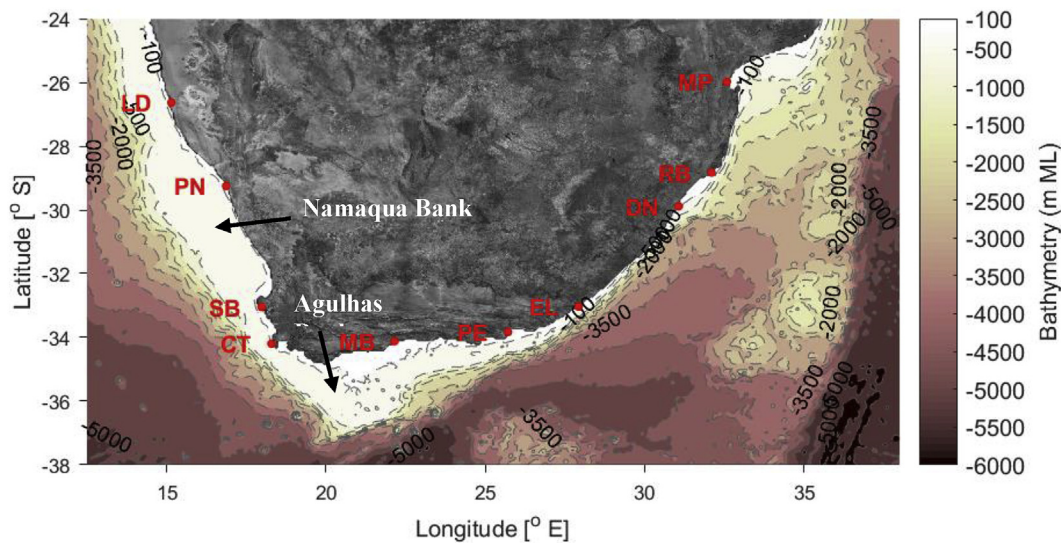


Fig. 1. Southern African bathymetry and major coastal cities.

on coastal ecology distributions and algal blooms (e.g. Lai et al., 2016; Lucas et al., 2014). During flood and ebb, varying water column height can also be associated with a change in coastal water temperature (Li and Zhong, 2009; Susanto et al., 2019), which has a dramatic influence on coastal biodiversity and fisheries, especially in tide dominated coastal flats.

A holistic overview of the accuracy of global barotropic ocean tide models is presented by Stammer et al. (2014). Data assimilative and deterministic hydrodynamic models are presented. In total 15 models were assessed, with the TPXO 8 model having the highest regional resolution ( $1/30^{\text{th}}$  of a geographical degree). The present study focused on the TPXO 8 validation (Stammer et al., 2014) but also included TPXO 7.2 results, as the latter has been widely used in previous studies (Daher et al., 2015).

This study presents the calibration and results of a newly developed tidal numerical model for South Africa. This model was developed in support of a coupled (atmospheric, wave and water level) storm surge model at the South African Weather Service (SAWS). To be able to predict elevated water levels accurately, a thorough understanding and thus, appropriate model, of the underlying tidal behaviour is required. In the past, some studies described the variation of the tide, coastal trapped waves (CTW), inertial oscillations and storm surge around the South African coast using various measurement and modelling campaigns (e.g. Brundrit, 1984, 1995; Mather and Stretch, 2012; Schumann, 1983; Schumann and Perrins, 1982; R. Van Ballegooyen, 1991). However, none of these studies presented the South African tidal characteristic holistically, having been based on sporadic measurement periods and locations and simplified numerical models.

In addressing this gap, this study aims to present the tidal patterns and characteristics for the South African coastline in both phase and amplitude for the primary (largest amplitude) tidal constituents. Comparisons between the TPXO 8 (G. D. Egbert and Erofeeva, 2002; Stammer et al., 2014) and the SAWS Tidal Model (TM) are also presented. Tidal levels and constituents derived from measured water levels from the South African Navy Hydrographic Office (SANHO) were assumed to be the benchmark for accuracy throughout the study. The characterization of the tidal behaviour was thus achieved by means of space-varying amplitude and phase lag plots, Form Factor analysis and tidal ellipses. The SAWS-TM model was employed to investigate and confirm the importance of the continental shelves for coastal semi-diurnal resonance (tidal amplification) and to present depth-averaged tidal currents. The extreme tidal currents are also illustrated 3 h after the initiation of both ebb and flood. The SAWS-TM water level results

were validated both in 2D using map plots, and via time series (including long-term tidal constituent amplitude and phase). Previous studies have only described some of the tidal constituents around the South African coast, accompanied by a high-level description of the tidal classification. The analysis, mappings, validations and regional characterizations, along with the identification and quantification of the shelf induced coastal resonance, are a first for southern Africa.

## 2. The study region

South Africa lies between the Indian and Atlantic Oceans (off the east and west coasts respectively). The country is situated between two semi-permanent atmospheric high-pressure cells. As a result, South Africa is a relatively dry country. The country receives predominantly summer rainfall via thunderstorms which are driven by heating of the interior and the presence of tropical moisture from the north and east (Engelbrecht et al., 2011; Reason et al., 2006). The south-western parts of the country are influenced by extra-tropical low pressure systems from the south, however, resulting in winter rainfall. The climatic differences between the western and eastern parts of the country are heavily influenced by the surrounding oceans. The cold Benguela current running along the west coast results in dry, semi-arid conditions. This cooler current does result in frequent advective fog banks over the west coast year-round, however. The warm Agulhas current flows southward along the east coast before separating from the south-east coast and turning westward (Hutchinson et al., 2018). It results in moist, humid, subtropical conditions on the east coast.

South Africa is the most southerly country in Africa and boasts a coastline of approximately 3000 km. Like many other countries in the world, a large percentage of the South African population resides within close proximity to the coast (Findlay, 2018). The bathymetry surrounding southern Africa is given in Fig. 1 together with the location of all the major coastal towns (Port Nolloth (PN), Saldanha Bay (SB), Cape Town (CT), Mossel Bay (MB), Port Elizabeth (PE), East London (EL), Durban (DN) and Richards Bay (RB). Luderitz (LD) in Namibia and Maputo (MP) in Mozambique, are also indicated.

In general, South Africa does not have a broad continental shelf, with the widest part extending southward offshore from Mossel Bay on the south coast (the Agulhas Bank). On the west coast, close to Lüderitz, Port Nolloth and Hondeklipbaai (HKB), the Orange River Fluvial Bank (in this manuscript called the Namaqua Bank) is the second broadest part of the South African continental shelf (R. C. van Ballegooyen, 1995). These broader shelf regions are known to be the bathymetric

cause of increased variability in water levels on the western and southern South African coasts (R. C. van Ballegooyen, 1995; Daher et al., 2015; Schumann, 1983; Schumann and Perrins, 1982). These wide, shallow areas are also suspected to be the origin of CTWs around the South African continental shelf (R. C. van Ballegooyen, 1995; Illig et al., 2018).

On the east coast of South Africa, the continental shelf is narrow, allowing the Agulhas current (a strong western boundary current) to meander close to the coast, resulting in higher water temperatures in contrast with the cold Benguela upwelling water on the west coast. The Benguela current should not be thought of as a strong current (like a western boundary currents) but must rather been seen as a slow northward moving current that can occasionally reverse in direction (Jackson-Veitch et al., 2010). Eddies may also be present. The west coast is known for its nutrient rich, cold, upwelling water and is thus associated with a very productive ecosystem, resulting in fisheries being the main source of the west coast GDP (Findlay, 2018; Sainsbury et al., 2018).

Schumann and Perrins (1982) presented some of the first research describing the semi-diurnal and diurnal tidal behaviour around South African's south and west coasts. They emphasized the importance of the Agulhas current off the east coast of South Africa and argued that due to its dominance, the energy associated with tidal currents can be negligible (Schumann and Perrins, 1982). The energy spectrum contribution of tidal and inertial currents becomes more important on the broader continental shelves where the energy spectrum is not dominated by a western boundary current. The tidal fluctuations are predominantly barotropic (surface fluctuations) while the inertial fluctuations tend to be mainly baroclinic (internal water column fluctuations) (Schumann and Perrins, 1982). The latter is mainly due to the complex vertical stratification of the water column on the west coast. These studies were based on a modal analysis performed on moorings on the west, south and east coasts of South Africa (Schumann and Perrins, 1982).

The northeastern coastline of South Africa (bordering Mozambique) is also occasionally subject to extreme wave and water level events associated with tropical cyclones traversing down the Mozambique Channel (Cabral et al., 2017).

The south coast of South Africa, adjacent to the Agulhas bank, is the coastal region which frequently experiences storm surge events (Searson and Brundrit, 1995b). This predisposition to high water levels is also reflected in the highest astronomical tide (HAT) as published by the South African Navy Hydrographic Office (SANHO) in Table 1, with Hermanus (HM) and Knysna (KN) abbreviated as indicated.

Searson and Brundrit, (1995a), presented the maximum observed water levels together with the maximum tidal levels for the entire South African coastline. They found that the maxima around the coastline for both variables were observed around Mossel Bay (south coast), followed by those around Port Nolloth (west coast), which were approximately 40 cm lower. Tidal waves propagate around the South African coast from the west to the east with the shoreline (in the southern hemisphere) to the left of the wave propagation direction (Schumann and Perrins, 1982). As the astronomic barotropic tide is not notably influenced by the narrow continental shelves, the South African tidal range does not exhibit high amplitude variability. Spring tide amplitudes range between 1.4 and 1.8 m and neap tide range between

0.5 and 0.6 m (Schumann and Perrins, 1982) with the maximum tidal amplitude adjacent to the broader shelf areas as mentioned previously.

### 3. Methodology

#### 3.1. Data

##### 3.1.1. Water level time series data

The South African Navy Hydrographic Office (SANHO) provided the time-series water level measurements utilized in the present study. In Table 2, the main tidal constituents are provided for 11 key points around the South African coastline, based on harmonic analysis of measurements. These measurements are obtained from a permanent tide gauge network owned and maintained by the SANHO. These values are accepted as the most accurate descriptors of the tidal constituents around South Africa as they are based on harmonic analysis of long time series, some of which date back to the 1960s.

Astronomical tidal periods have been grouped into species of tidal constituents. Each constituent is then identified based on a characteristic wave period. Constituents are usually grouped into periods centered at semi-diurnal, diurnal and longer-periods (Jay, 2009; Schumann and Perrins, 1982). The main semi-diurnal and diurnal tidal constituents considered in this study are listed in Table 3, based on the size of their amplitudes and species.

Water level recordings are provided at an hourly sampling rate. The numerical model used in the present study used a time step of 1 min and could thus provide output at any location at any multiple of 1 min (refer to Section 4.3 for more detail regarding the numerical model). From Table 2 it is evident that South Africa has a predominantly semi-diurnal tide because these constituents' amplitudes are an order of magnitude larger than the diurnal constituents (Canhanga and Dias, 2005). This was also confirmed using the Form Factor, as discussed in Section 6.3.

The amplitudes and phases provided in Table 2 are compared to the present study's model results in Section 5.2. Here it was concluded that the model produced reasonable amplitudes as compared to the long-term measurement harmonic analysis. All SANHO data were transformed from UTC + 2 to equilibrium theory (tidal datum and Greenwich phase epoch) (Cartwright and Tayler, 1971; Doodson and Warburg, 1941; D. T. Pugh, 2001). The equilibrium tide is one with idealized tidal constituents describing the propagation of the tides on a landless earth, measured from the Greenwich meridian (0° longitude) (Schureman, 1971). During the validation performed in Section 5.2, nodal/satellite, inference (M.G.G. Foreman and Henry, 1989) and reference dates corrections were thus taken into account using the freely available harmonic analysis code U-Tide (Codiga, 2011).

In Fig. 2, an example of the fortnightly spring-neap water level cycle observed at Mossel Bay is provided. As in Mozambique (Canhanga and Dias, 2005), the spring-neap cycle and daily inequality are important around the South African coast. Mean high water spring (MHWS) is the annual mean height of high water during spring tide periods referenced to Chart Datum (SA Navy, 2018). Thus, once per fortnight, a contribution to the average is calculated. The difference between the MHWS and mean low water spring (MLWS) can also be thought of as the mean spring tide range (MSR) and is approximately 1.5 m around the South African coastline (SA Navy, 2018). These values and their associated ranges are provided in Table 1. Similarly, the mean neap range (MNR) between the mean high water neaps (MHWN) and mean low water neaps (MLWN) can be calculated and is approximately 1 m around the coastline. Generally, the maximum tidal range around the South African coast has not exceeded 2.2 m over the last 20 years (SA Navy, 2018).

These tidal ranges are moderate compared to other locations around the world. Burcharth et al., (2007) reported on the observed macro-tidal environment MSR (of the predominantly semi-diurnal tide at Elbe estuary mouth in Germany) as 5.3 m. The MNR has been reported with a maximum value of 2.9 m and the spring tidal range can go as high a

**Table 1**

Heights above Chart Datum (CD) (in meters) at selected South African ports (SA Navy, 2018), with the Highest Astronomical Tide (HAT), Mean Level (ML), Mean Spring Range (MSR) and Mean Neap Range (MNR).

Place	PN	SB	CT	ST	HM	MB	KN	PE	EL	DN	RB
HAT	2.25	2.03	2.02	2.09	2.07	2.44	2.21	2.12	2.08	2.3	2.47
ML	1.09	0.99	0.98	1.00	1.02	1.17	1.06	1.04	1.02	1.11	1.20
MSR	1.63	1.51	1.49	1.55	1.51	1.84	1.69	1.65	1.59	1.80	1.84
MNR	1.12	1.03	1.01	1.05	1.02	1.20	1.10	1.08	1.02	1.15	1.21



**Table 2**

Amplitude and phases of the primary tidal constituents for 11 key points around the South African coastline. All amplitudes are in meters and phases in degrees. Constituents are based on harmonic analysis of water level measurements with total record length in years (as indicated) until November 2018 and relative to UTC.

City	Code	Record [years]	M2		S2		O1		K1	
			Amp	Phase	Amp	Phase	Amp	Phase	Amp	Phase
Port Nolloth	PN	52	0.549	32.19	0.232	50.04	0.019	221.55	0.054	91.93
Saldanha Bay	SB	32	0.503	32.78	0.219	52.23	0.015	231.76	0.057	105.70
Cape Town	CT	40	0.498	34.98	0.218	54.89	0.015	235.17	0.058	109.46
Simon's Town	ST	51	0.514	33.25	0.229	53.25	0.016	233.76	0.059	112.72
Mossel Bay	MB	40	0.588	42.87	0.298	66.39	0.019	254.46	0.072	136.86
Knysna	KN	39	0.545	51.43	0.271	76.97	0.019	268.87	0.064	144.13
Port Elizabeth	PE	33	0.522	43.13	0.271	69.71	0.016	265.91	0.059	137.85
East London	EL	30	0.507	46.13	0.271	73.47	0.015	278.83	0.057	141.25
Durban	DU	37	0.561	43.77	0.311	75.17	0.016	298.47	0.052	145.71
Richards Bay	RB	30	0.594	44.67	0.337	77.53	0.018	306.95	0.049	149.46

**Table 3**

The period of the six main semi-diurnal and diurnal tidal constituents.

Species	Tidal constituent	Period [hours]
Semi-diurnal	M <sub>2</sub> (principal lunar)	12.42
	S <sub>2</sub> (principal solar)	12.00
	K <sub>2</sub> (lunisolar declination)	11.97
Diurnal	O <sub>1</sub> (principal lunar)	25.82
	P <sub>1</sub> (principal solar)	24.07
	K <sub>1</sub> (lunisolar declinational)	23.93

6 m. Other large spring tidal ranges include the Bay of Fundy, the Bristol Channel and water levels on the Argentinian shelf, all of which can exceed 10 m (D. T. Pugh, 2001). It should also be noted that there are some embayments with near zero tidal ranges (Yincan et al., 2017) and thus the South African tidal ranges may be described as moderate.

### 3.1.2. TPXO data

The offshore boundary conditions for the numerical model, (see Section 4.3), were obtained from the TOPEX/Poseidon Global Inverse Solution (TPXO) (G. D. Egbert and Erofeeva, 2002; G. Egbert and Erofeeva, 2010). This product is the least squares best fit of the Laplace Tidal Equation and remotely sensed altimetry data. New versions of the TPXO model are frequently released when updated bathymetry is available and more data assimilations are performed (G. Egbert and Erofeeva, 2010). Tidal constituents were extracted along the present study's model boundaries. Where the bathymetry has steep gradients (continental shelf edges), higher resolution boundaries were extracted. For example, a constituent-set per computational grid cell boundary was used (as opposed to one set per few grid cells) to ensure that the

higher variability in these areas is communicated into the numerical model. TPXO provides eight primary, two long-period and three non-linear harmonic constituents (both amplitudes and phase lags) (G. Egbert and Erofeeva, 2010). Only 13 constituents were used for the present study (M2, S2, N2, K2, K1, O1, P1, Q1, MF, MM, M4, MS4 and MN4) and were confirmed to be sufficient in Section 5. Furner, Williams, Horsburgh and Saulter (2016) performed sensitivity analysis regarding the number of constituents required for accurate tidal prediction at United Kingdom (UK) ports. They also found that using 14 constituents (implemented by the UK Met Office's baroclinic NEMO model) described most of the tidal variation and that higher order constituents made little difference. The TPXO 8 model output with a resolution of 1/30<sup>th</sup> of a geographical degree was employed in the present study.

### 3.1.3. Bathymetry data

The majority of the model bathymetry was obtained from the General Bathymetric Chart of the Oceans (GEBCO). In the nearshore, higher resolution datasets from the SANHO were used. The model utilized in the present study was developed in support of a South African national storm surge model. To this end, a resolution of 1/16<sup>th</sup> of a geographical degree was used, as implemented successfully in the UK operational water level forecasting systems and now in the South African system as well (e.g. Furner et al., 2016; Neill and Saulter, 2017; O'Neill et al., 2016). The extent of the model domain is also provided in Fig. 1 (24S–38S and 12.5E to 38E).

In the present study the influence of various resolutions of coastal bathymetry was investigated. A first set of simulations was performed using only GEBCO data, followed by tests utilizing a hybrid of the GEBCO and higher resolution nearshore bathymetry. The results are

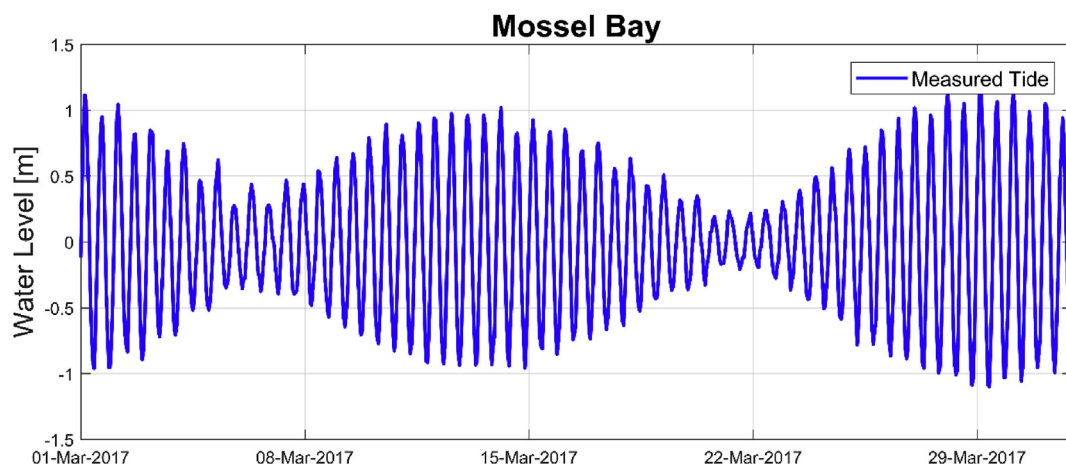


Fig. 2. Measured tidal water level over two spring tide cycles, highlighting the importance of the cycle.

presented in Section 5.1. The increase in coastal bathymetry resolution had a marginal effect on enhancing the numerical model prediction. The main reason for this is suspected to be due to the computational grid resolution which did not fully harness the benefit of higher bathymetric resolution. Similar tests on short-crested spectral wave model results (developed as part of the greater storm surge model) resulted in exceptional increases in prediction accuracy. This can be expected in coastal areas where local wave refraction may have a notable effect on short-crested wave propagation. Following the results of Section 5, the hybrid GEBCO-SANHO bathymetry was assumed to be adequate for the purposes of the present study (refer to Fig. 1).

### 3.2. Tidal analysis

The numerical model was used to produce both two-dimensional (map) and one-dimensional (time-series) output. Both of these were employed to describe the tidal characteristics of South Africa. The map results were compared to the output from the TPXO 8 model. These results are presented via difference map plots for all the primary lunar and solar constituents in Section 5.2.1.

In order to compare the time series of water level recordings to those produced by the model the root mean squared error (RMSE) was calculated and harmonic analyses were performed. The latter were performed using the freely available Unified Tidal (U-Tide) package (Codiga, 2011). The harmonic analysis package, T-Tide, was also employed due to the large number of previous studies making use of this tool (e.g. Leffler and Jay, 2009; Pawlowicz et al., 2002). Previous studies successfully employing T-Tide for the harmonic decomposition of water level signals include Chevane, Penven, Nehama, & Reason (2016); Fernández-Montblanc et al. (2019); Leffler & Jay (2009); Vilibić et al. (2018); Zhao et al. (2019). These packages can also be used for nodal and inference corrections; e.g. compensating for the start time of the model or measurement time series (including time zone) and correcting both phase lag and amplitude for some unresolved, smaller constituents. The modulation associated with the lunar perigee (period of 8.85 years) and the movement of lunar nodes (period of 18.61 years) are just two examples of a long-term and nodal corrections applied (Godin, 1986, 1993; Haigh et al., 2011; Pawlowicz et al., 2002; Penna and Stewart, 2003). As such, these packages take both the time-series start time and the time series latitude as input. The geodetic functions used by T-Tide to determine the equilibrium amplitude vary with species (groups of constituents with similar periods), latitude and some constants such as the radius of the earth and the masses of the earth, moon and sun (Pawlowicz et al., 2002). For each analysis performed in this study, the appropriate time-series start time and latitude were provided together with the time-series. For the purposes of this study, the time series harmonic analysis thus refers to:

$$\eta(t) = a_0 + \sum_{n=1}^N f_n a_n \cos(\omega_n t - \alpha_n + \beta_n), \quad (1)$$

where  $a_0$  is the mean sea level,  $a_n$  is the amplitude determined for constituent  $n$ ,  $f_n$  is the amplitude nodal correction,  $\omega_n$  is the angular velocity of constituent  $n$ ,  $t$  is time,  $\alpha_n$  is the phase lag and  $\beta_n$  is the nodal phase correction (Bosboom and Stive, 2015; M.G.G. Foreman and Neufeld, 1991). The resulting total water level at a particular time step  $t$  is then given by  $\eta(t)$ .  $N$  was set to the 13 largest constituents.

Even though some of the nodal modulations (or major constituents' minor satellite frequencies resulting from long-period modulations and perturbations) are taken into account (Godin, 1986; Haigh et al., 2011), there are some constraints on the time series that still need to be considered. If the water level model output or measurement campaign is shorter than a year, the annual solar constituents (Sa) will not be adequately resolved (Penna and Stewart, 2003). The output or sampling frequency must also be high enough to resolve the highest frequency constituents. In the present study a temporal output resolution of half

an hour was used, spanning a total of two years (2015–2017) which should also be sufficient for applying inference. It should still be noted that for short time-series records (e.g. shorter than nine years), long-period corrections might still be contaminated by smaller constituents (Pawlowicz et al., 2002). The treatment of inference also breaks down in T-Tide when the tidal amplitude reference constituent approach zero (e.g. close to an amphidromic point) (Codiga, 2011).

Thus the updated U-Tide analysis and prediction package was also employed in the present study (Codiga, 2011). This package presents some improved functionality compared to T-Tide. An example of this includes the two-dimensional generalization of the harmonic tidal analysis presented by Mike G.G. Foreman, et al. (2009), and thus provide exact times in nodal/satellite corrections and exact constituent inference (Codiga, 2011). This compared to the post-fitted, linearized times of T-Tide. Through these advances, nodal/satellite corrections, for time-series records shorter than one to two years, can be accurately estimated and inference correcting can be made for multiple constituents by making use of a single reference (Codiga, 2011).

The main goal of U-Tide was to collate all the previous tidal analysis methods. The main advancement in U-Tide is that it can handle multi-year, non-uniformly spaced time series records and gaps in data. Resistance against outliers and broad spectrum environmental noise (as presented by U-Tide vs. T-Tide) are more important for measured water levels than for consistent model outputs (Leffler and Jay, 2009). Nevertheless, both T-Tide and U-Tide analyses were performed and found to produce near-identical results for the two-year simulation results. Consequently, the remainder of the study will present only the U-Tide analysis.

### 3.3. Numerical model

For convenience, the numerical model developed during the course of the study will be called the South African Weather Service - Tidal Model (SAWS-TM).

According to Waterhouse et al. (2011), in deep water the tides propagate according to the wave equation (where the phase speed is independent of bottom friction). In shallow water, however, the tides propagate according to the diffusion relation, where bottom friction and advection are not neglected. The shallow water equations are taken into account via the shallow water approximations of the Navier-Stokes equations (Bosboom and Stive, 2015). The present study used the Delft3D numerical code developed by Deltares in the Netherlands (Deltares, 2018), and solves the governing equations for incompressible free surface flow. Using this numerical package, a few approximations and assumptions were made:

- Only a depth-averaged (2D) model was employed, without atmospheric or wave forcing. Atmospherics and waves were however added to the complete storm surge model.
- Variable density is only taken into account in the pressure term, also known as the Boussinesq approximation (Canhanga and Dias, 2005; Deltares, 2018),
- The long wave equation is solved using hydrostatic pressure. Short crested waves are not solved (Deltares, 2018).

The numerical grid is a rectangular grid with 1/16th geographical degree resolution in spherical coordinates, extending from 12.5 °E to 38 °E and 24 °S to 38 °S. Space and time-varying water level boundary conditions are provided on the open model boundaries using the TPXO 8 model constituents. Tide generating forces are also computed in the model domain itself. The model was executed with a 60 s time step and a five-day spin-up time (even though the model stabilized much sooner for most of the coastline).

The validation documentation provided by Deltares details the usefulness of Delft3D-Flow for the purposes of tidal modelling (Breyiannis et al., 2016; Deltares, 2008, 2018). Other studies employing

a similar methodology include Canhanga & Dias (2005), Chevane et al. (2016), Furner et al. (2016), Sete (2010) and Zu et al. (2008).

#### 4. Model calibration and validation

All of the model calibration simulations were performed for March, April and May 2017. These months were chosen as they represent typical autumn months without extreme weather events. A time series of three months was assumed to be representative of the typical spring-neap tidal cycle observed around the South African coastline (refer to Fig. 2). All of the model validation was conducted over two years, from 2015 to 06-01 to 2017-07-01. This time period was assumed to be adequate to analyze all of the major tidal constituents (refer to Section 4.2). In all cases the first five days of the numerical computations were ignored and assumed to be model spin-up time.

##### 4.1. Calibration

The three most important parameters for tidal modelling are bathymetry, tidal boundary conditions and bottom friction description and associated coefficients (Furner et al., 2016). In order to ensure that the SAWS-TM yielded accuracies which were fit for the purpose of this study, numerous calibration simulations were conducted. Each simulation was conducted by varying only one key configuration parameter at a time. The full list of parameters which were tested includes the tidal body forcing, open boundary reflection parameter, initial condition, bottom friction formulation and coefficients, horizontal eddy viscosity and bathymetry resolution. Of these, the bottom friction parameter had the greatest effect on the accuracy of the tidal simulation.

A brief description of each parameter, as a summary of its calibration results are presented in Section 5.1.1 to 5.1.4. It should be noted that the descriptions do not represent an exhaustive list of calibration tests. For the sake of brevity, a selected subset illustrating the effect of each parameter is given in each test case. The performance of each calibration setting was determined via direct comparison with the SANHO measured tides for each tidal station.

##### 4.1.1. Tidal forcing

This parameter stipulates whether the simulation of water levels should take into account the direct local influence of the forces which generate the tide (Deltaires, 2014). For smaller coastal water level models, these forces are often neglected. Given the large model domain in this study, the impact of including local tidal forcing was assessed. Interestingly, the effect of tidal forces on the simulation of water levels at various measurement sites was marginal. A mean improvement in RMSE between the nine measurement sites of 2 cm was obtained by including local tidal forcing. Thus all subsequent calibrations were conducted with local tidal forcing included.

##### 4.1.2. Bottom roughness

The bottom roughness associated with the seabed has an impact on the ease with which the progressive tidal wave propagates over it. This parameter can be set as a constant or made to vary spatially (as it would in reality with varying substrates, for example). In this study, a quadratic friction law is used to determine the shear stress at the seabed induced by a depth-averaged flow:

$$\vec{\tau}_b = \frac{\rho_0 g |\vec{U}|}{C_{2D}}, \quad (2)$$

where  $|\vec{U}|$  is the magnitude of the depth-averaged horizontal velocity,  $g$  is gravitational acceleration,  $\rho_0$  is the density and the 2D Chézy coefficient,  $C_{2D}$  [ $m^{1/2}/s$ ], is determined by one of three available formulations:

- The direct Chézy formulation is a useful first estimate of  $C_{2D}$  and

recommended values are water depth ( $H$ ) + 25 (Deltaires, 2018).

- The Manning's formulation,  $C_{2D} = \frac{49}{n}$ , where  $n$  is the user-specified Manning coefficient [ $s/m^{1/3}$ ]. Tests were conducted by increasing and decreasing  $n$  from its typical value of 0.02  $s/m^{1/3}$  (Deltaires, 2018).
- The White-Colebrook's formulation,  $C_{2D} = 18 \log\left(\frac{12H}{k_s}\right)$ , where  $k_s$  is the user-specified Nikuradse roughness length [ $m$ ]. Tests were conducted by varying  $k_s$  between 0.01 m (typical of very smooth surfaces), 0.15 m (typical of river beds) and 1.00 m (extremely rough surfaces) (Deltaires, 2018).

Manipulation of the Chézy coefficient (changing the value of  $C_{2D}$ ) and stipulating which of the above three formulations to use is the method by which the effect of varying bottom roughness was investigated. A total of 23 simulations were conducted which tested varying bottom roughness formulations directly. Ultimately, a constant direct Chézy coefficient value of 90 [ $m^{1/2}/s$ ] proved to be most successful, in agreement with the model settings employed by Sembiring et al. (2015). This approach allowed for an average (across calibration sites) modeled water level RMSE of approximately 8.9 cm.

##### 4.1.3. Bathymetry

Sensitivity was tested via two separate experiments. One using the GEBCO data set only and the other by merging it with the higher resolution datasets around the sites of interest, provided by SANHO (refer to Section 4.1.3). The effect of the higher quality bathymetry was then tested against the previous optimal configuration, but revealed no noticeable advantage. This is likely due to the horizontal grid resolution being too low to harness the potential of higher resolution bathymetry.

##### 4.1.4. Final flow model configuration and accuracy

The final parameter settings for the flow configuration are given in Table 4. This configuration, together with the other calibration parameter settings described in the present section, yielded an average RMSE for all nine coastal stations of approximately 8.9 cm between the SANHO measured tides and the SAWS-TM.

Fig. 3 gives a time series of March 2017, produced by the SAWS-TM with the final calibration configuration at (a) East London and (b) Durban (refer to Fig. 1). These sample time series show that the SAWS-TM captures the phasing and amplitude of the tide along the South African coast adequately.

In Table 5, the calibration results are given via standard statistical measures. The definitions of the bias between measured and model outputs and the root mean square error (RMSE) are defined as follows:

$$bias = \frac{1}{n} \sum_{i=1}^n (y_i - x_i), \quad (3)$$

$$RMSE = \sqrt{\frac{1}{n-1} \sum_{i=1}^n (y_i - x_i)^2}, \quad (4)$$

where each calculation is performed with a series of  $n$  values,  $y$  are the model values and  $x$  is the measurements for the corresponding time step. The Willmott index (Willmott et al., 2012), bound between [0,1],

**Table 4**  
Delft3D-Flow study configuration.

Description	Value	Unit
Time step	1	Minutes
Smoothing time	60	Minutes
Number of vertical layers	1 (depth averaged)	–
Advection scheme for momentum	Cyclic	–
Boundary reflection parameter ( $\alpha$ )	100	$s^2$
Horizontal Eddy Viscosity	100	$m^2/s$

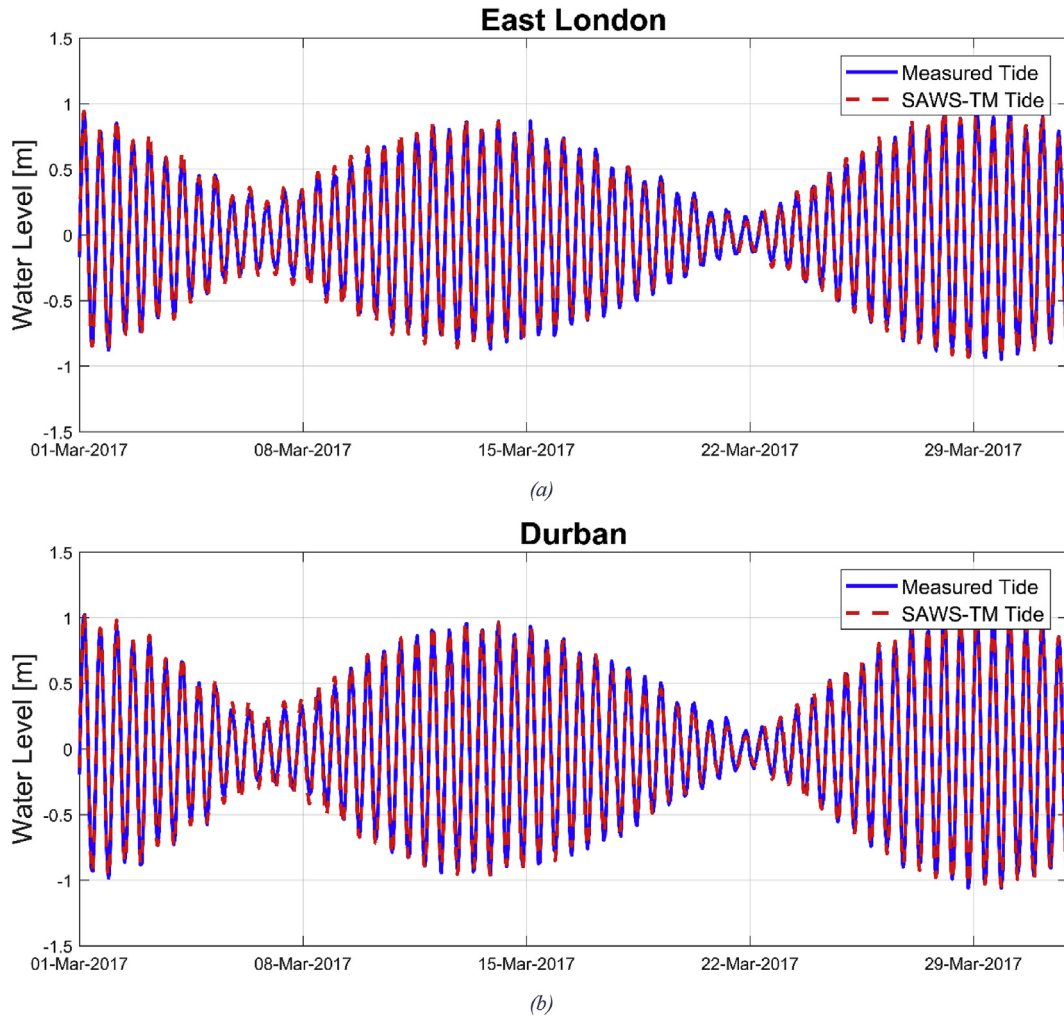


**Fig. 3.** (a) SAWS-TM time series output at East London compared against the measured tide provided by SANHO and (b) is the same comparison but at Durban.

was also employed in the present study and is defined as:

$$Willmott = 1 - \left[ \frac{\sum_{i=1}^n (y_i - x_i)^2}{\sum_{i=1}^n (|b'_i| - |x'_i|)^2} \right], \quad (5)$$

where  $y'_i = y_i - \bar{x}$ ,  $x'_i = x_i - \bar{x}$  and  $\bar{x}$  is the average of all the measured data. A Willmott index of 1 implies a perfect match between measurements and model outputs. These statistics were performed by comparing measured tides against the model outputs for March, April and May of 2017. These values are reasonable given accuracies obtained in other regions of the world employing a similar methodology (Fernández-Montblanc et al., 2019).

## 4.2. Validation

### 4.2.1. 2D tidal validation against TPXO 8

The TPXO 8 model is an updated version of TPXO 7.2 (Stammer et al., 2014). TPXO 7.2 is widely accepted to produce a good

approximation of the propagation of tides globally (Haigh et al., 2011). The present study conducted a spatial comparison of the SAWS-TM with TPXO 8. TPXO 8 provides output at a 1/30<sup>th</sup> geographical degree resolution and thus the 1/16<sup>th</sup> degree SAWS-TM output was only compared to TPXO 8 at the same output locations. Difference plots of both the amplitude and phase lag of the three largest amplitude semi-diurnal ( $M_2$ ,  $S_2$  and  $N_2$ ), and largest diurnal ( $K_1$ ) constituents are given in Fig. 4 and were created following harmonic analysis of SAWS-TM. Although the relationship between these amplitudes varies around the coastline, the  $K_1$  amplitude accounts fairly consistently for ~8% of the tidal range.  $M_2$  and  $S_2$  contribute approximately 75% of the total amplitude signal. The two primary semi-diurnal constituents are thus the most important for predicting the South African astronomical tide.

From Fig. 4, the tidal amplitude differences are acceptable, especially since South Africa is a predominantly semi-diurnal tidal coastline. Amplitude differences are relatively small compared to differences reported in similar studies (Furner et al., 2016). Differences are most

**Table 5**

Standard statistical comparison of the measured tide and model calibration results for March, April and May 2017. Simons Town statistics were only compared to measurements for May 2017 due to data availability.

Location	CT	ST	MB	PE	EL	DU	RB
RMSE	0.084	0.091	0.098	0.086	0.081	0.090	0.095
Bias	-8.68e-5	-1.78e-3	4.62e-4	4.49e-4	5.88e-4	-9.26e-5	8.26e-7
Willmott	0.904	0.894	0.908	0.908	0.911	0.910	0.911



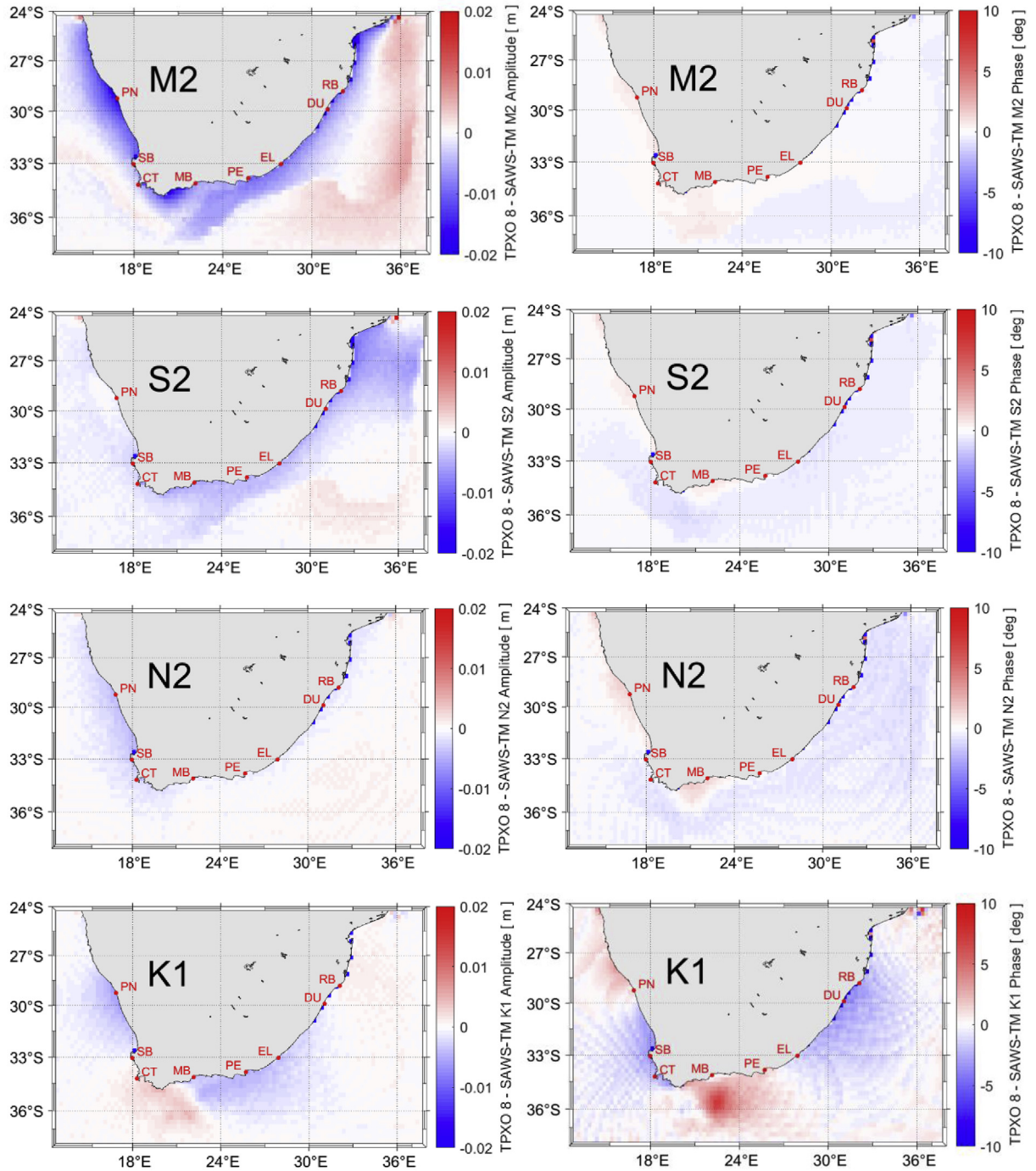


**Fig. 4.** Difference plots between the SAWS-TM and the TPXO 8 model for both the amplitude (left panels) and phase lags (right panels). Only the three largest amplitude semi-diurnal (M2, S2 and N2) and largest diurnal (K1) constituents are presented here.

evident around the coast and over the shelf areas. This might suggest that these friction models are resolving the bottom interactions differently. Nevertheless, an amplitude difference of less than 0.02 m is assumed to be insignificant for the M2 and S2 constituents.

Phase lag differences smaller than 10° were obtained for most constituents. The SAWS-TM and TPXO have different strengths and weaknesses. In the largest semi-diurnal constituents, the phase lag differences are small compared to the diurnal differences. This might be because the SAWS-TM accounts for bottom friction using the direct Chézy bottom roughness model (refer to Section 5.1.2). The most prominent phase lag difference was observed around Mossel Bay, followed by Port Nolloth (especially in N2). Both these locations are adjacent to

the wider continental shelf areas and are thus more sensitive to bathymetry and associated friction. Due to the shelf extents in these areas being approximately 300 km, semi-diurnal coastal resonance will also occur here (as described in Section 6.1). Thus, Delft3D's ability to resolve long wave propagation (and the associated resonance in the semi-diurnal wavelengths) is also investigated.

The time series results of Section 5.1, together with the time series validation against SANHO data (described in Section 5.2.2) also support the theory that the SAWS-TM resolves both the tidal amplitude and phase accurately. A 12-h semi-diurnal phase lag difference of 10° implies that a particular constituent wave (or high water) will arrive at a particular point 20 min later/earlier (Furner et al., 2016). Thus, the

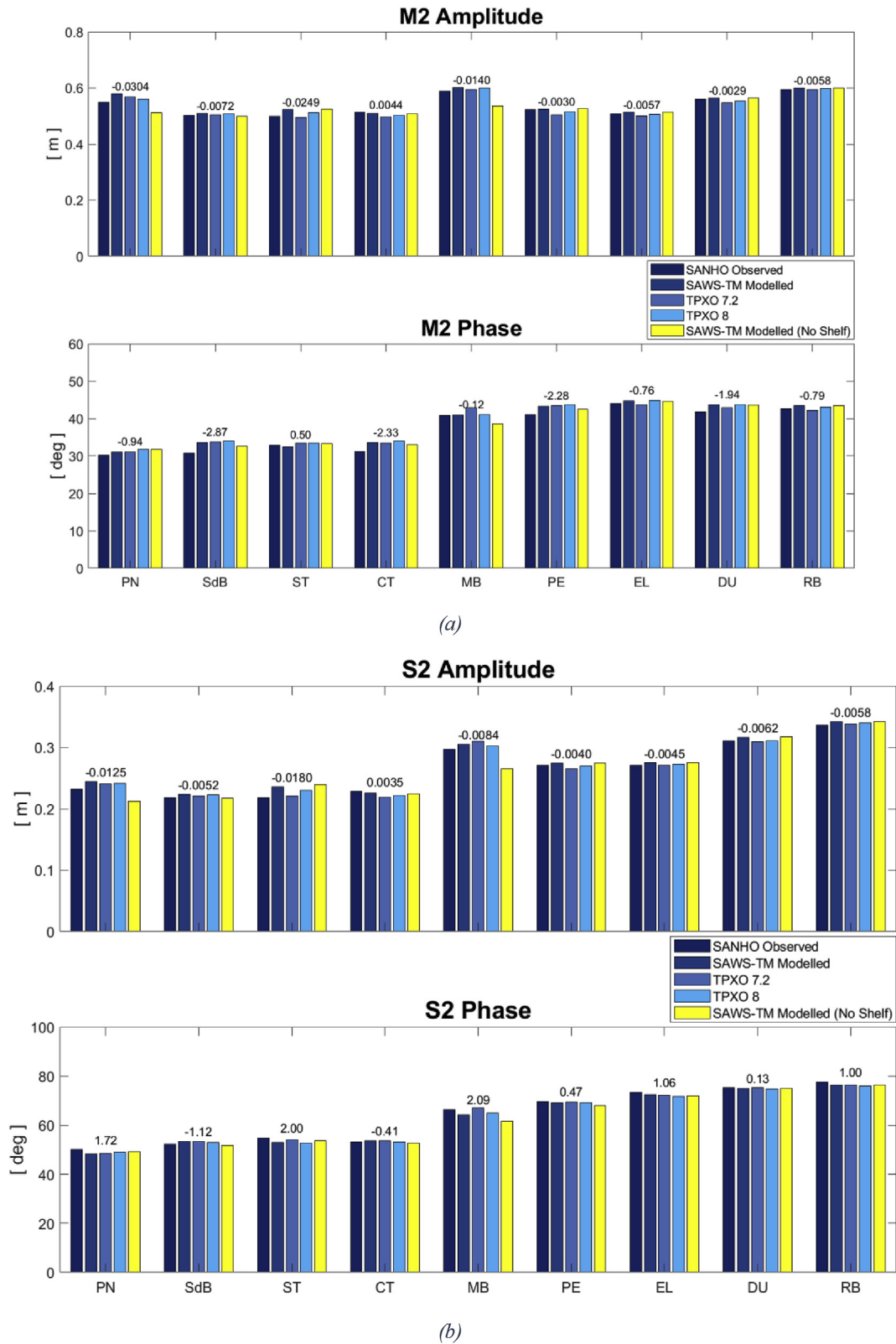


**Fig. 5.** Comparison between SANHO semi-diurnal constituent amplitude and phase for M2 (a) and S2 (b) and the corresponding constituent values produced in the present study's two-year simulation relative to UTC. Differences are provided above each location between SAWS-TM and measure constituent values. The closest TPXO 7.2 and 8 constituents' output points are also given. Lastly, the constituent values of the simulations without the Agulhas and Namaqua Banks are also provided and thus highlighting the coastal semi-diurnal resonance in the SAWS-TM.

phase lag differences observed in Fig. 4 correspond to M2 and S2 reaching Mossel Bay approximately 2 min earlier than the TPXO 8 prediction. At Port Nolloth, the SAWS-TM M2 and S2 arrived at almost the same time. In the deep seas, the predictions were essentially identical. Model accuracy is therefore deemed sufficient to describe the South African tidal characteristics and the associated tidal current.

#### 4.2.2. Time series harmonic validation

In Fig. 5 the results from SAWS-TM and the SANHO measurement-based semi-diurnal M2 and S2 constituents are provided. Time series data were extracted from the SAWS-TM at the coastal location where SANHO has tide gauge recordings (refer to Table 2). An average model time-series was created using a  $3 \times 3$  nearest neighbor search. This was done to avoid spurious coastal model outputs and thus create a more representative result. Measured water level time series were compared with model output (analysed using U-Tide (Codiga, 2011)). The closest TPXO 7.2 and 8 output points' amplitudes and phases were also included in the comparison.

In both amplitude and phase lag, the SAWS-TM compared well to measurements and TPXO. All around the coast the amplitude differences were acceptable (Canhanga and Dias, 2005; Furner et al., 2016; Le Provost, Genco, Lyard, Vincent and Canceil, 1994; Nzualo et al., 2018; Stammer et al., 2014). The pattern of highest M2 and S2 amplitudes resemble the pattern of HAT values presented in Table 1, with Port Nolloth and Mossel Bay revealing the highest values for both the SAWS-TM and SANHO harmonic analysis. Next largest is Richard's Bay. These high values can be explained by the large amplitudes crossing the Mozambique Channel (Arbic et al., 2009). The high water levels observed at Port Nolloth and Mossel Bay can be mainly explained by coastal tidal resonance of the semi-diurnal tidal constituents, as explained in Section 6.1 and 6.2. Overall, the TPXO 7.2, 8 and SAWS-TM models perform well compared to the measured water level harmonic analysis. At certain locations, especially around Cape Town, the SAWS-TM performed best. From this comparison it is reasonable to assume TPXO 7.2, 8 and SAWS-TM to be accurate around the South African coastline. Selection of an appropriate model for other purposes can be guided by resolution requirements.

Numerous South African nearshore studies have successfully used TPXO 7.2 for water level predictions for coastal numerical model boundary condition (e.g. Fearon, et al., 2017a, 2017b, 2018). For this reason, the outputs from TPXO 7.2 have also been added to the comparison presented in Fig. 5. The results from a numerical experiments, excluding the Agulhas and Namaqua Banks, are discussed in Section 6.1. For ease of reference, these results were also presented in Fig. 5.

At all of the coastal sites the phase difference was less than  $1.5^\circ$ , corresponding to an approximant semi-diurnal absolute time lag of less than 3 min. Only Simon's Town had a difference of  $2.78^\circ$  for M2, corresponding to approximately 5 min in absolute semi-diurnal time difference. The main reason for these phase lag differences might be found in the simplifications assumed in describing local friction in the numerical model (Zijl et al., 2013). Nevertheless, this phase discrepancy is small compared to other studies (e.g. Canhanga and Dias, 2005; Furner et al., 2016; Zijl et al., 2013). Waterhouse et al. (2011) stated that phase differences smaller than 10 min are negligible. Using this threshold, the phase lag at all nine coastal cities can be considered negligible. The systematic increases in phase from east to west is a result of the direction of propagation of the tidal wave around the southern tip of Africa. The pronounced increase in phase lag at Mossel Bay is also due to the friction and shallow water associated with the Agulhas bank. Both the SAWS-TM and TPXO 7.2 and 8 phases follow the SANHO data consistently. The performance of both models varies around the coastline but in general, both do well in describing the major semi-diurnal constituent phase lag.

Greenwich correction was applied to standardize the water level measurements and model outputs (Schumann, 1983). Given that not all the tidal constituents were used in the numerical model, slight

discrepancies, like those observed in Fig. 5, can be expected. The validation described here gives us confidence in the SAWS-TM, the study period used, and thus the suitability of the approach in characterizing the South African tide.

## 5. Tidal characterization

### 5.1. Coastal resonance

Tidal waves propagate over the deep oceans at high velocities. Once they interact with continental shelves they 'feel' the ocean floor and go through similar processes which short-crested waves encounter at coastlines (or in the nearshore). These include shoaling, which effectively increases the tidal amplitude while slowing down the progressive wave (Le Provost et al., 1994). This interplay between kinetic and potential energy (total mechanical energy) has been described in shallow water by Doodson & Warburg (1941), and gives the propagation velocity of the tidal wave as dependent on both depth and elevation:

$$c = \sqrt{g(h + 3\zeta)}, \quad (6)$$

where  $c$  is the phase speed,  $h$  is the water depth and  $\zeta$  is the water elevation. Linear wave theory (or Airy wave theory) (Holthuijsen, 2007) is also a convenient way to estimate whether a progressive surface wave is in shallow, intermediate or deep water. Looking at the main semi-diurnal and diurnal tidal components, we can thus estimate their wavelengths ( $\lambda$ ) and consequently the propagation velocity on and off the shelf. For a wave to be considered to be in deep-water,  $h > 1/2 \lambda$  and for shallow water  $h < 1/20 \lambda$ . The general expression according to linear wave theory may be used in all water depths, including intermediate water depths. This is an important point to note, as most of South Africa's short crested swell waves propagate to the coastline with a 12 s period, making large embayments like False Bay almost entirely intermediate water. Nevertheless, looking at the asymptotic condition describing shallow and deep-water waves is useful in understanding simplified wave behaviour.

Making the assumption that the off-shelf depths are approximately 4000 m and the on-shelf depths are 100 m (refer to Fig. 1), the accompanying semi-diurnal and diurnal tidal wave lengths are approximately 8553 km and 17 106 km off the shelf and 1352 km and 2705 km on the shelf, respectively. This was calculated assuming linear wave theory under shallow water assumptions.

Another possible cause of increased tidal amplitudes at coastal locations adjacent to a continental shelf is tidal resonance (Godin, 1993). This is also the reason why many islands surrounded by deep oceans display smaller tidal amplitude ranges. The Agulhas Bank and the Namaqua Bank extend approximately 300 km offshore from continental Africa (refer to Fig. 1). For a tide to be in resonance with itself there has to be an approximate relationship between the shelf width and the constituent wavelengths. This relationship has been observed in other locations around the world including the east China sea (Zu et al., 2008), northwest Australian shelf (Craig, 1988) and the Patagonian shelf offshore of Argentina (Arbic et al., 2009; Godin, 1993). In Africa, a lesser known coastal tidal resonance example exists at the Gulf of Gabes, in Tunisia (Sammari et al., 2006).

On the South African coast, both the semi-diurnal and diurnal components' wavelengths,  $\lambda$ , are approximate multiples of the continental shelf width. A quarter of the on-shelf  $\lambda$  for the semi-diurnal and diurnal tidal components are approximately 300 km and 600 km respectively. In this scenario, where  $1/4 \lambda$  is approximately equal to the shelf width, the incident wave and the reflected coastal wave creates the strongest semi-diurnal amplification (resonance between the coast and shelf edge) (Clarke and Battisti, 1981; Godin, 1993). These calculations were performed assuming a period of 12 h for semi-diurnal and 24 h for diurnal signals. Actual constituent periods deviate from these exact numbers and so do the continental widths. The greater the



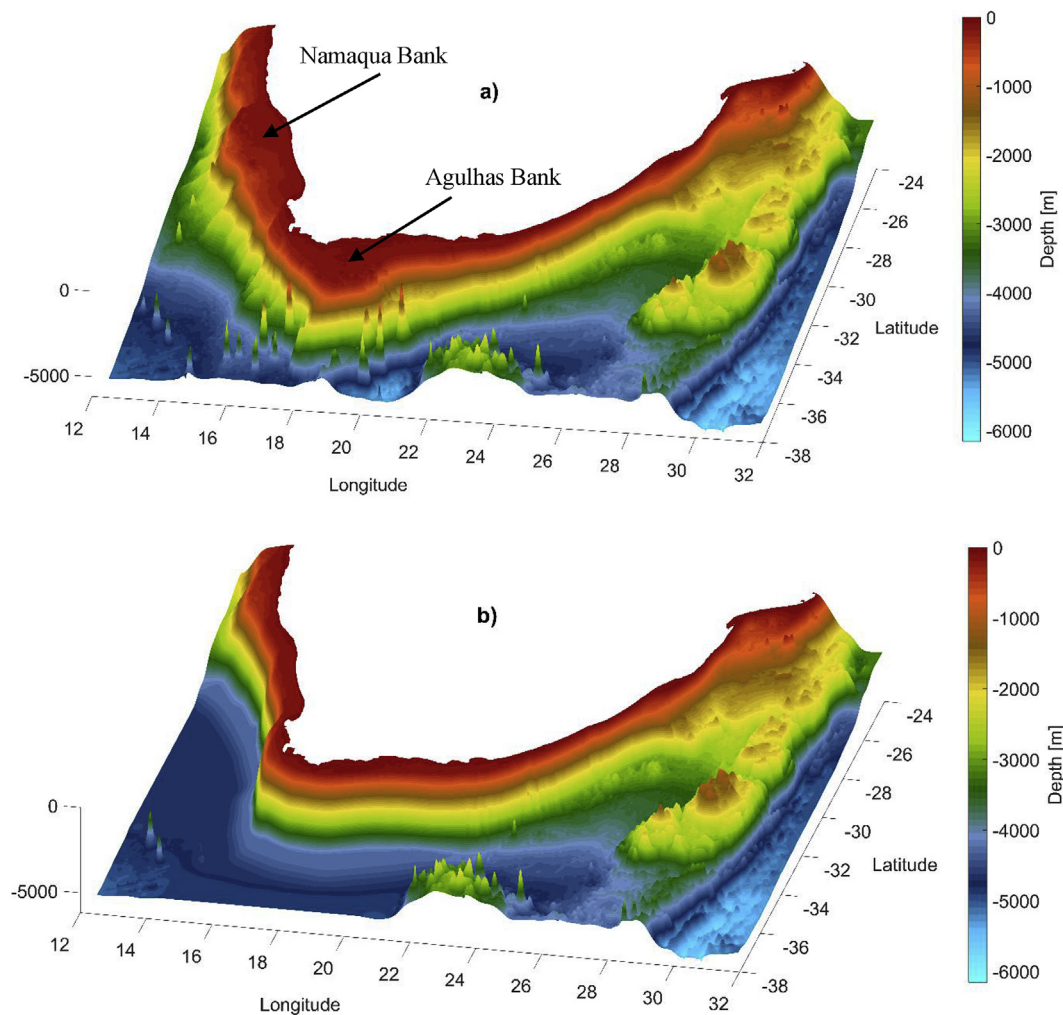


**Fig. 6.** (a) The SAWS-TM bathymetry employed for the analysis presented in the present study, (b) the model bathymetry without the continental shelves. E.g. both the Agulhas and Namaqua Banks removed, leaving only a continuous 100 km shelf.

mismatch between tidal wavelength and shelf width, the weaker the resonance-related amplification. Following this, the fact that the ratio between angular frequencies are  $\frac{\omega^2(\text{diurnal})}{\omega^2(\text{semi-diurnal})} \cong \frac{1}{4}$ , the diurnal coastal amplification does not occur (a standing wave node is not formed) around the south and west coast of South Africa (or is negligible).

Nevertheless, these rough calculations do support the notion that tidal resonance is probably present on the west and south coast and thus partially explains the elevated amplitudes observed in these areas. In Section 6.2 the elevated amplitudes are also clearly observed over the shallow shelf areas, together with the rapid phase lag changes over the shelf edges. Such rapid changes in phase lag are one of the clearest ways to identify tidal resonance per tidal constituent as presented in Section 6.2 (Arbic et al., 2009; Clarke and Battisti, 1981). The amplification of the semi-diurnal tides are especially clear while the diurnal signals show little amplification or phase lag change (other than the expected longshore variation). The resonance of major constituents over continental shelves together with friction-related dissipation also plays an important role in dampening the ocean tides (Arbic et al., 2009).

In Fig. 6, the basis of an experiment to quantify the semi-diurnal coastal resonance is shown. Fig. 6 (a) is a 3D plot of the bathymetry employed in the present study. Here, the sharp bathymetry gradients associated with the continental shelf edge are clearly visible and the extended shallow shelf areas of the Agulhas and Namaqua Banks. In Fig. 6 (b), the same bathymetry is presented but this time with the broader shelf areas of the Agulhas and Namaqua Banks removed.

Instead, an artificial shelf was created, where the shallower shelf seas followed the coastline with an approximate 100 km margin.

The experiment was designed to prove the hypothesis that the elevated water levels observed at Mossel Bay and Port Nolloth are predominantly caused by semi-diurnal coastal resonance. The results are presented in Fig. 5 via the yellow bars. Here it is clear that once the shelves were removed the amplification of the major tidal constituents (M2 and S2) at Mossel Bay and Port Nolloth disappears. The phase of the tidal constituents thus also change in response to the faster moving tidal wave. In Appendix 1, the resulting amplitude and phase plots for the resonance experiment are also provided and will be more fully discussed in Section 6.2. From this experiment, it is thus clear that semi-diurnal tidal resonance is the dominant factor in creating elevated tidal water levels on the west and south coast of South Africa. Numerous studies investigated the interaction between the diurnal atmospheric forcings found on the west coast with the diurnal inertial oscillations in the surface stratified layer (Monteiro et al., 2005; Senthil Kumar et al., 2016). The velocity response of the surface layer is also dependent on the layer thickness and thus its resonance response to the diurnal atmospheric forcing (Searson and Brundrit, 1995b; Senthil Kumar et al., 2016). The tidal and inertial currents can thus not be ignored on the south and west coast.

In addition to alternating local sea level, tides are also of importance due to the currents they can generate. Across the Agulhas and Namaqua Banks, tidal and inertial oscillation currents may form a significant part of the overall current variability and any offshore or coastal

development should understand their behaviour (Schumann and Perrins, 1982). Inertial currents are the movement of the water column due to wind stress over a rotating earth (Schumann and Perrins, 1982). Just like astronomic tidal movement, these currents are dependent on bathymetry and the ocean density structure (Schumann and Perrins, 1982). The period of the inertial oscillations around the earth is also known to be dependent on the latitude and roughly given by the relationship  $12.04/\sin(\text{latitude in degrees})$  hours (Schumann and Perrins, 1982). From Fig. 1 it can be seen that South Africa is approximately latitudinally centered around 30 °S, placing the inertial oscillation period at approximately diurnal (~24 h). The inertial period is thus equal to the diurnal constituents at both 26.5° and 30° while the semi-diurnal constituents periods are equal to the inertial periods at 71° and 90° (Schumann and Perrins, 1982). It can thus be asserted that there does exist a measure of resonance between the inertial oscillations and the diurnal constituents. The aforementioned resonance also makes it difficult to distinguish the resulting currents from one another. It should be noted, however, that resonance with tidal constituents is not the generating force for inertial oscillations. It is widely accepted that wind stress is the cause of these perturbations traversing over a rotating earth. In the present study, no wind forcing has been added to the numerical model and thus the tidal current described in Section 6.4 cannot be explained via resonance with this phenomenon. Therefore, no inertial currents were observed in the present model configuration. The boundary conditions of the numerical model are also based neither on *in situ* measurements nor remotely sensed altimetry data, but rather on extracted tidal constituents from TPXO 8 and. Due to the neglect of atmospheric forcing in this study, coastal trapped waves and atmospheric related storm surge are also not causes of the observed water level phenomena. Atmospheric forcing and associated surface modulations such as surge processes are considered in the full operational SAWS storm surge model, however.

### 5.2. Tidal amplitude and phase mapping

In Fig. 7 the phase variation (co-tidal lines) around the coastline indicates the propagation of the progressive tidal wave (Canhanga and Dias, 2005; H. O. Mofjeld and Larsen, 1984a, b; Stephenson, 2016) from the west to the east around the southern tip of Africa. The co-tidal phase (lines with constant tidal phase per constituent) indicates the deviation from the reference or equilibrium tide propagation; i.e. the deviation due to local bathymetric features and friction (Zijl et al., 2013). In Table 2, the phases of the primary semi-diurnal and diurnal tidal constituents are provided for coastal cities around South Africa. Here, the west-to-east propagation of the tide is observed with the west coast semi-diurnal constituents (M2 and S2) delayed by approximately 1.3 h and the east coast by 1.6 h. It is also interesting to note how the continental shelves and embayments with complex and/or shallow bathymetries delay the propagation of the tidal wave even further (Canhanga and Dias, 2005; Waterhouse et al., 2011; Zijl et al., 2013). Canhanga and Dias (2005) illustrated how the phase lag increases the further the tide propagates into the shallow bay. The semi-diurnal tide can thus take more than an additional hour to reach the further reaches of the Maputo bay (Canhanga and Dias, 2005). The tidal amplitudes and phase lags produced in the present study also closely correspond to the tidal propagation times (and thus phase lags) presented by Chevane et al. (2016) on the Sofala Bank, close to Beira, Mozambique.

Fig. 7 gives the behaviour of the major tidal constituents. As confirmed in Section 5.2.1, the behaviour is very similar to that presented by TPXO 8. Due to friction over the Agulhas and Namaqua Banks, together with coastal resonance, the M2 phase lag changes rapidly in these areas. This is accompanied by increases in constituent amplitude. This general pattern holds true for all the semi-diurnal constituents presented here. Only the primary solar component (O1) displays a pattern which deviates from the semi-diurnal components. The other major diurnal constituent, K1, display a similar pattern to most of the

semi-diurnal constituents. In Appendix 2, Fig. 13, the amplitude and phase mappings of the semi-diurnal coastal resonance experiment presented in Section 6.1 are given. Neither the rapid phase lag changes nor the amplitude amplification of the semi-diurnal constituents (observed in Fig. 7) are present. To highlight these differences, Fig. 14 is provided. Here the amplitude difference between the SAWS-TM simulations with and without the continental shelves are given. The large amplitude differences on the Agulhas and Namaqua Banks are a direct indication of the coastal resonance amplification due to the presence of the broader (~300 km) continental shelves. These results confirm the importance of the continental shelves, on the west and south coasts, for characterizing the South African tide.

For an ocean in the shape of a circular basin enclosed by a coastline, the co-tidal lines point radially inward and must eventually meet at a common point; the amphidromic point. Around islands like Madagascar and New Zealand, exceptions do occur. The high constituent amplitude values observed towards the Mozambique Channel are thus an effect of the channel itself, and the constriction due to the proximity of Madagascar to continental Africa. Similar effects are also observed in the English Channel (Roos et al., 2011) and is sometime referred to as a virtual amphidrome (Rizal, 2002). When interpreting Fig. 7 it is important to keep the amplitude colour scale in mind. From M2 to O1, the amplitudes progressively decrease even though the colours used remained the same.

### 5.3. Form Factor

In Fig. 8, the Form Factor for South Africa is presented. The dimensionless *Form Factor* (FF) is defined as the ratio of the major ocean tide (Adam Thomas Devlin et al., 2017) constituent amplitudes:

$$\text{Form Factor} = \frac{O1 + K1 (\text{diurnal})}{M2 + S2 (\text{semi} - \text{diurnal})}, \quad (8)$$

and thus represents the relationship between semi-diurnal, semi-diurnal with diurnal inequalities, mixed tides and diurnal dominance (Daher et al., 2015; D. Pugh, 2004) (D. Pugh, 2004). According to the Courtier coefficient, for a FF value of less than 0.25, a tidal system is classified as predominantly semi-diurnal (Amin, 1986; Daher et al., 2015). Fig. 8 shows the whole of the South African ocean to be clearly predominantly semi-diurnal (D. Pugh, 2004). The FF decreases into the Mozambique Channel, indicating that the tide becomes even more semi-diurnal. Across the Agulhas Bank, the diurnal signals becomes stronger, extending all the way up to Port Nolloth on the west coast and to Durban on the east coast. This phenomenon is also evidenced by the phase-amplitude plot of Fig. 7, where the relatively high amplitude values of the diurnal constituent, K1, are given. As expected, the South African coastline does not have a constant relationship between the semi-diurnal and diurnal tidal species. The FF values obtained at the mouth of Maputo Bay (~0.06) agree with the values obtained by Canhanga and Dias (2005).

### 5.4. Tidal currents

In Fig. 9 the tidal ellipses as computed with the U-Tide package (Codiga, 2011) for the two major semi-diurnal tidal constituents are shown. These were plotted together with the underlying bathymetry. For both M2 and S2 the bathymetry dependency is clear. Off the shelves the tidal ellipses are small. Areas of greatest tidal currents and directional variation are found on the shelves. Even shallower areas in the deep ocean off the east coast revealed more pronounced tidal currents. The semi-major axis of the tidal ellipses gives the dominant direction of tidal current movements, while the ellipse width is an indication of the directional variability (Schumann and Perrins, 1982). For example, in tide dominated channels, the ellipses typically have pronounced elongated shapes (rectilinear), aligned with the channel axes (H. Mofjeld and Larsen, 1984a, b). The ellipse eccentricities are thus close to 1



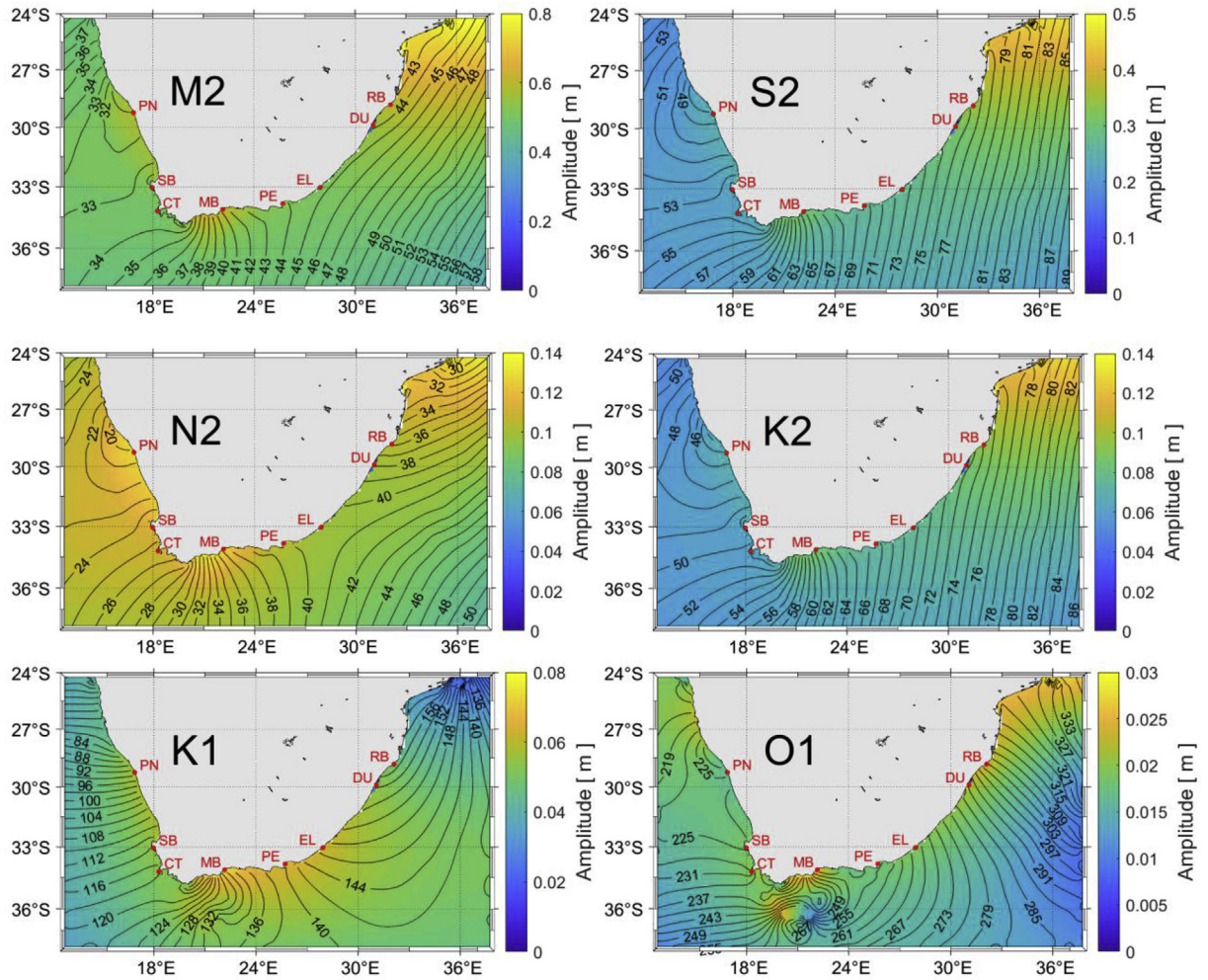


**Fig. 7.** Tidal amplitude and phase of six major semi-diurnal and diurnal tidal constituents. The colour scales give the amplitude, per constituent. Contours indicate co-tidal lines of phase lag relative to UCT. (For interpretation of the references to colour in this figure legend, the reader is referred to the Web version of this article.)

(Chevane et al., 2016). Where multidirectional tidal flow occurs the ellipses will be more circular (ellipse eccentricities close to 0) (H. O. Mofjeld and Larsen, 1984a, b). The semi-major and semi-minor axes are thus the two maximum current speed components simulated during a

particular period (Guillou et al., 2018). Around a particular point, tidal currents will trace out the circumference of a tidal ellipse and thus have a circulation direction associated with it. In Fig. 9, clockwise movements are given in blue while anti-clockwise rotation is given in orange.

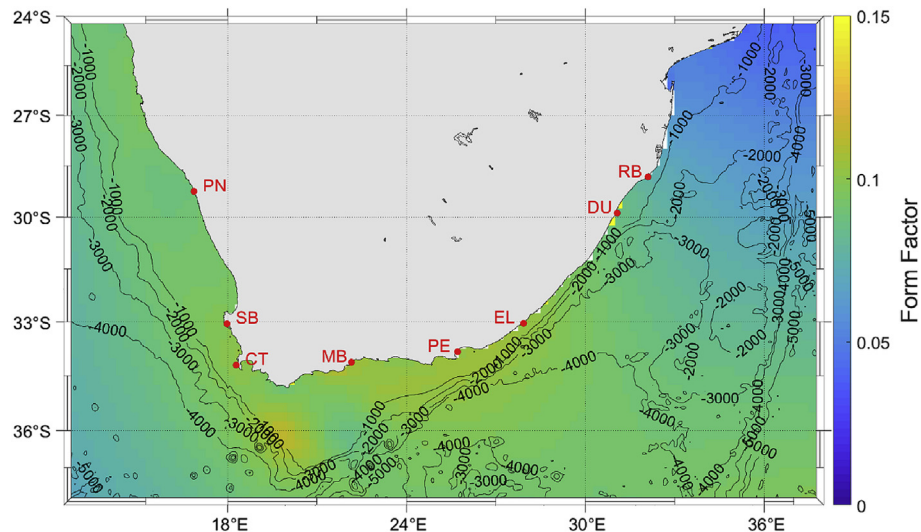


**Fig. 8.** Form Factor presented with bathymetry contours for South Africa.

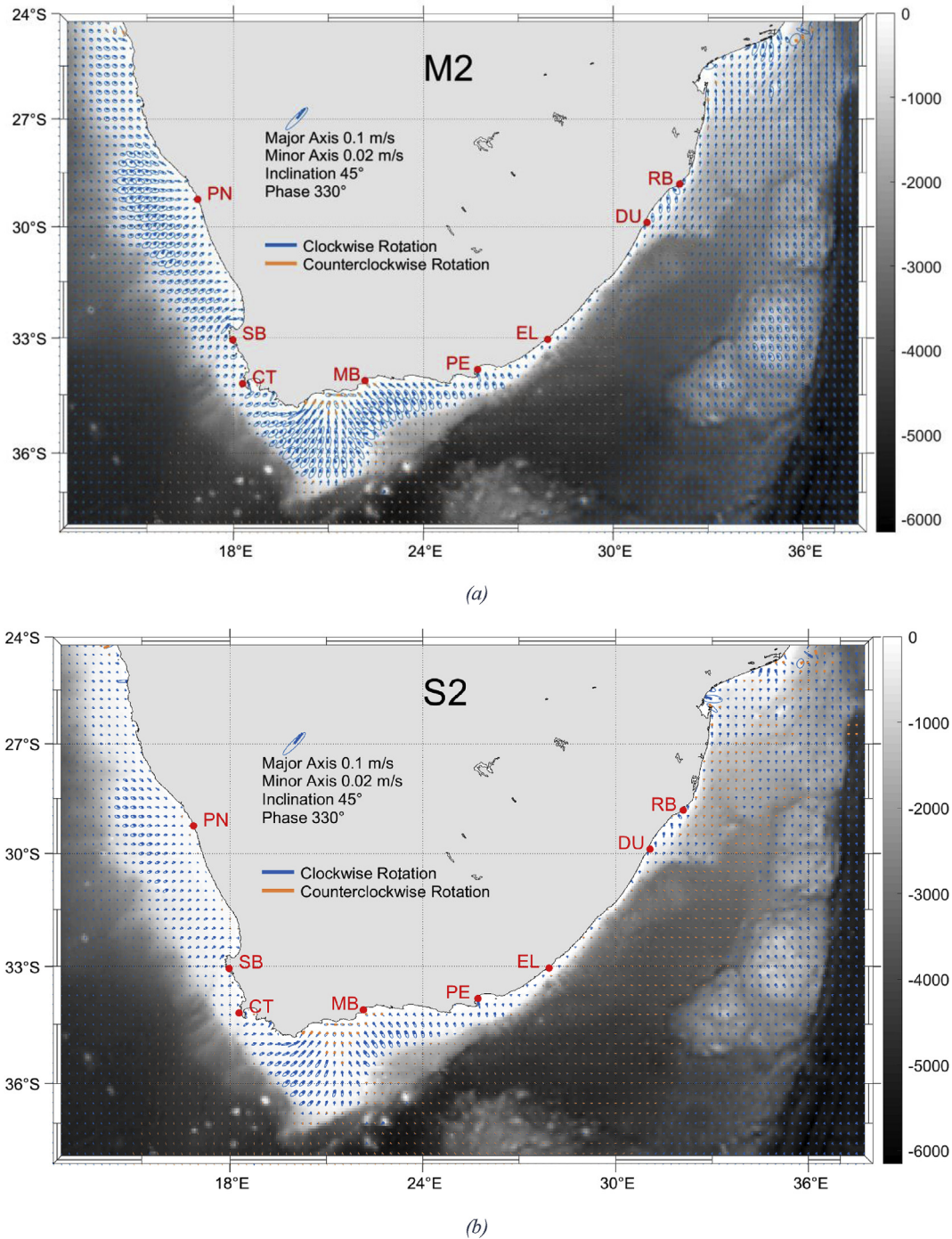


**Fig. 9.** Tidal ellipses (motion of water due to a particular tidal constituent) based on the depth averaged currents produced in the SAWS-TM, (a) for the M2 and (b) for the S2 constituent. GEBCO bathymetry is also provided via greyscale. Blue ellipses are clockwise rotations and orange is anti-clockwise rotations. (For interpretation of the references to colour in this figure legend, the reader is referred to the Web version of this article.)

The orientation of these rotational patterns is closely linked with the direction of the tidal progressive wave and local bathymetric features (Houwman and Hoekstra, 1998).

The on-shelf rotations are predominantly clockwise for both M2 and S2. The semi-diurnal currents are flowing in a cross-shelf direction, perpendicular to the bathymetry, as observed by DiMarco and Reid, 1998 at the Texas-Louisiana shelf. This was also the case for both the Agulhas Bank and the Namaqua Bank. Similar current behaviour has been observed on the Sofala Bank, offshore of Mozambique (Chevane et al., 2016). Due to the shape of the Agulhas bank, the tidal currents are focused towards the concave southern coastline. The coastline

shape influences the return flow close to Mossel Bay and might be the cause of the anti-clockwise rotation close to the south coast shore (Houwman and Hoekstra, 1998). Tidal currents also align themselves with the shoreline orientation close to the shore on the south coast. A similar tidal current movement is observed on the west coast with coastal tidal rotation reversing close to St. Helena Bay (e.g. counter-clockwise). Similar behaviour was observed for both M2 and S2, with the M2 current velocities being the dominant contribution.

In Fig. 10, the total tidal currents are given approximately 3 h after both high and low tide. In Fig. 11, the exact time of extraction during the tidal cycle is provided. It is interesting to note that not only do the



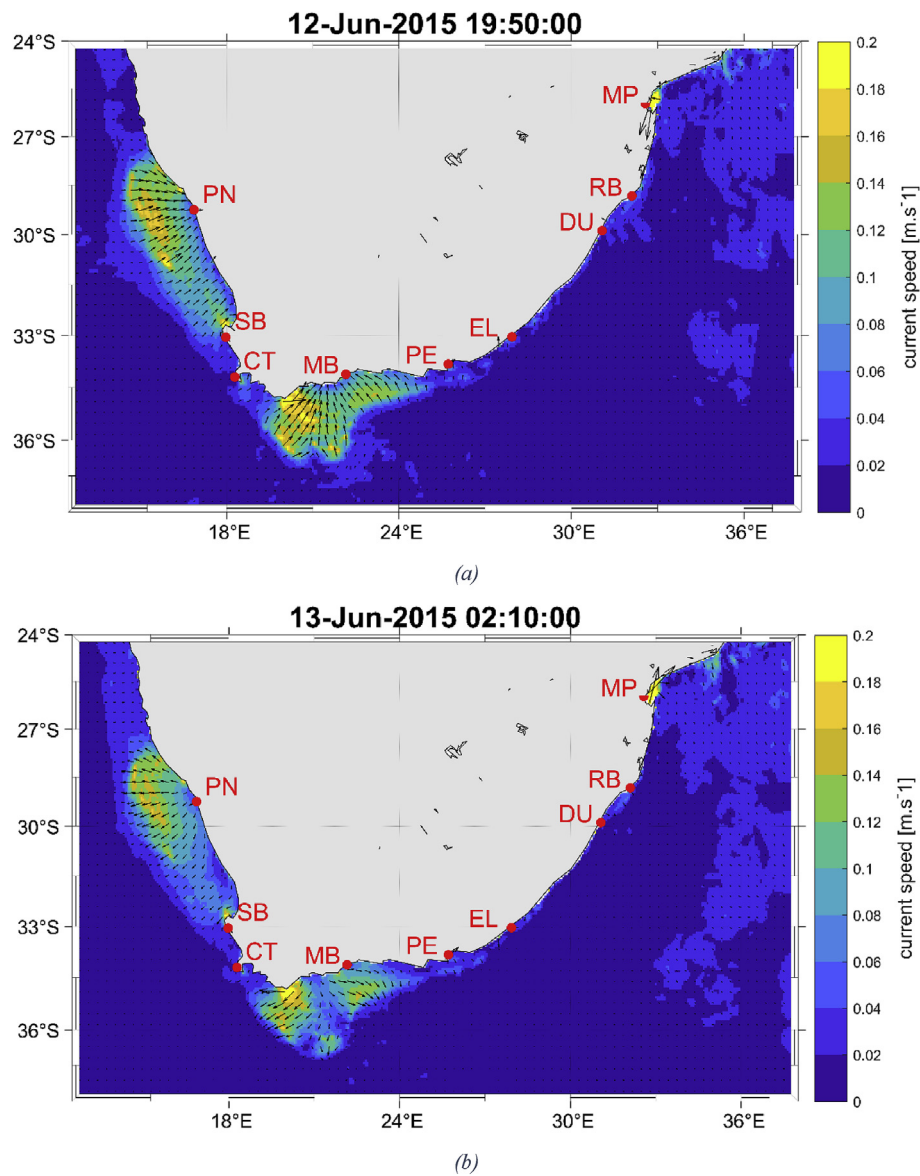


**Fig. 10.** Total tidal current 3 h after (a) high tide (flood moving towards slack and ebb) and (b) 3 h after low tide (ebb moving towards slack and flood) during a (high) spring tide.

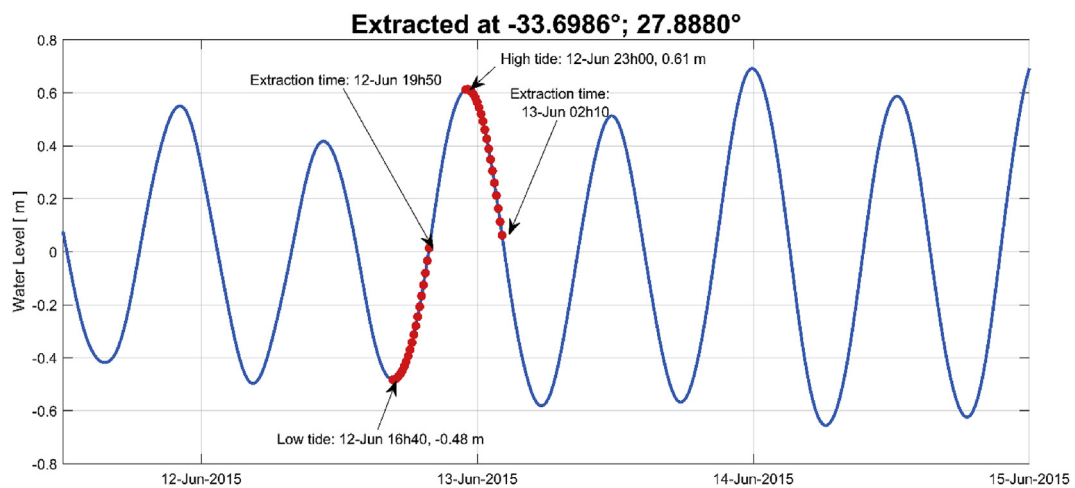


**Fig. 11.** Free surface tidal elevations and the time steps at which Fig. 10 (a) and (b) were extracted.



west and south coasts exhibit semi-diurnal coastal resonance, but both funnel the tidal currents into a concave coastline. This “pilling up” of water against the coastline could be a further contributing factor to the higher water levels observed at these two coastal locations. At the Agulhas Bank, ellipse eccentricities much closer to 1 are observed compared to those at the more-gently sloping west coast shelf. Just offshore of False Bay, the eccentricities are also close to 0, while the continental shelf slope in that region is also gentler than the Agulhas Bank edge.

On both shelves the maximum currents were obtained close to the mid-shelf location, in accordance with continuity between tidal velocity and elevation (Chevane et al., 2016; H. O. Mofjeld and Larsen, 1984a, b). For a propagating, progressive tidal wave, the tidal elevation is given by  $\eta = a \cos(kx - \omega t)$ . The tidal velocity (the velocity of actual water movement) can then be described in an ideal, frictionless deep ocean as:

$$u = a \sqrt{\frac{g}{H}} \cos(kx - \omega t) \quad 9$$

where  $u$  is the x-directional velocity,  $H$  is water depth,  $k$  is the angular wave number ( $2\pi/\lambda$ ) and  $x$  is the horizontal position. Current velocities increase from the shelf edge to the maximum velocity and then decrease towards the shoreline. The strongest currents are obtained over both shelves during flood. In an ideal scenario the maximum free surface water elevations will be in phase with the maximum tidal velocity (H. O. Mofjeld and Larsen, 1984a, b).

In Fig. 12 the phase difference between the free surface elevations and tidal currents are given for M2 and S2. The bathymetry is shown via contours. Like most tidal behaviour, the bathymetry has a direct influence on the elevation and current's phase relationship. The regions over both banks, where maximum current velocities were observed in Fig. 10, also give a localized increased phase lag in Fig. 12. A phase difference of  $100^\circ$  corresponds to a 3h 45 min difference between the maximum free surface elevation and maximum tidal currents for the M2 constituent. As most of the phase difference around South Africa is approximately  $100^\circ$ , an approximate 3 h delay after high and low tide was chosen in Figs. 10 and 11. To the west of South Africa, the phase lag was approximately  $0^\circ$  and thus little to no lag between tidal water level and current extremes is expected. Just outside Maputo bay, similar phase lags were obtained by (Canhanga and Dias, 2005).

## 6. Conclusion

The South African tide propagates around the approximately-3000 km coast from the west to the east. To date, the tidal characteristics of this country have not been analysed and presented in detail. The numerical model presented here was fully calibrated and validated against various benchmark data. These include another widely used and accepted model (TPXO), as well as long-term sea surface elevation time series and their corresponding harmonic analyses (presented as tidal constituents). Harmonic analysis validation was performed at each

major coastal port around the South African coastline. Two-dimensional validation was also performed, establishing confidence in the numerical model's ability to characterize the South African tide spatially.

Tidal constituent amplitude and phase lag regional plots were used to classify the South African tide. These, together with the calculated Form Factor confirmed the semi-diurnal tidal dominance for this coastline. The importance of the continental shelves on the west and south coast was also highlighted. These shallower areas (approximately 300 km in width) are the main reason for the elevated water levels observed at coastal cities adjacent to them. Semi-diurnal coastal resonance was established as the predominant cause of these high water levels. The continental shelves were also shown to be the areas where the strongest tidal currents occurred and the largest variability in elliptical tidal motion was observed. Continental shelf friction causes delays in tidal wave propagation and results in an approximate 3-h lag between free surface water levels and tidal currents. These analyses and results are a first for South Africa, as previous studies only provided limited constituent information and high level descriptions of the tide classification. The description and identification of the semi-diurnal coastal resonance is also novel and a first for the southern African continental shelves.

An accurate description of tidal characteristics is crucial for the development of a reliable storm surge forecasting system. As such, the tidal description presented here underpins the South African Weather Service storm surge prediction model. Users of this prediction tool are thus afforded a full grasp of the accuracy of the underpinning tidal forecast and are made aware of the fact that M2 and S2 amplitudes tend to be slightly over predicted by the SAWS-TM. Due to the resolution of the SAWS-TM model, embayments like St. Helena Bay, False Bay and Algoa Bay remain inadequately resolved. In order to capture the full hydrodynamics of such embayments, a 3D baroclinic model should be employed that can also considers internal tide propagation and inertial currents.

## Acknowledgments

The authors would like to thank the South African Navy Hydrographic Office (SANHO) for providing the study with long-term tidal constituents required for model validation. The SANHO also provided recorded sea surface elevations and high-resolution coastal bathymetry required for model calibration and final validation. The authors would also like to acknowledge Professor Kevin Horsburgh, Chief Scientist for International Development at the National Oceanography Centre in the United Kingdom, for being a sounding board for our operational storm surge model development project. Finally, this work is based on the research supported in part by the National Research Foundation of South Africa (Grant Numbers: 116359).

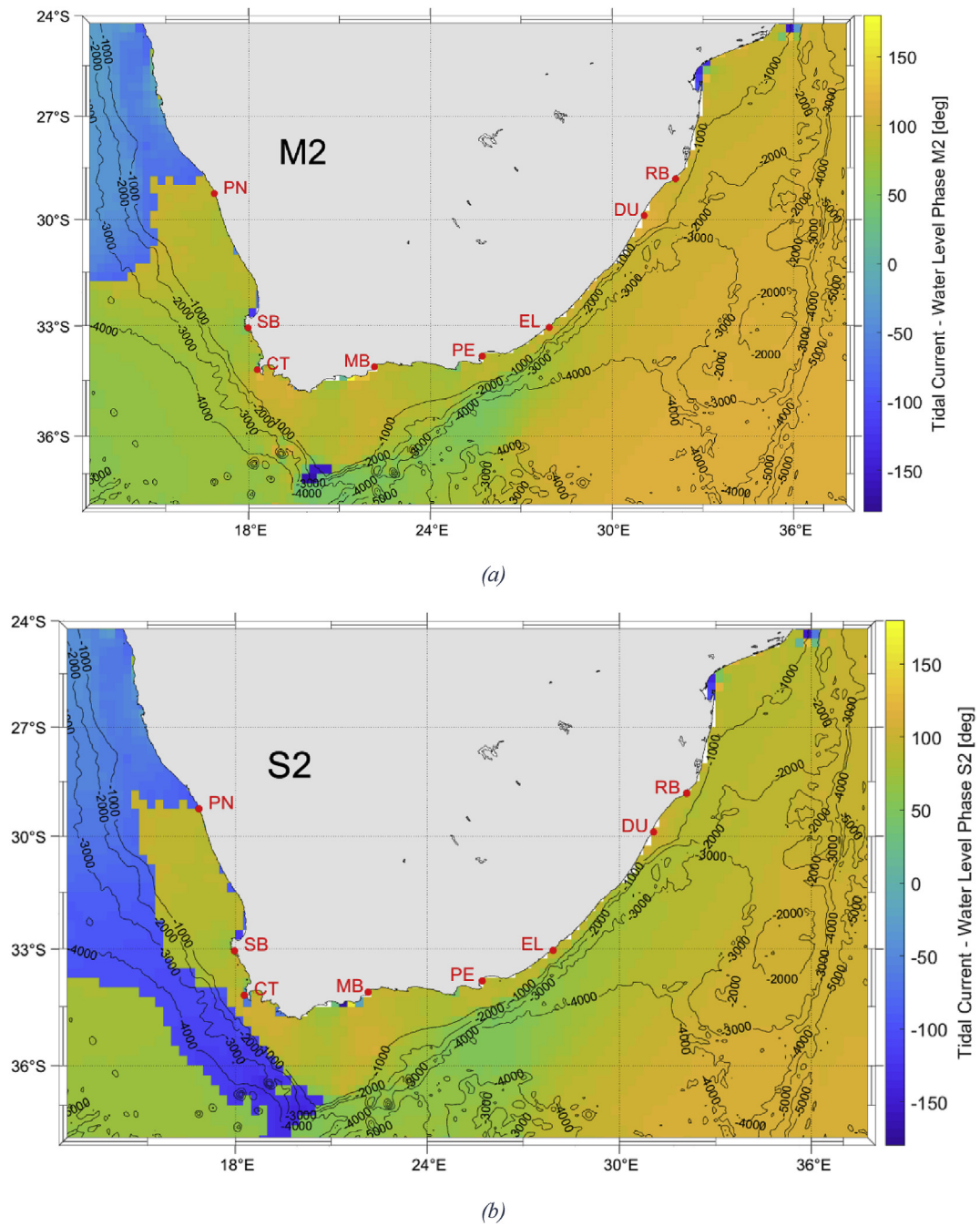


Fig. 12. Phase difference between the sea surface elevation phase and the tidal currents for the (a) M2 and (b) S2 constituent.

## Appendix 1. Shelf-less tidal amplitude and phase mapping

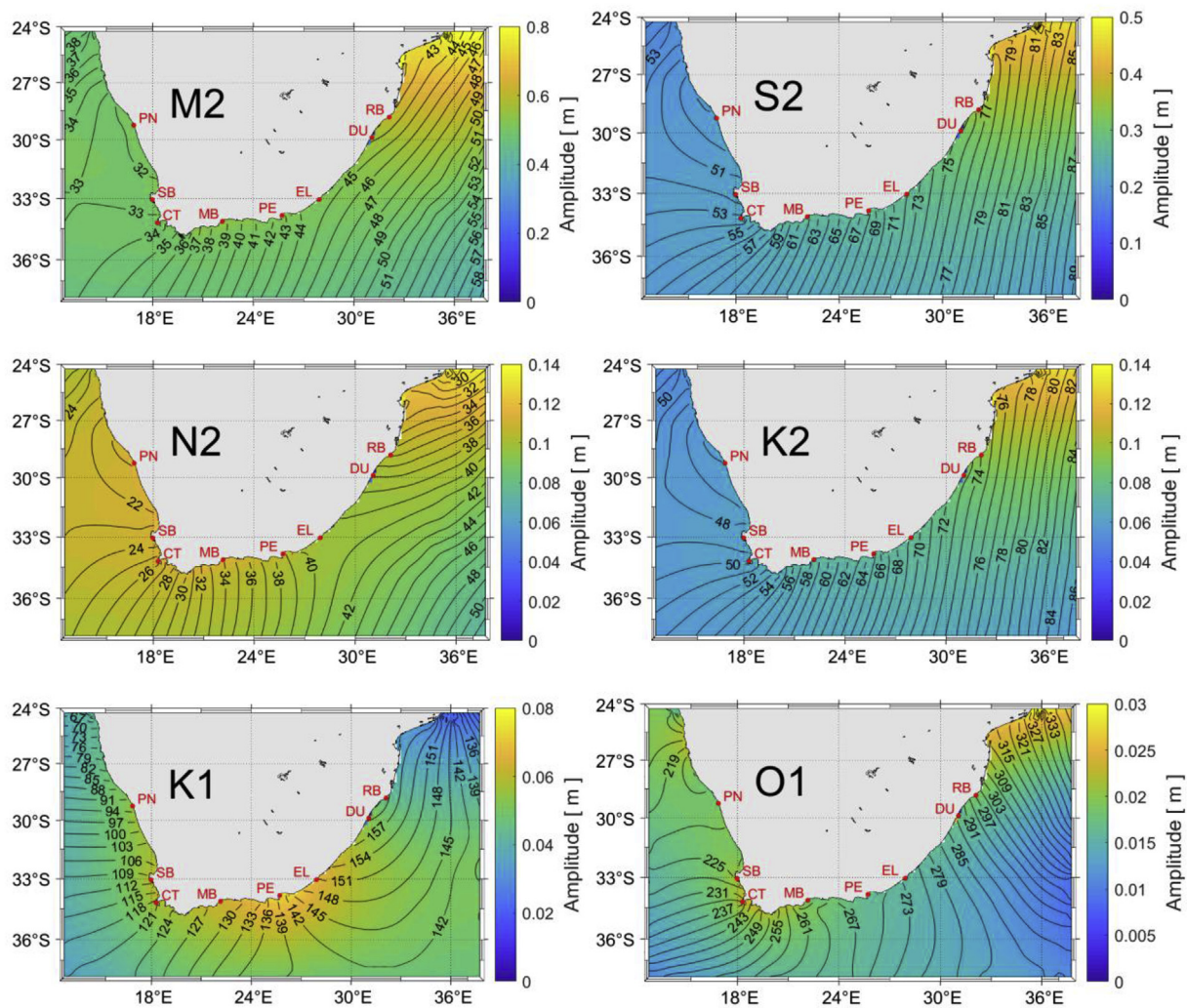


Fig. 13. Tidal amplitude and phase of six major semi-diurnal and diurnal tidal constituents for the coastal resonance experiment. These results were obtained with no broad continental shelves as indicated in Fig. 6 (b). The colour scales give the amplitude, per constituent. Contours indicate co-tidal lines of phase lag relative to UCT.

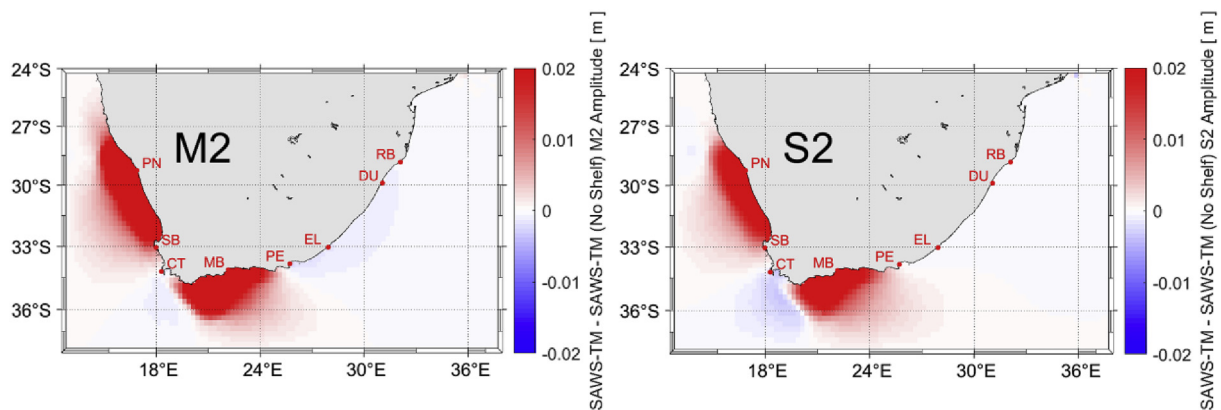


Fig. 14. SAWS-TM M2 and S2 amplitudes difference with and without the continental shelves.

## References

- Amin, A., 1986. On the conditions for classification of tides. In: *International Hydrographic Review*, (Monaco).
- Arbic, B.K., Karsten, R.H., Garrett, C., 2009. On tidal resonance in the global ocean and the back-effect of coastal tides upon open-ocean tides. *Atmos.-Ocean* 47 (4), 239–266. <https://doi.org/10.3137/OC311.2009>.
- Ballagooyen, R. C. van, 1995. *Forced Synoptic Coastal-Trapped Waves along the Southern African Coastline*. University of Cape, Town.
- Bosboom, J., Stive, M., 2015. *Coastal Dynamics I*. Delft University of Technology, Delft.
- Breyaniis, G., Petroligakis, T.I., Annunziato, A., 2016. Exploring DELFT3D as an Operational Tool. <https://doi.org/10.2788/783821>.
- Brundrit, G.B., 1984. Monthly mean sea level variability along the west coast of southern



- Africa. S. Afr. J. Mar. Sci. 2 (1), 195–203. <https://doi.org/10.2989/02577618409504368>.
- Brundrit, G.B., 1995. Trends of Southern African sea level: statistical analysis and interpretation. S. Afr. J. Mar. Sci. 16 (1), 9–17. <https://doi.org/10.2989/025776195784156449>.
- Burcharth, H.F., Hawkins, S.J., Zanuttigh, B., Lamberti, A., 2007. Case studies. In: Environmental Design Guidelines for Low Crested Coastal Structures. Elsevier, pp. 73–136. <https://doi.org/10.1016/B978-008044951-7/50031-2>.
- Cabral, P., Augusto, G., Akande, A., Costa, A., Amade, N., Niquisse, S., et al., 2017. Assessing Mozambique's exposure to coastal climate hazards and erosion. Int. J. Disaster Risk Reduct. 23 (April), 45–52. <https://doi.org/10.1016/j.ijdrr.2017.04.002>.
- Canhanga, S., Dias, J.M., 2005. Tidal characteristics of Maputo bay, Mozambique. J. Mar. Syst. 58 (3–4), 83–97. <https://doi.org/10.1016/j.jmarsys.2005.08.001>.
- Cartwright, D.E., Tayler, R.J., 1971. New computations of the tide-generating potential. Geophys. J. R. Astron. Soc. 23 (1), 45–73. <https://doi.org/10.1111/j.1365-246X.1971.tb01803.x>.
- Chevane, C.M., Penven, P., Nehama, F.P.J., Reason, C.J.C., 2016. Modelling the tides and their impacts on the vertical stratification over the Sofala Bank, Mozambique. Afr. J. Mar. Sci. 38 (4), 465–479. <https://doi.org/10.2989/1814232X.2016.1236039>.
- Clarke, A.J., Battisti, D.S., 1981. The effect of continental shelves on tides. Deep Sea Res. Part A, Oceanographic Research Papers 28 (7), 665–682. [https://doi.org/10.1016/0198-0149\(81\)90128-X](https://doi.org/10.1016/0198-0149(81)90128-X).
- Codiga, D.L., 2011. Unified tidal analysis and prediction using the UTide Matlab functions. Narragansett. <https://doi.org/10.13140/RG.2.1.3761.2008>.
- Craig, P., 1988. A numerical model study of internal tides on the Australian Northwest Shelf. J. Mar. Res. 46 (1976), 59–76.
- Daher, V.B., Paes R. C., de O.V., França, G.B., Alvarenga, J.B.R., Teixeira, G.L.G., 2015. Extraction of tide constituents by harmonic analysis using altimetry satellite data in the Brazilian coast. J. Atmos. Ocean. Technol. 32 (3), 614–626. <https://doi.org/10.1175/JTECH-D-14-00091.1>.
- Deltares, 2008. Validation Document Delft3D- FLOW Validation Document Delft3D-FLOW.
- Deltares, 2014. 3D/2D modelling suite for integral water solutions -waves. Deltares.
- Deltares, 2018. Delft3D-FLOW, User Manual. Delft3D Flexible Mesh Suite. <https://doi.org/10.1007/s00231-009-0509-6>.
- Devlin, Adam Thomas, Jay, D.A., Zaron, E.D., Talke, S.A., Pan, J., Lin, H., 2017. Tidal variability related to sea level variability in the Pacific Ocean. J. Geophys. Res.: Oceans 122 (11), 8445–8463. <https://doi.org/10.1002/2017JC013165>.
- Devlin, Adam T., Pan, J., Lin, H., 2019. Extended spectral analysis of tidal variability in the north Atlantic Ocean. J. Geophys. Res.: Oceans 124 (1), 506–526. <https://doi.org/10.1029/2018JC014694>.
- DiMarco, S., Reid, R., 1998. Characterization of the principal tidal current constituents on the Texas-Louisiana shelf. J. Geophys. Res. C Ocean. 103 (C2), 3093–3109.
- Doodson, A., Warburg, H., 1941. Admiralty Manual of Tides. H.M.S.O., London.
- Egbert, G.D., Erofeeva, S.Y., 2002. Efficient Inverse modeling of barotropic ocean tides. J. Atmos. Ocean. Technol. 19 (2), 183–204. [https://doi.org/10.1175/1520-0426\(2002\)019<0183:EIMBO>2.0.CO;2](https://doi.org/10.1175/1520-0426(2002)019<0183:EIMBO>2.0.CO;2).
- Egbert, G., Erofeeva, L., 2010. The OSU TOPEX/Poseidon Global Inverse Solution TPXO 8 Atlas v.1 Africa. Retrieved from. <http://volkov.oce.orst.edu/tides/global.html>.
- Engelbrecht, F., Landman, W., Engelbrecht, C., Landman, S., Bopape, M., Roux, B., et al., 2011. Multi-scale climate modelling over Southern Africa using a variable-resolution global model. WaterSA 37 (5), 647–658. <https://doi.org/10.4314/wsa.v37i5.2>.
- Fearon, G., Rautenbach, C., Vilaplana, A., 2017a. Monwabisi Outfall - Brine Dispersion Modelling Study. Cape Town. Retrieved from. [www.advisian.com](http://www.advisian.com).
- Fearon, G., Rautenbach, C., Vilaplana, A.D., 2017b. Strandfontein - Brine Dispersion Modelling Study. Cape Town. Retrieved from. [www.advisian.com](http://www.advisian.com).
- Fearon, G., Rautenbach, C., Vilaplana, A.D., 2018. V&A Waterfront - Brine Dispersion Modelling Study. Cape Town. Retrieved from. <http://www.sawater.com.au/SAWater/WhatsNew/MajorProjects/ADP/ProjectInfo.htm>.
- Fernández-Montblanc, T., Voudoukas, M.I., Ciavola, P., Voukouvalas, E., Mentaschi, L., Breyaniannis, G., et al., 2019. Towards robust pan-European storm surge forecasting. Ocean Model. 133 (December 2018), 129–144. <https://doi.org/10.1016/j.ocemod.2018.12.001>.
- Findlay, K., 2018. Operation Phakisa and unlocking South Africa's ocean economy. J. Indian Ocean Reg. 14 (May), 248–254. <https://doi.org/10.1080/19480881.2018.1475857>.
- Foreman, M.G.G., Henry, R.F., 1989. The harmonic analysis of tidal model time series. Adv. Water Resour. 12 (3), 109–120. [https://doi.org/10.1016/0309-1708\(89\)90017-1](https://doi.org/10.1016/0309-1708(89)90017-1).
- Foreman, M.G.G., Neufeld, E.T., 1991. Harmonic tidal analyses of long time series. In: International Hydrographic Review, pp. 85–108 (Monaco).
- Foreman, Mike G.G., Cherniawsky, J.Y., Ballantyne, V.A., 2009. Versatile harmonic tidal analysis: improvements and applications. J. Atmos. Ocean. Technol. 26 (4), 806–817. <https://doi.org/10.1175/2008JTECH0615.1>.
- Furner, R., Williams, J., Horsburgh, K., Saulter, A., 2016. NEMO-surge: setting up an accurate tidal model.
- Godin, G., 1986. The use of nodal corrections in the calculation of harmonic constants. Int. Hydrogr. Rev. LXIII (2), 20 July.
- Godin, G., 1993. On tidal resonance. Cont. Shelf Res. 13 (1), 89–107. [https://doi.org/10.1016/0278-4343\(93\)90037-X](https://doi.org/10.1016/0278-4343(93)90037-X).
- Guillou, N., Neill, S.P., Robins, P.E., 2018. Characterising the tidal stream power resource around France using a high-resolution harmonic database. Renew. Energy 123 (March), 706–718. <https://doi.org/10.1016/j.renene.2017.12.033>.
- Haigh, I.D., Eliot, M., Pattiaratchi, C., 2011. Global influences of the 18.61 year nodal cycle and 8.85 year cycle of lunar perigee on high tidal levels. J. Geophys. Res.: Oceans 116 (6), 1–16. <https://doi.org/10.1029/2010JC006645>.
- Holthuijsen, L.H., 2007. Waves in Oceanic and Coastal Waters. Cambridge University Press Cambridge University Press. <https://doi.org/10.1017/CBO9780511618536>.
- Houwman, K.T., Hoekstra, P., 1998. Tidal ellipses in the near-shore zone (-3 to -10 m); modelling and observations. Coast Eng. 773–786.
- Hutchinson, K., Beal, L.M., Penven, P., Ansorge, I., Hermes, J., 2018. Seasonal phasing of Agulhas current transport tied to a baroclinic adjustment of near-field winds. J. Geophys. Res.: Oceans 123, 7067–7083. <https://doi.org/10.1029/2018JC014319>.
- Illig, S., Cadier, E., Bachélery, M., Lou, Kersalé, M., 2018. Subseasonal coastal-trapped wave propagations in the southeastern Pacific and Atlantic Oceans: 1. A new approach to estimate wave amplitude. J. Geophys. Res.: Oceans 123 (6), 3915–3941. <https://doi.org/10.1029/2017JC013539>.
- Jackson-Veitch, J., Penven, P., Shillington, F., 2010. Modeling equilibrium dynamics of the Benguela current system. J. Phys. Oceanogr. 40, 1942–1964. <https://doi.org/10.1175/2010JPO4382.1>.
- Jay, D.A., 2009. Evolution of tidal amplitudes in the eastern Pacific Ocean. Geophys. Res. Lett. 36 (January), 1–5. <https://doi.org/10.1029/2008GL036185>.
- Jithin, A.K., Unnikrishnan, A.S., Fernando, V., Subeesh, M.P., Fernandes, R., Khalap, S., et al., 2017. Observed tidal currents on the continental shelf off the east coast of India. Cont. Shelf Res. 141, 51–67. <https://doi.org/10.1016/j.csr.2017.04.001>.
- Lai, Z., Ma, R., Huang, M., Chen, C., Chen, Y., Xie, C., Beardsley, R., 2016. Downwelling wind, tides, and estuarine plume dynamics. J. Geophys. Res.: Oceans 121 (6), 4245–4263. <https://doi.org/10.1002/2015JC011486>.Received.
- Le Provost, C., Genco, M.L., Lyard, F., Vincent, P., Canceil, P., 1994. Spectroscopy of the world ocean tides from a finite element hydrodynamic model. J. Geophys. Res. 99 (C12), 24777–24797.
- Leffler, K.E., Jay, D.A., 2009. Enhancing tidal harmonic analysis: robust (hybrid L1/L2) solutions. Cont. Shelf Res. 29 (1), 78–88. <https://doi.org/10.1016/j.csr.2008.04.011>.
- Li, M., Zhong, L., 2009. Flood-ebb and spring-neap variations of mixing, stratification and circulation in Chesapeake Bay. Cont. Shelf Res. 29 (1), 4–14. <https://doi.org/10.1016/j.csr.2007.06.012>.
- Lucas, A.J., Pitcher, G.C., Probyn, T.A., Kudela, R.M., 2014. The influence of diurnal winds on phytoplankton dynamics in a coastal upwelling system off southwestern Africa. Deep-Sea Res. Part II Top. Stud. Oceanogr. 101 (March), 50–62. <https://doi.org/10.1016/j.jdsr.2013.01.016>.
- Mather, A.A., Stretch, D.D., 2012. A Perspective on sea level rise and coastal storm surge from southern and eastern Africa: a case study near Durban, South Africa. Water (Switzerland) 4 (1), 237–259. <https://doi.org/10.3390/w4010237>.
- Mawdsley, R.J., Haigh, I.D., Wells, N.C., 2015. Global secular changes in different tidal high water, low water and range levels. Earth's Future 3, 66–81. <https://doi.org/10.1002/2014EF000282>.Abstract.
- Mofjeld, H., Larsen, L., 1984a. Tides and Tidal Currents in the Inland Waters of Western. (Washington).
- Mofjeld, H.O., Larsen, L.H., 1984b. Tides and Tidal Currents of the Inland Waters of Western Washington. Washington. Retrieved from. <http://search.proquest.com/docview/14049295?accountid=14656>.
- Monteiro, P.M.S., Nelson, G., Van Der Plas, A., Mabilhe, E., Bailey, G.W., Klingelhoeffer, E., 2005. Internal tide - shelf topography interactions as a forcing factor governing the large-scale distribution and burial fluxes of particulate organic matter (POM) in the Benguela upwelling system. Cont. Shelf Res. 25 (15), 1864–1876. <https://doi.org/10.1016/j.csr.2005.06.012>.
- Navy, S.A., 2018. 2018 South African Tide Tables. South African Hydrographic Office.
- Neill, C.O., Saulter, A., 2017. NEMO-Surge: Forecast Performance during 2016-2017 Winter Trial Technical Report 622.
- Nzualo, T.N.M., Gallo, M.N., Vinzon, S.B., 2018. Short-term tidal asymmetry inversion in a macrotidal estuary (Beira, Mozambique). Geomorphology 308, 107–117. <https://doi.org/10.1016/j.geomorph.2018.01.029>.
- O'Neill, C., Saulter, A., Williams, J., Horsburgh, K., 2016. NEMO-surge: Application of Atmospheric Forcing and Surge Evaluation. Technical report 619, (December). pp. 57. Retrieved from. [http://www.metoffice.gov.uk/binaries/content/assets/mohipdf/pdf/library/frtr\\_619\\_2016.pdf](http://www.metoffice.gov.uk/binaries/content/assets/mohipdf/pdf/library/frtr_619_2016.pdf).
- Pawlowski, R., Beardsley, B., Lentz, S., 2002. Classical tidal harmonic analysis with error analysis in MATLAB using T.TIDE. Comput. Geosci. 28. <https://doi.org/10.1109/APS.2007.4396859>.
- Penna, N.T., Stewart, M.P., 2003. Aliased tidal signatures in continuous GPS height time series. Geophys. Res. Lett. 30 (23), 1–4. <https://doi.org/10.1029/2003GL018828>.
- Pugh, D.T., 2001. Tides. In: Encyclopedia of Ocean Sciences. Elsevier, pp. 32–39. <https://doi.org/10.1016/B978-012374473-9.00123-5>.
- Pugh, D., 2004. Changing Sea Levels: Effects of Tides, Weather and Climate. Cambridge University Press.
- Reason, C., Landman, W., Tennant, W., 2006. Seasonal to decadal prediction of southern African climate and its links with variability of the Atlantic Ocean. Bull. Am. Meteorol. Soc. 87 (7), 941–956. <https://doi.org/10.1175/BAMS-87-7-941>.
- Rizal, S., 2002. Taylor's problem—influences on the spatial distribution of real and virtual amphidroms. Cont. Shelf Res. 22 (15), 2147–2158. [https://doi.org/10.1016/S0278-4343\(02\)00068-7](https://doi.org/10.1016/S0278-4343(02)00068-7).
- Roos, P.C., Velema, J.J., Hulscher, S.J.M.H., Stolk, A., 2011. An idealized model of tidal dynamics in the North Sea: resonance properties and response to large-scale changes. Ocean Dynam. 61 (12), 2019–2035. <https://doi.org/10.1007/s10236-011-0456-x>.
- Sainsbury, N.C., Genner, M.J., Saville, G.R., Pinnegar, J.K., O'Neill, C.K., Simpson, S.D., Turner, R.A., 2018. Changing storminess and global capture fisheries. Nat. Clim. Change 8 (8), 655–659. <https://doi.org/10.1038/s41558-018-0206-x>.
- Sammari, C., Koutitonsky, V.G., Moussa, M., 2006. Sea level variability and tidal resonance in the Gulf of Gabes, Tunisia. Cont. Shelf Res. 26 (3), 338–350. <https://doi.org/10.1016/j.csr.2005.11.006>.
- Schumann, E.H., 1983. Long-period coastal trapped waves off the southeast coast of

- Southern Africa. Cont. Shelf Res. 2 (2–3), 97–107. [https://doi.org/10.1016/0278-4343\(83\)90010-9](https://doi.org/10.1016/0278-4343(83)90010-9).
- Schumann, E.H., Perrins, L.-A., 1982. Tidal and inertial currents around South Africa. Proceedings of 18th Conference on Coastal Engineering. pp. 2562–2580. November 1982, Cape Town, South Africa. <https://doi.org/10.1061/9780872623736.156>.
- Schureman, P., 1971. Manual of Harmonic Analysis and Prediction of Tides/by Paul Schureman. U.S. Coast and Geodetic Survey, Washington, D.C. <https://doi.org/10.5962/bhl.title.38116>.
- Searson, S., Brundrit, G., 1995a. Extreme High Sea Levels Around the Coast of Southern Africa. University of Cape, Town.
- Searson, S., Brundrit, G.B., 1995b. Extreme high sea levels around the coast of southern Africa. South Afr. J. Sci. 91 (11–12), 579–588.
- Sembiiring, L., Van Ormondt, M., Van Dongeren, A., Roelvink, D., 2015. A validation of an operational wave and surge prediction system for the Dutch coast. Nat. Hazards Earth Syst. Sci. 15 (6), 1231–1242. <https://doi.org/10.5194/nhess-15-1231-2015>.
- Senthil Kumar, J., Rajasekaran, P., David Paul Raj, R.S., Gopal, N.O., 2016. Observations over an annual cycle and simulations of wind-forced oscillations near the critical latitude for diurnal–inertial resonance. Int. J. Pharm. Sci. Rev. Res. 39 (1), 315–317. <https://doi.org/10.1016/j.csr.2011.06.001>.
- Sete, C., 2010. Tides Structures and Mixing along the Mozambique Coast. University of Bergen, Norway.
- Stammer, D., Ray, R.D., Andersen, O.B., Arbic, B.K., Bosch, W., Carrere, L., et al., 2014. Reviews of Geophysics Accuracy assessment of global barotropic ocean tide models. Rev. Geophys. 52 (3), 243–282. <https://doi.org/10.1002/2014RG000450>. Received.
- Stephenson, A., 2016. Harmonic Analysis of Tides Using TideHarmonics. Retrieved from. <https://cran.r-project.org/package=TideHarmonics>.
- Susanto, R.D., Pan, J., Devlin, A.T., 2019. Tidal mixing signatures in the Hong Kong coastal waters from satellite-derived sea surface temperature. Rem. Sens. 11 (1). <https://doi.org/10.3390/rs11010005>.
- Van Ballegooyen, R., 1991. The dynamics relevant to the modelling of synoptic scale circulations within False Bay. (Transactions of the Royal Society of South Africa).
- Vilibić, I., Horvath, K., Palau, J.L., 2018. Meteorology and climatology of the mediterranean and black seas: introduction. Pure Appl. Geophys. 175 (11), 3721–3725. <https://doi.org/10.1007/s00024-018-2021-8>.
- Waterhouse, A.F., Valle-Levinson, A., Winant, C.D., 2011. Tides in a system of connected estuaries. J. Phys. Oceanogr. 41 (5), 946–959. <https://doi.org/10.1175/2010JPO4504.1>.
- Willmott, C.J., Robeson, S.M., Matsuura, K., 2012. A refined index of model performance. Int. J. Climatol. 32 (13), 2088–2094. <https://doi.org/10.1002/joc.2419>.
- Woodworth, P.L., 2010. A survey of recent changes in the main components of the ocean tide. Cont. Shelf Res. 30 (15), 1680–1691. <https://doi.org/10.1016/j.csr.2010.07.002>.
- Yincan, Y., et al., 2017. Submarine sand waves and sand ridges. In: Marine Geo-Hazards in China. Elsevier, pp. 523–554. <https://doi.org/10.1016/B978-0-12-812726-1.00012-7>.
- Zaron, E.D., Jay, D.A., 2014. An analysis of secular change in tides at open-ocean sites in the pacific. J. Phys. Oceanogr. 44 (7), 1704–1726. <https://doi.org/10.1175/jpo-d-13-0266.1>.
- Zhao, Z., Wang, J., Menemenlis, D., Fu, L.-L., Chen, S., Qiu, B., 2019. Decomposition of the multimodal multidirectional  $M_2$  internal tide field. J. Atmos. Ocean. Technol. JTECH-D-19-0022.1. <https://doi.org/10.1175/JTECH-D-19-0022.1>.
- Zijl, F., Verlaan, M., Gerritsen, H., 2013. Improved water-level forecasting for the northwest european shelf and north sea through direct modelling of tide, surge and non-linear interaction topical collection on the 16th biennial workshop of the joint numerical sea modelling group (JONSMOD) in bre. Ocean Dynam. 63 (7), 823–847. <https://doi.org/10.1007/s10236-013-0624-2>.
- Zu, T., Gan, J., Erofeeva, S.Y., 2008. Numerical study of the tide and tidal dynamics in the South China Sea. Deep Sea Res. Oceanogr. Res. Pap. 55, 137–154. <https://doi.org/10.1016/j.dsr.2007.10.007>.

## Chapter 4

### *A coupled wave, tide and storm surge operational forecasting system for South Africa – validation and physical description*

---



Figure 4-1: An original linoleum print made during the course of the present study. This artwork was inspired by the atmosphere-ocean interactions described in the present chapter. In the distance a coastline can also be seen, highlighting the importance of this study to coastal vulnerability considerations.

## **4.1 Abstract**

Regional storm tidal levels of the South African coastline are investigated by means of a calibrated and validated numerical model. The model was developed utilizing the shallow water hydrodynamic model, Delft3D. This model was coupled (online) with a non-stationary spectral wave model (developed in the Simulating Waves in the Nearshore (SWAN) numerical code). A local, 4.4 km version of the Unified Model (UM) was applied as atmospheric forcing for the coupled system. The models presented in this study form part of the operational marine forecasts of the South African Weather Service (SAWS), Wave and Storm Surge (SWaSS) model. The operational protocol and model calibration and validation are presented via statistical correlations with measured water levels at six South African coastal locations. The main calibration parameters and thus physical drivers were winds, atmospheric pressure and waves. The validated numerical model is used to provide an experimental physical description of South African storm surge characteristics, per coastline. The dominant driver of South African storm surge is winds associated with mid-latitude cyclones. Further novelty in the present study is the quantification of the relative contribution of extreme storm wave set-up to the South African storm surge signal. This wave set-up contributes approximately 20 % of the total surge signal in the southwest, with winds contributing approximately 55 %. The importance of the continental shelves is also elucidated concerning the frictional shoaling effects of the long surge wave propagation. (Rautenbach, Daniels, de Vos, & Barnes, 2020)

## **4.2 Publication details**

Rautenbach, C., Daniels, T., de Vos, M., & Barnes, M. A. (2020). A coupled wave, tide and storm surge operational forecasting system for South Africa: validation and physical description. *Natural Hazards*. <https://doi.org/10.1007/s11069-020-04042-4>. Available in this thesis with the Springer Nature, licence number 4918011040861

## **4.3 Author contributions (as appeared in paper)**

Dr. Christo Rautenbach wrote the manuscript. He formulated the research questions and the resulting methodology. He designed and ran the calibration and validation simulations and co-developed most of the post-processing scripts, statistics and figures. Ms. Tania Daniels processed the Unified Model outputs and executed their statistical validation. She also wrote and contributed towards the atmospheric descriptions. Mr. Marc de Vos pre-processed the raw water level data obtained from SANHO and wave data obtained from



TNPA. Mr. Michael A. Barnes helped with the post-processing of the model results and figure production. He also helped in scheduling and running the considerable amount of calibration simulations. All the authors contributed towards the general discussions and reasoning pertaining to the main research results and conclusions presented here.

#### 4.4 Errata

In the present publication, Figure 8 (a) was misplaced during the publication process. It has now been added here for completeness.

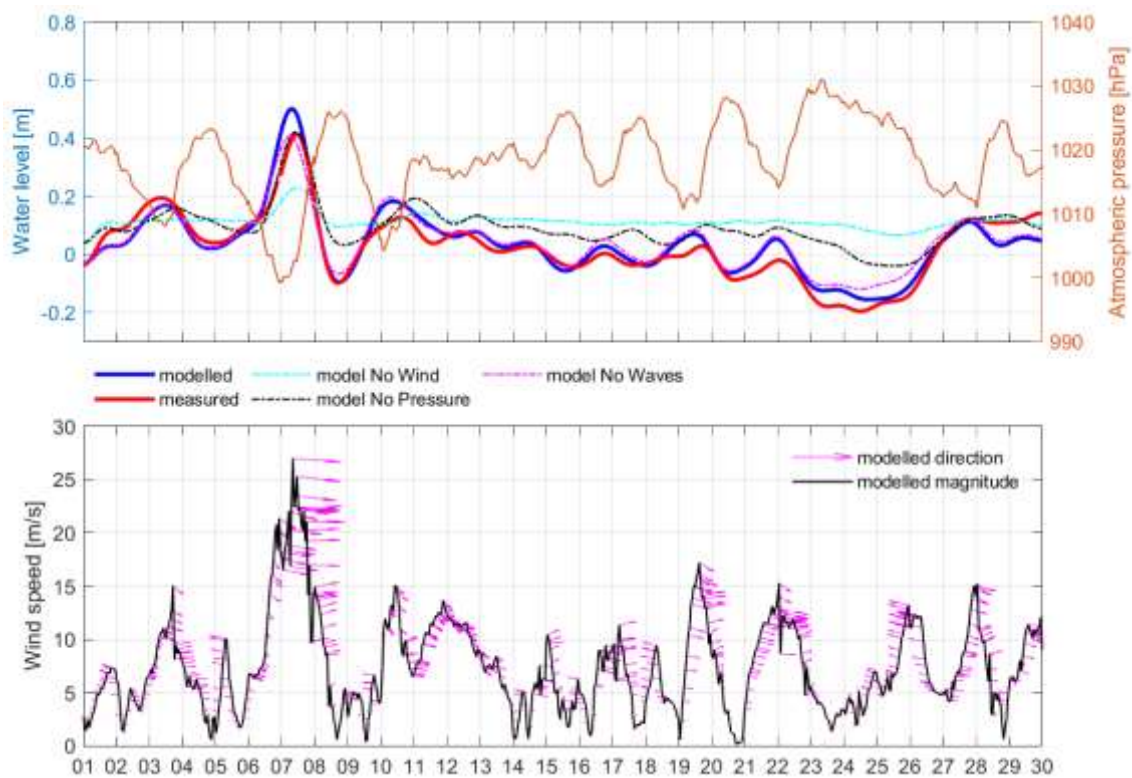


**Figure 4-2: {Fig. 8} Final model calibration results for Cape Town. Each upper panel indicates the modelled and measured water levels on the left axis, after the tidal signals have been filtered out. On the right-hand axis, the prevailing atmospheric pressure close to the coastal city of interest is provided. Each lower panel indicates the associated near shore UM wind speeds together with their directions as magenta, True North arrows.**



# A coupled wave, tide and storm surge operational forecasting system for South Africa: validation and physical description

Christo Rautenbach<sup>1,2,3</sup> · Tania Daniels<sup>1,4</sup> · Marc de Vos<sup>1,3</sup> · Michael A. Barnes<sup>1,5</sup>

Received: 28 October 2019 / Accepted: 1 May 2020  
© Springer Nature B.V. 2020

## Abstract

Regional storm tidal levels of the South African coastline are investigated by means of a calibrated and validated numerical model. The model was developed utilizing the shallow water hydrodynamic model, Delft3D. This model was coupled (online) with a non-stationary spectral wave model (developed in the Simulating WAVes in the Nearshore (SWAN) numerical code). A local, 4.4 km version of the Unified Model was applied as atmospheric forcing for the coupled system. The models presented in this study form part of the operational marine forecasts of the South African Weather Service, Wave and Storm Surge model. The operational protocol and model calibration and validation are presented via statistical correlations with measured water levels at six South African coastal locations. The main calibration parameters and thus physical drivers were winds, atmospheric pressure and waves. The validated numerical model is used to provide an experimental physical description of South African storm surge characteristics, per coastline. The dominant driver of South African storm surge is winds associated with mid-latitude cyclones. Further novelty in the present study is the quantification of the relative contribution of extreme storm wave set-up to the South African storm surge signal. This wave set-up contributes approximately 20% of the total surge signal in the southwest, with winds contributing approximately 55%. The importance of the continental shelves is also elucidated concerning the frictional shoaling effects of the long surge wave propagation.

**Keywords** Storm surge · Waves · Extreme events · Operational forecasting · Numerical modelling · Mid-latitude cyclones · Delft 3D · SWAN · South Africa

---

✉ Christo Rautenbach  
rautenbachchristo@gmail.com

<sup>1</sup> Marine Research Unit, South African Weather Service, Cape Town, South Africa

<sup>2</sup> Institute for Coastal and Marine Research, Nelson Mandela University, Port Elizabeth, South Africa

<sup>3</sup> Department of Oceanography and Marine Research Institute, University of Cape Town, Cape Town, South Africa

<sup>4</sup> Climate Systems Analysis Group, University of Cape Town, Cape Town, South Africa

<sup>5</sup> Department of Geography, Geoinformatics and Meteorology, University of Pretoria, Pretoria, South Africa

# 1 Introduction

Storm surge is one of the most widely misunderstood physical coastal phenomena among coastal communities. Numerous people perceive storm surges to be high wave events. While they do frequently co-occur with storm surges, waves are not storm surges. Storm surge is the residual water level (deviation from the predicted tide) as a result of atmospheric and wave water level set-ups. As such, storm surge is calculated by subtracting (or filtering out) the predicted astronomical tidal signal from the total observed or modelled sea surface elevation. In numerous studies, the term for the total sea surface elevation (tidal water level plus storm surge water level) is referred to as *storm tide* (Buskey et al. 2015). The same terminology will be utilized in this study.

Storm surge can have the effect of raising and lowering the sea water level and is assumed to be *positive* (rise) and *negative* (fall) in storm surge water levels (Peng et al. 2006). Storm surge is most sensitive to atmospheric barometric pressure [via the inverse barometer or isostatic signals (Ponte 2006)], wind and wave set-up and local bathymetry. Baroclinic waves (internal waves) are not considered in the present study. The inverted barometer (IB) ocean response is also an idealized assumption and does not always hold true, especially in the Southern Hemisphere (Mathers and Woodworth 2004). The assumption is that an increase (*decrease*) of 1 hPa causes a sea-level ocean reaction (at a quasi-immediate time scale) of a negative (*positive*) surge, approximately equal to 1 cm (Mathers and Woodworth 2004). This assumption translates to a 0 hPa pressure change at the ocean floor.

Areas adjacent to large expanses of continental shelves are generally most vulnerable to storm surge events. Wind-driven set-up is directly proportional to the reciprocal of the water depth. Thus, on-shore winds have the effect of “pilling up” water against the coastlines of shallow seas (Bosboom and Stive 2015). This is exacerbated if the coastline shape is conducive to funnelling accumulated water towards the coastline. On the South African coastline, this happens on the Agulhas and Namaqua Bank (refer to Fig. 1). The rest of

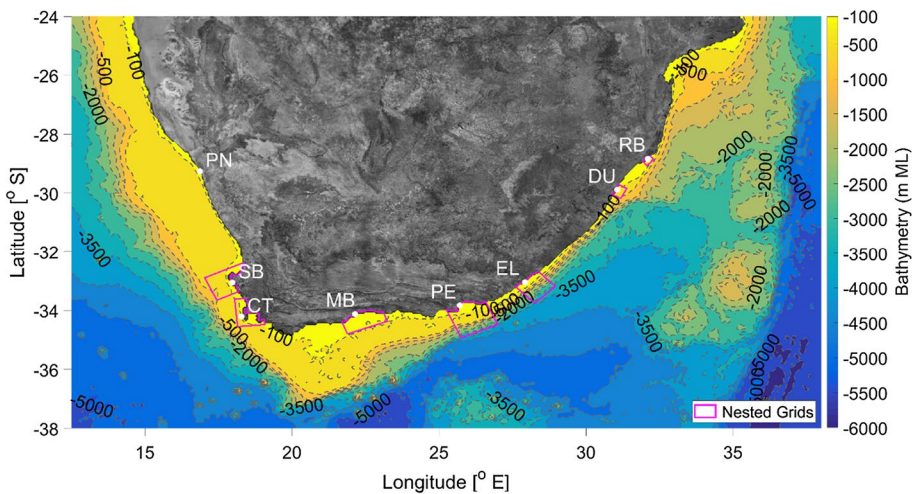


**Fig. 1** The extent of the 1/16th of a geographical degree wave, tide and storm surge model, together with the South African bathymetry and major coastal cities. The magenta enclosures indicate the high-resolution nested wave model domains at 1/48th of a geographical degree resolution

the coastline has a narrow continental shelf, and thus, water cannot pile up on the shelf as easily. This does not mean that surge cannot occur on those coastlines, however. It simply implies that the physical manifestation will have different characteristics and will be due to a varying interplay of physical phenomena. For example, on the east coast of South Africa, storm surges are expected to be mainly due to low atmospheric pressure.

Storm surge signals usually have a wavelength (and thus period) longer than tidal signals (Bosboom and Stive 2015). The duration of these events is closely linked to the atmospheric storm conditions driving them. As the astronomic tidal signal is an important contributor to coastal water levels, the high and low water timing is a crucial factor in the resulting coastal impacts (Rautenbach et al. 2019). If a storm surge event lasts longer than half a day, the probability of co-occurring with a high tide or even spring high tide is given. Depending on the particular location, these extreme water levels can inundate coastal infrastructure or residential areas (Athanasίου et al. 2019). Elevated sea levels are also associated with episodic erosion that could also potentially compromise infrastructure (e.g. Mather and Stretch 2012). Storm conditions are usually associated with large wave events, and high-water levels extend the reach of these waves. In the case of negative surge levels, water levels below chart datum (CD) (also known as lowest low astronomical tide) could possibly occur which has serious implications for ship traffic when navigating depth critical channels.

The benefits of an accurate operational wave and storm surge forecasting system are thus clear. Such a system also enables improved preparedness of disaster management (DM) and coastal management/governmental agencies (Sembiring et al. 2015). Countries famous for extreme coastal storm surges levels are the Netherlands (e.g. Sembiring et al. 2015; Verboom et al. 1992) and USA, owing to hurricane-related inundation (e.g. Veeramony et al. 2017). Other examples include the frequent, cyclone-related coastal flooding of India (e.g. Vatvani et al. 2002), Madagascar (Bloemendaal et al. 2019), Mozambique (e.g. Cabral et al. 2017) and island states such as Mauritius and La Reunion (e.g. Muthige et al. 2018). For South Africa, no operational storm surge models have yet been developed or presented in the open literature.

## 1.1 Study region

South Africa has a coastline that spans over 3000 km, with large percentages of the population living in areas sensitive to coastal inundation (Findlay 2018). In Fig. 1, the extent of the coupled South African Weather Service (SAWS) numerical Wave and Storm Surge (SWaSS) model is shown. Major coastal towns are indicated with the following abbreviations: Port Nolloth (PN), Saldanha Bay (SB), Cape Town (CT), Mossel Bay (MB), Port Elizabeth (PE), East London (EL), Durban (DN) and Richards Bay (RB).

South Africa does not have a broad continental shelf, with the exception of the Agulhas and Namaqua Banks where semi-diurnal tidal resonance occurs (Rautenbach et al. 2019). These shallower shelf areas have also been reported to be the cause of the larger variability in observed water levels on the South African south and west coasts (Ballegooyen 1995; Schumann 1983; Schumann and Perrins 1982). Searson and Brundrit (1995) also reported that the South African south coast is the most vulnerable to storm surge events, as quantified and confirmed in the present study. A national research report, focusing on water levels for the South African coastline, is presented by Theron et al. (2013). Using extreme value analysis, they observed the highest storm surge levels along the south coast, with levels of approximately 0.9 m above Mean Sea Level (MSL) for the 1:50 year return period. Along

most of the west and east coast, values were approximately 0.6 m for the same return period. An exception is the area adjacent to Port Nolloth, where the broad continental shelf elevated these values to approximately 0.8 m. Nhantumbo (2019) represents the latest water level research in South African using in situ tide gauge data to analyse time scales of water level variability. They acknowledge the fact that very limited research has been done on how South African water levels are linked with the dominant forcing mechanisms (Nhantumbo 2019). Through their sub-annual sea-level variability analysis, they confirm that atmospheric drivers were the most important, along with local dynamics caused by the Agulhas Current on the South African east coast (especially close to East London, where the continental shelf is exceptionally narrow). No previous study, however, has quantified the relative importance of each driver, for example analysis of the proportion of an extreme storm surge signal which is wind, wave or atmospheric pressure driven. Using a calibrated numerical model, each driving mechanism can be sequentially neglected to investigate their relative influence on the resulting storm surge signal. This research question will thus also be addressed in this study and fully discussed in Sect. 5.3. Nhantumbo (2019) did not consider the importance of wave set-up to the total storm surge signal. This was included in the present study. The influence of the Agulhas Current was not included, however, and the inaccuracies (on the east coast) associated with this exclusion became clear from the results presented in Sect. 5.

## 1.2 Southern African atmospherics and low-pressure systems

South Africa is located in the subtropics, and weather is thus dominated by semi-permanent subtropical high-pressure cells (Tyson et al. 1996), namely the South Atlantic and the South Indian high-pressure cells (presented schematically in Fig. 2). These cells form as a result of the Hadley cell circulation, in which heated air from the tropics rises and moves

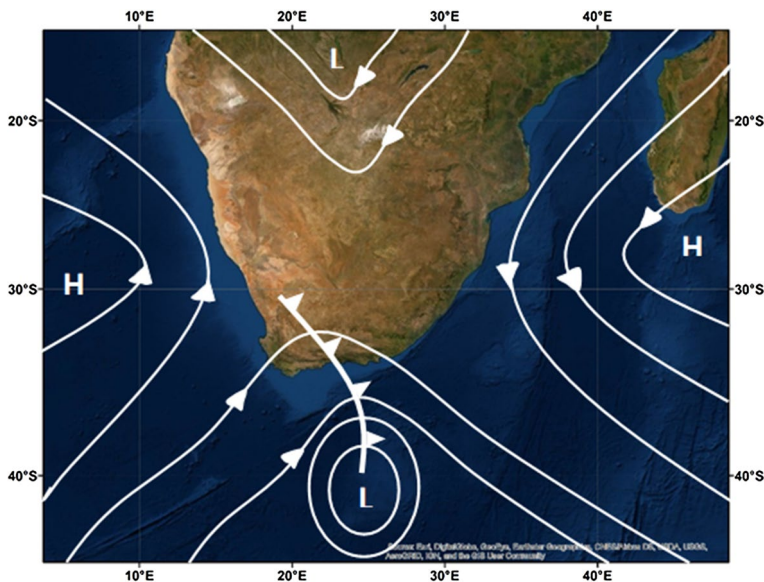


Fig. 2 A schematic of the weather systems around southern Africa (Lutjeharms et al. 2001)



southward. Descending air then forms the two semi-permanent subtropical high-pressure cells. The intensity of these cells is greatest at the end of winter due to the increased intensity of the Hadley cell and mid-latitude westerlies (Seager et al. 2003). The location of the South Atlantic and South Indian subtropical high-pressure cells varies significantly during the year with both shifting northwards during austral winter and moving back south during summer.

The latitudinal position of South Africa permits the influence of mid-latitude low-pressure systems associated with the westerly wind belt (Tyson et al. 1996). Disturbed air in the westerly wind belt creates the low-pressure systems of the South Atlantic. The centre of these low-pressure systems moves eastwards south of Africa. The associated cold frontal bands reach the South African coast mostly in winter when the pressure belts and wind systems move northward. Strong north-westerly winds ahead of the frontal band generate large waves and storm surge signals, which affect the South African coastline (Rossouw 1989). Behind the front, strong south-westerlies can also bring strong winds and large swell to the east coast. In Fig. 2, a typical winter synoptic pattern is shown with the mid-latitude low pressure to south of the country and associated cold front moving over the country (Joubert 1997).

### 1.3 South African wave climate

Highly dynamic weather, oceanography and coastal characteristics give rise to considerable wave variability around the South African coastline. Most of the coastline has a strong swell signal, originating from deep-sea storms. The west and south coast swell predominantly originates from Southern Ocean storms, while the east coast swell might have an addition signal from Indian Ocean storms, especially those associated with tropical cyclones and slow-moving low-pressure systems (Fitchett and Grab 2014). The South African coastline also has numerous complex embayments, some of which are surrounded by high and complex orography. Such orography results in steep temporal and spatial gradients in the wind field. Here, high-resolution wave and flow models are required to understand and predict the dynamics in such embayments, as illustrated in the study of (Williams and Rautenbach 2019) in False Bay and Table Bay (coastal waters surrounding Cape Town) and by Cavaleri and Bertotti (2006) in the Mediterranean Sea.

Sembiring et al. (2015) noted the importance of simulating storm surge via a coupled hydrodynamics and wave model. A coupled wave-flow model has the ability to improve the skill of both model components (Sembiring et al. 2015; Veeramony et al. 2017). For example, wave breaking and refraction can respond to the fluctuation in water depths associated with astronomical tide and storm surge signals. At the same time, surge might be affected by wave set-up. A two-way coupled numerical model is therefore employed in this study.

## 2 Aims and objectives

In the present study, the calibration and validation of the coupled SAWS, Wave and Storm Surge (SWaSS) model is presented. First, the operational protocol currently employed in executing the SWaSS model is described, together with relevant data sources and physical drivers to be calibrated. Next, calibration against a regionally significant storm (locally referred to as Cape Storm) was performed (June 2017). Calibration results are presented for the entire South African coastline at six water-level measurement sites. Sensitivity analyses

are also given as a first attempt at describing the physical drivers of South African storm surge levels. Validation results for two consecutive winter months (July and August 2017) are then investigated, and commentary is provided on the final model performance. The study aims to share the performance of the SWaSS model as well as to inform early warning and disaster response agencies to the unexpected dominant physical drivers of southern African storm tide prediction.

### 3 Data and methods

#### 3.1 Operational protocol and model set-up

An important aspect of operational forecasting is the conceptualization and execution of reliable operational protocols. In Fig. 3, the protocol developed as part of the present study is shown. The downscaled atmospheric model is first initialized at 00:00 UTC and then again at 12:00 UTC. A downscaled grid of the Unified Model (UM) (Brown et al. 2012) is employed, as described in Sects. 4.3.4 and 4.4. As soon as the atmospheric run is complete, the next step is initialized. Parameter wave boundary conditions are extracted from the National Centre for Environmental Prediction (NCEP) operational forecasting model (WaveWatch III), at a half a geographical degree resolution. These are applied to the boundaries, assuming a JONSWAP spectrum (Battjes et al. 1987) with constant peak enhancement factor of 2.5 (Gwebu 2018). A constant wave directional spreading of  $25^\circ$  was also assumed. The limitations of this assumption (e.g. not using space and time varying spectral information) is currently being investigated and falls outside the scope of the present study. The spectrum was interpolated between

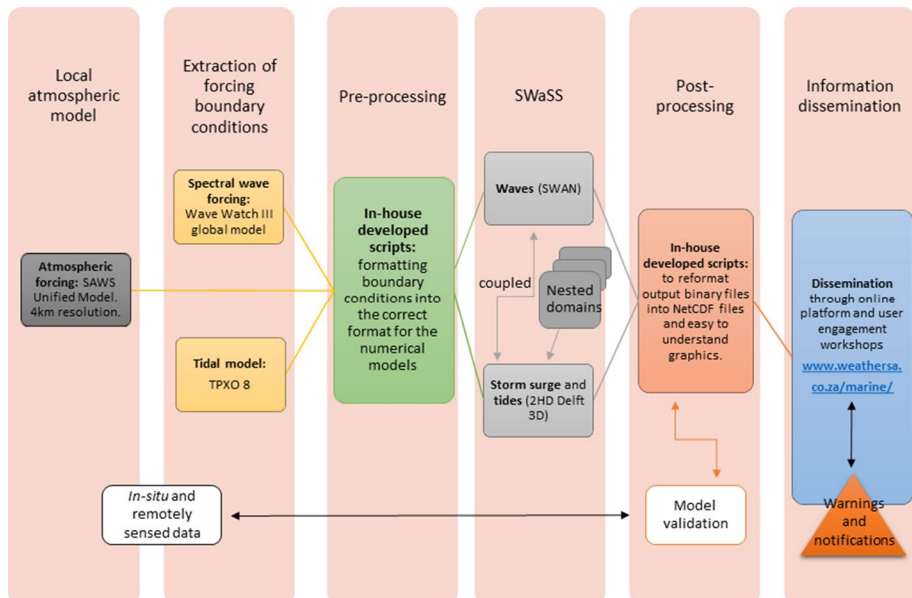


**Fig. 3** Flow diagram of the operational SWaSS protocol



adjacent boundary definition points, and swell boundaries were updated 3-hourly. The wave model validations are presented in Sect. 4.3.5.

Tidal boundary conditions are operationally extracted from the Poseidon Global Inverse Solution model TPXO 8 (Egbert and Erofeeva 2010; Rautenbach et al. 2019). These temporal and spatial varying boundary conditions are responsible for the tidal signal within the overall model. In boundary areas with steep changes in the bathymetry (continental shelf edges), the length of each boundary segment was accordingly reduced to ensure the correct tidal boundary condition variability is captured. For a detailed description of the tidal model underpinning the present operational wave and storm surge model, refer to the work by Rautenbach et al. (2019).

Numerous pre-processing scripts were developed to reformat the various data feeds for easy ingestion into the core numerical models. The Delft 3D Wave and Flow modules were run in online-coupled mode. Communication between the models is on an hourly scale, corresponding to the temporal resolution of the atmospheric forcing. Various nested wave domains were created to ensure high resolution in areas of particular interest. These are mainly around large ports in South Africa. From the west to east coast, these 1/48th geographical degree resolution nested domains are at Saldanha, Cape Peninsula (Cape Town, Simons Town, etc.), Port Elizabeth, East London, Durban and Richards Bay. In Fig. 1, these nested domain enclosures are shown. Making use of local refinement, the output resolution in the vicinity of the measurement wave buoys was approximately 500 m. The extent of the parent grid covers the domain indicated in Fig. 1. In both cases, a rectilinear grid was employed as detailed in Sect. 4.4.

After the model runs are complete, the result files are post-processed using more scripts developed in-house in MATLAB. These post-processed map and time series results files are then intended to allow real-time model validation via live wave buoy data feeds. These validations are based on both in situ measurements, mainly provided by Transnet National Port Authorities (TNPA) and remotely sensed Altimetry data. In the present study, the hindcast validation of the model in question is presented in Sect. 5.

The final step in the operational protocol is the dissemination of marine forecasts. To this end, a website was developed and may be viewed at <https://marine.weathersa.co.za/>. The portal presents a clear and easy to understand forecast information. Both regional and local map outputs of wind, waves and water level fields are provided. Time series outputs at wave buoy locations are also provided. As part of the operational functions of SAWS, forecast extreme or hazardous conditions should be communicated to both disaster management (DM) authorities and the general public. To this end, SAWS has a dedicated team of forecasters disseminating warnings via numerous platforms. Prior to the development of the present operational model, no fit-for-purpose, high-resolution marine forecasts were available for the South African coastline.

### 3.2 Drivers of southern African storm surge

To be able to understand, quantify and calibrate the physical parameters driving storm surge, the governing equations must be understood. In Eq. (1), the Cartesian depth-averaged conservation of momentum relationship is given for an incompressible fluid, assuming the shallow water, hydrostatic (Vreugdenhil 1994) and Boussinesq approximations (Cobb and Blain 2002):

$$\partial \mathbf{v} / \partial t + \mathbf{v} \cdot \nabla \mathbf{v} + \mathbf{f} \times \mathbf{v} = -g \nabla (\zeta - \zeta_a) + (\boldsymbol{\tau}_s - \boldsymbol{\tau}_b) / (\rho H) + M / H \quad (1)$$

here  $t$  denotes time and  $\mathbf{v} = (\overline{U}, \overline{V})$  is the depth-averaged horizontal velocity expressed as:

$$\mathbf{v} = \frac{1}{H} \int_h^\zeta \mathbf{V} dz \quad (2)$$

Total water depth is denoted by  $H = \zeta + d$ , with  $\zeta$  the free water surface elevation and  $d$  the bathymetric depth (both relative to the geoid). The Coriolis term is given by  $\mathbf{f} = 2\Omega \sin(\theta)$  as an upwards facing unit vector, with  $\Omega$  the angular frequency of the rotation of the earth and  $\theta$  geographical degree of latitude. Gravitational acceleration is denoted by  $g$ , and  $\zeta_a = -P_{\text{atm}}/\rho g$  is the free surface elevation due to the inverted barometer effect (discussed in Sect. 4.3.3) where  $P_{\text{atm}}$  is the atmospheric pressure.

$\tau_s$  is the applied horizontal surface stresses (due to winds and waves), and  $\tau_b$  is the horizontal bottom stress vector (usually a quadratic friction law as described in Sect. 4.4) (Cobb and Blain 2002; Ferrarin et al. 2013).  $\rho$  is water density and  $M$  is the horizontal momentum diffusion/dispersion given as  $E(\nabla^2 H \mathbf{v})$ , with  $E$  the horizontal eddy viscosity coefficient. The continuity equation is then given as  $\frac{\partial \zeta}{\partial t} + H \nabla \cdot \mathbf{v} = 0$ .

From these equations, it becomes clear that some of the major drivers or parameters of storm surge are bottom friction, surface stresses (winds and waves) and the inverted barometer effect. The bottom friction is not discussed or calibrated in the present study and will be employed as summarized in Sect. 4.4. The sensitivity of the bottom friction ( $\tau_b$  in Eq. 1) was tested and described in (Rautenbach et al. 2019). Attention will be given to the effect of wind-drag break points, coupled wave stresses ( $\tau_s$  in Eq. 1) and reference pressures (in the calculation of the boundary inverted barometer water elevations, ( $\zeta_a$  in Eq. 1)) on the simulated storm surge. Detail of the model calibration is provided in Sect. 5.1.

Rautenbach et al. (2019) were the first to identify and quantify semi-diurnal tidal resonance on the continental shelves of southern Africa. In 2017, the so called “Cape Storm”—an extreme storm event with violent wind, wave and storm surge—passed Cape Town. In Fig. 4, the two-dimensional storm surge water elevations of Cape Storm are presented. The amplification of the storm surge signal over the continental shelves is again evident (refer to Fig. 1). Even though storm surges are also long wave signals, this amplification is not due to resonance but rather due to bottom friction. With strong onshore wind, water tends to ‘pile up’ or get set-up against the coastline, contributing to storm surge (Buskey et al. 2015). The extended area of water level set-up over the shelf area, observed in Fig. 4, is due to the shallow bathymetry of the shelf. The one directional equilibrium condition of water level set-up against a coastline maybe be expressed as:

$$\frac{d\zeta_{\text{wind}}}{dx} = \frac{\tau_{\text{wind},x}}{\rho g h} \quad (3)$$

with  $\tau_{\text{wind},x}$  the ocean surface shear stress exerted by the wind and usually given as another quadratic, piece-wise friction law (Bosboom and Stive 2015), as described in Sect. 4.4. Due to the inverse proportional relationship of the water level gradient (left side of Eq. 3) and the water depth, shallower, shelf seas will always be more susceptible to storm surge. This is clearly illustrated in Fig. 4, where the local shoaling of the storm surge long wave can be seen on the continental shelf. If the coastline is also enclosed around such an area, the phenomenon is further amplified. The Netherlands is an example of where a north-westerly wind will cause storm surge over the continental shelf of the North Sea (Verboom et al. 1992). Due to South Africa’s predominantly convex coastline, extreme storm tidal levels (exceeding 2 m) are not generated (SA Navy 2018). It is, however, safe to assume

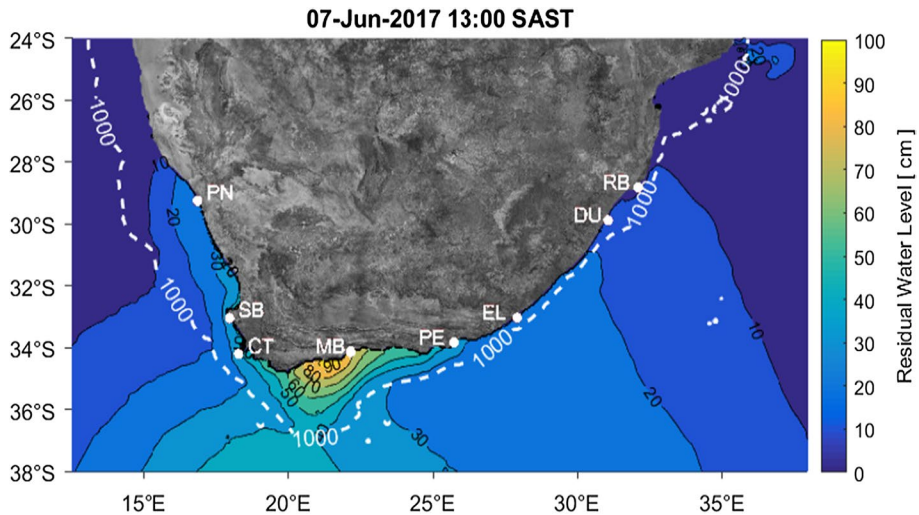


**Fig. 4** Storm surge water levels associated with Cape Storm during early June 2017. The storm surge signal is based on the calibrated operational numerical model presented in the present study. The edge of the continental shelf is also illustrated as the 1000 m depth contour

that extreme storm tidal events are prone to be observed on the South African south coast (Mossel Bay, Port Elizabeth) and/ or on the West Coast (Port Nolloth). These are due to semi-diurnal tidal resonance and the water depth-related storm water level set-up. The importance of the timing of these two phenomena should not be ignored. Given that the typical South African storm lasts approximately two to three days (refer to Sect. 2.2), a storm surge is likely to coincide with at least a few high tides. The southern boundary increase in water elevation, evident in Fig. 4, was due to the proximity of the low-pressure core of the passing mid-latitude cyclone (also refer to Fig. 2).

### 3.3 Data

#### 3.3.1 Water level

Water level measurements were obtained from the South African Navy Hydrographic Office (SANHO). A low-pass filter published by Signell (2014) was applied to ensure all tidal signals were removed. The six locations where measurements were obtained are presented in Fig. 1.

#### 3.3.2 Bathymetry

The model bathymetry is shown in Fig. 1 and is a combination of the General Bathymetric Chart of the Oceans (GEBCO) in deep water and local, port-specific, high-resolution bathymetry supplied by SANHO.

### 3.3.3 Reference pressure

It stands to reason that a restricted modelling domain would be insufficient in generating all the required long wave water elevation signals. Due to computational constraints, it is not always feasible to have a global forecast (or even hind-cast) water level model. Muis et al. (2016) presented a global reanalysis model of extreme water levels. These global studies could readily provide water level boundary conditions for higher-resolution regional and local models. Unfortunately, the study by Muis et al. (2016) only ran until 2014 and was thus not suitable to provide boundary conditions for the present study. The Vrije Universiteit Amsterdam (together with collaborators) is, however, planning to extend their model to the present day.

In the absence of the aforementioned global models, an alternative, widely used method was employed to compensate for water level offsets on the model domain boundary. In the present study, the IB assumption was used to describe the water level adjustments on the model open boundaries and is described as:

$$\delta_{\text{atm}} = \frac{P_{\text{average}} - P_{\text{atm}}}{\rho g}, \quad (4)$$

where  $P_{\text{average}}$  is the spatial average reference pressure,  $P_{\text{atm}}$  is the locally prescribed atmospheric pressure,  $\rho$  is the ocean water density, and  $g$  is gravitational acceleration (Ponte 2006). In numerous studies,  $P_{\text{average}}$  is assumed to be the global mean surface pressure and approximately equal to 1013.3 hPa (Dorandeu and Le Traon 1999). In Fig. 5, the long-term average seasonal atmospheric surface pressure for southern Africa is shown. These average atmospheric mean surface pressures were produced from data provided by the National Oceanic and Atmospheric Administration (NOAA) in the USA (Kalnay et al. 1996). These model data span from 1948 to 2018, are based on a reanalysis model, and are sampled six-hourly.

Other studies exploring seasonal atmospheric pressure variability include Dorandeu and Le Traon (1999), Mathers and Woodworth (2004), and Ponte (2006). From these studies and Fig. 5, not only is the seasonal variability clear, the space varying nature of the atmospheric pressure globally and regionally is also evident. This is especially true in the Southern Ocean, where water level signals associated with the inverted barometer displayed high variability when analysed in two reanalysis products (Ponte 2006). Over southern Africa, the seasonal difference in atmospheric pressure is also clear (Reason et al. 2006). The

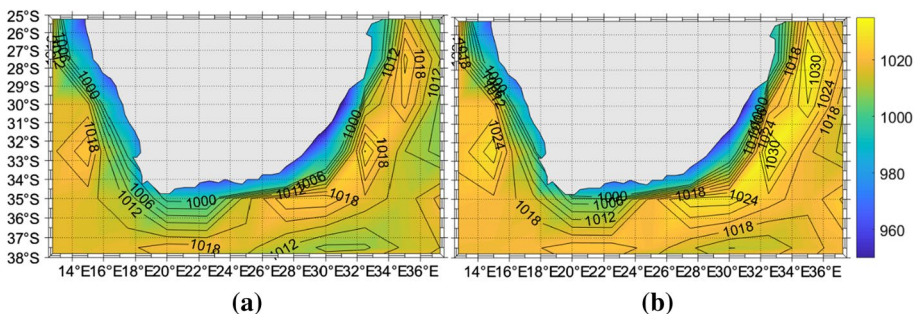


**Fig. 5** Long-term (1948 to 2018) average atmospheric pressure for southern Africa during **a** DJF and **b** JJA (Kalnay et al. 1996)

long-term mean atmospheric pressures vary latitudinally and are not as ideal as in the case presented for the UK by O'Neill et al. (2016). A long-term average over the boundary conditions of the present study revealed a reference pressure of approximately 1020 hPa for most of the boundaries, and especially towards the southwest.

In the present study, sensitivity to model boundary reference pressure was evaluated according to a similar methodology described by O'Neill et al. (2016) and applied by using Eq. (4) on the open water level boundary conditions. Details of these calibrations results are described in Sect. 5.1. O'Neill et al. (2016) also noted that choosing a spatially and temporally constant reference atmospheric pressure could lead to spurious boundary water level corrections, favouring accuracy in areas with average reference boundary pressures closest to the selected constant value. They suggested a temporally constant, space varying reference atmospheric pressure ( $P_{\text{average}}$  in Eq. 4) be investigated for the UK storm surge models. In the present study, space varying reference boundary pressures were thus not implemented (mainly due to the rigidity of implementation in Delft 3D).

### 3.3.4 Wind

Wind data were obtained from the South African Weather Service (SAWS), which has a network of automatic weather stations throughout South Africa. These data were used to validate the downscaled Unified Model (UM) (Brown et al. 2012) at seven coastal locations. Verification of the numerical model should preferably also be done over the open ocean, but due to limited data availability, this was not possible. Performance statistics for the UM at each of the verification sites is provided in Table 1. The accuracy of the UM in both magnitude and direction is clear, thereby instilling confidence in the use of this atmospheric model as storm surge forcing. These results present the first published estimations of the locally downscaled UM accuracy.

Standard deviation (SD) was added to the statistical description of the wind measurements to provide a sense of the wind variability at the particular coastal location. These values correspond well to the seasonal variability described by Young (1999). To highlight the variance in atmospheric behaviour around the coastline, wind roses for all three coastlines are given in Fig. 6.

In general, the strong winds of Cape Town are clear, with the predominant summer Southeaster. Neither Mossel Bay nor sub-tropical Richards Bay encounters frequent, strong winds. The east coast does, however, have a wider range of variability as observed in Table 1 and from the simulated storm surge signals presented in Sect. 5.

### 3.3.5 Waves

Wave measurements were obtained from Transnet National Port Authorities (TNPA). TNPA owns a network of wave-rider buoys around the South African coastline. Wave measurements from seven coastal locations were available during the present study. In Table 2, basic statistical correlations of these data are provided in comparison with the SWAN model developed as part of SWaSS. Here,  $W_i$  refers to the Willmott index (Willmott 1981). For details on the SWAN configuration, refer to Sect. 4.4. From these results, the two-way, online coupled, spectral wave model was assumed adequately accurate for estimating the contribution of wave set-up to the total storm surge signal. Detailed spectral wave model sensitivity analysis and calibration will be presented in a follow-up study in due course. It is worth mentioning that nested wave domains were required for the accurate

**Table 1** Summary of automatic weather station data used in the present study for the calendar year 2017. The Unified Model (UM) statistical performance compare with those data are also provided

Code	Latitude, Longitude	% data availability	Wind speed [m/s]			Wind direction [degrees]			$P_{\text{atm}}$ [hPa]		
			RMSE	Bias	SD	RMSE	Bias	SD	RMSE	Bias	SD
PN	– 29.25 16.8685	89.14	2.68	1.93	1.85	64.84	13.46	73.95	0.65	– 0.10	4.20
LN	– 32.0351 18.3326	95.24	1.66	0.67	1.65	93.15	– 10.60	93.15	0.93	0.52	4.81
SK*	– 34.15 18.32	91.04	3.40	2.26	3.30	80.63	8.01	96.23	0.83	– 0.40	5.11
MB	– 34.1894 22.1318	77.11	3.55	2.73	1.42	65.60	– 5.09	95.18	1.01	0.64	5.69
PE	– 33.98 25.6	97.09	2.31	– 1.14	3.27	64.22	– 3.25	91.06	0.84	– 0.20	5.98
DU	– 29.9569 30.9733	77.40	2.63	1.71	1.89	83.36	4.28	97.46	1.03	0.37	5.81
RB	– 28.7378 32.0934	87.44	2.25	1.34	2.08	104.14	– 10.73	115.88	1.16	– 0.17	5.73

\*SK here refers to Slangkop, a local name for the directional wave-rider buoy just south of Cape Town (CT)

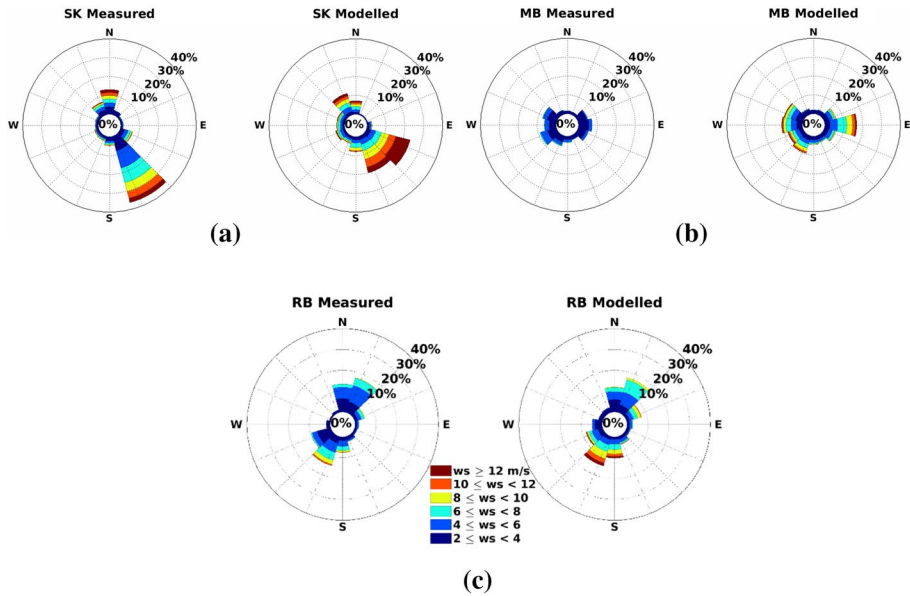


**Fig. 6** Wind roses comparing the measure wind speed, direction and occurrence to the same parameters produced by the Unified Model during 2017. **a** Slangkop (just outside of Cape Town), **b** Mossel Bay and **c** Richards Bay

**Table 2** Directional wave-rider buoys situated around the South African coastline with increasing longitude. All measurements we compared with the SWAN spectral wave model component of SWaSS during June 2017. Water depth, RMSE, Bias and standard deviation (StDev) are all in metres

Code	Water Depth [m]	Latitude Longitude	$H_{m0}$			$T_p$			Direction		
			RMSE	Bias	$W_i$	RMSE	Bias	$W_i$	RMSE	Bias	$W_i$
SB	23	– 33.05 17.978	0.58	0.50	0.90	1.09	0.24	0.88	–	–	–
SK*	70	– 34.204 18.28667	0.67	0.42	0.95	1.18	– 0.05	0.88	19.96	10.38	0.69
MB	24	– 34.12467 22.1535	0.37	0.26	0.83	2.04	– 0.53	0.71	–	–	–
PE	21	– 33.83333 25.71666	0.40	0.30	0.81	3.57	– 1.78	0.57	21.21	– 5.22	0.44
EL	27	– 33.038 27.93083	0.60	0.45	0.77	2.82	– 1.40	0.62	34.25	– 22.21	0.34
DB	30	– 29.884 31.07067	0.51	0.38	0.76	4.39	– 2.91	0.54	31.03	– 14.26	0.80
RB	22	– 28.8265 32.104	0.30	0.19	0.94	4.91	– 3.62	0.53	37.09	– 21.48	0.49

\*SK here refers to Slangkop, a local name for the directional wave-rider buoy just south of Cape Town (CT) modelling of the wave and thus storm surge signal. Without high-resolution nested wave



domains, a great deal of wave driven set-up is missed and thus, the storm tidal peaks are not resolved. Model resolutions in the vicinity of the wave rider buoys were between 500 m and 1 km.

### 3.4 Numerical models

The downscaled UM (Brown et al. 2012) is run locally on SAWS super computers at a 4.4 km resolution. This model was then coupled online with SWaSS, on an hourly temporal resolution. Wind speed, wind direction and atmospheric pressure were communicated to the coupled SWaSS model. This was, however, only a one-way coupling, i.e. the ocean could not influence the atmospheric simulation (refer to Sect. 4.1).

In the present study, the atmospheric pressure's influence on the sea surface elevation is taken into account via the following barotropic pressure gradients:

$$\frac{1}{\rho\sqrt{G_{\xi\xi}}}P_{\xi} = \frac{g}{\sqrt{G_{\xi\xi}}}\frac{\partial\zeta}{\partial\xi} + \frac{1}{\rho\sqrt{G_{\xi\xi}}}\frac{\partial P_{\text{atm}}}{\partial\xi}, \quad (5)$$

$$\frac{1}{\rho\sqrt{G_{\eta\eta}}}P_{\eta} = \frac{g}{\sqrt{G_{\eta\eta}}}\frac{\partial\zeta}{\partial\eta} + \frac{1}{\rho\sqrt{G_{\eta\eta}}}\frac{\partial P_{\text{atm}}}{\partial\eta}. \quad (6)$$

here  $\xi$  and  $\eta$  represents the two axes (longitude and latitude, respectively) of the spherical coordinate system employed in the present study (Deltare 2018).  $\rho$  is the reference density of water,  $\sqrt{G_{\xi\xi}}$  and  $\sqrt{G_{\eta\eta}}$  are the coefficients to transform the curvilinear grid to rectangular coordinates,  $\zeta$  is the sea surface elevation above the reference plane,  $P_{\text{atm}}$  is the atmospheric pressure, and finally,  $P_{\xi}$  and  $P_{\eta}$  are the hydrostatic pressure gradients in the indicated spherical coordinate directions (Deltare 2018). It should also be noted that due to the spherical coordinate system,  $\sqrt{G_{\xi\xi}} = R \cos \eta$  and  $\sqrt{G_{\eta\eta}} = R$ , where  $R$  is the radius of the Earth in the WGS84 global reference system (6 378.137 km). The accuracy and validation of this approach may be found in the Delft 3D validation documentation (Deltare 2008).

The computational grid used was an orthogonal curvilinear  $\sigma$ -coordinate system, extending from 12.5° E to 38° E and 24° S to 38° S. A 1/16th geographical degree grid resolution in spherical coordinates was employed for the flow computations. Equation (5) and (6) are based on the shallow water approximations, with constant density, where the vertical momentum equation is simplified to the hydrostatic pressure assumption. This was a reasonable assumption as the model was executed in a depth-averaged mode (vertical accelerations of the water column itself was not included in the present model). In Eqs. (5) and (6), the atmospheric pressure is included and thus modulates the ocean free-surface response to storm conditions. The atmospheric pressure gradient is usually the largest external forcing term contributing towards the barotropic pressure gradients (gradients in the ocean free surface level) (Deltare 2018).

The numerical model parameter setting used is summarized in Table 3. Wind-drag coefficients have been a topic of long-standing experimental and numerical investigation. In Table 3, two literature-based approximations of the wind-drag breakpoints are given. These correlations have been determined via numerous experimental campaigns and numerical methods (e.g. Large and Pond (1981) and Soloviev et al. (2015)). These measurement campaigns were mainly focused on wind-drag correlations for wind speeds greater than hurricane speed (33 m/s), but also highlighted the most important

**Table 3** Summary of numerical parameterization settings. Here  $U_{10}$  is the wind speed at 10 m above Mean Sea Level (MSL)

SWAN version 40.72	Model (3rd generation mode)	Coefficient
Bottom friction	Madsen et al. (1989)	$K_n$ (Eqv. roughness length)=0.05 m
Depth-induced breaking	Battjes and Janssen (1978)	Alpha (dissipation)=1 Gamma (breaker)=0.8
Whitcapping	Komen et al. (1984)	$C_{ds}$ (dissipation rate)=2.36e-5
Delft3D FLOW version 6.03.00		
Bottom roughness	Chezy (depth-averaged quadratic friction law)	$C_{2D}$ (roughness)=( $H+25$ ) $\sqrt{m/s}$
Boundary reflection parameter	–	$\alpha=0\ s^{-2}$
Wave surface stress	Fredsøe (1984)	–
Wind drag breakpoints:	Fairall et al. (2003), Large and Pond (1981), Powell et al. (2003), Soloviev et al. (2015)	$C_d \times 10^{-3}$ (wind drag) =
Case 1, $U_{10}=11\ m/s$ , 33 m/s, 50 m/s		$A^\dagger=1.2$ , $B=2.64$ , $C=1.51$
Case 2, $U_{10}=0\ m/s$ , 100 m/s	(Sembiring et al. 2015)	$A=0.63$ , $B=7.23$

$\dagger$  Refer to Delft 3D FLOW user manual, page 67 – Fig. 4.31, for definition of break points A, B and C

wind breakpoints for weak to moderate winds. Numerical studies (e.g. Soloviev et al. (2015)) agree to a large extent with experimental studies (e.g. Large and Pond (1981) and Powell et al. (2003)) and prescribe wind-drag breakpoints at approximately 10 m/s and between 25 and 33 m/s. Above 33 m/s, the wind velocities are well within tropical cyclone wind speeds. During Cape Storm 2017, the maximum wind velocity over the Southern Ocean exceeded 33 m/s periodically, especially directly south of the South African south coast. Therefore, an additional wind-drag breakpoint was added to the model presented by Large and Pond (1981) at 50 m/s (refer to Table 3). This extra breakpoint was based on the experimental results provided by Soloviev et al. (2015), and the second breakpoint was set at 33 m/s as per the newest findings by Powell et al. (2003). The weak-to-moderate linear wind trend was based on Large and Pond (1981).

Soloviev et al. (2015) produced a unified parameterization for estimating the continuous wind-drag coefficients, but the linear, piecewise, breakpoint approximations presented in Table 3 closely resemble the characteristics of this parameterization. These wind-drag coefficients are only approximations to the real-world wind drag-coefficients. Literature reports on a large variability in measured wind-drag coefficients due to the influence of the prevailing waves and currents (Kara et al. 2007). These breakpoint estimations can therefore contribute to the storm surge model inaccuracies but are the best contemporary estimates.

TPXO 8 tidal boundary conditions are applied as space and time varying open boundaries, together with the corresponding inverted barometer water-level correction scenario (refer to Sect. 4.3.3). The computational time-step was set at one minute to conform to the Courant number criterion (Courant et al. 1967).

SWAN contains a number of physical processes that add or withdraw wave energy to or from the wave field. The processes included are wind input, whitecapping, bottom friction, depth-induced wave breaking, obstacle transmission, nonlinear wave–wave interactions (quadruplets and triads) and wave-induced set-up. The chosen settings are presented in Table 3. The model was run at the same 1/16th degree resolution as the flow model but with the addition of 1/48th degree resolution nests at all the in situ measurement locations (as indicated in Fig. 1). Local grid refinement near the in situ buoy locations produced results at approximately 500 m to 1 km resolution. SWAN was coupled with the flow model on an hourly temporal resolution and deployed in non-stationary mode.

## 4 Results and discussion

The results presented here are deterministic and do not include any data assimilation or post-processed corrections. The results present the calibration simulations, followed by the final validation results. During validation, no parameter settings were permuted and were solely based on the final calibration parameters and model settings. The calibration period was June 2017, while validation was performed for July and August 2017. JJA 2017 presented multiple storm surge events. Some of these affected mostly the southwest coast (June 2017) and others, the east coast (August 2017). Therefore, JJA 2017 was chosen as a sufficiently representative hindcast period over which to assess the operational storm surge model performance.

#### 4.1 Calibration

Numerous calibration simulations were performed during the present study with the most elucidating of these presented here. The two main parameters for calibration were the wind-drag coefficient and the boundary reference pressure.

As given in Table 3, two wind-drag breakpoint models were investigated in the present study (based on literature). Both models captured the water-level undulations and most importantly the peak storm surge events. Negligible differences were produced between Case 1 and Case 2. The Willmott indices of correlation (Willmott 1981; Willmott et al. 2012) for Case 1 and 2 are given in Table 4. The most pronounced difference between these cases was that Mossel Bay and Port Elizabeth (adjacent to the Agulhas Bank) improved in bias prediction (approximately by 1 cm) but worsened in RMSE prediction (approximately 0.5 cm). The total statistical and time series results closely resembled each other for all reference boundary conditions scenarios (not shown here). Therefore, either Case 1 or 2 may be used to accurately predict the storm surge behaviour for South Africa. Case 1 has been used for the remainder of the study due to the vast amount of measurements supporting the wind-drag breakpoint definitions.

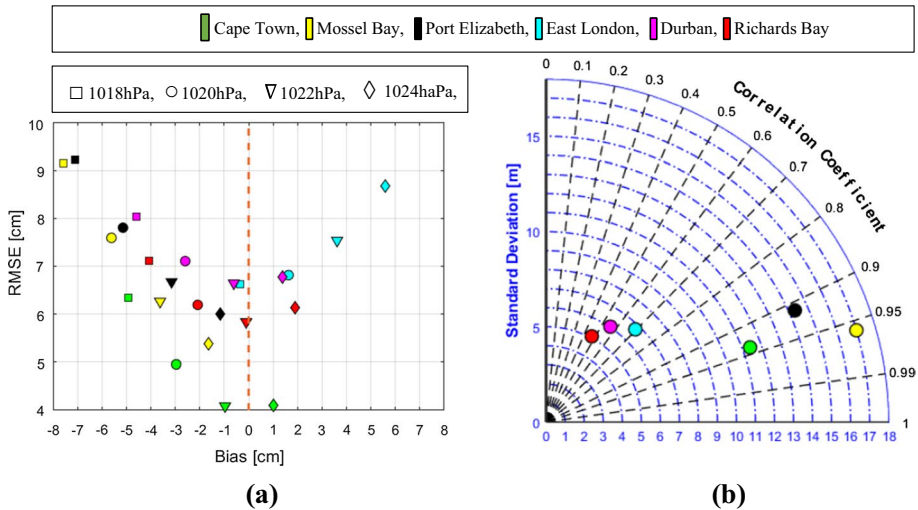
In Fig. 7, a summary of the calibration results is provided. Colours correspond to coastal cities, while the marker shapes correspond to run scenarios. Four separate statistical measures were used to describe the model accuracy. In Fig. 7a, the bias (difference between predicted and measure mean values) and root mean square error (RMSE) are given, while in Fig. 7b, the standard deviation (SD) and correlation coefficients ( $r$ ) are given.

Figure 7 reveals numerous interesting phenomena. As a whole, the SWaSS model performs adequately with RMSE values always below 10 cm. Sembiring et al. (2015) reported on the operational storm surge accuracy of the Coastal Storm Modeling System (CoSMoS) and found RMSE values ranging between 10 and 20 cm, depending on the season. Their results were also based on a Delft 3D model, online coupled with SWAN. They also highlight the importance of coupling water levels and waves based on the studies by Brown et al. (2010). The tide-surge-wave modelling platform for the Mediterranean Sea (named *Kassandra*) reported storm surge prediction accuracies between 4 and 8 cm, very similar to the accuracies presented here (Ferrarin et al. 2013). One of the latest storm surge models for Europe is presented by Fernández-Montblanc et al. (2019). Their model covers the majority of western Europe and reported validation results of  $4 \text{ cm} < \text{RMSE} < 21 \text{ cm}$ . Veeramony et al. (2017) also employed a Delft 3D model in modelling Hurricane Ike in the northern Gulf of Mexico. They reported RMSE accuracies between 20 and 60 cm and bias values ranging from -38 cm until +1 cm given that the SD of a hurricane will be large.

In Fig. 7, accuracy varied according to measurement location. The results presented in the present study produced water level prediction accuracies well within the limits of

**Table 4** Willmott et al. (2012) refined index of model performance and the commonly used Willmott (1981) index for model validation for the two wind-drag models considered in the present study. The scenario of a constant boundary reference pressure of 1024 hPa was used

		CT	MB	PE	EL	DU	RB
Case 1	Willmott et al. (2012)	0.8191	0.8076	0.7127	0.4731	0.5389	0.4649
	Willmott (1981)	0.9668	0.9706	0.9486	0.7266	0.7314	0.6658
Case 2	Willmott et al. (2012)	0.8152	0.8203	0.7237	0.4783	0.5441	0.4741
	Willmott (1981)	0.9672	0.9675	0.9462	0.7324	0.7298	0.6641



**Fig. 7** Model calibration results via **a** Bias versus RMSE and **b** standard deviation versus correlation coefficient. These results represent the Case 1 model setting in Table 3 for all the available coastal water level monitoring station of South Africa. The markers indicate the calibration variations of the constant Inverted Barometer reference boundary pressure

published literature. Model bias shows a clear dependency on the boundary reference pressure. An increase in the reference pressure has the effect of increasing the predicted water levels by a near constant amount, resulting in increased bias. This result is consistent with what O'Neill et al. (2016) concluded using the Nucleus for European Modeling of the Ocean (NEMO) model, simulation storm surge signals of the UK.

The final reference boundary pressure selected after calibration was 1024 hPa, as this value produced the most accurate results for the majority of the coastal locations. One of the explanations for the location-dependent variable response to the reference boundary pressure is the actual spatial non-uniformity. A higher reference boundary pressure might increase the prediction accuracy around the south coast, but worsen the prediction around the east coast due to the non-uniform nature of the actual average pressure fields (refer to Figs. 2 and 5). Unfortunately, a space-varying reference boundary pressure is not readily employed in Delft 3D and is thus a clear recommendation for future improvement.

The locational grouping is clear in both Fig. 7a, b. Figure 7b especially highlights this behaviour. The east coast output locations produced results with low correlation and StDev values. This implies that the water level signal was not extreme and did not exhibit large variability. On the other hand, the southwest coast locations presented high accuracies with large StDev values. The exception was Mossel Bay, where exceptionally large variability was observed in both measured and modelled values. This is due to the water depth of the adjacent Agulhas Bank, as mentioned in Sect. 4.2 and further elucidated in Sect. 5.3. The calibrated SWaSS model is thus appropriate for prediction extreme water level events with high accuracy (correlation values above 0.9).

Figure 8 presents a time-series comparison of the final model settings for three coastal locations (one on each coast: southwest, south and east coast). The behaviour described statistically in Fig. 7 is confirmed by this visualization. The accurate response of the SWaSS model to extreme events along the southwest and south coast is clear. These do not just



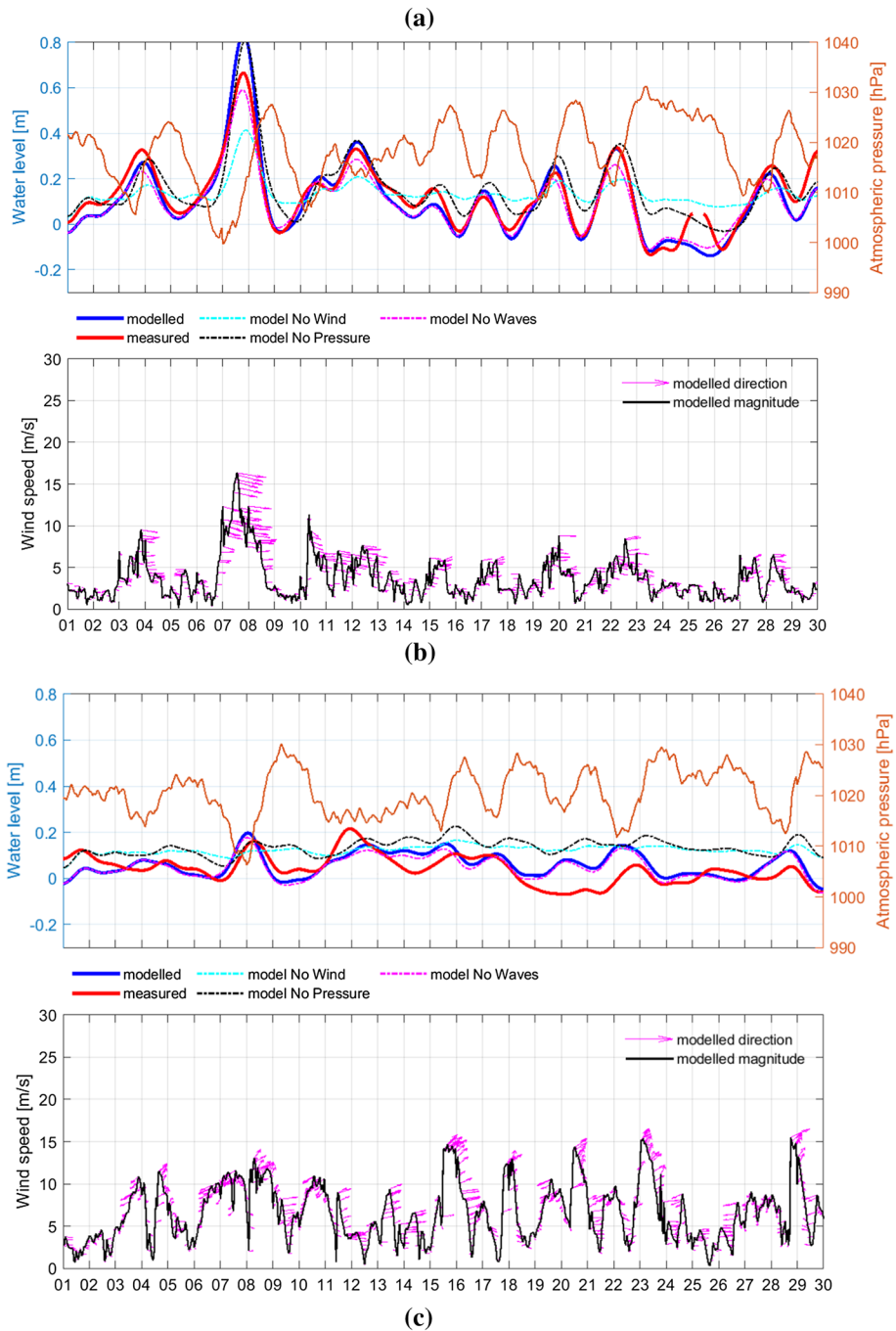


**Fig. 8** Final model calibration results for **a** Cape Town, **b** Mossel Bay and **c** Richards Bay. Each upper panel indicates the modelled and measured water levels on the left axis, after the tidal signals have been filtered out. On the right-hand axis, the prevailing atmospheric pressure close to the coastal city of interest is provided. Each lower panel indicates the associated near shore UM wind speeds together with their directions as magenta, True North arrows

include the extreme positive surge associated with Cape Storm (around 07/06/2017) but also the negative surge associated with the passing of Cape Storm (high pressure following the cold front) and another event from the 23 until 27 of June 2017. Accurate predictions of negative surge are arguably even more important than positive surge in the South African context. This is due to the limited under keel clearance available for large cargo ships in South African harbours. During low tide conditions, ships are routinely piloted into Cape Town, Durban and Richards Bay harbours with clearances in the order of 30 cm.

The timing of most of the significant events, presented in Fig. 8, was accurate to be within an hour. A broader physical discussion of these results will follow in Sect. 5.3. It is important to interpret Fig. 8 in the context of coastal orientation. For example, a west-south-west wind will tend to cause positive surge in Cape Town (southwest coast) but negative surge at Durban and Richards Bay (east coast).

## 4.2 Validation

Validation was performed with only the final model parameterization determined through calibration. The statistical summary of these results is provided in Fig. 9. July and August 2017 were characterized by fewer extreme storms. Figure 9a indicates high RMSE values for the east coast during July 2017, while Fig. 9b clearly indicates a small SD for the same sites during both July and August 2017. In Fig. 13, the time series plot during these two months at Richards Bay are provided. There are some events that SWaSS does not resolve properly, especially towards the end of August 2017. Like June, the general storm surge signal was not large on the east coast (associated with smaller SD values).

The mismatch between the SWaSS prediction and the measured data is nonetheless curious. After examining the time series comparison of the UM with AWS data at corresponding times, it was clear that the UM was performing well. Thus, the underestimation

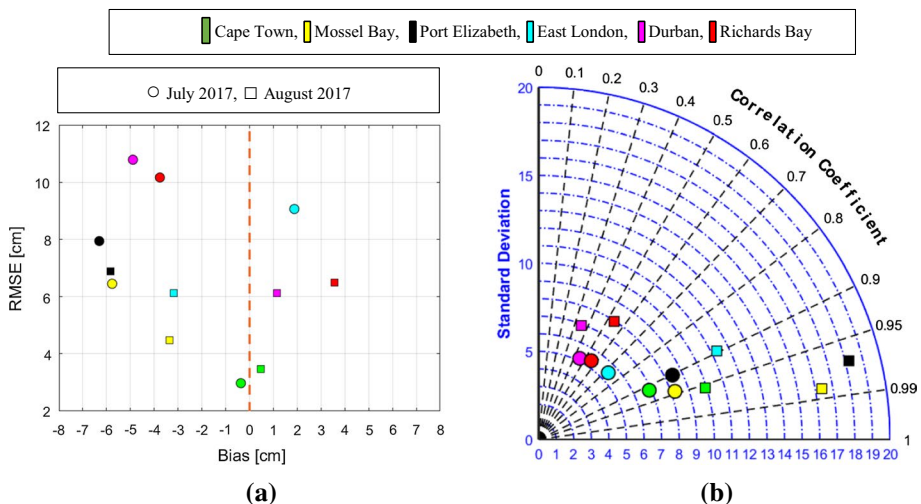


**Fig. 9** Model validation results via **a** Bias versus RMSE and **b** Standard Deviation versus Correlation Coefficient. These results represent the calibrated model setting in Table 3 for all the available coastal water level monitoring station of South Africa. The markers indicate the validation variations of the two winter months considered

of the storm surge signal on the east coast was not due to atmospheric model inaccuracies. The high atmospheric pressure and offshore wind (refer to Fig. 13) are also conducive to negative surge, not positive surge observed in the measured data. By checking media reports, it became evident that there was an extreme storm surge event during the latter part of August 2017. This was most prominently observed at East London. The reason for the mismatch is thus unclear. A possible explanation might again be found in the Agulhas Current. Barnes and Rautenbach (2019) recently undertook a study where the accuracy of wave predictions on the South African east coast was investigated. The main parameters were waves (height, period, directions) and the connection with the underpinning Agulhas Current system. They found that in extreme cases, neglecting the influence of the Agulhas Current could lead to a 20 to 60% underestimation of extreme waves. During this event, large waves, up to 8 m significant wave heights, were recorded at East London. The SWaSS SWAN model only predicted approximately 4.8 m significant wave height. This lack of wave set-up could be a contributing factor to the underestimation in the observed storm surge signal on the east coast observed in Figs. 9 and 13. Nhamtumbo (2019) also found that the Agulhas Current could be responsible for approximately 62% of the monthly water level fluctuations at East London. To which extent the Agulhas Current influences storm surge prediction on an event scale basis is still unclear.

The validation summary presented in Fig. 9 indicates that the model performance is adequate. Most coastal locations produced RMSE values under 10 cm. The general trend observed during calibration is reiterated: large eventful storm surge periods (large SD) produce better correlations. This was also the reasoning behind not normalizing Fig. 9b. Mossel Bay and Port Elizabeth again produced the largest storm surge signals due to their proximity to the Agulhas Bank and the shoaling associated with the decrease in water depth (refer to Eq. 3).

During the validation months, no significant storm surge signal was observed at Cape Town. Figure 10 gives the time series comparison at Cape Town for the months of July and August 2017. Due to the decrease in the wind velocity at Cape Town, the dominant physical drive became atmospheric pressure and will be more fully discussed in Sect. 5.3.

In Fig. 11, the time series comparisons of the validation results for Mossel Bay are provided. During August 2017, Mossel Bay did not produce the largest storm surge signal but rather Port Elizabeth (also situated across from the Agulhas Bank). Figure 14 gives the time series comparison for Port Elizabeth. Interestingly both July and August had significant negative surge events associated with high atmospheric pressures and relatively weak winds. This was observed in various degrees around the southwest coast. Referring to Fig. 11a, b, a typical progression of south coast atmospheric maybe be observed around the 16th. The cold front passes (low pressure) with the associated strongest winds immediately behind the front (southwest along the south coast as it passes). After the passing, the high-pressure ridges in wind speed decrease and the pressure increases which causes the water levels to drop.

### 4.3 Discussion

The physical drivers of storm surge around the South African coast were also investigated using the calibrated and validated numerical model. This was done via a set of experiments where the main drivers of storm surge were sequentially turned on and off. These experiments were executed for JJA and for all the coastal locations where water level data were available. The discussion will be structured by calibration/validation month.

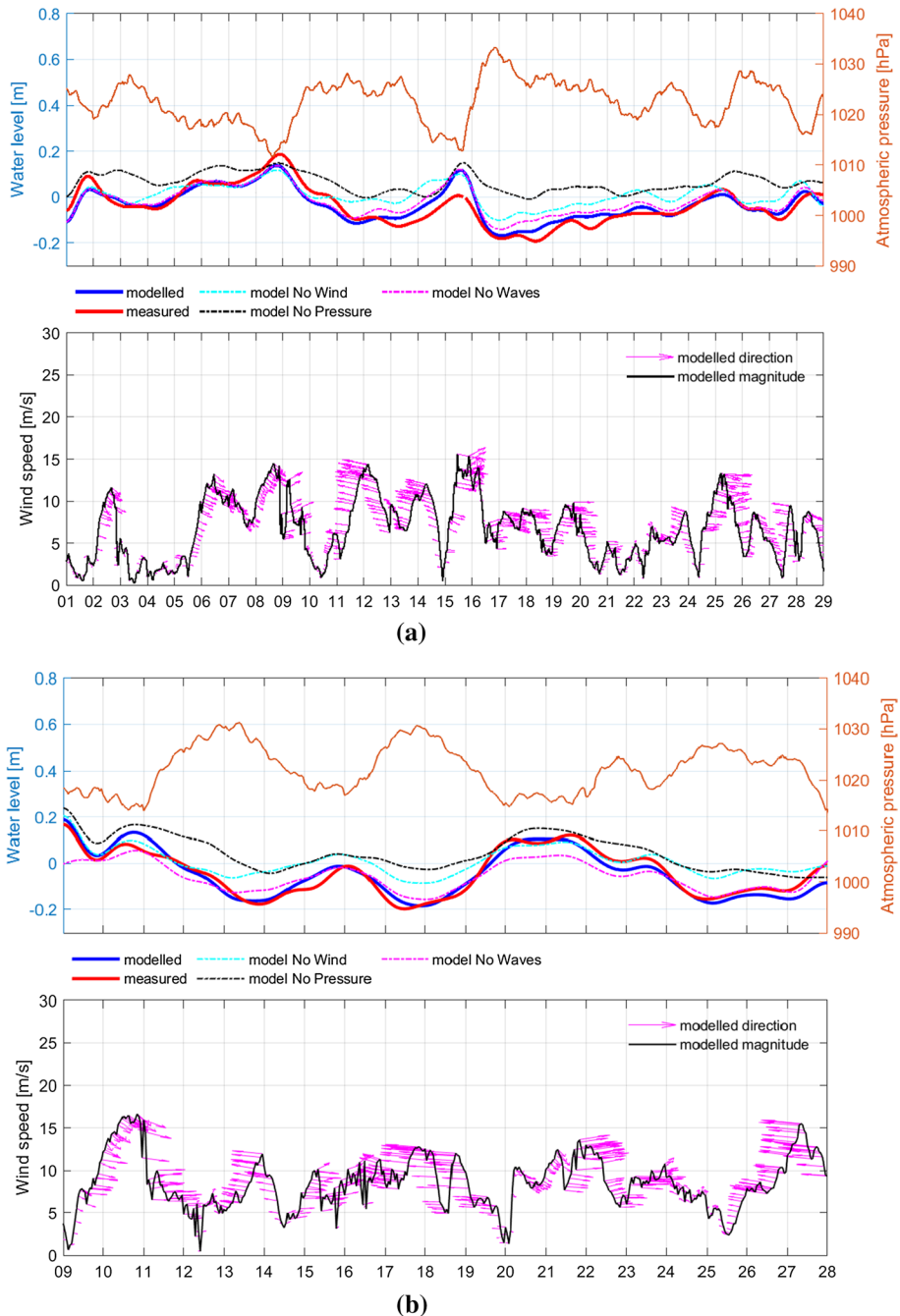


**Fig. 10** Final model validation results for Cape Town during **a** July 2017 and **b** August 2017. Each upper panel indicates the modelled and measured water levels on the left axis, after the tidal signals have been filtered out. On the right-hand axis, the prevailing atmospheric pressure close to Cape Town is provided. Each lower panel indicates the associated near shore UM wind speeds together with their directions as magenta, True North arrows

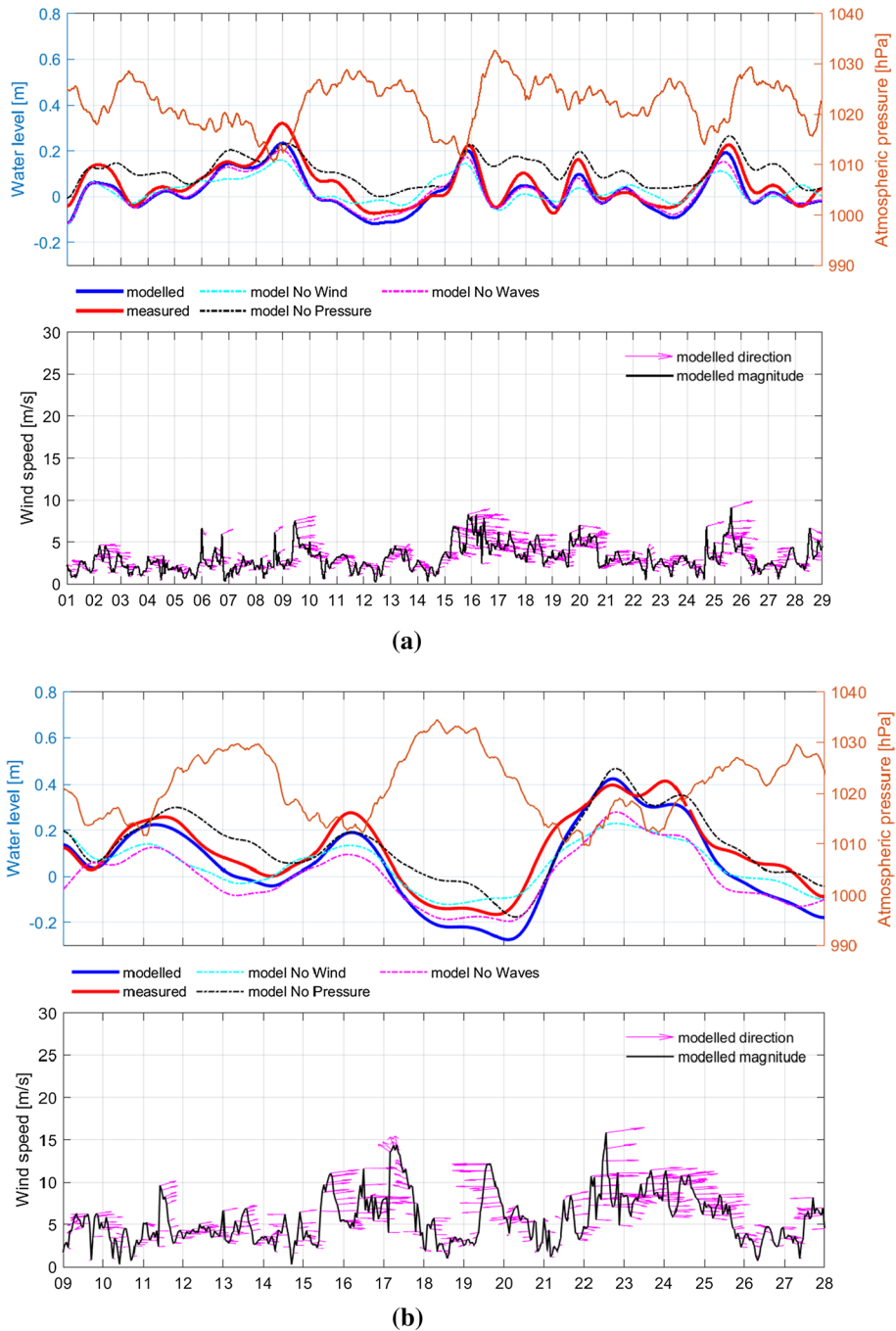


**Fig. 11** Final model validation results for Mossel Bay during **a** July 2017 and **b** August 2017. Each upper panel indicates the modelled and measured water levels on the left axis, after the tidal signals have been filtered out. On the right-hand axis, the prevailing atmospheric pressure close to Mossel Bay is provided. Each lower panel indicates the associated near shore UM wind speeds together with their directions as magenta, True North arrows



### 4.3.1 June 2017

In Fig. 8, the time series comparison between the final model configuration, measurements and the experiments are provided. The importance of the wind in the total storm surge signal at Cape Town is clear. When wind is neglected, only approximately 45% of the total simulated storm surge peak, during Cape Storm, is described. When either atmospheric pressure or the coupled waves are neglected, only approximately 80 to 82% of the storm surge peak is described. The simulated wind speed exceeded 25 m/s at Cape Town during the storm and contributed the most to the storm surge peak. This was associated with gale force winds from the northwest, directly onshore into Table Bay, ahead of the storm. The negative surge observed directly after the storm is associated with the sudden increase in atmospheric pressure as the cold front moved past. After the passing of the front, winds turned southwest (longshore). The negative surge observed around the 24th was much more atmospheric pressure driven. When the pressure was neglected, the full extent of the negative surge was not simulated. It is important to note what contribution wave set-up made during the storm peak. During the non-storm period, the residual water level signal remained almost unchanged without waves. Thus, if the aim of a numerical model is to predict extreme water level during storm conditions, and the area of interest can experience relatively large waves, a coupled model must be employed. During the Cape Storm peak, significant wave heights of 12 m were recorded just outside of Cape Town.

In Fig. 8b, the time series results at Mossel Bay are given. The storm surge peak is significantly higher than the peak observed at Cape Town. The same is true for the storm signal at Port Elizabeth (not shown here). Neglecting atmospheric pressure on the south coast had almost no influence on the storm peak. Neglecting coupled waves resulted in only approximately 72% of the storm peak being described and neglecting winds resulted in only 50% of the signal remaining. Wind speeds recorded on the south coast were significantly less than those at Cape Town. The sudden amplification in the general storm surge signal on the continental shelf is thus due to Eq. 3, as illustrated in Fig. 4. High water level on the south coast is thus a combined result of strong winds and long waves shoaling on the continental shelf. The semi-diurnal tidal resonance (Rautenbach et al. 2019) will thus worsen the total storm tide experience on the south coast. The strong adulation of the storm surge signal on the shelf is also clear.

The peak of Cape Storm can also be traced all the way from the signals at Cape Town to the signal at Richards Bay (Fig. 8c). The peaked reached Richards Bay on 8 June at 00:00 South African Standard Time (SAST). The storm peak was recorded around 06:00 SAST on the seventh at Cape Town and at 21:00 SAST the same day at Mossel Bay. Even though Cape Town and Mossel Bay are much closer to each other (approximately 400 km), the long wave travelled slower over the Agulhas Bank compared to the time it took the same signal to travel the approximate 1 200 km from Mossel Bay to Richards Bay (refer to Fig. 1). On the east coast, the low variability of the signal is clear, as is the much stronger atmospheric pressure dependence. At Richards Bay and Durban, the waves had almost no contribution in describing the residual water level signal. The east coast displays a directional wind and atmospheric pressure dominated storm surge signal during JJA, 2017. According to Smith et al. (2007) and Smith et al. (2010), the majority of recent coastal erosion events on the east coast was due to persistent wave events coinciding with the peak of the lunar cycle (Smith et al. 2010). These events were not necessarily extreme due to the wave heights but due to the persistence (Smith et al. 2013). Therefore, wave set-up was not necessarily the cause of coastal erosion. Persistent events on the east coast are sometimes

associated with semi-stationary cyclones south of Madagascar or even numerous cyclones traversing towards Madagascar and Mozambique in close succession (Mather and Stretch 2012). The erosion events of 2006, 2007 and 2011 occurred during JJA. Thus, even though the east coast has a sub-tropical climate with an austral summer rainfall season, austral winter is still the time of year sensitive to extreme coastal events (Smith et al. 2013). The narrow continental shelf is also partially responsible for the low storm surge signals.

In Fig. 12, the principle component analysis (PCA) of the drivers of the storm surge signal is provided for Cape Town, Mossel Bay and Richards Bay. These are based on a combined data set: model outputs from the Unified Model (UM) at both nearshore and offshore locations and measured residual water levels. There were no distinct differences in the PCs when utilizing only the offshore versus nearshore UM data.

In all the PCAs, the inverse relationship between atmospheric pressure and storm surge water level is confirmed. At Cape Town, PC1 describes 36.4% of the variability of these data and PC2, 21.7%. Thus, wind speed, direction and atmospheric pressure are again confirmed to be the main drivers to describe the adulations and variability of the data cloud. This is due to the length and angle between these components and the PC1 axis. This behaviour has also been noted by Suursaar et al. (2006) where the wind direction was highlighted as important. Significant wave height and peak period are mostly described by PC2.

A similar narrative holds true for Mossel Bay, except that the wind direction became less important as the shelf, frictional and shoaling effects became more important (refer to Sect. 5.1). Here, PC1 described 36% of the data variability and PC2, 22.2%. The South African southwest therefore displays a strong dependence on the wave climate. This strong dependence on waves (around 20%) of the storm surge peak is scarce. South African disaster response agencies should thus not only monitor the atmospheric pressure but should especially focus on the directional wind forecast and should not neglect the wave forecast. All of which is now operationally available through SWaSS.

On the east coasts, the drivers of storm surge are less directly connected to the produced storm surge signal. PC1 described 28.3% of the data variability and PC2, 22.5%. This lack in a clear relationship between the east coast storm surge signal and the atmospheric and wave drives suggest that some process is yet still unresolved in SWaSS. This postulation is confirmed by the fact that the UM model was proved to be sufficiently accurate via validation. As mentioned earlier, the Agulhas Current could be a main cause of inaccurate

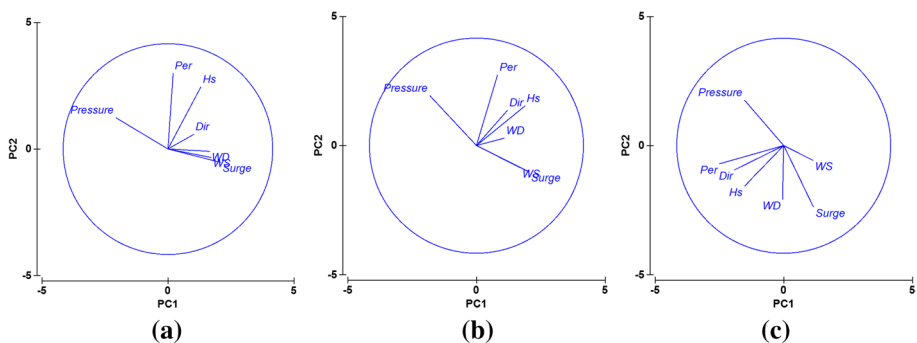


**Fig. 12** Principle component analysis (PCA) of the measured storm surge signal and its drives for **a** Cape Town, **b** Mossel Bay and **c** Richards Bay. Here Hs is the significant wave height, Dir is the wave mean direction, Per is the wave peak period, WS is the wind speed and WD is the wind direction. Surge is the storm surge signal and Pressure is the modelled atmospheric pressure at the site of interest

predictions (Nhantumbo 2019) together with event scale wave inaccuracies (due to wave-current interactions). The relatively small amplitudes of the east coast storm surge signal could also further contribute to the unpredictable behaviour, as illustrated in Figs. 7 and 9. In these figures, it is shown that with a stronger signal much better prediction correlations were achieved. Given that extreme events are the focus of storm surge forecasting (disaster management) this characteristic is favourable and acceptable. Further improvement to the deterministic model predictions presented here may be achieved by making use of ensemble member statistics and simulations (O'Neill et al. 2016; Suursaar et al. 2006). Post-processing techniques, e.g. by using machine-learned protocols, could also compensate for the physical processes not resolved in SWaSS. These topics fall outside the scope for the present study and are clearly recommended as future research.

#### 4.3.2 July and August 2017

The characteristics of these months are given in Figs. 10, 11, 13 and 14. The general storm surge signal around the entire South African coastline was weak during July 2017. Due to the weak winds, the atmospheric pressure became a larger driver of the residual water levels. Even these small amplitudes in the residual water levels were, however, still amplified over the Agulhas Bank. During July, the wave climate had negligible to no effect on the residual water levels.

August 2017 saw some storm surge events on the east coast of South Africa. Although both the August and the June events were as a result of passing low-pressure systems, their origins are completely different. Cape Storm in June 2017 resulted from a cut-off low-pressure system that extended towards the surface. The intense system resulted in the development of a deep low-pressure centre ( $<990$  hPa) just offshore of the south-west coast and a strong pressure gradient. The intensity of the low-pressure centre and its proximity to the coastline make this event a rare event for the southern African region. The system in the August 2017 case was a typical intense cold front associated with a mid-latitude cyclone that affects the South African coastline as shown conceptually in Fig. 2. The low-pressure centre in this case is far offshore in the Southern Ocean with the frontal band extending northwards towards the African continent. As the frontal band passes, pressure drops leading to negative surge events. This significant storm surge peak, towards the end of August, can be traced from Mossel Bay, past Port Elizabeth and East London and all the way to Durban and Richards Bay. After the cold front has passed, the south Atlantic high-pressure cell ridges in over the country resulting in a surface pressure increase. The results in the subsequent positive surge events experienced around the coast. Strong waves are generated by strong southerly to south-westerly winds resulting from the steep pressure gradient of the ridging high behind the cold front.

The 40 cm storm surge peak at East London (during a spring high tide) cause significant coastal infrastructure damage while the 40 cm peak at Mossel Bay and Port Elizabeth did not cause wide spread damage. A possible explanation for this is because the south coast is frequently exposed to high water level event while the surge, recorded at East London appeared to be anomalous. This event also coincided with 8 m significant wave heights, recorded close to the East London harbour, which is also an infrequent event.

## 5 Conclusion

A calibrated and validated storm surge model is presented in the present study. The model was built in the Delft 3D numerical code, in depth-averaged mode. The hydrodynamic model was coupled, online, with the Simulating WAVes in the Nearshore (SWAN), spectral wave model. The atmospheric forcing was obtained from a local, 4.4 km downscaling of the Unified Model (UM). The resulting operational storm surge model is called the South African Weather Service (SAWS), Wave and Storm Surge (SWaSS) model. The model is currently running in full operational mode and provides 72-h forecasts of winds, waves and extreme tidal surge levels. The operational protocol was fully described in the present study (refer to Sect. 4.1).

The various components of SWaSS were also validated against available measurements. The UM validation is presented in Sect. 4.3.4. These results represent the first coastal validation of the downscaled UM for South Africa. The model performance was sufficiently accurate to driving South African residual water levels. This includes both wind and atmospheric pressure parameters. In Sect. 4.3.5, the SWAN model performance was validated and found to be accurate in prediction the South African wave record. All model settings are provided in Sect. 4.4.

The storm surge component of SWaSS was calibrated focusing on two main parameters: boundary reference pressure and wind drag breakpoints. Bottom related friction was calibrated and dealt with in a recent publication that solely focused on the tidal component of the SWaSS model (Rautenbach et al. 2019). A space and time constant boundary reference pressure of 1024 hPa was used in the final model settings as this value produced the most accurate results for the most South African coastal locations. A space varying, time constant, boundary reference pressure is however suggested for future research as this might improve site specific correlations and biases. The wind drag breakpoints are described in Table 3. The two models investigated produced very similar storm surge results. The final model used was based on numerous and extensive experimental data.

The storm surge model compared well to measured water level data during JJA 2017. Comparisons were made at six coastal water level measurement location, covering the South African southwest, south and eastern coastlines. The west coast had no measured water level data during this time period. The accuracies and biases were well within published acceptable ranges. Each month presented different storm surge characteristics associated with the varying atmospheric systems during that time. In general, SWaSS performs best when predicting an extreme storm where the water level variations are relatively large. Where the storm surge signal was not distinct, a strong correlation between atmospheric drivers and the resulting storm surge was not pertinent.

The validated model was used to investigate the drivers of South African storm surge by sequentially neglecting each driver (wind, atmospheric pressure and waves). The wind-driven dominance of South African storm surge was confirmed. The atmospheric pressure was the second most important driver with wave set-up having a surprisingly significant influence on the final storm surge levels during storm conditions. This was especially true on the southwest and south coast. The long wave shoaling over the continental shelf of the

Agulhas Bank was also identified and explained why the south coast has the highest storm surge levels. The same behaviour (to a lesser extent) can be expected on the west coast, directly adjacent the Namaqua continental shelf (refer to Fig. 4).

Further research is suggested into the possibility of using ensemble member statistic to improve on the prediction accuracy of the single, deterministic model presented here. Machine learned post-processing of the predicted water level signals might also help in compensating for physical processes not resolved in the present SWaSS model.

**Acknowledgements** The authors would like to thank the South African Navy Hydrographic Office (SANHO) for providing recorded sea surface elevations and high-resolution coastal bathymetry required for model calibration and validation. We acknowledge Transnet National Port Authorities (TNPA) for the directional wave rider buoy data used in the present study. We would also like to acknowledge the use of NCEP Reanalysis data provided by the NOAA/OAR/ESRL PSD, Boulder, Colorado, USA, from their Web site at <https://www.esrl.noaa.gov/psd/>. Thank you for making these data freely available. Finally, this work is based on the research supported in part by the National Research Foundation of South Africa (Grant Numbers: 116359).

**Author contributions** Dr. Christo Rautenbach wrote the manuscript. He formulated the research questions and the resulting methodology. He designed and ran the calibration and validation simulations and co-developed most of the post-processing scripts, statistics and figures. Me. Tania Daniels processed the Unified Model outputs and executed their statistical validation. She also wrote and contributed towards the atmospheric descriptions. Mr. Marc de Vos pre-processes the raw water level data obtained from SANHO and wave data obtained from TNPA. Mr. Michael A. Barnes helped with the post-processing of the model results and figure production. He also helped in scheduling and running the considerable amount of calibration simulations. All the authors contributed towards the general discussions and reasoning pertaining to the main research results and conclusions presented here.

## Compliance with ethical standards

**Conflict of interest** The authors declare that they have no conflict of interest.

## Appendix

See Figs. 13 and 14.



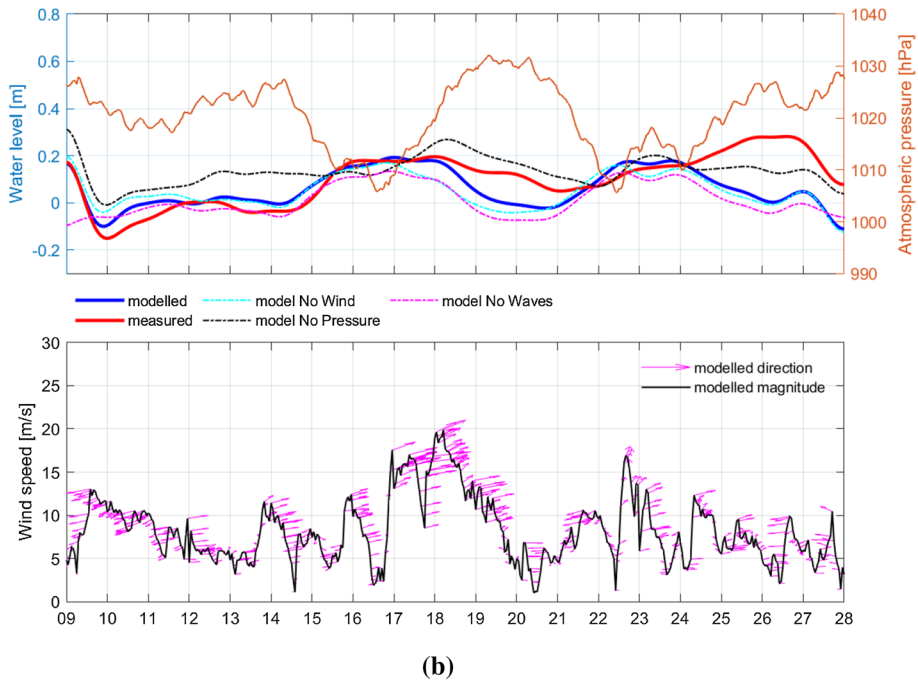
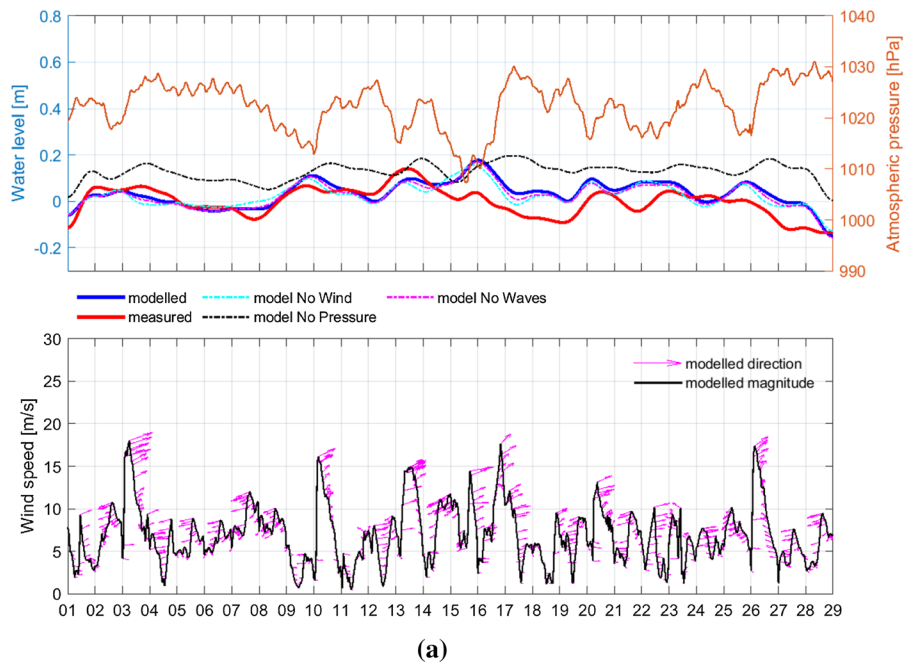


**Fig. 13** Final model validation results for Richards Bay during **a** July 2017 and **b** August 2017. Each upper panel indicates the modelled and measured water levels on the left axis, after the tidal signals have been filtered out. On the right-hand axis, the prevailing atmospheric pressure close to Richards Bay is provided. Each lower panel indicates the associated near shore UM wind speeds together with their directions as magenta, True North arrows

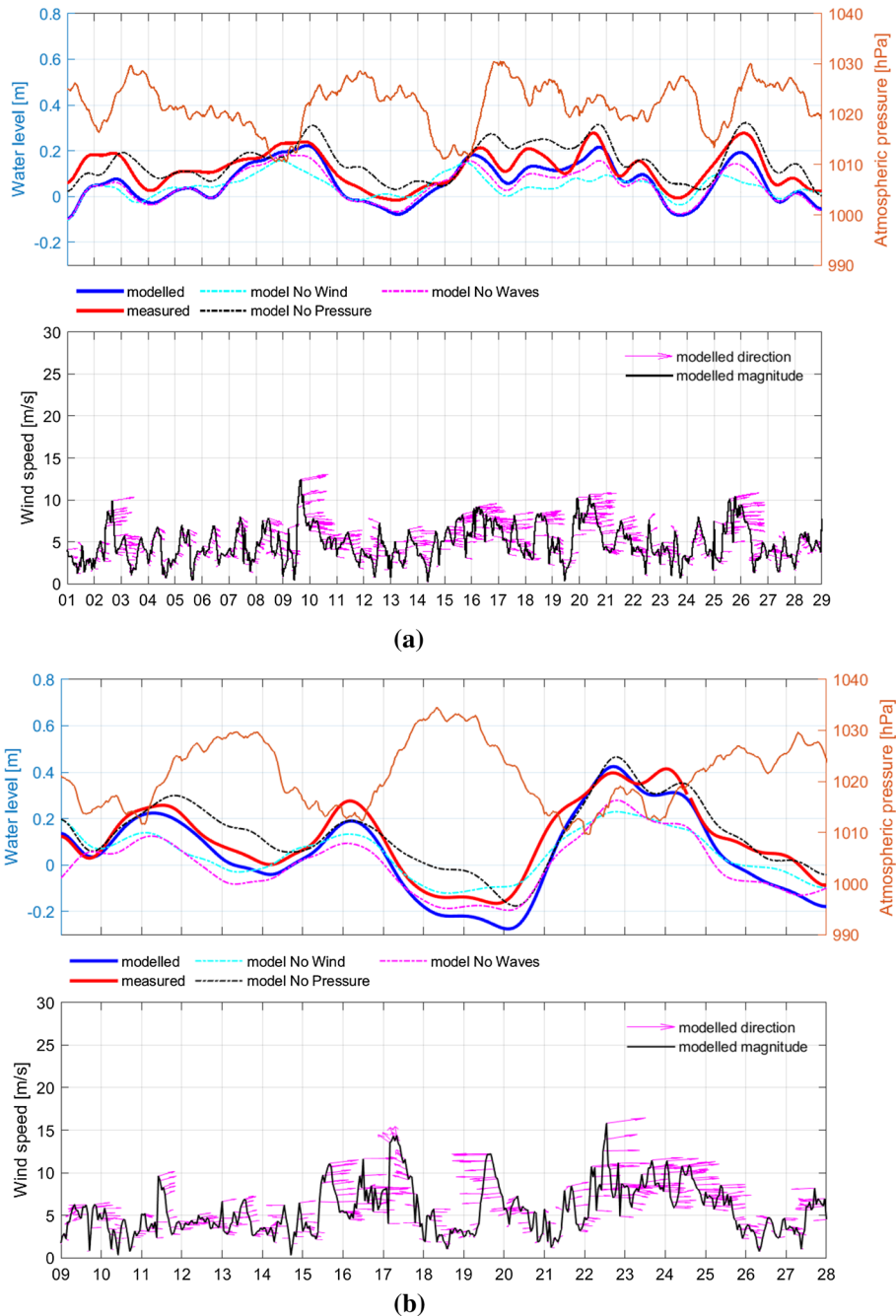


**Fig. 14** Final model validation results for Port Elizabeth during **a** July 2017 and **b** August 2017. Each upper panel indicates the modelled and measured water levels on the left axis, after the tidal signals have been filtered out. On the right-hand axis, the prevailing atmospheric pressure close to Port Elizabeth is provided. Each lower panel indicates the associated near shore UM wind speeds together with their directions as magenta, True North arrows

## References

- Athanasios P, van Dongeren A, Giardino A, Vousdoukas M, Gaytan-Aguilar S, Ranasinghe R (2019) Global distribution of nearshore slopes with implications for coastal retreat. *Earth Syst Sci Data Discuss.* <https://doi.org/10.5194/essd-2019-71>
- Barnes MA, Rautenbach C (2019) Towards quantified wave-current interactions in the Agulhas system: a modeling investigation. *Ocean Model* (under review)
- Battjes JA, Janssen JPFM (1978) Energy loss and set-up due to breaking of random waves. *Coastal engineering* 1978. American Society of Civil Engineers, New York, NY, pp 569–587. <https://doi.org/10.1061/9780872621909.034>
- Battjes JA, Zitman TJ, Holthuijsen LH (1987) Re-analysis of the spectra observed in Jonswap. In: *Proceedings of the coastal engineering conference*
- Bloemendaal N, Muis S, Haarsma RJ, Verlaan M, Irazoqui Apecechea M, de Moel H, Ward PJ, Aerts JCJH (2019) Global modeling of tropical cyclone storm surges using high-resolution forecasts. *Clim Dyn* 52(7–8):5031–5044. <https://doi.org/10.1007/s00382-018-4430-x>
- Bosboom J, Stive M (2015) Coastal dynamics I. Delft University of Technology, Delft
- Brown JM, Souza AJ, Wolf J (2010) Surge modelling in the eastern Irish Sea: present and future storm impact. *Ocean Dyn* 60(2):227–236. <https://doi.org/10.1007/s10236-009-0248-8>
- Brown A, Milton S, Cullen M, Golding B, Mitchell J, Shelly A (2012) Unified modeling and prediction of weather and climate: a 25-year journey. *Bull Am Meteorol Soc* 93(12):1865–1877. <https://doi.org/10.1175/BAMS-D-12-00018.1>
- Buskey EJ, Bundy M, Ferner MC, Porter DE, Reay WG, Smith E, Trueblood D (2015) System-wide monitoring program of the national estuarine research reserve system. In: *Coastal ocean observing systems*. Elsevier, pp 392–415. <https://doi.org/10.1016/B978-0-12-802022-7.00021-3>
- Cabral P, Augusto G, Akande A, Costa A, Amade N, Niquisse S, Atumane A, Cuna A, Kazemi K, Mlucasse R, Santha R (2017) Assessing Mozambique's exposure to coastal climate hazards and erosion. *Int J Disaster Risk Reduct* 23(April):45–52. <https://doi.org/10.1016/j.ijdrr.2017.04.002>
- Cavaleri L, Bertotti L (2006) The improvement of modelled wind and wave fields with increasing resolution. *Ocean Eng* 33(5–6):553–565. <https://doi.org/10.1016/j.oceaneng.2005.07.004>
- Cobb M, Blain CA (2002) A coupled hydrodynamic-wave model for simulating wave and tidally-driven 2D circulation in inlets. In: *Proceedings of the international conference on estuarine and coastal modeling*, (Code 7322), pp 725–744. [https://doi.org/10.1061/40628\(268\)47](https://doi.org/10.1061/40628(268)47)
- Courant R, Friedrichs K, Lewy H (1967) On the partial difference equations of mathematical physics. *IBM J Res Dev* 11(2):215–234. <https://doi.org/10.1147/rd.112.0215>
- Deltares. Validation Document Delft3D- FLOW Validation Document Delft3D-FLOW (2008).
- Deltares (2018) Delft3D-FLOW, User Manual. Delft3D Flexible Mesh Suite. <https://doi.org/10.1007/s00231-009-0509-6>
- Dorandeu J, Le Traon PY (1999) Effects of global mean atmospheric pressure variations on mean sea level changes from TOPEX / Poseidon. *J Atmos Ocean Technol* 16(9):1279–1283
- Egbert G, Erofeeva L (2010) The OSU TOPEX/Poseidon global inverse solution TPXO 8 atlas v.1 Africa. Retrieved from <https://volkov.oce.orst.edu/tides/global.html>
- Fernández-Montblanc T, Vousdoukas MI, Ciavola P, Voukouvalas E, Mentaschi L, Breyiannis G, Feyen L, Salamon P (2019) Towards robust pan-European storm surge forecasting. *Ocean Model* 133(October 2018):129–144. <https://doi.org/10.1016/j.ocemod.2018.12.001>
- Ferrarin C, Roland A, Bajo M, Umgieser G, Cucco A, Davolio S, Buzzi A, Malguzzi P, Drofa O (2013) Tide-surge-wave modelling and forecasting in the Mediterranean Sea with focus on the Italian coast. *Ocean Model* 61(January):38–48. <https://doi.org/10.1016/j.ocemod.2012.10.003>
- Findlay K (2018) Operation Phakisa and unlocking South Africa 's ocean economy. *J Indian Ocean Region* 14(May):248–254. <https://doi.org/10.1080/19480881.2018.1475857>
- Fitchett JM, Grab SW (2014) A 66-year tropical cyclone record for South-East Africa: temporal trends in a global context. *Int J Climatol* 34(13):3604–3615. <https://doi.org/10.1002/joc.3932>
- Gweba B (2018) Developing a methodology for the assessment of wave energy along the South African Coast. University of Stellenbosch
- Joubert AM (1997) Simulations by the atmospheric model intercomparison project of atmospheric circulation over Southern Africa. *Int J Climatol* 17(11):1129–1154
- Kalnay E, Kanamitsu M, Kistler R, Collins W, Deaven D, Gandin L, Iredell M, Saha S, White G, Woolen J, Zhu Y, Joseph D (1996) The NCEP/NCAR 40-Year reanalysis project. *Bull Am Meteor Soc* 77(3):437–471. [https://doi.org/10.1175/1520-0477\(1996\)077%3c0437:TNYRP%3e2.0.CO;2](https://doi.org/10.1175/1520-0477(1996)077%3c0437:TNYRP%3e2.0.CO;2)
- Kara AB, Metzger EJ, Bourassa MA (2007) Ocean current and wave effects on wind stress drag coefficient over the global ocean. *Geophys Res Lett.* <https://doi.org/10.1029/2006GL027849>

- Komen GJ, Hasselmann K, Hasselmann K (1984) On the existence of a fully developed wind-sea spectrum. *J Phys Oceanogr* 14(8):1271–1285. [https://doi.org/10.1175/1520-0485\(1984\)014<1271:OTEOAF>2.0.CO;2](https://doi.org/10.1175/1520-0485(1984)014<1271:OTEOAF>2.0.CO;2)
- Large WG, Pond S (1981) Open ocean momentum flux measurements in moderate to strong winds. *J Phys Oceanogr* 11(3):324–336. [https://doi.org/10.1175/1520-0485\(1981\)011%3c0324:OOMFM1%3e2.0.CO;2](https://doi.org/10.1175/1520-0485(1981)011%3c0324:OOMFM1%3e2.0.CO;2)
- Lutjeharms JRE, Monteiro PMS, Tyson PD, Obura D (2001) The oceans around southern Africa and regional effects of global change. *S Afr J Sci* 97(3–4):119–130
- Madsen OS, Poon Y, Graber HC (1989) Spectral wave attenuation by bottom friction: theory. Coastal engineering 1988. American Society of Civil Engineers., New York, NY, pp 492–504. <https://doi.org/10.1061/9780872626874.035>
- Mather AA, Stretch DD (2012) A Perspective on sea level rise and coastal storm surge from southern and eastern Africa: a case study near Durban, south Africa. *Water (Switzerland)* 4(1):237–259. <https://doi.org/10.3390/w4010237>
- Mathers EL, Woodworth PL (2004) A study of departures from the inverse-barometer response of sea level to air-pressure forcing at a period of 5 days. *Q J R Meteorol Soc* 130(597):725–738. <https://doi.org/10.1256/qj.03.46>
- Muis S, Verlaan M, Winsemius HC, Aerts JCJH, Ward PJ (2016) A global reanalysis of storm surges and extreme sea levels. *Nat Commun* 7(1):11969. <https://doi.org/10.1038/ncomms11969>
- Muthige MS, Malherbe J, Englebrecht FA, Grab S, Beraki A, Maisha TR, Van Der Merwe J (2018) Projected changes in tropical cyclones over the South West Indian Ocean under different extents of global warming. *Environ Res Lett*. <https://doi.org/10.1088/1748-9326/aabc60>
- Nhantumbo BJ (2019) Drivers of coastal sea level variability along the east and south of South Africa. University of Cape Town. Retrieved from <https://open.uct.ac.za/handle/11427/30348>
- O'Neill C, Saulter A, Williams J, Horsburgh K (2016) NEMO-surge: Application of atmospheric forcing and surge evaluation. Technical report 619, (December), 57. Retrieved from [https://www.metoffice.gov.uk/binaries/content/assets/mohippo/pdf/library/frtr\\_619\\_2016p.pdf](https://www.metoffice.gov.uk/binaries/content/assets/mohippo/pdf/library/frtr_619_2016p.pdf)
- Peng M, Xie L, Pietrafesa LJ (2006) Tropical cyclone induced asymmetry of sea level surge and fall and its presentation in a storm surge model with parametric wind fields. *Ocean Model* 14(1–2):81–101. <https://doi.org/10.1016/j.ocemod.2006.03.004>
- Ponte RM (2006) Low-frequency sea level variability and the inverted barometer effect. *J Atmos Ocean Technol* 23(4):619–629. <https://doi.org/10.1175/JTECH1864.1>
- Powell MD, Vickery PJ, Reinhold TA (2003) Reduced drag coefficient for high wind speeds in tropical cyclones. *Nature* 422(6929):279–283. <https://doi.org/10.1038/nature01481>
- Rautenbach C, Barnes MA, de Vos M (2019) Tidal characteristics of South Africa. *Deep Sea Res Part I* 150(Febuary):103079. <https://doi.org/10.1016/j.dsr.2019.103079>
- Reason C, Landman W, Tennant W (2006) Seasonal to Decadal Prediction of Southern African Climate and Its Links with Variability of the Atlantic Ocean. *Bull Am Meteor Soc* 87(7):941–956. <https://doi.org/10.1175/BAMS-87-7-941>
- Rossouw JAN (1989) Design waves for the south african coastline. University of Stellenbosch
- SA Navy (2018) 2018 South African tide tables. South African Hydrographic Office.
- Schumann EH (1983) Long-period coastal trapped waves off the southeast coast of Southern Africa. *Cont Shelf Res* 2(2–3):97–107. [https://doi.org/10.1016/0278-4343\(83\)90010-9](https://doi.org/10.1016/0278-4343(83)90010-9)
- Schumann EH, Perrins L-A (1982) Tidal and inertial currents around South Africa. In: Proceedings of 18th conference on coastal engineering, Cape Town, South Africa, (November 1982), pp 2562–2580. <https://doi.org/10.1061/9780872623736.156>
- Seager R, Murtugudde R, Naik N, Clement A, Gordon N, Miller J (2003) Air-sea interaction and the seasonal cycle of the subtropical anticyclones. *J Clim* 16(12):1948–1966. [https://doi.org/10.1175/1520-0442\(2003\)016%3c1948:AIATSC%3e2.0.CO;2](https://doi.org/10.1175/1520-0442(2003)016%3c1948:AIATSC%3e2.0.CO;2)
- Searson S, Brundrit GB (1995) Extreme high sea levels around the coast of southern Africa. *S Afr J Sci* 91(11–12):579–588
- Sembiring L, Van Ormondt M, Van Dongeren A, Roelvink D (2015) A validation of an operational wave and surge prediction system for the Dutch coast. *Nat Hazards Earth Syst Sci* 15(6):1231–1242. <https://doi.org/10.5194/nhess-15-1231-2015>
- Signell R (2014) SEA-MAT: Matlab tools for oceanographic analysis. Creative Commons Attribution-NonCommercial-ShareAlike 3.0 Unported License. Retrieved from <https://sea-mat.github.io/sea-mat/>
- Smith AM, Guastella LA, Bundy SC, Mather AA (2007) Combined marine storm and Saros spring high tide erosion events along the KwaZulu-Natal coast in March 2007. *S Afr J Sci* 103(7–8):274–276

- Smith AM, Mather AA, Bundy SC, Cooper JAG, Guastella LA, Ramsay PJ, Theron A (2010) Contrasting styles of swell-driven coastal erosion: examples from KwaZulu-Natal, South Africa. *Geol Mag* 147(6):940–953. <https://doi.org/10.1017/S0016756810000361>
- Smith A, Guastella LA, Mather AA, Bundy SC, Haigh ID (2013) KwaZulu-Natal coastal erosion events of 2006/2007 and 2011: a predictive tool? *S Afr J Sci* 109(3/4):1–4. <https://doi.org/10.1590/sajs.2013/20120025>
- Soloviev AV, Lukas R, Donelan MA, Haus BK, Ginis I (2015) The air-sea interface and surface stress under tropical cyclones. *Sci Rep* 4(1):5306. <https://doi.org/10.1038/srep05306>
- Suursaar Ü, Kullas T, Otsmann M, Saaremäe I, Kuik J, Merilain M (2006) Cyclone Gudrun in January 2005 and modelling its hydrodynamic consequences in the Estonian coastal waters. *Boreal Environ Res* 11(2):143–159
- Theron A, Rossouw M, Rautenbach C, Ange U von Saint Maherry A, August M (2013) Determination of inshore wave climate along the south african coast- phase 1 for coastal hazard and vulnerability assessment.
- Tyson PD, Garstang M, Swap R, Kållberg P, Edwards M (1996) An air transport climatology for subtropical Southern Africa. *Int J Climatol* 16(3):265–291. [https://doi.org/10.1002/\(SICI\)1097-0088\(199603\)16:3%3c265:AID-JOC8%3e3.0.CO;2-M](https://doi.org/10.1002/(SICI)1097-0088(199603)16:3%3c265:AID-JOC8%3e3.0.CO;2-M)
- van Ballegooyen RC (1995) Forced synoptic coastal-trapped waves along the southern African Coastline. University of Cape Town
- Vatvani DK, Gerritsen H, Stelling GS, Rao AVRK (2002) Cyclone induced storm surge and flood forecasting system for India. In: *Solutions to coastal disasters '02*. Reston, VA: American Society of Civil Engineers, pp 473–487. [https://doi.org/10.1061/40605\(258\)42](https://doi.org/10.1061/40605(258)42)
- Veeramony J, Condon A, van Ormondt M (2017) Forecasting storm surge and inundation: model validation. *Weather Forecast* 32(6):2045–2063. <https://doi.org/10.1175/WAF-D-17-0015.1>
- Verboom GK, de Ronde JG, van Dijk RP (1992) A fine grid tidal flow and storm surge model of the North Sea. *Cont Shelf Res* 12(2–3):213–233. [https://doi.org/10.1016/0278-4343\(92\)90030-N](https://doi.org/10.1016/0278-4343(92)90030-N)
- Vreugdenhil CB (1994) Numerical methods for shallow-water flow, vol 13. Springer, Dordrecht. <https://doi.org/10.1007/978-94-015-8354-1>
- Williams T, Rautenbach C (2019) On the importance of wind generated waves in embayments with complex orographic features: a South African case study. *Marine Syst* (under review)
- Willmott CJ (1981) On the validation of models. *Phys Geogr* 2(2):184–194. <https://doi.org/10.1080/02723646.1981.10642213>
- Willmott CJ, Robeson SM, Matsuura K (2012) A refined index of model performance. *Int J Climatol* 32(13):2088–2094. <https://doi.org/10.1002/joc.2419>
- Young IR (1999) Seasonal variability of the global ocean wind and wave climate. *Int J Climatol* 19(9):931–950. [https://doi.org/10.1002/\(SICI\)1097-0088\(199907\)19:9%3c931:AID-JOC412%3e3.0.CO;2-O](https://doi.org/10.1002/(SICI)1097-0088(199907)19:9%3c931:AID-JOC412%3e3.0.CO;2-O)

**Publisher's Note** Springer Nature remains neutral with regard to jurisdictional claims in published maps and institutional affiliations.



## Chapter 5

### *Southern African wave model sensitivities and accuracies*

---



Figure 5-1: A linoleum print inspired by the physical wave dynamics described in the present study. To everything in nature, and life, these must be balance: push and pull, cause and effect, fasting and the feast. This is also known as spiritual symmetry and presented here as the tides and waves.

## 5.1 Abstract

Numerous studies identified the complexities of the wave climatology around the South African coast, but limited studies investigated these complex dynamics in the open literature. Several freely available parameterized wave boundary conditions are produced around southern Africa. However, none of these are fully spectral outputs from global or larger regional spectral wave models. This constraint results in local engineering and scientific organizations, reconstructing their own spectral boundary conditions. For coastal models, this is a reasonable assumption. Given that, the single parameterization is accurate and a reasonable representation of a non-multimodal seas state. The South African Weather Service (SAWS) Marine unit has recently launched their coupled, operational wave and storm surge forecasting model. The aim of the SAWS Wave and Storm Surge (SWaSS) platform was to provide accurate, high-resolution coastal forecasts for the entire South African coastline. The present investigation thus presents the validation of the spectral wave component of the coupled system, developed in Delft3D. Various wave boundary reconstructions are investigated together with the two most used and well-known whitecapping formulations. Validation is performed with both *in situ* wave-rider buoy data (at nine locations around the coastline) and regional remotely sensed, along track, altimetry data. Full model performance statistics are provided, and the accuracy of the model is discussed.

## 5.2 Publication details



Rautenbach, C., Barnes, M. A., Wang, D. W., and Dykes, J. (2020). Southern African Wave Model Sensitivities and Accuracies. *Journal of Marine Science and Engineering*, Special issue: *Wave Climates*. <https://doi.org/10.3390/jmse8100773>.

## 5.3 Author contributions (as appeared in paper)

Conceptualization, C. Rautenbach; methodology, C. Rautenbach.; software, C. Rautenbach, M. A Barnes, D. Wang and J. Dykes.; validation, C. Rautenbach, M. A. Barnes, D. Wang and J. Dykes; formal analysis, C. Rautenbach, M. A Barnes, D. Wang and J. Dykes; investigation, C. Rautenbach; resources, C. Rautenbach, M. A Barnes, D. Wang and J. Dykes; data curation, C. Rautenbach, M. A Barnes and J. Dykes; writing—original draft preparation, C. Rautenbach.; writing—review and editing, J. Dykes and M. A. Barnes; visualization, C. Rautenbach, M. A Barnes and J. Dykes; supervision, C. Rautenbach; project administration, C. Rautenbach; funding acquisition, C. Rautenbach. All authors have read and agreed to the published version of the manuscript.

## Article

# Southern African Wave Model Sensitivities and Accuracies

Christo Rautenbach <sup>1,2,3,4,\*</sup> , Michael A. Barnes <sup>5</sup> , David W. Wang <sup>6</sup> and James Dykes <sup>6</sup> <sup>1</sup> Research and development, MetOcean (a division of the Meteorological Service), Raglan 3225, New Zealand<sup>2</sup> Environmental Research Institute, University of Waikato, Hamilton 3240, New Zealand<sup>3</sup> Institute for Coastal and Marine Research, Nelson Mandela University, Port Elizabeth 6031, South Africa<sup>4</sup> Department of Oceanography and Marine Research Institute, University of Cape Town, Rondebosch 7701, South Africa<sup>5</sup> Marine Research Unit, South African Weather Service, Cape Town 7525, South Africa; michael.barnes@weathersa.co.za<sup>6</sup> Oceanography Division, Naval Research Laboratory, Stennis Space Center, MS 39529, USA; David.Wang@nrlssc.navy.mil (D.W.W.); jimddykes@gmail.com (J.D.)

\* Correspondence: rautenbachchristo@gmail.com

Received: 30 August 2020; Accepted: 26 September 2020; Published: 1 October 2020



**Abstract:** Numerous studies have identified the complexities of the wave climatology around the South African coast, but limited studies have investigated these complex dynamics in the available literature. Several freely available parameterized wave boundary conditions are produced around southern Africa. However, none of these are fully spectral outputs from global or larger regional spectral wave models. This constraint results in local engineering and scientific organizations, reconstructing their own spectral boundary conditions. For coastal models, this is a reasonable assumption, assuming that the single parameterization is accurate and a representation of a non-multimodal sea state. The South African Weather Service (SAWS) Marine unit recently launched their coupled, operational wave and storm surge forecasting model. The aim of the SAWS Wave and Storm Surge (SWaSS) platform was to provide accurate, high-resolution coastal forecasts for the entire South African coastline. The present investigation thus presents the validation of the spectral wave component of the coupled system, developed in Delft3D. Various wave boundary reconstructions are investigated together with the two most used and well-known whitecapping formulations. Validation is performed with both in situ wave-rider buoy data (at nine locations along the coastline) and regional remotely sensed, along track, altimetry data. Full model performance statistics are provided, and the accuracy of the model is discussed.

**Keywords:** waves; spectral wave modelling; extreme events; operational forecasting; numerical modelling; WAVEWATCH III; SWAN; South Africa; boundary conditions; whitecapping

## 1. Introduction

Southern Africa has been known for its extreme wave climate for centuries. In the 1600s, the Cape Peninsula was dubbed the “Cape of Good Hope”, but also the “Cape of Storms”, due to the large number of merchant ships that sank in extreme storm conditions [1]. Since then, South Africa has developed into a cosmopolitan African nation with over nine major ports. The coastline stretches over 3000 km from the Namibian boarder on the west to the Mozambique boarder on the east. The climatology of South Africa also varies significantly around the coastline [2]. The wave climate follows suit, with different atmospheric drivers dictating the timing and intensity of wave events around the coastline [3–5].

The characteristics of the atmospheric and oceanographic systems affecting the wave climate in a particular area is important for accurate wave model setups. Both the spectral wave model settings and physics and the assumptions made with regard to forcing and boundary conditions are important for accurate wave predictions [6]. According to [7], the southern Indian Ocean (in the so-called Roaring Forties wind belt) requires approximately 30 h to produce a swell signal, which then propagates through the entire Indian Ocean. The same is true for the swell signals generated in the Roaring Forties in the Atlantic Ocean [8]. It takes approximately 84 h for the swell waves to travel to the tropical water of the southern Indian Ocean while the swell waves will reach South Africa much sooner [9]. Ref. [10] presented austral summer and winter averages of both swell and wind wave significant wave heights. Here, the non-homogeneous pattern of global wave fields is clear, especially on the edges of the Roaring Forties. The dominance of wind waves (the so-called “wind wave zones”) in the Southern Ocean is also evident, in this classification called “swell pools” [7,11]. The majority of the oceans surrounding southern Africa is a mixture between swell- and wind-dominant waves, according the same classification [11,12], also presenting patterns of wave generation zones, with southern Africa being distinctly in its own zone. Global distributions of wind sea and swell probabilities, indices and significant wave heights (based on collocated TOPEX/NSCAT and TOPEX/QSCAT datasets) also confirm the heterogeneous behaviour of the southern African wave fields [11]. Simulating, understanding and capturing this heterogeneous behaviour for the global wave fields is also important for future projections of expected wave climate changes [12–14]. According to a recent study, approximately 50% of the world’s coastlines are at risk due to projected global wave climate change [13,15]. On the west and south coast of South Africa, the projected mean wave directional changes are between 1 and 3 degrees (counter-clockwise) by 2100 [13].

The accurate coastal prediction of waves is important for coastal planning, management and governance [16,17]. Even small changes in wave direction or total experienced energy could have drastic effects on coastal sediment transport rates (e.g., [18]) and ecosystem stability (e.g., [19]). Waves also play a crucial role in coastal storm surge forecasting, especially in areas frequented by large wave events, like southern Africa [4,5,20].

The South African Weather Service (SAWS) recently developed an operational Wave and Storm Surge (SWaSS) [21] forecasting platform [4]. The model was developed as an online, coupled system between the Simulating Waves in the Nearshore (SWAN) model and a depth-averaged Delft3D hydrodynamic (FLOW) model. As part of the total SWaSS model calibration, the sensitivity of the wave model component is assessed and presented here. Limited research has been done on the regional wave climate behaviour around South Africa. Recently, the importance of wave–current interactions over the Agulhas retroflexion area [22] and the core of the Agulhas Current (close to the South African east coast) [23] have been noted.

The sensitivities of regional- and local-scale (down to approximately 300 to 500 m resolution) spectral wave models have not yet been investigated for southern Africa. Similar studies have, however, been performed in other regions, such as in the Mediterranean Sea (e.g., [24]), the Indian east coast (e.g., [6]), and the Arabian Sea (e.g., [6]). Global models lack the resolution required for bay-scale accuracy due to local bathymetric features, local friction, and local orography related to wind-wave growth and whitecapping energy dissipation. Therefore, global models are predominantly unable to accurately reproduce local wave measurements [6,25]. Local wave forecasting is also not the main aim of global wave models. The aforementioned models do, however, provide boundary conditions to regional models and are archived in numerous, storage space-efficient, ways. These storage techniques can vary in reliability in terms of representing the correct wave energy distribution at a particular point (e.g., the amount of energy associated with wind or swell seas). The parameter and/or partition reconstruction method used in a regional or local model could then lead to wave energy (significant wave height and period), directional and/or event arrival time mismatches at a particular coastline.

In the present study, the prediction sensitivity of a regional SWAN spectral wave model for southern Africa is thus investigated. Three spectral boundary condition reconstructions are implemented



to investigate their ability to reproduce observed coastal wave records and regional wave fields. The creation of the wave parameters and partitions are discussed, and the assumptions related to the reconstruction of representative spectral boundary conditions are elucidated. These boundary conditions are spatially and temporally varying and are compared through the results of a regional SWAN model forced with fully spectral boundary conditions, as produced by a global WAVEWATCH III® model (WW3). Variations in wind forcing are not tested here (as discussed by [24] for the Mediterranean Sea) and are assumed to be accurate based on a recent study by [4]. The prediction accuracy effects of two well-established whitcapping formulations are, however, investigated and discussed, similar to the recent investigation by [26].

## 2. Data

### 2.1. Bathymetry Data

The bathymetry used in the present study was primarily based on the General Bathymetric Chart of the Oceans (GEBCO) and supplemented with high-resolution bathymetry in the vicinity of South African ports and in situ measurement locations. These data were provided by the South African Navy Hydrographic Office (SANHO). In Figure 1, the southern African model bathymetry is given. From the west to the east, the major coastal locations are Saldanha Bay (SB), Cape Town (CT), Mossel Bay (MB), Port Elizabeth (PE), East London (EL), Durban (DU) and Richard's Bay (RB).

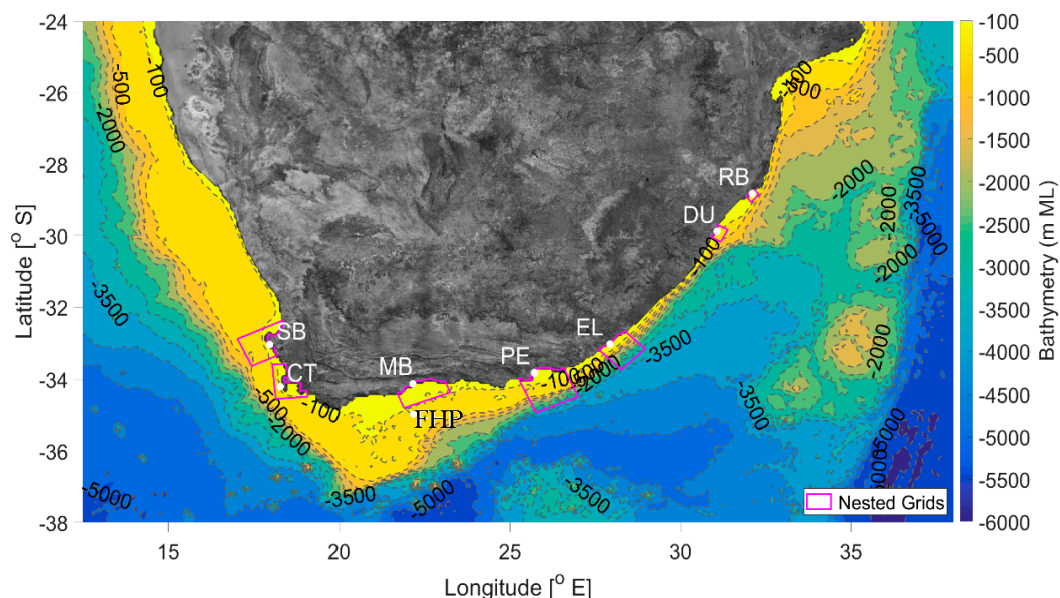


**Figure 1.** South African bathymetry and regional model extent. Magenta enclosures indicate SWAN nested domains. Major coastal city locations are given via acronyms.

### 2.2. Wave Data

Wave buoy data were provided by Transnet National Port Authorities (TNPA) for all nine coastal in situ measurement locations. These data are archived and maintained by the Council for Scientific and Industrial Research (CSIR) in Stellenbosch, South Africa. The wave rider buoy mooring depths varied between 21 m and 95 m, chart datum (CD) (here, CD values are determined by the South African hydrographic office and is usually defined as the vertical datum corresponding to the lowest low astronomical tide or land levelling datum). The FH Platform buoy (refer to Figure 1) is the in situ observation location furthest offshore and is situated adjacent to the south coast, close to the edge of the Agulhas Bank (southern South Africa's continental shelf [27]). A summary of the in situ wave rider buoy data used in the present study is presented in Table 1.

**Table 1.** Datawell wave rider buoy mooring depths (CD) and geographical coordinate location. Data quality control was performed at the Council for Scientific and Industrial Research (CSIR) in Stellenbosch, South Africa. The Datawell wave rider buoy used at each location is described as non-directional (ND) or multi-directional (MD), together with the model description. FHP was the only location where a WaMoS II wave radar system was used to gather data.

Description	SB	SK * (CT)	MB	PE	EL	FHP	DB	RB
Water depth [m]	23	70	24	21	27	95	30	22
Latitude [°]	−33.05	−34.204	−34.12467	−33.83333	−33.038	−34.97	−29.884	−28.8265
Longitude [°]	17.978	18.28667	22.1535	25.71666	27.93083	22.17	31.07067	32.104
Directional	ND	MD	ND	MD	MD	MD	MD	MD
Model	SG	MK2	SG	MK3	MK3	WMS II	MK4	MK 4

\* Slangkop (SK) is the local name for the mooring location just outside of Cape Town, offshore of Hout Bay.

### 2.3. Altimetry Data

Global measurements of significant wave heights are provided along tracks of satellite radar altimeters. In the present study, data from the JASON-3 [28] and AltiKa [29] missions were used for the regional SWAN model performance evaluation. These types of satellites are usually placed in near-polar, sun-synchronous orbits. Their nadir-looking instruments, which measure along a narrow beam directly below the satellite, measure scattered energy, which is the basis for the derived wave height and wind speed. The along-track resolution of the altimeter data is approximately 7 km, and their separation, depending on orbit geometry, can be up to 400 km at the equator. Satellites repeat the same ground tracks on a 3- to 10-day repeat cycle. This provides a reasonable coverage of the ocean surface in large scales but is not suitable for smaller domains in the littoral.

The altimeter data used in the WW3 model data assimilation and model performance evaluations were processed through an application from the Navy Coupled Ocean Data Assimilation (NCODA) [30] software. The global WW3 model (used as the source of the fully spectral boundary conditions in the present study) validation results is known as Ocean Quality Control (OCNQC) and these results are made available on the Global Ocean Data Assimilation Experiment (USGODAE) server (<https://usgodae.org>) [31].

### 2.4. Wind Data

The South African Weather Service (SAWS) operational Unified Model (UM) output was used as atmospheric forcing for all the SAWS wave and surge models. The model resolution was approximately 4.4 km [32]. Model wind parameters and atmospheric pressure were assumed to be accurate for the purposes of the present study based on coastal validations presented by [4]. Atmospheric forcing for the Navy global WW3 model, from which boundary conditions were obtained, consisting of 10 m winds from the U.S. Navy Global Environmental Model (NAVGEM), run at Fleet Numerical Oceanography and Meteorology Centre (FNMOC).

## 3. Numerical Models

Two spectral numerical wave models are implemented in the present study. WW3 is used to simulate global scale wave dynamics and produced boundary conditions for a regional and local scale SWAN domain. The SWAN domains were thus off-line nested in the Wave Watch III global computational grid.

### 3.1. WAVEWATCH III® (WW3)

This is a third-generation phase-averaged wave model that solves the spectral action-density balance equation for wave number-direction spectra [33–35]. Developed by [36], the multi-grid approach of WW3 allows the computation of multiple grids using a single model run. With two-way communication between grids, wave spectra cross all domain boundaries in both directions at frequency



intervals. The resulting advantages include (1) increased accuracy in the vicinity of the boundaries assuming the wind conditions are also consistent, (2) decreased human error in model domain setup, where the interpolation and other logistics are internally handled, and (3) a streamlined model setup, eliminating the additional steps of managing additional nested runs.

The U.S. Navy currently runs global WW3 systems at the Fleet Numerical Meteorology and Oceanography Center (FNMOC) at both Stennis Space Center, Mississippi, and Monterey California. Since the global grids used in these systems typically operated with regular latitude/longitude spacing, it attempts to cover the Arctic region with small time steps at the risk of violating the Courant-Friedrichs-Lewy (CFL) condition. Consequentially, an upgrade to a three-grid system to cover the globe has been validated and has nearly been transitioned to operation. This new system was implemented for the experiments described in the current study.

The United States Naval Research Laboratory (NRL) developed a set of new configurations consisting of an irregular-regular-irregular (IRI) multi-grid system of three grids: one with regular spacing (in terms of latitude and longitude) at low latitudes and two polar stereographic grids at high latitude in the northern and southern hemisphere respectively [37]. The northern polar stereographic grid includes the entire Arctic Ocean (albeit with the North Pole masked to prevent a singularity associated with angle conventions in WW3). Of the collection of configurations with their different resolutions, NRL selected the  $1/4^\circ$  geographical degree grid system for the transition to operations. The resolutions of the polar stereographic grids are such that grid spacing (in this case  $\sim 18$  km) are roughly similar to that of the low-latitude grid at the grid boundaries, noting that this boundary is the latitude where both have the highest resolution. One advantage of the IRI system is that each grid has more uniform grid spacing (in terms of real distances) than any alternative single-grid global system, which means that the limiting time step for CFL stability is larger, thus making the system more efficient. More details about the specifics of these grids can be found in [37].

Data assimilation was a recent enhancement to the operational WW3 model runs at FNMOC bringing in satellite altimeter measurements of significant wave height [38]. The latest application of NCODA [30] uses WW3 software libraries to directly access files and interpolate fields.

One of the main purposes of the U.S. Navy operational global WW3 model simulations is to provide boundary conditions to the nested wave model simulations, in support of various missions throughout the globe. The global model was also set up to supply boundary conditions to the operational SWaSS model. For the purposes of the present study, the model was run for a period of three months, over which time full spectral boundary conditions were output every three hours, with 35 directional bins and 31 frequency bins starting at 0.0418 Hz and ranging up to 0.7295 Hz, the same specification as the state variables.

In addition, WW3 can write the spectra in a reduced form consisting of the five first moments of the spectra based on a limited set of Fourier coefficients. These reduced spectra are expandable to approximately the original full spectral values using techniques described in Section 4.2.

### 3.2. Simulating Waves in the Nearshore (SWAN)

The spectral SWAN model was coupled hourly with a Delft3D [39], depth-averaged hydrodynamic model. The details of the hydrodynamic model are described in [27] and [4], respectively, for the tidal and storm tidal water level calibration and validation. The combined modelling system is called the SWaSS model. The regional SWAN numerical grid extent (shown in Figure 1) extends from  $24^\circ\text{S}$  to  $38^\circ\text{S}$  and  $12.5^\circ\text{E}$  to  $38^\circ\text{E}$  at  $1/16^\circ$  geographical degree resolution. High-resolution nested numerical grids were developed for all the coastal port locations (refer to Figure 1). These nests were developed at  $1/48^\circ$ -degree resolution with local refinements down to between 700 m and 1 km resolution at measurement locations. All the computational SWAN grids were curvilinear and orthogonal. The extent of the grid depends on its relative distance from steep changes in location bathymetry. SWAN version 40.72 is currently used in the SWaSS model with basic physical parametrisations

describe in Table 2. Both the directional and frequency bins (or resolutions) were set to 36 with the frequencies ranging from 0.05 to 1 Hz.

Ref. [40] made use of a similar coupled SWAN model setup for the Dutch Continental Shelf Model (DCSM). They employed the Van der Westhuysen wind growth and source term settings. In the present study two whitecapping source term formulations were investigated, as listed in Table 2. The spectrally averaged wave steepness model of [41] has a tendency to over-predict significant wave heights in the presence of locally generated wind waves in the presence of swell signals (mixed seas) [41] and was also evident in the present study (as elucidated in Section 6). The uncoupled (from swell energy) local estimation of wind-sea whitecapping model presented by [42,43] is the second model.

**Table 2.** Summary of physical parametrization setting for SWAN 40.72, used in the present study.

SWAN 40.72 (3rd-Generation Model)	Model	Additional Information
Open boundaries	WW3 Global	NRL model
Meteorological forcing	Down scaled Unified Model	SAWS operational model
Bottom Friction	Madsen [44]	$K_n = 0.05\text{m}$
Depth induced breaking	Battjes [45]	Alpha (dissipation) = 1, Gamma (breaker) = 0.8. Exponential growth, Dissipation rate coeff. (Cds) = $2.36 \times 10^{-5}$ ,
Whitecapping	Komen [41]	Pierson-Moskowitz spectrum wave steepness = $3.02 \times 10^{-3}$ .
	Van der Westhuysen [42]	Non-linear saturation-based whitecapping.

Due to the extent of the regional SWAN domains, all models were executed in non-stationary mode. In Figure 2 some examples of the operational output from SWaSS are given. The enclosures of each of these nested domain (used in the present study) is given in Figure 1 Local refinements were also used in the vicinity of the in situ buoy locations.

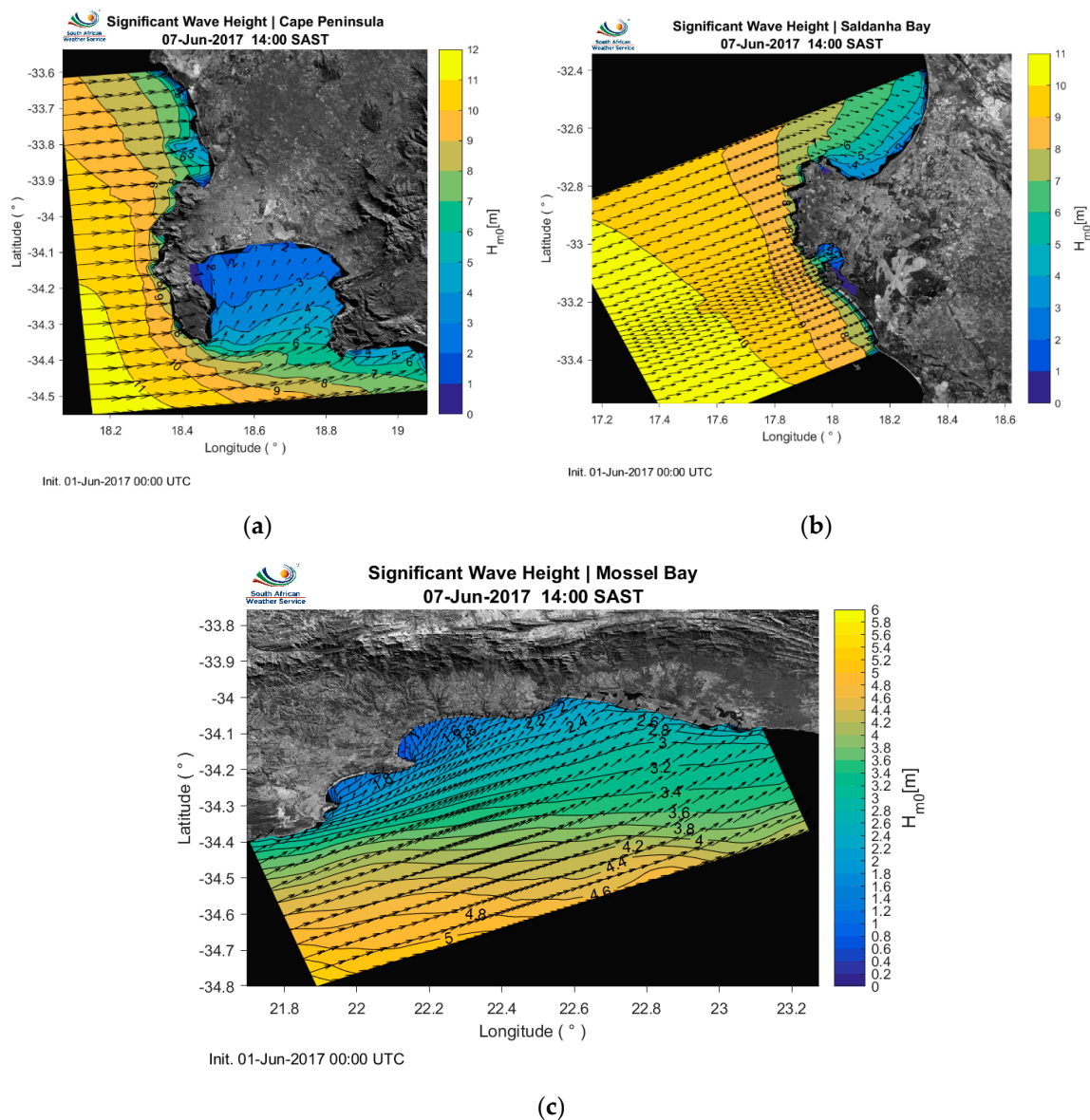


**Figure 2.** Example output from the SWaSS operational systems. Each of these is an example of the nearshore, high resolution, nested domains. Local refinements are also applied in the immediate vicinity of each buoy location. (a) Cape Town (CT) nested domain, (b) Saldanha Bay (SB) nested domain, and (c) the Mossel Bay (MB) nested domain.

## 4. Boundary Spectral Reconstruction

### 4.1. Singular Partition Reconstruction

Single partition reconstruction is one of the most common ways of using and saving global wave datasets for localized models. The spectrum is reduced to a single set of representative conditions. These are usually the significant wave height, peak or mean period, peak or mean direction and a directional spreading value. Using well-known wave spectrum shapes (like the Joint North Sea Wave Project (JONSWAP)), these parameters can be reconstructed into a representative spectrum. The age or peakedness of the spectrum can also be varied via the peak enhancement factor ( $\gamma$ ) [46]. Typically, a single  $\gamma$  is estimated for the whole domain, as well as a singular directional distribution. For small coastal domains, this is usually a reasonable assumption. For regional domains, this might be a bad assumption due to the heterogeneity of the wave and atmospheric conditions on the boundary.

In Section 6.2, the regional comparisons of a single partition, parameter, or JONSWAP spectrum are compared with the same model forced with fully spectral WW3 boundaries. The  $\gamma$  was chosen as 2.5 [47] and the directional spreading a constant  $25^\circ$ . This is the current implementation of the wave forecasts predicted in SWaSS. The  $\gamma$  and directional spreading is spatially and temporally constant.

#### 4.2. Five-Moment Reconstruction

The directional wave spectrum  $S(f, \theta)$  quantifies the wave energy distribution as a function of wave frequency,  $f$ , and direction,  $\theta$ , and is expressed as the product of the omni-directional wave spectrum  $E(f)$  and the directional distribution function  $D(f, \theta)$  as:

$$S(f, \theta) = E(f)D(f, \theta) \quad (1)$$

where the directional distribution can be decomposed into a Fourier series expansion [48]:

$$D(f, \theta) = \frac{1}{\pi} \left\{ 0.5 + \sum_{n=1}^{\infty} [a_n \cos(n\theta) + b_n \sin(n\theta)] \right\}, \quad (2)$$

and  $a_n$  and  $b_n$  are the Fourier coefficients of the  $n$ th harmonic component and can be computed as:

$$a_n = \int_0^{2\pi} D(f, \theta) \cos(n\theta) d\theta, \quad (3)$$

$$b_n(f) = \int_0^{2\pi} D(f, \theta) \sin(n\theta) d\theta. \quad (4)$$

In practice, [48] proposed the use of the first two Fourier harmonics to approximate the directional spreading as:

$$D(f, \alpha) \approx \frac{1}{\pi} \{0.5 + r_1 \cos(\alpha - \alpha_1) + r_2 \cos[2(\alpha - \alpha_2)]\} \quad (5)$$

where  $\alpha$  follows the meteorological convention that the direction from which waves come measured clockwise from the north, and the coefficients  $r_1, r_2, \alpha_1$  and  $\alpha_2$  are computed as:

$$\begin{aligned} r_1 &= \sqrt{a_1^2 + b_1^2}, \\ r_2 &= \sqrt{a_2^2 + b_2^2}, \\ \alpha_1 &= 3\pi/2 - \tan^{-1}(b_1/a_1), \\ \alpha_2 &= 3\pi/2 - \frac{1}{2} \tan^{-1}(b_2/a_2). \end{aligned}$$

Several data-adaptive methods have been developed for providing higher directional resolution using the one-directional frequency spectra, and these coefficients,  $r_1, r_2, \alpha_1$  and  $\alpha_2$ , of the Fourier series. The Maximum Likelihood Method (MLM) [49] and the Maximum Entropy Method (MEM) [50] are widely used in practice [51], providing more discussions for the data-adaptive methods. In the present study, we show the application of WW3 output, omni-directional wave energy spectrum and the Fourier coefficients  $r_1, r_2, \alpha_1$  and  $\alpha_2$  (with the above equations) to produce directional spreading and directional wave spectra with high directional resolution by means of MEM or MLM.

## 5. Methodology

Both regional and in situ validation were performed. Six scenarios were constructed as listed in Table 3. Each scenario aimed at investigating both the influence of the whitecapping formulation and the various boundary conditions described in Section 4. Each scenario was compared with measurements

at the nine coastal wave rider buoy locations described in Section 2.2. The results of these comparisons are given in Section 6. To be able to understand the spatial distribution of these scenarios, difference map plot comparisons were produced. Each difference plot was made in comparison with the fully spectral model boundary conditions simulation, given by M3 and M4 in Table 3. Based on these results, recommendations for the operational SWaSS model's wave forecasting component are presented.

**Table 3.** Description of the various permutations used in the present study to investigate the best combinations of whitecapping formulation and swell boundary conditions.

M1		M2		M3	
<i>Spectrum</i>	<i>Whitecapping</i>	<i>Spectrum</i>	<i>Whitecapping</i>	<i>Spectrum</i>	<i>Whitecapping</i>
JONSWAP	van der Westhuysen	JONSWAP	Komen	Fully Spectral	van der Westhuysen
M4		M5		M6	
<i>Spectrum</i>	<i>Whitecapping</i>	<i>Spectrum</i>	<i>Whitecapping</i>	<i>Spectrum</i>	<i>Whitecapping</i>
Fully Spectral	Komen	5-parm	van der Westhuysen	5-parm	Komen

The focus of the present study is on the relative influence of various boundary conditions and established whitecapping formulations on the produced wave field evolution and the ultimate coastal wave response. The validation presented in the present study is well aligned with published validation principles (e.g., [52,53]).

In this study, the centred-Root-Mean-Square Difference (cRMSD) is given by:

$$cRMSD^2 = \sum_{n=1}^N ((p - \bar{p}) - (r - \bar{r}))^2 / N \quad (6)$$

where  $p$  is the predicted values,  $r$  is the reference values, and  $N$  is the total number of values being compared. The bias is given as the difference between the mean predicted minus the mean reference data. In the present study, the reference data will be the measured wave rider buoy or altimetry data. Data sets described as normalized were normalized with regard to the standard deviation of the reference field.

## 6. Results and Discussion

The austral winter months (June, July and August (JJA)) of 2017 were used in the present wave field evolution investigation. During June, a mid-latitude cyclone, locally referred to as the Cape Storm, caused widespread disruptions on the South African southwestern and southern coasts. Significant wave heights in excess of 12 m were recorded at the Slangkop wave rider buoy (refer to Table 1 and Figure 3) and contributed to significant storm surge water levels [4].

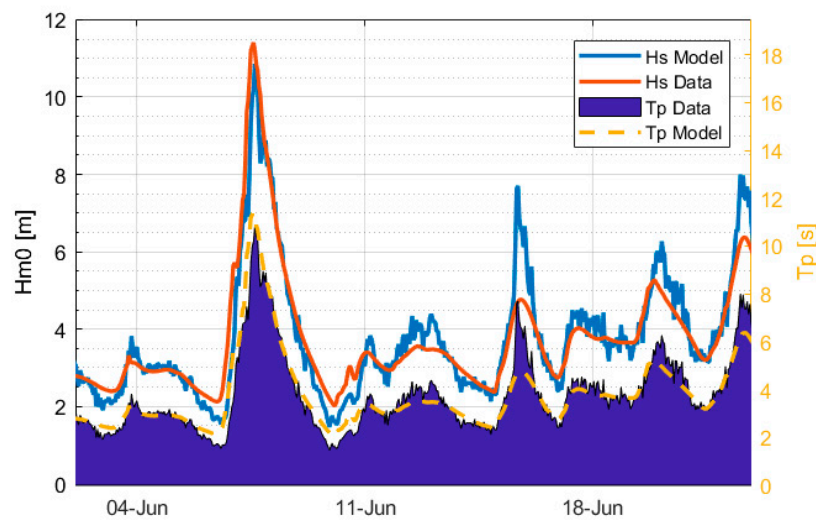


**Figure 3.** Time series comparison of modelled vs. measured significant wave heights (left axis) and peak periods (right axis) during June 2017 for scenario M3.

The wave conditions during JJA were thus characterized by both swell and locally generated wind seas and were deemed adequate for evaluating the SWAN model performance and sensitivity, similar to a study performed at Nova Scotia, Canada, where an extra-tropical storm (Nicole) was used to test their local SWAN model sensitivities [43]. Due to their small computational domain, they also investigated the relevance of stationary versus non-stationary computations. The coupled water levels during storm events significantly influenced the wave model accuracy during storm conditions and vice versa [4]. This is especially true in shallower water or when waves move over shallow areas like the Agulhas Bank.

### 6.1. In situ Comparisons

The buoys listed in Table 1 were used for nearshore validation. In Figure 4, the Taylor diagram [54] comparisons of all the model scenarios are presented for a few selected coastal wave rider buoy locations. All statistical correlation definitions are provided in Appendix C. Sites were chosen to represent each of the three major coastlines (western, southern, and eastern coasts of South Africa). FH Platform is also the location furthest south on the edge of the Agulhas Bank (refer to Table 1 and Figure 1). A useful manner of interpreting these figures is by remembering that even model scenario numbers (M2, M4 and M6) were executed with the Komen whitecapping formulation while odd numbers (M1, M3 and M5) were executed with the Van der Westhuysen formulation. For the full model performance statistics (including peak period and direction), for all the coastal measurement locations and model configuration scenarios, please refer to Appendix A.



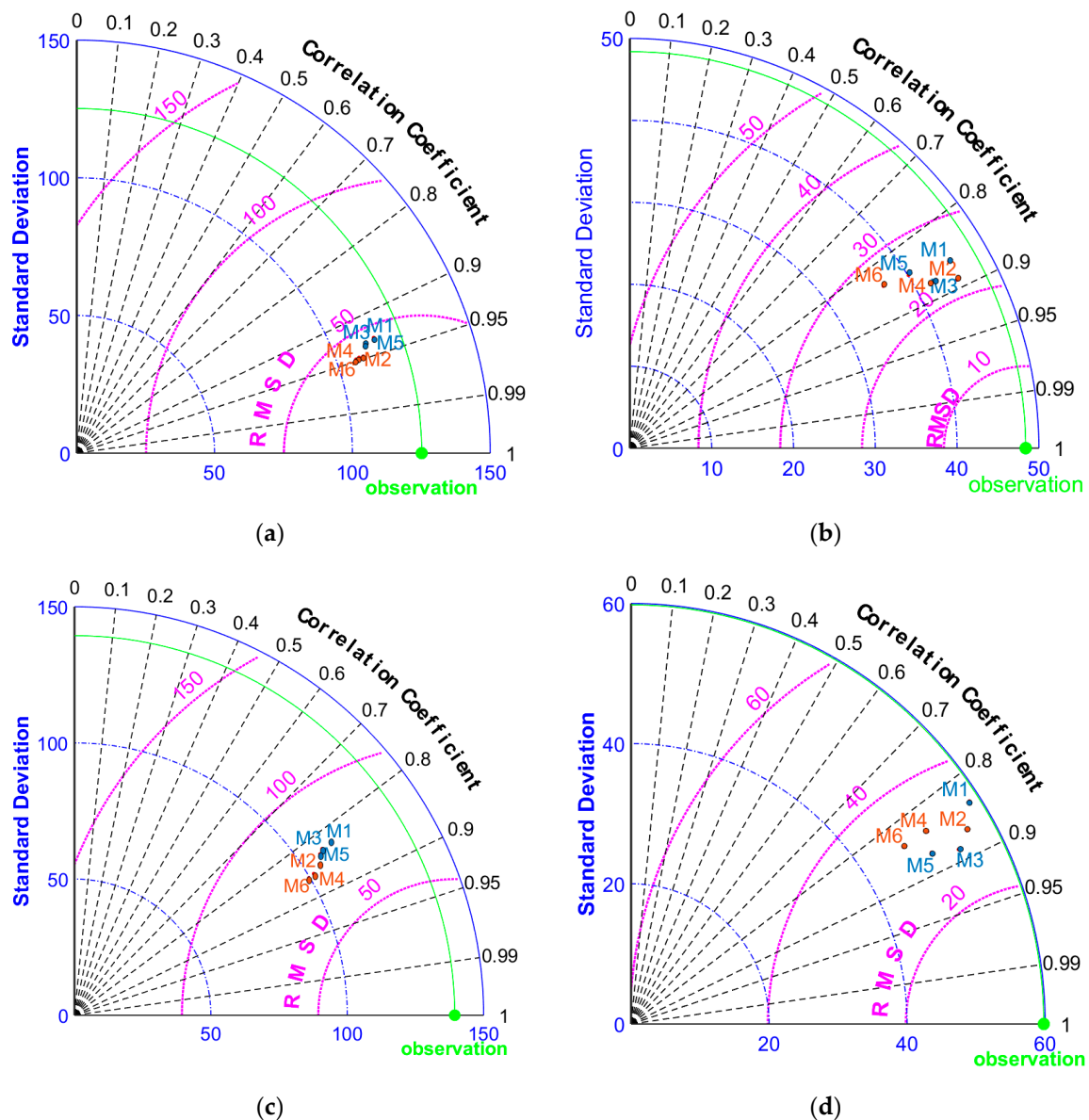


**Figure 4.** Selected Taylor diagrams [54,55] illustrating significant wave height ( $H_{m0}$ ) model performance as a function of centered-Root-Mean-Square Difference (cRMSD), the correlation coefficient and standard deviation [54]. Units are in centimetres [cm] and are situated at the following locations: (a) Cape Town (CT), (b) Port Elizabeth (PE), (c) FH Platform (FHP), and (d) Richards Bay (RB). These results are for JJA 2017. The scenarios (M1 to M6) are prescribed in Table 3.

The various combinations of physics and spectral boundary conditions given in Table 3 produce varying accuracies around the South African coastline. On the western coast, the results are similar. All west coast scenarios congregate with high correlation values (between 0.90 and 0.96). The Saldanha Bay buoy is located within the bay and thus experiences a degree of sheltering, as presented by the lower standard deviation (refer to Appendix B). Figure 4a indicates the large standard deviations at Cape Town. This is due to the geographical location of the Cape Town (Slangkop) wave rider buoy. Due to the narrow continental shelf, the deep southwesterly Southern Ocean swell loses little of its energy as it propagates towards the continent (and hence the high correlation values). The same cannot be said of the areas adjacent to the continental shelves as large swell will lose some of its energy over these shallower regions [56]. The dominant wave direction for most of the South African coastline is from the southwest, thus rendering the western and southwestern coasts exposed [5,23]. The full wave

climatology is provided in Appendix B. Within the scenarios, there does exist a measure of grouping. At Cape Town, the groupings are divided by whitecapping formulation, with the Komen formulation performing slightly better for all boundary conditions. At Saldanha Bay, the groupings are based more on the type of boundary conditions. Here, Komen again performed marginally better with the fully spectral boundary conditions. This is an indication that on the western and southwestern coasts, the wave climate is southwesterly swell driven, and the boundary reconstruction method or white capping formulation is less important in the nearshore. It should be noted that an improved physics description of the locally and offshore generated wind waves might lead to a better overall prediction of the wave climate.

On the southern coast, the FH platform results in large standard deviations due to its proximity to the Agulhas Bank shelf edge. On the southern coast, the various scenarios perform differently, but with the Komen whitecapping formulation performing the best. In both cases, correlation values between 0.8 and 0.9 are obtained. The fully spectral boundary conditions provide slightly better results at FH Platform (refer to Figure 4c), but in general all the model predictions are similar. On the southeastern coast, all correlations are again above 0.8, with measurements at Port Elizabeth (refer to Figure 4b) performing slightly better. The spread of predictions is mostly related with the modelled standard deviation similar to the southern and eastern coasts results. The Komen whitecapping formulation once again performed slightly better. At Durban, the model correlations performed with correlations values under 0.8. This might be due to neglecting the complex wave–current interaction in the current spectral wave model implementation as noted by [23]. Richards Bay (refer to Figure 4d) produced high correlation and adequate cRMSD values. In general, the largest variation was observed along the standard deviation axis. The Komen formulation (refer to Table 2) gave the best results, while the boundary condition specification did not produce significant variations in the results. The JONSWAP boundary reconstruction method performed adequately, while the range of cRMSD values compared well with other modelled wave climate validations from published literature around the world (e.g., India [6], The Netherlands [40] and southwestern Australia [57]). The India focused model produced RMSD values ranging between 0.15 and 0.24 m, even though extreme  $H_{m0}$  events had a tendency to be underpredicted [6]. The Dutch coast operational system produced  $H_{m0}$ , RMSD values ranging from 0.2 to 0.6 m, depending on the season [40]. The largest errors were observed during winter months, but the normalized RMSD indicated a stable error estimation.

Another aspect to investigate the performance of the model is via the normalized bias. Figure 5 presents the normalized target diagrams [58] for all the in situ measurement locations for JJA. The model scenarios were divided per coastline grouping (similar locations). An effective manner of interpreting Figure 5 is to access the model performance with regard to its relative position to the center of the plot.

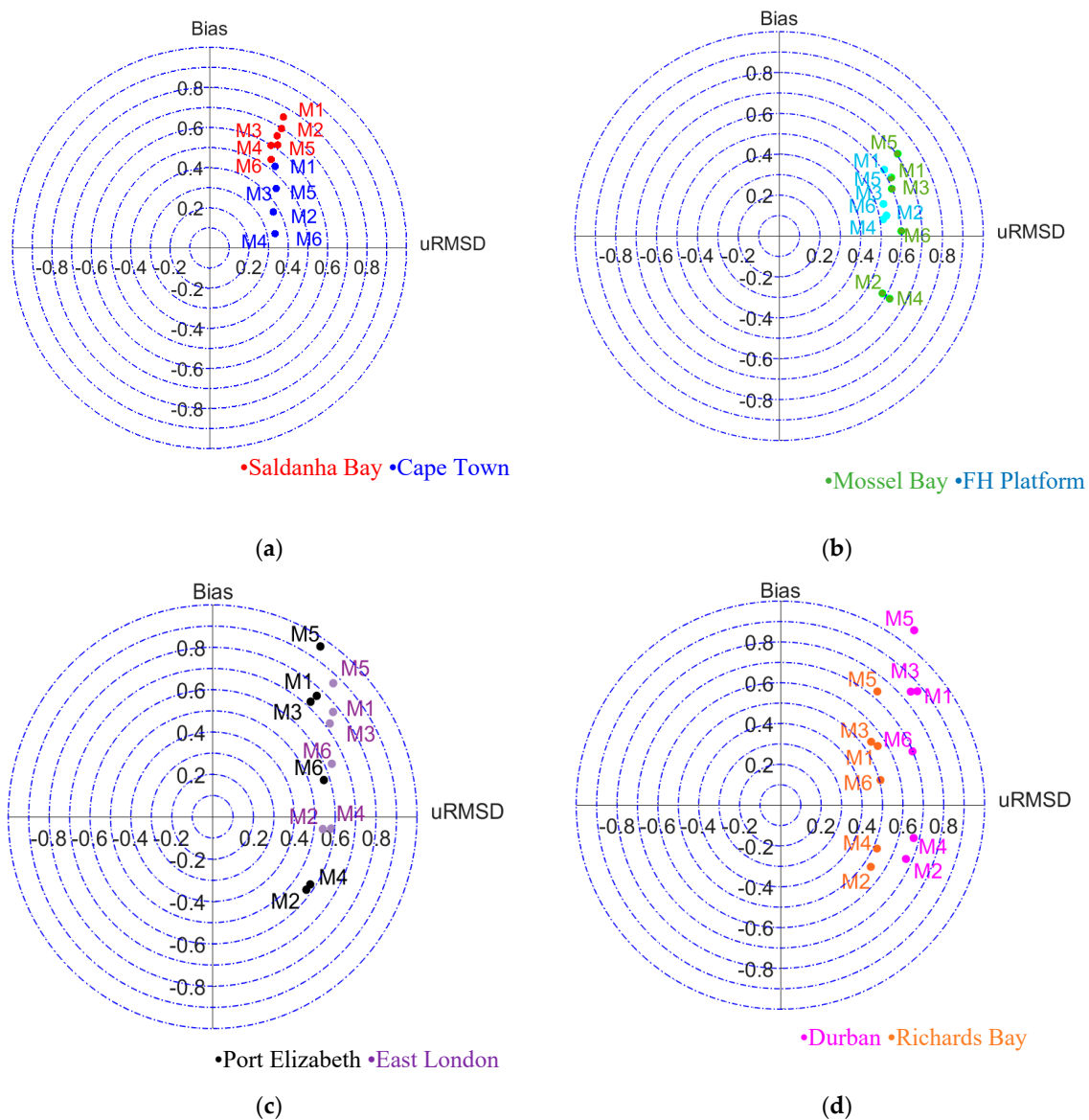


**Figure 5.** Target diagrams according to [58] with normalized, unbiased, Root-Mean-Square Difference (uRMSD)  $H_{m0}$  against normalized bias for (a) the western coast, (b) the southern coast, (c) the southeastern coast, and (d) the eastern coast.

Here, the Komen whitecapping simulations performed the best at Cape Town, together with fully spectral boundary conditions and the five-parameter reconstruction method. Saldanha Bay performed worse and probably due to the sheltered nature of the wave rider buoy. The model performance spreading was also less varied compared to the results at Cape Town. On the south coast, the model performance presented varied biases. At Port Elizabeth, the Komen whitecapping formulation performing the best, with M4 and M6 within the 0.6 target segment. East London presented a similar result pattern. On the eastern coast, the model performed better at Richards Bay than at Durban, but with both locations revealing a similar validation pattern. In both cases, the Komen formulation performed best, with only scenario M5, at Durban and East London, performing worse than most simulations.

## 6.2. Regional Altimetry Validation

The regional validation described in Sections 2.3 and 5 are presented in Figure 6 and Table 4. For the regional model performance, the Van der Westhuysen whitecapping outperforms

the Komen formulation. Whitecapping formulations ultimately established a relationship between wind input driven dynamics and quadruplet wave interactions [59]. Ref. [59] reported some limitation of the default SWAN (40.51) model. Calibrating the model with regard to bottom friction and breaking parameters presented some significant improvement. Among these were an  $H_{m0}$  bias reduction from  $-3\%$  to  $-1\%$ . Within the experimental setup of [59], they found that the Van der Westhuysen whitecapping formulation performed well under storm conditions in tidal inlet seas. They did, however, notice some aspects of the model that required further investigation, including the penetration of low-frequency wind waves into the inlet seas [59]. Van der Westhuysen mentioned and improvement over the Komen whitecapping formulation in depth limited wave growth simulations. Even with these improvements, wave heights and periods were underestimated by approximately 12% and 10%, respectively, in the Wadden Sea interior. According to [60], whitecapping is still one of the most prominent tuning factors in spectral wave modelling, even though it is not limited to shallow or enclosed ocean considerations. In Figure 6, the relative difference between the Van der Westhuysen and Komen whitecapping model are given for the month of June 2017, with fully spectral boundary conditions.

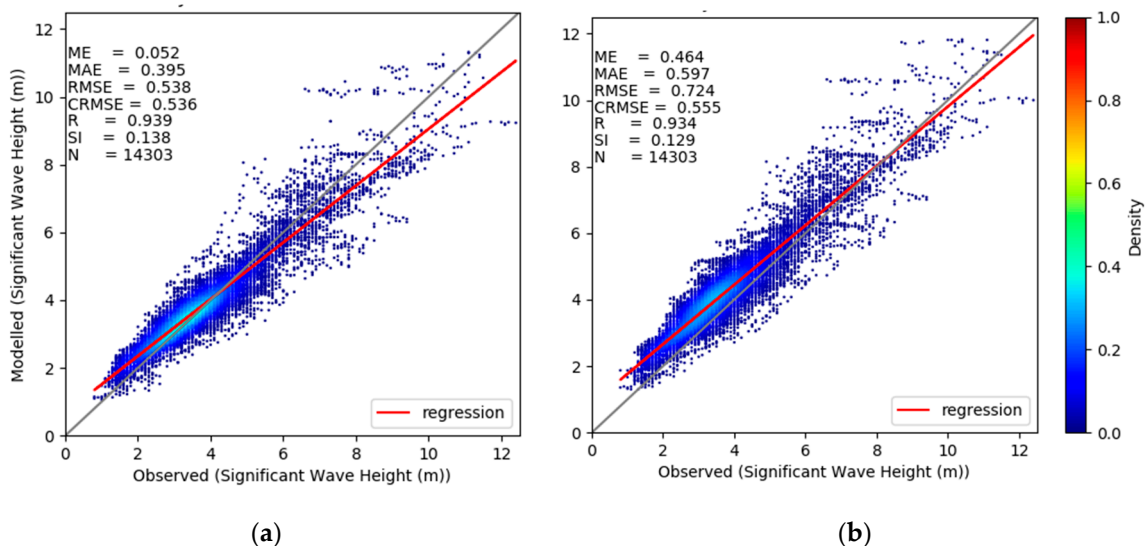


**Figure 6.** Correlation between co-located Altimetry measurements and the regional SWAN model results for (a) June M3 and (b) June M4.

The Komen formulation implicitly made the assumption that the wave field was wind driven (wind seas) [53]. Once one or more swell signals are present, the assumption within the Komen model starts to lose its usefulness, and thus its intended meaning [53]. This could be the explanation for the difference in the results between the in situ measurements in Section 6.2 and the regional validation presented in the present section. All the in situ buoys were in coastal seas, which would be closer to the assumptions presented by the Komen whitecapping model. The Komen model tends to overpredict wind seas and underpredict swell seas (in a mixed seas state due to dissipation rates) [53]. This behaviour is evident in Figure 6, where the regression lines for a Van der Westhuysen (M3) and Komen (M4) model are given.

In the coastal regions, bottom friction is also an important calibration parameter, as it is intertwined with the other wave energy sources and sinks. The [44] model is described as a “sophisticated eddy viscosity model” [53] and was employed in the present study. Other widely used formulations include the [61] prediction of shallow-water spectra. [26] performed similar investigations in The Canadian Beaufort Sea. They also reported that the Van der Westhuysen formulation performed better than Komen in deep water. In shallow water, they found that either formulation performed adequately and that  $H_{m0}$  was not that sensitive to either formulation. They also reported limited sensitivity to bottom friction and the inclusion of triad mechanisms [26].

In Table 4, the RMSD, centred-Root-Mean-Square Difference (cRMSD), Scatter Index (SI) and correlation coefficient (R) for all the regional model comparisons are given. The fully spectral boundary conditions scenarios performed the best with the Komen formulation. Unlike the formulation by Komen, the Van der Westhuysen formulation calculates wind sea whitecapping locally in the spectrum and uncoupled from the swell energy [42]. Thus, either the swell signal has an important influence on the dissipation of the wind seas (Komen), or it has little importance (Van der Westhuysen) [42]. As also indicated by the results presented here, the composition of the predicted sea state must be considered in choosing the appropriate whitecapping formulation.

**Table 4.** Regional wave model performance compared with the co-located altimetry measurements (refer to Section 2.3) per investigated month. Each model configuration (M1 to M6) is described in Table 3.

Month	June				July				August			
Stats	RMSD	cRMSD	SI	R	RMSD	cRMSD	SI	R	RMSD	cRMSD	SI	R
<b>M1</b>	0.56	0.55	0.14	0.93	0.55	0.47	0.12	0.94	0.49	0.48	0.14	0.93
<b>M2</b>	0.79	0.61	0.13	0.93	0.89	0.51	0.12	0.93	0.49	0.48	0.14	0.92
<b>M3</b>	0.54	0.54	0.13	0.94	0.45	0.43	0.12	0.94	0.45	0.45	0.13	0.94
<b>M4</b>	0.72	0.56	0.13	0.94	0.67	0.46	0.12	0.94	0.45	0.45	0.12	0.94
<b>M5</b>	0.59	0.57	0.14	0.94	0.49	0.45	0.12	0.94	0.50	0.46	0.13	0.94
<b>M6</b>	0.80	0.57	0.13	0.94	0.75	0.45	0.11	0.94	0.66	0.48	0.12	0.93

In general, the scatter plots of both June and August 2017 indicated very similar behaviour, while July presented slightly different results. During July, the Komen model produced a near constant bias, while the Van der Westhuysen model produced high correlation values. The behaviour between the various model runs were similar per month per whitecapping formulation.

### 6.3. Spatial Variations

The different boundary conditions have direct consequences on the introduction of energy into the regional domain. If the directional spreading is too broad or too narrow, energy will dissipate into the regional at an incorrect tempo. This might result in the underestimation of deep-sea swell signals that are not generated by local winds. In Figure 7, the spatial comparison of all modelled scenarios for June 2017 is compared with the fully spectral boundary condition scenario.

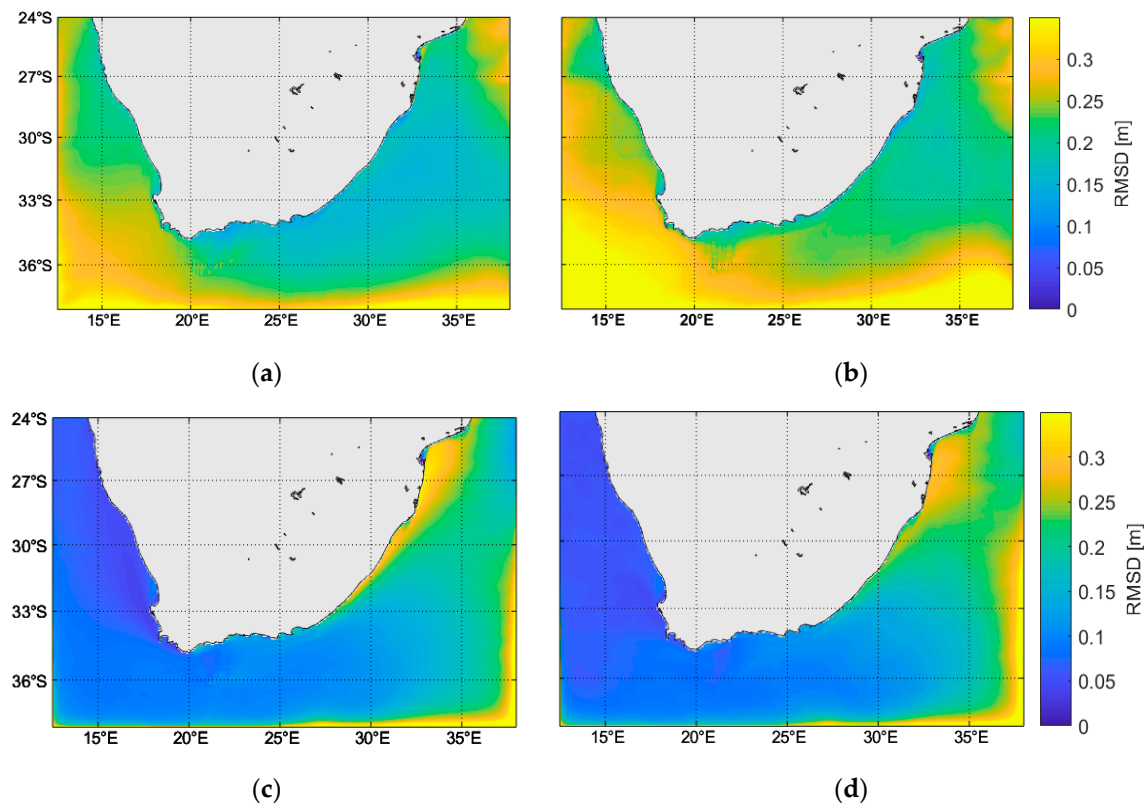


**Figure 7.** Spatial RMSD maps for June 2017. Here all the reconstructed boundary condition scenarios are compared with the fully spectral output boundary conditions. The particular scenarios are (a) M1, (b) M2, (c) M5, and (d) M6.

From Figure 7a,b, it is given that the parameterized JONSWAP boundary reconstruction method differs most. Together with the boundary conditions, the Komen whitecapping formulation produced the largest differences in the open ocean. Each scenario compared the same whitecapping formulation, implying that the mixed wave open ocean was clearly misrepresented with the Komen formulation. From the wave climatology presented in Appendix A, it is clear that South Africa's main wave approach direction is from the southwest, and due to this predominant swell signal, the errors produced by the JONSWAP reconstruction and the Komen formulation were the largest in the southwest. On the eastern coast, the RMSD values were lower due to the dominance of locally generated wind seas. Hence the dependence on the boundary conditions decreases. The long-period wave interactions with the continental shelf edge is also visible due to the differences in the scenarios. In Figure 7c,d the map result followed a different pattern. Here, the reconstructions are generally performing well except on the southeast coast.

In general, the RMSD values on the continental shelves were low, indicating the dominance of locally generated wind waves. This could potentially also be the explanation for the differences in model accuracies when comparing the results to remotely sensed and in situ wave buoys, also noted by [27].

## 7. Conclusions

SAWS developed a regional wave and storm surge forecasting platform called the SAWS Wave and Storm Surge (SWaSS) model. The various components of this online coupled, marine forecasting system have been calibrated and validated, with the tidal dynamic described by [28] and the storm surge dynamics described by [4]. The operational flow, configuration and atmospheric forcing details are also described in [4]. The present study aimed to elucidate the accuracies associated with the wave



component of SWaSS. The spectral wave model Simulating Waves in the Nearshore (SWAN) was used for this purpose. The regional model was implemented with a series of nested, high-resolution domains at nine South African ports. Even higher local resolutions were described in the immediate vicinity of in situ wave ride buoys, via local refinements. Both in situ and regional altimetry measurements were used in the validation of the wave model. Model sensitivities were investigated with regard to boundary conditions and whitecapping formulations employed. Similar to [26], the well-established formulations of Komen [41] and Van der Westhuysen [42] were investigated. In the near shore (in situ buoy locations), the Komen formulation marginally outperformed the Van der Westhuysen correlation. With the regional altimetry validation, the Van der Westhuysen formulation produced the best results. Thus, in general, the use of the Van der Westhuysen model is recommended. The main reason for this is because the latter correlation better solves the wind-sea spectral peak in the presence of swell signals [42].

Various boundary reconstruction methods were also investigated. The main motivation for this was due to the computational constraints a lot of public and private engineering and scientific institutes face. Parameter-based, reconstructed, spectral boundary conditions are commonplace and an acceptable standard due to the limited availability of free fully spectral boundary conditions (usually from larger, global spectral models (e.g., WW33)). The commonly used, unpartitioned, JONSWAP [46] spectral reconstruction method was compared with a five-parameter (or moment) reconstruction method, together with fully spectral boundary conditions, provided by the US Navy. The biggest differences were observed on the southeastern boundary of the model, aligned with the predominant swell direction. Here, the underlying assumptions in the reconstruction methods became clear, with the single partition reconstruction presenting the largest discrepancies, compared with the fully spectral boundary conditions. Either method is thus acceptable for regional and local wave modelling around South Africa, depending on the accuracies required for a particular study or investigation. Further increases in accuracies could be observed with various combinations of bottom friction and energy sources and sinks, such as the new physics described by [62].

**Author Contributions:** Conceptualization, C.R.; methodology, C.R.; software, C.R., M.A.B., D.W.W. and J.D.; validation, C.R., M.A.B., D.W.W. and J.D.; formal analysis, C.R., M.A.B., D.W.W. and J.D.; investigation, C.R.; resources, C.R., M.A.B., D.W.W. and J.D.; data curation, C.R., M.A.B. and J.D.; writing—original draft preparation, C.R.; writing—review and editing, J.D. and M.A.B.; visualization, C.R., M.A.B. and J.D.; supervision, C.R.; project administration, C.R.; funding acquisition, C.R. All authors have read and agreed to the published version of the manuscript.

**Funding:** This research was funded by the National Research Foundation of South Africa (Grant Numbers: 116359).

**Acknowledgments:** The authors would like to thank the South African Navy Hydrographic Office (SANHO) for providing high-resolution coastal bathymetry required for model calibration and validation. We acknowledge Transnet National Port Authorities (TNPA) for the in situ wave measurements used in the present study.

**Conflicts of Interest:** The authors declare no conflict of interest.

## Appendix A

Here the seasonal wave climatology of the South African coastline is presented via wave roses per coastline.

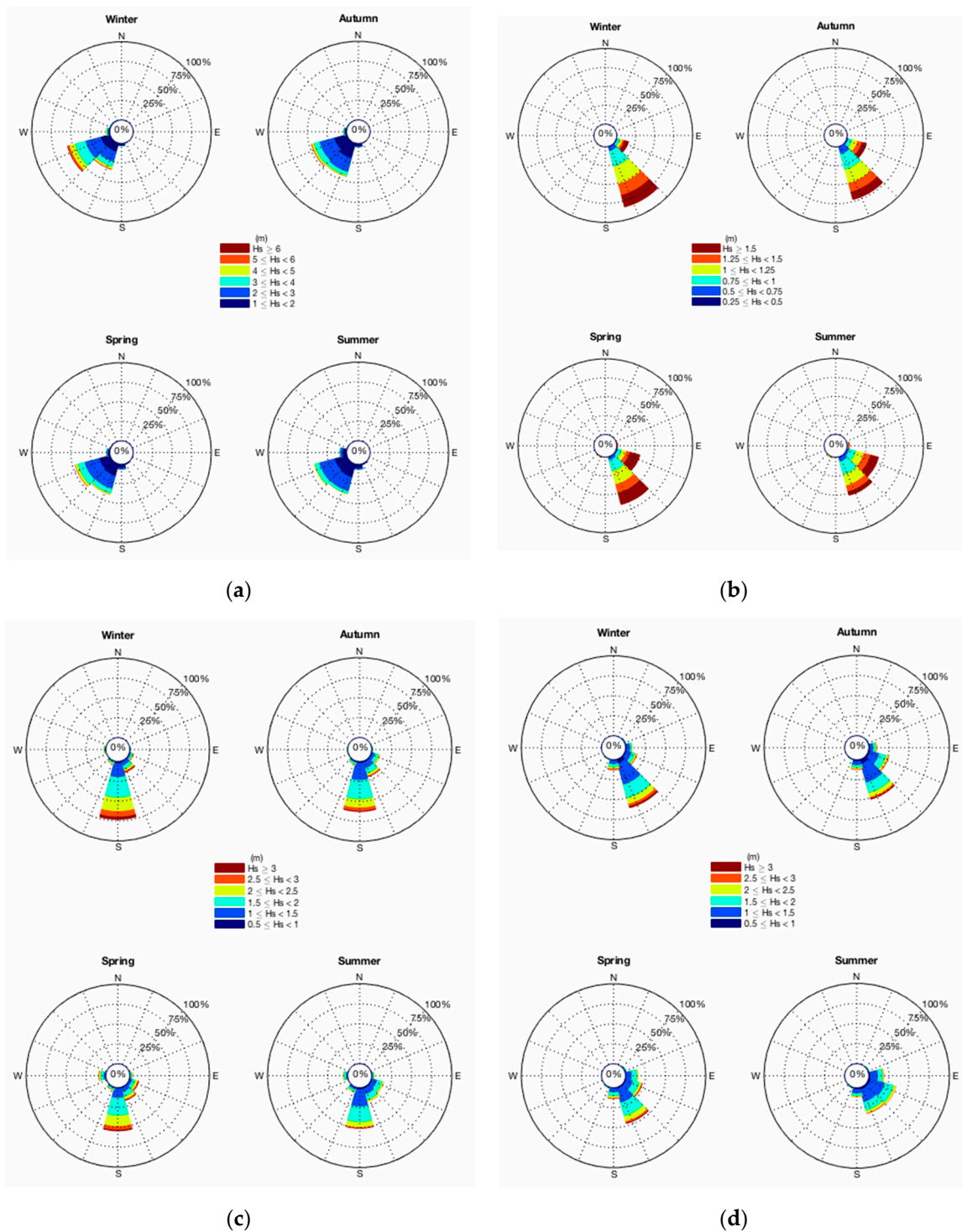


**Figure A1.** The  $H_{m0}$  seasonal, wave climatology for the South African coastline based on all available in situ wave rider buoy data at (a) Slangkop (Cape Town), (b) Port Elizabeth, (c) East London, and (d) Richards Bay.

## Appendix B

Here, an extensive resource of model validation statistics is provided. Due to the limited local benchmarking data available in the open literature, these values could enable future studies with increasing accuracy and physical descriptions. In these statistics, reference is made to the [63] methods

of assessing model performance (also refer to [4] for a description and reference to the newer model performance correlation presented by [64]). Statistical definitions are provided in Appendix C.

**Table A1.** Model performance statistics per coastal buoy location for JJA 2017, M1.

Station		$H_{m0}$			$T_p$		Peak Direction		
ID	RMSD	Bias	Willmott	RMSD	Bias	Willmott	RMSD	Bias	Willmott
CP	0.39	0.09	0.97	1.55	0.09	0.76	16.79	−1.35	0.54
DB	0.38	0.03	0.90	2.97	−0.32	0.73	39.89	−6.92	0.73
MB	0.39	−0.20	0.85	1.40	−0.22	0.87	-	-	-
NG	0.35	−0.24	0.88	1.57	−0.13	0.85	19.66	7.33	0.59
OL	0.42	0.02	0.91	2.05	−0.56	0.75	37.46	−9.08	0.53
RB	0.35	−0.16	0.92	2.51	−0.05	0.80	32.39	−6.58	0.68
SB	0.49	0.40	0.88	1.77	0.07	0.76	-	-	-
FA	0.74	0.10	0.88	2.88	1.93	0.57	40.75	-2.58	0.69

**Table A2.** Model performance statistics per coastal buoy location for JJA 2017, M2.

Station		$H_{m0}$			$T_p$		Peak Direction		
ID	RMSD	Bias	Willmott	RMSD	Bias	Willmott	RMSD	Bias	Willmott
CP	0.72	0.66	0.85	1.06	0.16	0.81	13.71	−0.68	0.76
DB	0.47	0.34	0.75	4.71	−3.49	0.60	28.87	−5.15	0.82
MB	0.33	0.22	0.82	2.66	−1.07	0.54	-	-	-
NG	0.37	0.30	0.74	3.19	−1.41	0.49	22.13	11.80	0.31
OL	0.55	0.39	0.78	2.03	−0.41	0.72	31.80	−7.22	0.35
RB	0.34	0.23	0.87	4.71	−3.28	0.61	35.24	−6.56	0.61
SB	0.58	0.52	0.76	1.08	0.37	0.81	-	-	-
FA	0.97	0.77	0.58	2.56	1.99	0.45	27.84	−1.65	0.60

**Table A3.** Model performance statistics per coastal buoy location for JJA 2017, M3.

Station		$H_{m0}$			$T_p$		Peak Direction		
ID	RMSD	Bias	Willmott	RMSD	Bias	Willmott	RMSD	Bias	Willmott
CP	0.40	0.04	0.96	1.17	0.05	0.84	12.56	−1.35	0.73
DB	0.39	0.00	0.83	3.04	−0.99	0.71	37.32	−12.39	0.75
MB	0.34	−0.18	0.84	1.40	0.05	0.83	-	-	-
NG	0.31	−0.20	0.86	1.59	0.19	0.81	18.37	8.54	0.53
OL	0.41	0.00	0.88	1.75	−0.50	0.79	38.18	−11.19	0.42
RB	0.34	−0.11	0.88	2.73	−1.04	0.76	40.25	−18.52	0.58
SB	0.44	0.37	0.88	1.36	0.24	0.81	-	-	-
FA	0.72	0.11	0.82	2.89	1.88	0.50	32.48	0.88	0.65

**Table A4.** Model performance statistics per coastal buoy location for JJA 2017, M4.

Station		$H_{m0}$			$T_p$		Peak Direction		
ID	RMSD	Bias	Willmott	RMSD	Bias	Willmott	RMSD	Bias	Willmott
CP	0.51	0.25	0.95	1.52	0.12	0.79	18.30	−0.65	0.54
DB	0.58	0.46	0.77	4.59	−3.32	0.48	40.98	−15.92	0.72
MB	0.37	0.06	0.85	2.84	−1.18	0.69	-	-	-
NG	0.29	0.13	0.90	3.75	−1.83	0.59	19.69	4.00	0.64
OL	0.61	0.43	0.82	3.59	−2.43	0.57	45.38	−14.43	0.46
RB	0.35	0.21	0.92	4.86	−3.48	0.56	44.71	−23.61	0.56
SB	0.46	0.38	0.88	1.69	0.39	0.78	-	-	-
FA	0.89	0.42	0.82	4.03	1.81	0.46	36.97	0.19	0.75

**Table A5.** Model performance statistics per coastal buoy location for JJA 2017, M5.

Station		H <sub>m0</sub>			T <sub>p</sub>		Peak Direction		
ID	RMSD	Bias	Willmott	RMSD	Bias	Willmott	RMSD	Bias	Willmott
CP	0.40	0.03	0.96	1.18	−0.03	0.84	12.84	−2.27	0.76
DB	0.44	0.23	0.79	2.68	0.13	0.71	30.90	−7.90	0.79
MB	0.33	0.02	0.82	1.39	−0.53	0.82	-	-	-
NG	0.27	0.05	0.85	1.61	−0.38	0.78	15.20	6.13	0.51
OL	0.46	0.22	0.84	1.62	−0.52	0.78	29.99	−10.09	0.50
RB	0.33	0.09	0.88	2.43	−0.38	0.75	31.41	−13.68	0.66
SB	0.39	0.31	0.91	1.37	0.24	0.81	-	-	-
FA	0.74	0.21	0.81	3.65	1.98	0.41	32.99	0.44	0.66

**Table A6.** Model performance statistics per coastal buoy location for JJA 2017, M6.

Station		H <sub>m0</sub>			T <sub>p</sub>		Peak Direction		
ID	RMSD	Bias	Willmott	RMSD	Bias	Willmott	RMSD	Bias	Willmott
CP	0.52	0.29	0.93	1.37	−0.08	0.80	17.04	−2.11	0.72
DB	0.67	0.58	0.68	4.25	−2.52	0.53	35.58	−11.37	0.76
MB	0.40	0.21	0.78	1.81	−0.62	0.74	-	-	-
NG	0.41	0.31	0.77	2.09	−0.54	0.70	17.29	4.76	0.50
OL	0.67	0.53	0.75	2.31	−1.06	0.69	43.33	−16.97	0.35
RB	0.47	0.36	0.82	3.69	−1.89	0.65	40.25	−19.87	0.57
SB	0.43	0.35	0.88	1.46	0.32	0.79	-	-	-
FA	0.91	0.51	0.76	2.90	1.51	0.55	36.71	−2.85	0.64

### Appendix C (Statistical Correlations Used in the Present Study)

Here,  $p$  will be the predicted values and  $r$  the reference values.  $N$  is the total number of values being compared. In the following definitions an overbar denotes an average. The following statistical definitions thus follow:

$$\text{bias} = \frac{\sum_{n=1}^N p_n - r_n}{N},$$

$$\text{RMSD}^2 = \frac{\sum_{n=1}^N (p_n - r_n)^2}{N},$$

$$c\text{RMSD}^2 = \frac{\sum_{n=1}^N [(p_n - \bar{p}_n) - (r_n - \bar{r}_n)]^2}{N}$$

$$\text{and Willmott} = 1 - \left[ \sum_{n=1}^N \frac{(p_n - r_n)^2}{\sum_{n=1}^N (|p'_n| - |r'_n|)^2} \right],$$

where  $p'_n = p_n - \bar{r}$  and  $r'_n = r_n - \bar{r}$  and  $\bar{r}$  is the average of all the reference data. A Willmott index equal to 1, indicates a perfect match between predicted and reference. SI (the Scatter Index) is determined by dividing the RMSD by the mean of the observations and multiplying it by 100.

### References

- McKinney, T.E.; Davidson, B. Facts about the African Past. *Phylon* (1960-) **1960**, *21*, 196. [\[CrossRef\]](#)
- Cr  tat, J.; Richard, Y.; Pohl, B.; Rouault, M.; Reason, C.; Fauchereau, N. Recurrent daily rainfall patterns over South Africa and associated dynamics during the core of the austral summer. *Int. J. Clim.* **2010**, *32*, 261–273. [\[CrossRef\]](#)
- Gramscianinov, C.B.; Hodges, K.I.; De Camargo, R. The properties and genesis environments of South Atlantic cyclones. *Clim. Dyn.* **2019**, *53*, 4115–4140. [\[CrossRef\]](#)

4. Rautenbach, C.; Daniels, T.; De Vos, M.; Barnes, M.A. A coupled wave, tide and storm surge operational forecasting system for South Africa: Validation and physical description. *Nat. Hazards* **2020**, *103*, 1407–1439. [\[CrossRef\]](#)
5. Veitch, J.; Rautenbach, C.; Hermes, J.; Reason, C. The Cape Point wave record, extreme events and the role of large-scale modes of climate variability. *J. Mar. Syst.* **2019**, *198*, 103185. [\[CrossRef\]](#)
6. Amrutha, M.; Kumar, V.S.; Sandhya, K.; Nair, T.M.B.; Rathod, J. Wave hindcast studies using SWAN nested in WAVEWATCH III—comparison with measured nearshore buoy data off Karwar, eastern Arabian Sea. *Ocean Eng.* **2016**, *119*, 114–124. [\[CrossRef\]](#)
7. Zheng, C.; Li, C.Y. Analysis of temporal and spatial characteristics of waves in the Indian Ocean based on ERA-40 wave reanalysis. *Appl. Ocean Res.* **2017**, *63*, 217–228. [\[CrossRef\]](#)
8. Pérez, J.; Méndez, F.; Menéndez, M.; Losada, I.J. ESTELA: A method for evaluating the source and travel time of the wave energy reaching a local area. *Ocean Dyn.* **2014**, *64*, 1181–1191. [\[CrossRef\]](#)
9. Camus, P.; Menéndez, M.; Méndez, F.; Izaguirre, C.; Espejo, A.; Cánovas, V.; Pérez, J.; Rueda, A.; Losada, I.J.; Medina, R. A weather-type statistical downscaling framework for ocean wave climate. *J. Geophys. Res. Oceans* **2014**, *119*, 7389–7405. [\[CrossRef\]](#)
10. Semedo, A.; Suselj, K.; Rutgersson, A.; Sterl, A. A Global View on the Wind Sea and Swell Climate and Variability from ERA-40. *J. Clim.* **2011**, *24*, 1461–1479. [\[CrossRef\]](#)
11. Chen, G.; Chapron, B.; Ezraty, R.; VanDeMark, D. A Global View of Swell and Wind Sea Climate in the Ocean by Satellite Altimeter and Scatterometer. *J. Atmos. Ocean. Technol.* **2002**, *19*, 1849–1859. [\[CrossRef\]](#)
12. Camus, P.; Losada, I.J.; Izaguirre, C.; Espejo, A.; Menéndez, M.; Pérez, J. Statistical wave climate projections for coastal impact assessments. *Earth's Future* **2017**, *5*, 918–933. [\[CrossRef\]](#)
13. Morim, J.; Hemer, M.; Wang, X.L.; Cartwright, N.; Trenham, C.; Semedo, A.; Young, I.; Bricheno, L.; Camus, P.; Casas-Prat, M.; et al. Robustness and uncertainties in global multivariate wind-wave climate projections. *Nat. Clim. Chang.* **2019**, *9*, 711–718. [\[CrossRef\]](#)
14. Young, I.; Ribal, A. Multiplatform evaluation of global trends in wind speed and wave height. *Science* **2019**, *364*, 548–552. [\[CrossRef\]](#) [\[PubMed\]](#)
15. Marcos, M.; Rohmer, J.; Vousedoukas, M.I.; Mentaschi, L.; Le Cozannet, G.; Amores, A. Increased Extreme Coastal Water Levels Due to the Combined Action of Storm Surges and Wind Waves. *Geophys. Res. Lett.* **2019**, *46*, 4356–4364. [\[CrossRef\]](#)
16. Ardhuin, F.; Stopa, J.E.; Chapron, B.; Collard, F.; Husson, R.; Jensen, R.E.; Johannessen, J.; Mouche, A.; Passaro, M.; Quartly, G.; et al. Observing Sea States. *Front. Mar. Sci.* **2019**, *6*, 1–29. [\[CrossRef\]](#)
17. Anderson, R.; Bill, C.; Branch, G.; Brown, B.; Hara, M.; Harris, J. *Waves of Change*; University of Cape Town Press: Cape Town, South Africa, 2003.
18. Corbella, S.; Stretch, D.D. Multivariate return periods of sea storms for coastal erosion risk assessment. *Nat. Hazards Earth Syst. Sci.* **2012**, *12*, 2699–2708. [\[CrossRef\]](#)
19. Seabloom, E.W.; Ruggiero, P.; Hacker, S.D.; Mull, J.; Zarnetske, P.L. Invasive grasses, climate change, and exposure to storm-wave overtopping in coastal dune ecosystems. *Glob. Chang. Biol.* **2012**, *19*, 824–832. [\[CrossRef\]](#)
20. Melet, A.; Meyssignac, B.; Almar, R.; le Cozannet, G. Under-estimated wave contribution to coastal sea-level rise. *Nat. Clim. Chang.* **2018**, *8*, 234–239. [\[CrossRef\]](#)
21. Morris, T.; Rautenbach, C.; Stander, J. A new era for marine forecasting in South Africa. *S. Afr. J. Sci.* **2019**, *115*, 1–2. [\[CrossRef\]](#)
22. Quilfen, Y.; Yurovskaya, M.V.; Chapron, B.; Ardhuin, F. Storm waves focusing and steepening in the Agulhas current: Satellite observations and modeling. *Remote Sens. Environ.* **2018**, *216*, 561–571. [\[CrossRef\]](#)
23. Barnes, M.A.; Rautenbach, C. Toward Operational Wave-Current Interactions over the Agulhas Current System. *J. Geophys. Res. Oceans* **2020**, *125*, 1–21. [\[CrossRef\]](#)
24. De León, S.P.; Soares, C.G. Sensitivity of wave model predictions to wind fields in the Western Mediterranean sea. *Coast. Eng.* **2008**, *55*, 920–929. [\[CrossRef\]](#)
25. Gorrell, L.; Raubenheimer, B.; Elgar, S.; Guza, R. SWAN predictions of waves observed in shallow water onshore of complex bathymetry. *Coast. Eng.* **2011**, *58*, 510–516. [\[CrossRef\]](#)
26. Hoque, A.; Perrie, W.; Solomon, S.M. Application of SWAN model for storm generated wave simulation in the Canadian Beaufort Sea. *J. Ocean Eng. Sci.* **2020**, *5*, 19–34. [\[CrossRef\]](#)



27. Rautenbach, C.; Barnes, M.A.; De Vos, M. Tidal characteristics of South Africa. *Deep. Sea Res. Part I Oceanogr. Res. Pap.* **2019**, *150*, 103079. [CrossRef]
28. Vaze, P.; Neeck, S.; Bannoura, W.; Green, J.; Wade, A.; Mignogno, M.; Zaouche, G.; Couderc, V.; Thouvenot, E.; Parisot, F. The Jason-3 Mission: Completing the transition of ocean altimetry from research to operations. In Proceedings of the Sensors, Systems, and Next-Generation Satellites XIV, Toulouse, France, 20–23 September 2010; Volume 7826, p. 78260Y.
29. Verron, J.; Sengenès, P.; Lambin, J.; Noubel, J.; Steunou, N.; Guillot, A.; Picot, N.; Coutin-Faye, S.; Sharma, R.; Gairola, R.M.; et al. The SARAL/AltiKa Altimetry Satellite Mission. *Mar. Geodesy* **2015**, *38*, 2–21. [CrossRef]
30. Cummings, J.A.; Smedstad, O.M. Variational Data Assimilation for the Global Ocean. In *Data Assimilation for Atmospheric, Oceanic and Hydrologic Applications (Vol. II)*; Springer: Berlin/Heidelberg, Germany, 2013; pp. 303–343.
31. Harding, J.; Rigney, J. Operational Oceanography in the U.S. Navy: A GODAE Perspective. In *Ocean Weather Forecasting*; Springer: Berlin/Heidelberg, Germany, 2006; pp. 467–482.
32. Brown1, A.R.; Milton, S.; Cullen, M.; Golding, B.; Mitchell, J.; Shelly, A. Unified Modeling and Prediction of Weather and Climate: A 25-Year Journey. *Bull. Am. Meteorol. Soc.* **2012**, *93*, 1865–1877. [CrossRef]
33. Tolman, H.L. A Third-Generation Model for Wind Waves on Slowly Varying, Unsteady, and Inhomogeneous Depths and Currents. *J. Phys. Oceanogr.* **1991**, *21*, 782–797. [CrossRef]
34. Tolman, H.L.; Balasubramanian, B.; Burroughs, L.D.; Chalikov, D.V.; Chao, Y.Y.; Chen, H.S.; Gerald, V.M. Development and Implementation of Wind-Generated Ocean Surface Wave Models at NCEP. *Weather Forecast.* **2002**, *17*, 311–333. [CrossRef]
35. WAVEWATCH III Development Group. *User Manual and System Documentation of WAVEWATCH III® version 5.16*; NOAA/NWS/NCEP/MMAB, Technical Note 329; College Park, MD, USA, 2016.
36. Tolman, H.L. A mosaic approach to wind wave modeling. *Ocean Model.* **2008**, *25*, 35–47. [CrossRef]
37. Rogers, W.E.; Linzell, R.S. *The IRI Grid System for Use with WAVEWATCH III®*; NRL Memorandum Report 7320-18; Naval Research Laboratory: Washington, DC, USA, 2018.
38. Wittmann, P.A.; Cummings, J.A. Assimilation of Altimeter Wave Measurements into Wavewatch III, In 8th International Workshop on Wave Hindcasting and Forecasting and 2nd Coastal Hazards Symposium, 2004; pp. 14–19. Available online: <https://www.semanticscholar.org/paper/Assimilation-of-Altimeter-Wave-Measurements-into-Wittmann-Cummings/5d28aa4f6df6f93aaf9eda8a03e1b4ef2cc121fc> (accessed on 30 August 2020).
39. Deltares, D. Delft3D Flexible Mesh Suite. In *Delft3D-FLOW, User Manual*; Deltares: Delft, The Netherlands, 2018.
40. Sembiring, L.; Van Ormondt, M.; Van Dongeren, A.; Roelvink, D. A validation of an operational wave and surge prediction system for the Dutch coast. *Nat. Hazards Earth Syst. Sci.* **2015**, *15*, 1231–1242. [CrossRef]
41. Komen, G.J.; Hasselmann, K. On the Existence of a Fully Developed Wind-Sea Spectrum. *J. Phys. Oceanogr.* **1984**, *14*, 1271–1285. [CrossRef]
42. Van Der Westhuysen, A.J.; Zijlema, M.; Battjes, J.A. Nonlinear saturation-based whitecapping dissipation in SWAN for deep and shallow water. *Coast. Eng.* **2007**, *54*, 151–170. [CrossRef]
43. Mulligan, R.P.; Bowen, A.J.; Hay, A.E.; Van Der Westhuysen, A.J.; Battjes, J.A. Whitecapping and wave field evolution in a coastal bay. *J. Geophys. Res. Space Phys.* **2008**, *113*, 1–16. [CrossRef]
44. Madsen, O.S.; Poon, Y.-K.; Graber, H.C. Spectral Wave Attenuation by Bottom Friction: Theory. In Proceedings of the 21st International Conference on Coastal Engineering, Malaga, Spain, 20–25 June 1988; pp. 492–504.
45. Battjes, J.A.; Janssen, J.P. Energy Loss and Set-Up Due to Breaking of Random Waves. *Coast. Eng.* **1978**, *2*, 569–587.
46. Holthuijsen, L.H. *Waves in Oceanic and Coastal Waters*; Cambridge University Press (CUP): Cambridge, UK, 2007.
47. Gweba, B. Developing a Methodology for the Assessment of Wave Energy along the South African Coast. Ph.D. Thesis, Stellenbosch University, Stellenbosch, South Africa, 2018.
48. Longuet-Higgins, M.S.; Cartwright, D.E.; Smith, N. Observations of the directional spectrum of sea waves using the motions of a floating buoy. *Ocean Wave Spectra* **1961**, 111–132.
49. Oltman-Shay, J.; Guza, R.T. A Data-Adaptive Ocean Wave Directional-Spectrum Estimator for Pitch and Roll Type Measurements. *J. Phys. Oceanogr.* **1984**, *14*, 1800–1810. [CrossRef]
50. Lygre, A.; Krogstad, H.E. Maximum Entropy Estimation of the Directional Distribution in Ocean Wave Spectra. *J. Phys. Oceanogr.* **1986**, *16*, 2052–2060. [CrossRef]



51. Earle, M.; Steele, K.; Wang, D. Use of advanced directional wave spectra analysis methods. *Ocean Eng.* **1999**, *26*, 1421–1434. [\[CrossRef\]](#)
52. Williams, J.J.; Esteves, L.S. Guidance on Setup, Calibration, and Validation of Hydrodynamic, Wave, and Sediment Models for Shelf Seas and Estuaries. *Adv. Civ. Eng.* **2017**, *2017*, 1–25. [\[CrossRef\]](#)
53. Cavaleri, L.; Abdalla, S.; Benetazzo, A.; Bertotti, L.; Bidlot, J.-R.; Øyvind, B.; Carniel, S.; Jensen, R.; Portilla-Yandún, J.; Rogers, E.; et al. Wave modelling in coastal and inner seas. *Prog. Oceanogr.* **2018**, *167*, 164–233. [\[CrossRef\]](#)
54. Taylor, K.E. Summarizing multiple aspects of model performance in a single diagram. *J. Geophys. Res. Space Phys.* **2001**, *106*, 7183–7192. [\[CrossRef\]](#)
55. Maze, G. Taylor Diagram. 2010. Available online: <http://codes.guillaumemaze.org/> (accessed on 5 July 2020).
56. Toffoli, A.; Bitner-Gregersen, E.M. Types of Ocean Surface Waves, Wave Classification. In *Encyclopedia of Maritime and Offshore Engineering*; John Wiley & Sons, Ltd.: Chichester, UK, 2017; pp. 1–8.
57. Kolbusz, J.; Pattiaratchi, C.; Mann, L. Validation of the wave climate in south-west Australia predicted using the Climate Forecast System Reanalysis. *Aust. J. Marit. Ocean Aff.* **2015**, *7*, 3–11. [\[CrossRef\]](#)
58. Jolliff, J.; Kindle, J.C.; Shulman, I.; Penta, B.; Friedrichs, M.A.M.; Helber, R.; Arnone, R.A. Summary diagrams for coupled hydrodynamic-ecosystem model skill assessment. *J. Mar. Syst.* **2009**, *76*, 64–82. [\[CrossRef\]](#)
59. Van Der Westhuysen, A.; Van Dongeren, A.; Groeneweg, J.; Van Vledder, G.P.; Peters, H.; Gautier, C.; Van Nieuwkoop, J.C.C. Improvements in spectral wave modeling in tidal inlet seas. *J. Geophys. Res. Space Phys.* **2012**, *117*, C11. [\[CrossRef\]](#)
60. Van Der Westhuysen, A.J. Modeling of depth-induced wave breaking under finite depth wave growth conditions. *J. Geophys. Res. Space Phys.* **2010**, *115*, C01008. [\[CrossRef\]](#)
61. Collins, J.I. Prediction of shallow-water spectra. *J. Geophys. Res. Space Phys.* **1972**, *77*, 2693–2707. [\[CrossRef\]](#)
62. Rogers, D.E.; Babanin, A.; Wang, D.W. Observation-Consistent Input and Whitecapping Dissipation in a Model for Wind-Generated Surface Waves: Description and Simple Calculations. *J. Atmos. Ocean. Technol.* **2012**, *29*, 1329–1346. [\[CrossRef\]](#)
63. Willmott, C.J. On the validation of models. *Phys. Geogr.* **1987**, *2*, 184–194. [\[CrossRef\]](#)
64. Willmott, C.J.; Robeson, M.; Matsuura, K. Short Communication A refined index of model performance. *Int. J. Climatol.* **2012**, *2094*, 2088–2094. [\[CrossRef\]](#)



© 2020 by the authors. Licensee MDPI, Basel, Switzerland. This article is an open access article distributed under the terms and conditions of the Creative Commons Attribution (CC BY) license (<http://creativecommons.org/licenses/by/4.0/>).

## Chapter 6

### *Parallel computing efficiency of SWAN*

---



**Figure 6-1:** Another original linoleum print made during the course of the present study. This print was inspired by the freedom and hope that a new day and season brings. It also highlights the importance that the Sun has on all Earth-system dynamics.

## **6.1 Abstract**

Effective and accurate ocean and coastal wave prediction is an important topic due to our changing global wave climatology. Simulating WAVes in the Nearshore (SWAN) is a widely used spectral wave modelling tool employed by coastal engineers and scientists. It is a tool commonly used for operational wave forecasting purposes. These fore- and hindcasts can span from hours to decades and a detailed understanding of the computational efficiencies are required to design optimized operational protocols and hindcast scenarios. To date, there exists limited knowledge between the size of a SWAN computational domain and the optimal amount of parallel computational threads required to execute a simulation effectively. A hindcast cluster of 28 computational nodes were used to determine the computation efficiencies of a SWAN model configuration for southern Africa. Both OpenMP and the Message Passing Interface (MPI) were implemented as distributing memory architectures and compared. The model extent and resolution emulate the current operational wave forecasting configuration, developed by the South African Weather Service (SAWS). Three sequential simulations (corresponding to typical grid cell numbers) were compared to various permutations of parallel computations via the speed-up ratio, time saving ratio and efficiency tests. Pre- and post-processing requirements were also analysed. Generally, a computational node configuration of 6 threads produced the most effective computational set-up based on wave hindcasts of a week. More than 20 threads resulted in a decrease in speed-up ratio for the smallest computation domain. This phenomenon is due to the increasing dominance of sub-domain communication times for limited domain sizes.

## **6.2 Publication details**

Submitted to Geoscientific Model Development. An interactive open-access journal of the European Geoscience Union.

## **6.3 Author contributions (as appeared in paper)**

Dr. C. Rautenbach executed the models and conceptualized the study methodology, based on a thorough literature review. Dr. J. Mullarney and Prof. K. Bryan reviewed the manuscript.



# Parallel computing efficiency of SWAN

Christo Rautenbach<sup>1, 2, 3, 4</sup>, Julia C. Mullarney<sup>4</sup>, Karin R. Bryan<sup>4</sup>

<sup>1</sup> Institute for Coastal and Marine Research, Nelson Mandela University, South Africa

<sup>2</sup> Department of Oceanography and Marine Research Institute, University of Cape Town, South Africa

<sup>3</sup> Research and development, MetOcean (a division of the Meteorological Service), Raglan, New Zealand

<sup>4</sup> Environmental Research Institute, University of Waikato, Hamilton, New Zealand

*Correspondence to:* Christo Rautenbach (rautenbachchristo@gmail.com)

**Abstract.** Effective and accurate ocean and coastal wave predictions are necessary for engineering, safety and recreational purposes. Refining predictive capabilities is increasingly critical to reduce the uncertainties faced with a changing global wave climatology. Simulating WAVes in the Nearshore (SWAN) is a widely used spectral wave modelling tool employed by coastal engineers and scientists, including for operational wave forecasting purposes. Fore- and hindcasts can span hours to decades and a detailed understanding of the computational efficiencies is required to design optimized operational protocols and hindcast scenarios. To date, there exists limited knowledge on the relationship between the size of a SWAN computational domain and the optimal amount of parallel computational threads required to execute a simulation effectively. To test this, a hindcast cluster of 28 computational threads (1 node) was used to determine the computation efficiencies of a SWAN model configuration for southern Africa. The model extent and resolution emulate the current operational wave forecasting configuration developed by the South African Weather Service (SAWS). We implemented and compared both OpenMP and the Message Passing Interface (MPI) distributing memory architectures. Three sequential simulations (corresponding to typical grid cell numbers) were compared to various permutations of parallel computations via the speed-up ratio, time saving ratio and efficiency tests. Generally, a computational node configuration of 6 threads produced the most effective computational set-up based on wave hindcasts of one-week duration. The use of more than 20 threads resulted in a decrease in speed-up ratio for the smallest computation domain, owing to the increased sub-domain communication times for limited domain sizes.

*Keywords:* SWAN, Parallel computing, Forecasting, Hindcasting, South Africa

## 1 Introduction

The computational efficiency of Met-ocean (Meteorological-Ocean) modelling has been the topic of ongoing deliberation for decades. The applications range from long-term atmospheric and ocean hindcast simulations to the fast responding simulations related to operational forecasting. Long-duration simulations are usually associated with climate change related research, with simulation periods of a least 30-years across multiple spatial and temporal resolutions needed to capture key oscillations (Babatunde et al., 2013). Such hindcasts are frequently used by coastal and offshore engineering consultancies for purposes such as those related to infrastructure design (Kamphuis, 2020), or environmental impact assessments (Frihy, 2001; Liu, Sheu, & Tseng, 2013).

Operational (or forecasting) agencies are usually concerned with achieving simulation speeds that would allow them to accurately forewarn their stakeholders of immediate, imminent and upcoming met-ocean hazards. The main stakeholders are usually other governmental agencies (e.g. disaster response or environmental affairs departments), commercial entities and the public. Both atmospheric and marine forecasts share similar numerical schemes that solve the governing equations and thus share a similar need in computational efficiency. Fast simulation times are also required for other forecasting fields such as hydrological dam-break models (e.g. Zhang, et al., (2014)). Significant advancement in operational forecasting can be made by examining the way in which the code interfaces with the computation nodes, and how results are stored during simulation. Numerous operational agencies (both private and public) makes use of Simulating Waves in the Nearshore (SWAN) to predict nearshore wave dynamics (refer to Genseberger & Donners, (2020) for details regarding the SWAN numerical code and solution schemes). These agencies include the South African Weather Service (e.g. Rautenbach, et al., (2020)), MetOcean Solutions (a division of the Metrological Office of New Zealand) (e.g. de Souza, et al., (2020)), the United Kingdom MetOffice (e.g. O'Neill et al., (2016)) and the Norwegian Metrological Service (e.g. Jeuring, et al., (2019)). In general, these agencies have substantial computational facilities but nonetheless still face the challenge of optimizing the use of their computational clusters between various models (being executed simultaneously). These models may include atmospheric models (e.g. the Weather Research and Forecasting (WRF) model), Hydrodynamic models (e.g. Regional Ocean Modeling System (ROMS) and the Semi-implicit Cross-scale Hydrosience Integrated System Model (SCHISM)) and spectral waves models (e.g. Wave Watch III (WW3) and SWAN). There must also be a balance between hindcast and forecast priorities and client needs. Some of these agencies use a regular grid (instead of irregular grids (e.g. Zhang, et al., (2016))), with nested domains in many of their operational and hindcast projects. Here we focus only on the computational performance of a structured regular grid (typically implemented for spectral wave models).

Kerr et al., (2013) performed an inter-model comparison of computational efficiencies by comparing SWAN, coupled with ADCIRC, and the NOAA official storm surge forecasting model, SLOSH, however, did not investigate the optimal thread usage of a single model. Other examples of a coupled wave and storm surge model computational benchmarking experiments include Tanaka, et al, (2011) and Dietrich et al., (2012) for a unstructured meshes during Hurricanes Katrina, Rita, Gustav and Ike in the Mexican Gulf. These models also present their results on a log-log scale and their experimental design tested

computational thread numbers not easily obtainable by smaller agencies and companies. The latter rather require sequential versus paralleled computational efficiencies using smaller scale efficiency metrics. Genseberger & Donners, (2015), explored the scalability of SWAN using a case study focused on the Wadden Sea in the Netherlands. By investigating the efficiency of both the OpenMP (OMP) and MPI version of the then current SWAN, they found that the OpenMP was more efficient on a single node. They also proposed a hybrid version of SWAN, to combine the strengths of both implementations of SWAN: using OpenMP to more optimally share memory and MPI to distribute memory over the computational nodes.

Here we build on the case study of Genseberger & Donners using results produced in the present study for southern Africa, to answer the following research questions: 1) when using SWAN, is it always better to have as many threads as possible available to solve the problem at hand? 2) What is the speed-up relationship between number of threads and computational grid size? 3) At what point (number of threads) does the domain sub-communications start to make the whole computation less effective? 4) What is the scalability of a rectangular grid, SWAN set-up?

## **Methodology and background**

Details of the model configuration can be found in (Rautenbach, et al., 2020 (a)) and (Rautenbach, et al., 2020 (b)). The computational domain and physics used here were the same as presented in those studies. All computations were performed on Intel Xeon E5-2670, 2.3GHz computational nodes. Twenty-eight threads (cores) each with 96 GB RAM were used. A modified version of SWAN 40.91 was implemented with the Van der Westhuysen whitecapping formulation (van der Westhuysen, et al., 2007) and Collins bottom friction correlation (Collins, 1972) with a coefficient value of 0.015. Fully spectral wave boundary conditions were extracted from a global Wave Watch III model at 0.5 geographical degree resolution. Here, the validation of the model was not the main aim but rather the relative computational scalabilities, as described at the end of the previous section. However, it should be noted that no nested domains were employed during the present study. Only the parent domain was used as a measure for scalability. The computational extent given in (Rautenbach, et al., 2020 (a)) and (Rautenbach, et al., 2020 (b)) contains numerous non-wet grid cells that are not included in the computational expense of the current study. In Table 1, the size of the computational domain and resolution, together with the labelling convention are given. For clarity, we define the resolutions as low, medium and high, denoted L, M and H, respectively, in the present study (noting that given the domain size, these resolutions would be classified as intermediate to high regional resolution for operational purposes).



**Table 1: SWAN grid resolution, grid cell numbers and reference labels.**

Label	SWAN grid resolution	Computational grid cell number
<b>L</b>	0.1000	31 500
<b>M</b>	0.0625	91 392
<b>H</b>	0.0500	142 800

The test for scalability ability of a model used here was the ability to respond to an increased number of computations with an increasing amount of resources. In the present study these resources are computational threads. An arbitrary week of computations were performed to assess model performance. Model spin-up was done via a single stationary computation. The rest of the computation was performed using a non-stationary computation using an hourly time-step. This implied wind-wave generation within the model occurred on the timescale of the wind forcing resolution. The grid resolutions used in the present study corresponded to 0.1, 0.0625 and 0.05 geographical degrees. Local bathymetric features were typically resolved through downscaled, rotated, rectangular grids, like the methodology employed by Rautenbach, et al., (2020) (a). A nested resolution increase of more than 5-times is also not recommended (given that the regional model is nested in the global Wave Watch III output at 0.5 geographical degree resolution, refer to (Rautenbach, et al., 2020) (a). Given these constraints, these resolutions represent realistic and typical SWAN model set-up, for both operational and hindcast scenarios.

The three main metrics for estimating computational efficiency are: the *Speed-up*, *Time saving* and *Efficiency ratios*. The fourth parameter, and arguably the most important, is the *Scalability* and is estimated using the other three parameters as metrics.

The *Speed-up* ratio is given as:

$$S_p = T_1/T_p \quad (1)$$

where  $T_1$  is the time in seconds it takes for a sequential computation on one thread and  $T_p$  is the time a simulation takes with  $p$  computational threads (S. Zhang et al., 2014).

The *Time saving* ratio is given by:

$$T_1 S_p = (T_1 - T_p)/T_1 \quad (2)$$

and the *Efficiency* ratio follow with the same variables definitions as:

$$E_p = S_p/p. \quad (3)$$

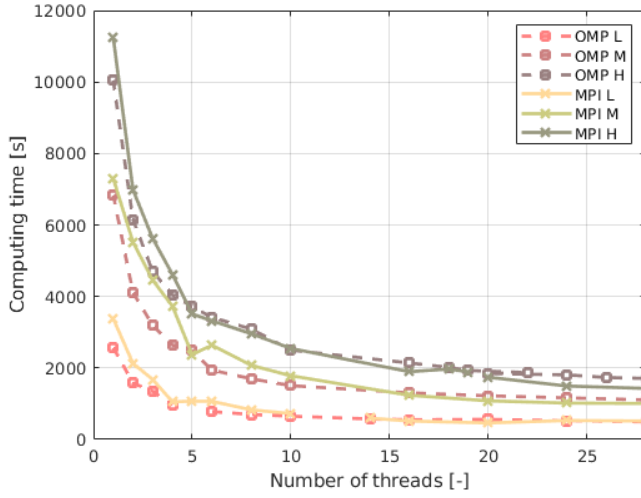
The Scalability of SWAN was tested based on the Speed-up ratios for the grid resolutions in Table 1.

Zafari, Larsson, & Tilleenius, (2019) recently presented some of the first results investigating the effect of different compilers on the scalability of a shallow water equation solver. Their experiments compared a model compiled with GNU Compiler Collection (gcc) 7.2.0 and linked with OpenMPI and Intel C++ compilers with Intel MPI for relatively small computational problems. Their numerical computation considered models with 600K, 300K and 150K grid cell sizes (what they called matrix size). These computational grid sizes were deemed “small”, but they still acknowledged the significant computational resources required to execute geographical models of this size due to the large number of time steps usually involved to solve these problems.

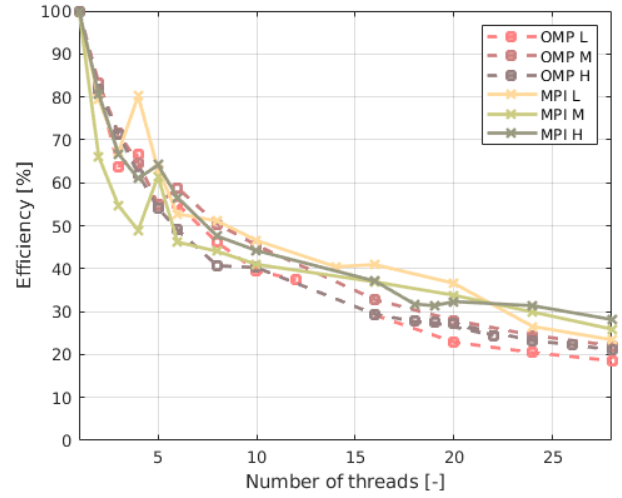
From a practical point of view, regular SWAN grids will rarely be used in dimensions exceeding the resolutions presented in the previous section. The reason for this statement is twofold: 1) to downscale a spectral wave model from a global resolution to a regional resolution may not exceed a five-times refinement factor and 2) when reasonably higher resolutions are required in the nearshore (to take complex bathymetric features into account), nested domain are preferred. The reasoning will be different for an unstructured grid approach (Dietrich et al., 2012). Given these limitations on the widely used structured SWAN grid approach, SWAN grids will almost exclusively be deemed as a low spatial computational demand model. Small tasks create a sharp drop in performance via the Intel C++ compiler due to the “work stealing” algorithm, aimed at balancing out the computational load between threads (Zafari et al., 2019). In this scenario, the threads compete against each other resulting in an unproductive simulation. In our experiments, each task performed via Intel was approximately 13-times faster but the overall performance was 16-time slower than the equivalent gcc compiled version of the compiled shallow water model presented by Zafari et al. (2019).

## Results

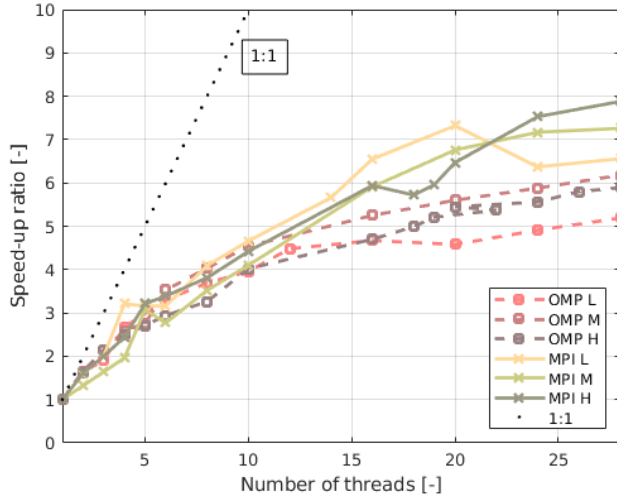
In Figure 1, the computational scalability of SWAN is given as a function of number of computational threads. In Figure 1 (a) the computational time in seconds is presented. Here the model resolutions grouped together with not much differentiation between them. These results also highlight the need for performance metrics, like described in the previous section. From Figure 1 (b) the MPI version of SWAN is more efficient for all the computational domain sizes. There is also a clear grouping between OMP and MPI. Figure 1 (c) presents the speed-up ratios and clearly indicates that the MPI version of SWAN outperforms the OMP version. The closer the result are to the 1:1 line, the better the scalability.



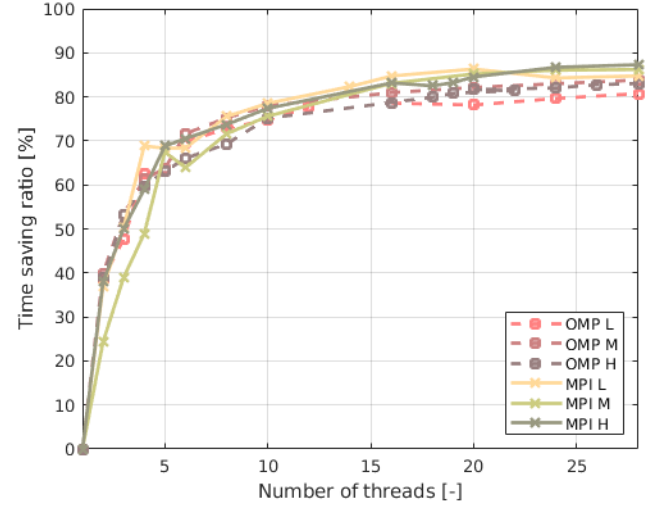
(a)



(b)



(c)



(d)

**Figure 1: Model performance as a function of the number of computational threads. (a) Computing time in seconds, (b) Efficiency (Equation (3)), (c) Speed-up ratio (Equation (1)) and (d) the Time saving ratio (Equation (2)).**

Near linear speed up is observed for a small number of computational threads. This agrees with the results reported by Zafari et al., (2019). In Figure 1 (d) the same results are obtained via the time saving ratio. Here a clear and distinct flattening down is observed with thread counts larger than approximately 6.

## Discussion

The behaviour noted in the results is similar to the dam breaking computational results reported by S. Zhang et al., (2014). Genseberger & Donners, (2020) presents the latest finding on the scalability and benchmarking of SWAN. However, their focus was quantifying the performance of their new hybrid version of SWAN. In their benchmarking experiments (for the Wadden Sea, in the Netherlands), they obtained very similar results to Figure 1 (a), with OMP producing faster wall-clock computational times. They also considered the physical distances between computational threads and found that this parameter has a negligible effect compared to OMP vs MPI, over an increasing number of threads. Their benchmarking also differed from the results presented here as they only provided results as a function of node number. Each one of their nodes consisted of 24 threads. In the present study, the benchmarking of a single node (28 threads) is evaluated compared with a serial computation on a single thread. For benchmarking, without performance metrics, they found that the wall clock times, for the iterations and not a full simulation, reached a minimum (for large computational domains) at 16 nodes ( $16 \times 25$  threads) for the MPI SWAN and 64 nodes ( $16 \times 24$  threads) for the hybrid SWAN. These results were based on using the Cartesius 2690 v3 (Genseberger & Donners, 2020). With the hybrid SWAN, the optimal wall-clock time turn point, for iterations, increased with increased number of computational cells. All the reported turn points (optimal points) occurred at node counts well above 4 nodes ( $4 \times 24$  threads). The wall-clock performance estimation of Genseberger & Donners, (2015) did however indicate similar result to those presented in Figure 1 (a), with OMP running faster than MPI. It must still be noted that with an increased number of nodes, and thus threads, the total computational time should continue to decrease up until the point where the internal domain decomposition, communication efficiencies, starts to outweigh the gaining of computational power. Based on results of Genseberger & Donners, (2020), we can estimate that, for our node configuration and region of interest, the communication inefficiencies will become dominant at approximately 16 nodes ( $16 \times 24$  threads).

## Conclusion

The present study investigated the scalability of SWAN, a widely used spectral wave model. Three typical wave model resolutions were used for these purposes. Both the OpenMP (OMP) and the Message Passing Interface (MPI) implementations of SWAN were tested. The scalability is presented via three performance metrics: the efficiency, speed-up ratio and the timesaving ratio. The MPI version of SWAN outperformed the OMP version based on all three metrics. The MPI version of SWAN performed best with the largest computational domain resolution, resulting in the highest speed-up ratios. The time saving ratio indicated a decrease after approximately six computational threads. This result suggests that six threads are the most effective configuration for executing SWAN. The largest increases in speed-up and efficiency was observed with small thread counts. According to Genseberger & Donners, (2020), computational times decrease up to  $\sim 16$  nodes ( $16 \times 24$  threads), indicating the wall-clock optimal computational time for their cases study. This result suggests that multiple nodes will be required to reach the optimal wall-clock computational time – even though this turn point might not be the most efficient computational configuration. Ultimately, the efficiencies recommended here can improve operational performance

substantially, particularly when implemented over the range of modelling software needed to produce useful metocean forecasts.

### **Code/Data availability**

The open source version of SWAN was run for the purposes of the present study. SWAN maybe be downloaded from here: <http://swanmodel.sourceforge.net/>. The bathymetry used for the present study may be downloaded here: <https://www.gebco.net/> and the wind forcing may be found here: <https://climatedataguide.ucar.edu/climate-data/climate-forecast-system-reanalysis-cfsr>.

### **Author contribution**

Dr. C. Rautenbach conceptualised the study, executed the experiments and wrote the manuscript. He also secured the publication funding. Dr. J. C. Mullarney and Professor K. R. Bryan reviewed the manuscript.

### **Competing interests**

No conflict of interests.

### **Funding**

This research was funded by the National Research Foundation of South Africa (Grant Numbers: 116359).

### **References**

- Babatunde, A., Pascale, B., Sin, C. C., William, C., Peter, C., Fatima, D., ... Markku, R. (2013). *Evaluation of Climate Models. In: Climate Change 2013: The Physical Science Basis. Contribution of Working Group I to the Fifth Assessment Report of the Intergovernmental Panel on Climate Change.* (T. F. Stocker, D. Qin, G.-K. Plattner, M. Tignor, S. K. Allen, J. Boschung, ... P. M. Midgley, Eds.). Cambridge, UK.: Cambridge University Press.
- Collins, J. I. (1972). Prediction of shallow-water spectra. *Journal of Geophysical Research*, 77(15), 2693–2707. <https://doi.org/10.1029/JC077i015p02693>
- de Souza, J. M. A. C., Couto, P., Soutelino, R., & Roughan, M. (2020). Evaluation of four global ocean reanalysis products for New Zealand waters—A guide for regional ocean modelling. *New Zealand Journal of Marine and Freshwater Research*, 0(0), 1–24. <https://doi.org/10.1080/00288330.2020.1713179>
- Dietrich, J. C., Tanaka, S., Westerink, J. J., Dawson, C. N., Luettich, R. A., Zijlema, M., ... Westerink, H. J. (2012).

- Performance of the Unstructured-Mesh, SWAN+ADCIRC Model in Computing Hurricane Waves and Surge. *Journal of Scientific Computing*, 52(2), 468–497. <https://doi.org/10.1007/s10915-011-9555-6>
- Flyer, N., & Wright, G. B. (2009). A radial basis function method for the shallow water equations on a sphere. *Proceedings of the Royal Society A: Mathematical, Physical and Engineering Sciences*, 465(2106), 1949–1976. <https://doi.org/10.1098/rspa.2009.0033>
- Frihy, O. E. (2001). The necessity of environmental impact assessment ( EIA ) in implementing coastal projects : lessons learned from the Egyptian Mediterranean Coast, 44, 489–516.
- Genseberger, M., & Donners, J. (2015). A Hybrid SWAN Version for Fast and Efficient Practical Wave Modelling. *Procedia Computer Science*, 51(1), 1524–1533. <https://doi.org/10.1016/j.procs.2015.05.342>
- Genseberger, M., & Donners, J. (2020). Hybrid SWAN for Fast and Efficient Practical Wave Modelling - Part 2. In V. V. Krzhizhanovskaya, G. Závodszky, M. H. Lees, J. J. Dongarra, P. M. A. Sloot, S. Brissos, & J. Teixeira (Eds.) (Vol. 12139, pp. 87–100). Cham: Springer International Publishing. [https://doi.org/10.1007/978-3-030-50420-5\\_7](https://doi.org/10.1007/978-3-030-50420-5_7)
- Jeuring, J., Knol-kauffman, M., & Sivle, A. (2019). Toward valuable weather and sea-ice services for the marine Arctic : exploring user – producer interfaces of the Norwegian Meteorological. *Polar Geography*, 0(0), 1–21. <https://doi.org/10.1080/1088937X.2019.1679270>
- Kamphuis, J. W. (2020). *Introduction to coastal engineering and management - Advanced series on ocean engineering - Volume 48*. Singapore: World scientific publishing Co. Pte. Ltd.
- Kerr, P. C., Donahue, A. S., Westerink, J. J., Luettich, R. A., Zheng, L. Y., Weisberg, R. H., ... Cox, A. T. (2013). U.S. IOOS coastal and ocean modeling testbed: Inter-model evaluation of tides, waves, and hurricane surge in the Gulf of Mexico. *Journal of Geophysical Research: Oceans*, 118(10), 5129–5172. <https://doi.org/10.1002/jgrc.20376>
- Liu, T. K., Sheu, H. Y., & Tseng, C. N. (2013). Environmental impact assessment of seawater desalination plant under the framework of integrated coastal management. *Desalination*, 326, 10–18. <https://doi.org/10.1016/j.desal.2013.07.003>
- O'Neill, C., Saulter, A., Williams, J., & Horsburgh, K. (2016). NEMO-surge: Application of atmospheric forcing and surge evaluation. Technical report 619, (December), 57. Retrieved from [http://www.metoffice.gov.uk/binaries/content/assets/mohippo/pdf/library/frtr\\_619\\_2016p.pdf](http://www.metoffice.gov.uk/binaries/content/assets/mohippo/pdf/library/frtr_619_2016p.pdf)
- Rautenbach, C., Barnes, M. A., Wang, D. W., & Dykes, J. (2020). Southern African wave model sensitivities and accuracies. *Journal of Marine Science and Engineering*, Under revi.
- Rautenbach, C., Daniels, T., de Vos, M., & Barnes, M. A. (2020). A coupled wave, tide and storm surge operational forecasting system for South Africa: validation and physical description. *Natural Hazards*. <https://doi.org/10.1007/s11069-020-04042-4>
- Tanaka, S., Bunya, S., Westerink, J. J., Dawson, C., & Luettich, R. A. (2011). Scalability of an unstructured grid continuous Galerkin based hurricane storm surge model. *Journal of Scientific Computing*, 46(3), 329–358. <https://doi.org/10.1007/s10915-010-9402-1>
- van der Westhuysen, A. J., Zijlema, M., & Battjes, J. A. (2007). Nonlinear saturation-based whitecapping dissipation in SWAN



- for deep and shallow water. *Coastal Engineering*, 54(2), 151–170. <https://doi.org/10.1016/j.coastaleng.2006.08.006>
- Zafari, A., Larsson, E., & Tillenius, M. (2019). DuctTeip: An efficient programming model for distributed task-based parallel computing. *Parallel Computing*, 90, 102582. <https://doi.org/10.1016/j.parco.2019.102582>
- Zhang, S., Xia, Z., Yuan, R., & Jiang, X. (2014). Parallel computation of a dam-break flow model using OpenMP on a multi-core computer. *Journal of Hydrology*, 512, 126–133. <https://doi.org/10.1016/j.jhydrol.2014.02.035>
- Zhang, Y. J., Ye, F., Stanev, E. V., & Grashorn, S. (2016). Seamless cross-scale modeling with SCHISM. *Ocean Modelling*, 102, 64–81. <https://doi.org/10.1016/j.ocemod.2016.05.002>

# Chapter 7

## *Future studies*

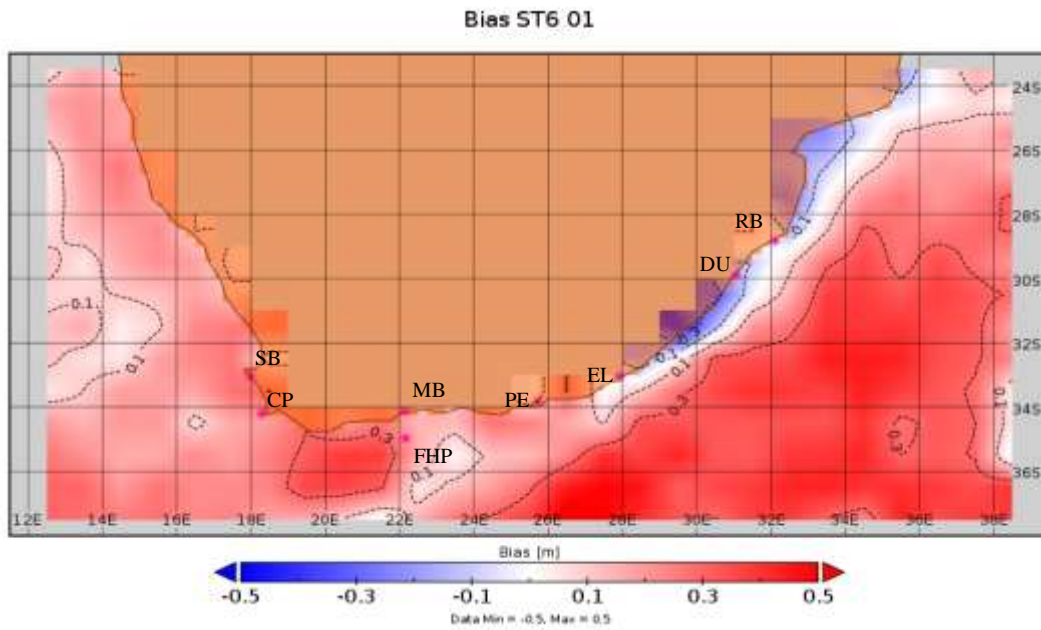
---

Due to the complex dynamics between the atmosphere and the ocean around southern Africa ongoing research is strongly recommended. These studies should not only focus on the current atmospheric and ocean dynamics but strive to elucidate future dynamics as well. Changes in mid-latitude cyclone dynamics might significantly influence the observed storm surge signals on the southwest and south coast of South Africa. On the east coast, tropical cyclone trajectory change could have similar effects (Muthige et al., 2018). These changes might also influence the approach direction of waves and modulate their intensities (Morim et al., 2019; Veitch, et al., 2019). Atmospheric and oceanographic changes directly relate to coastal impacts. For example a change in wave approach direction and intensity will ultimately relate to coastal sediment transport rate changes (Rautenbach & Theron, 2018). Coastal infrastructure as well as some coastal ecosystems might also be under more pressure (Coppin, et al., 2020). To this extent, it is important to understand the current metocean dynamics to be able to accurately predict changes on various time scales.

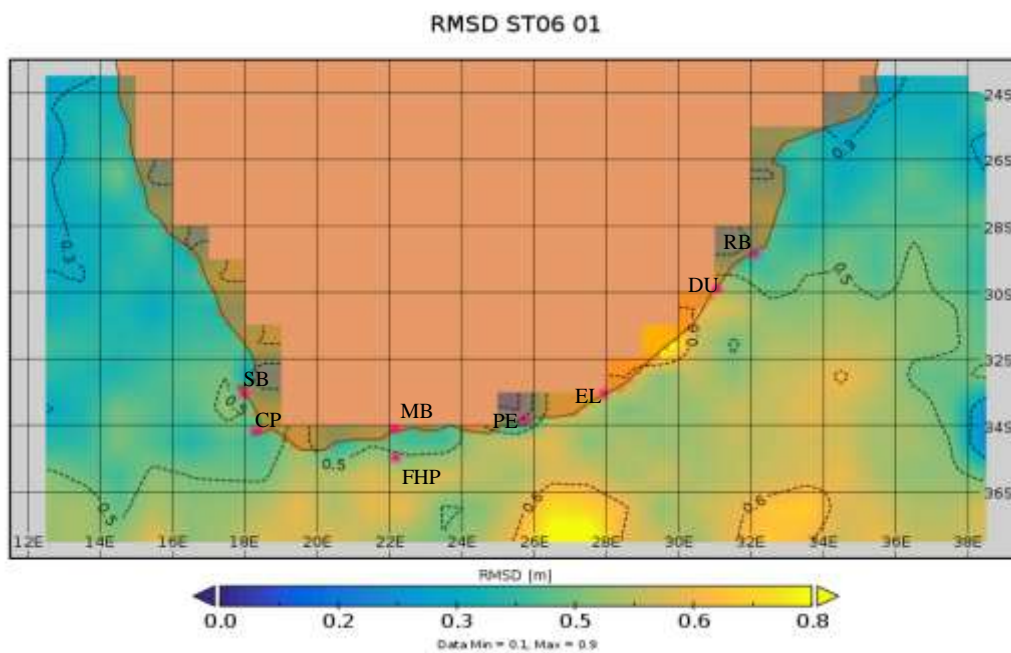
One aspect of the studies presented in the current dissertation that should be investigated next is the physics implemented within the spectral wave models. The two well established whitecapping formulation of Komen, et al., (1984) and Van der Westhuysen, et al., (2007) were thoroughly investigated. More recently the so called ST6 configurations have been suggested by Rogers, et al., (2012). Based on field observations around Australia, a new wind-input and -breaking dissipation is proposed for phased averaged, spectral wave models, like SWAN (utilised in the present studies). The way the newly incorporated physical features (in the source terms) takes the dissipation into account may be varied through a calibration process (e.g. Aijaz, et al., (2016)).

In an attempt to illustrate the sensitivities presented by Rogers, et al., (2012), some initial validation results are presented in Figure 7-1. Here the average basic statistical performance is presented for the SWAN computational domain used in the present study. All statistics are based on the average performance over the entire 2016 (January to December) with all available, co-located Altimetry measurements. For a thorough

comparison with Chapter 5, the same simulation period must be investigated together with the same boundary forcing (winds and waves). The results presented here are just the tip of the iceberg of what could be a very useful and valuable study. These remotely sensed, satellite campaigns thus are ERS-1, ERS-2, ENVISAT, TOPEX, POSEIDON, JASON-1, GFO, JASON-2, CRYOSAT-2 and SARAL (between 1991 and 2017). The co-located track statistics were then interpolated to produce the spatial results presented in Figure 7-1. From the west to the east, the major coastal locations are Saldanha Bay (SB), Cape Town (CT), Mossel Bay (MB), Port Elizabeth (PE), East London (EL), Durban (DU) and Richard's Bay (RB). The FH Platform (FHP) is also given for easy reference to Chapter 5.

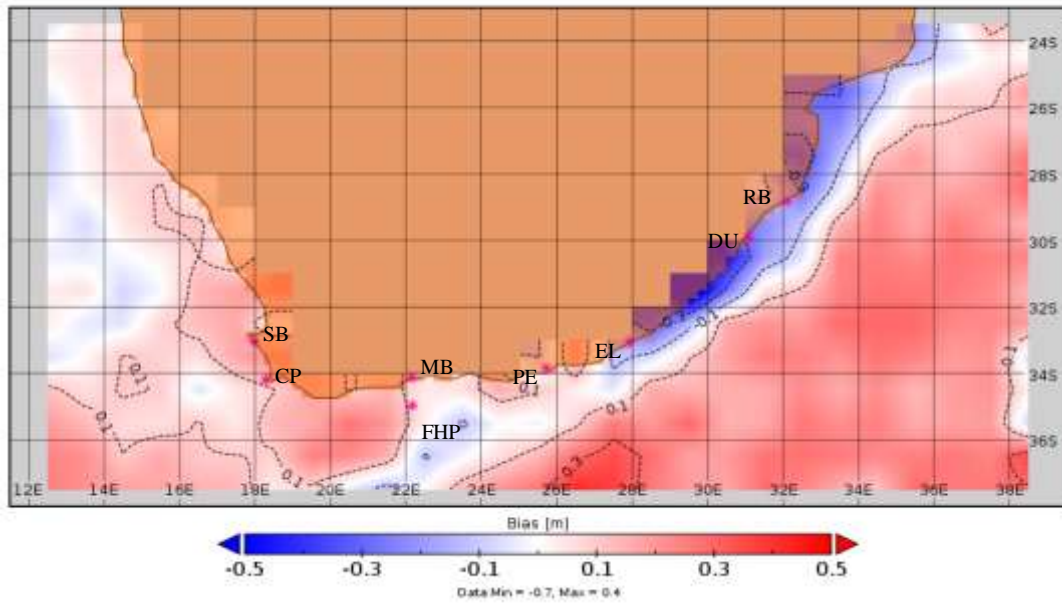


(a)



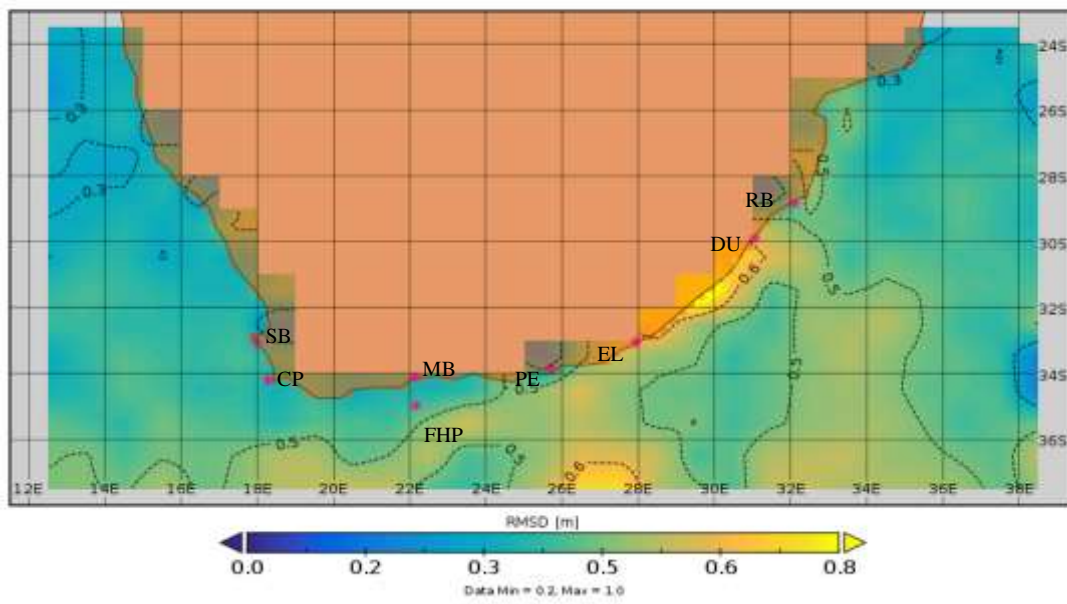
(b)

Bias ST6 02

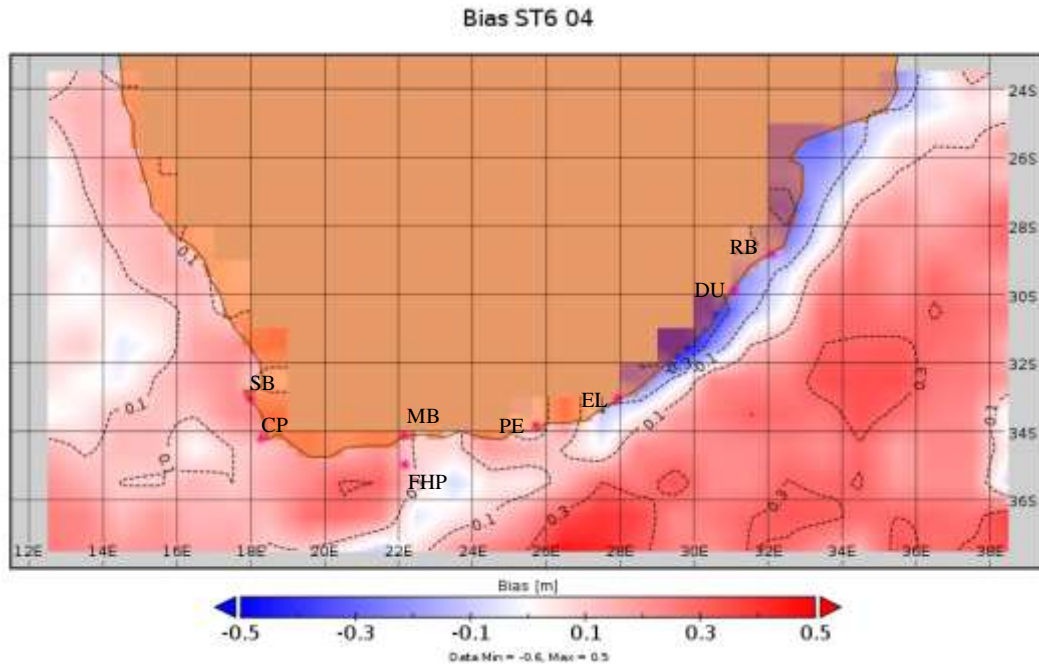


(c)

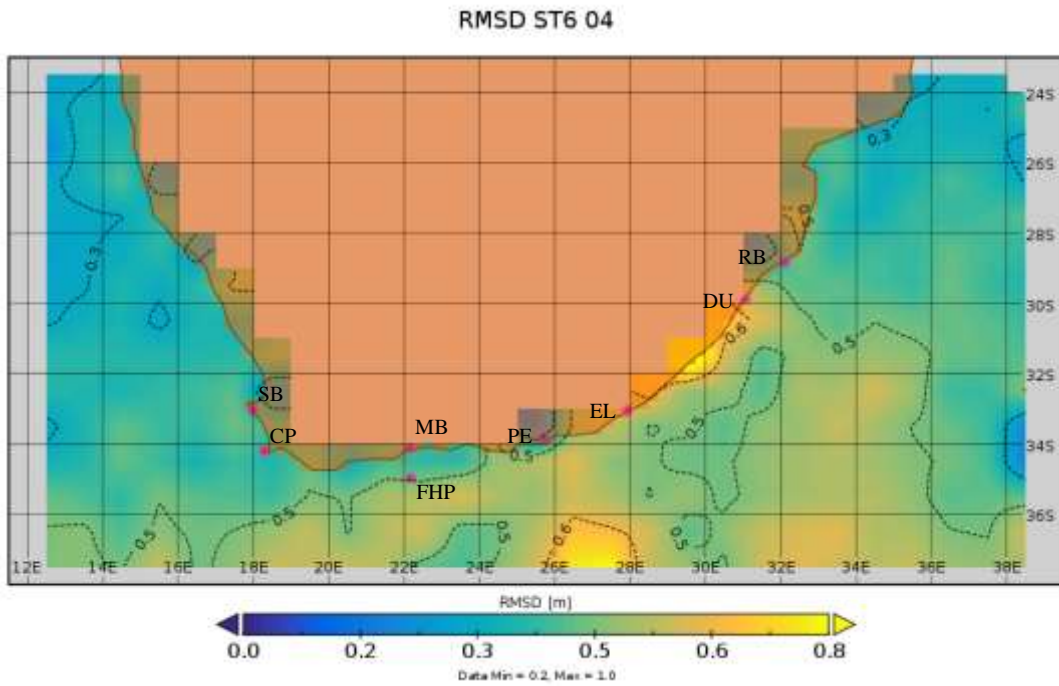
RMSD ST6 02



(d)



(e)



(f)

**Figure 7-1: Basic statistical performance of SWAN compared with co-located Altimetry measurements for 2016. (a) Bias for the ST6 01 configuration (refer to Table 7-1), (b) Root-Mean-Square-Difference (RMSD) for the ST6 01 configuration, (c) Bias for the ST6 02 configuration, (d) RMSD for the ST6 02 configuration, (e) Bias for the ST6 04 configuration, (f) RMSD for the ST6 04 configuration.**

The physical variable within the results presented in Figure 7-1 were free simulations based on parameters elucidated in Rogers, et al., (2012). These are the dissipation term coefficients ( $a_1$  and  $a_2$ ), which should be determined through calibration. Additionally,

there exist  $L$  and  $M$ , subjective power coefficients that can be employed in various combinations to modulate how the dissipation term reacts to exceeded thresholds (Rogers, et al., 2012). Only one combination ( $L=M=4$ ) will be used in this initial investigation (Aijaz, et al., 2016). A jump from, e.g. 4 to 8 will result in a large increase in dissipation.

The model must be scaled with the friction velocity ( $U_*$ ), instead of the wind speed at 10 m elevation ( $U_{10}$ ) (Alves & Banner, 2003). To achieve this, a coefficient may be used to relate the representative wind speed ( $U$ ) to  $U_*$ , (e.g.  $U = cU_*$ , with  $c$  the coefficient). This will force the model to scale with  $U_*$ . The last parameter considered during this initial study is the negative wind input,  $a_o$  (Aijaz et al., 2016). This factor helps to compensate for adverse winds resulting in a negative growth rate. This is also a parameter that should ideally be calibrated for annually (or even seasonally) as it accounts for the conditions where there are large directional differences between the wind and waves. In Table 7-1 a summary of the permutations presented in Figure 7-1 is given. Here  $C_D$  in Table 7-1 shows the citations for the wind drag coefficients used.

**Table 7-1: ST6 parameter sensitivity testing scenarios.**

<b>Configuration scenario</b>	<b><math>a_1</math></b>	<b><math>a_2</math></b>	<b><math>c</math></b>	<b><math>a_o</math></b>	<b><math>C_D</math></b>
<b>ST6 01</b>	4.7e-7	6.6e-6	28	0.00	(Fan & Rogers, 2016)
<b>ST6 02</b>	4.7e-7	6.6e-6	28	0.00	(Hwang, 2011)
<b>ST6 04</b>	2.8e-6	3.5e-5	32	0.89	(Hwang, 2011)

These simulation were all driven by Climate Forecast System Reanalysis (CFRS) winds and using the bottom friction correlation of Collins, (1972) equal to 0.015. The spectral boundary conditions were extracted from a global Wave Watch III model at a 0.5 geographical degree resolution. The SWAN model was executed in non-stationary mode and an hourly time step increment.

In Table 7-2 the regionally averaged performance of Figure 7-1 is given. These results indicate a marked improvement from the results presented in Chapter 5. Further calibration could potentially reveal even better results regionally. Following the same logic as Chapter 5, both *in situ* nearshore calibration and regional calibration should be attempted in future studies. The spatial distributions presented in Figure 7-1 could also be used to understand the physics related to the regional growth of wind-waves and how



they related to the seasonal distributions of mesoscale atmospheric features over southern Africa.

**Table 7-2: Regionally averaged, basic statistical summary.**

	<b>RMSD [m]</b>	<b>Bias [m]</b>	<b>SI</b>
<b>ST6 01</b>	0.4469	0.1802	0.1474
<b>ST6 02</b>	0.4156	0.0719	0.1478
<b>ST6 04</b>	0.4229	0.1113	0.1470

These new developments in sources and sinks in the estimation of wind driven waves are an interesting topic for further investigation. Alongside these physical descriptions, Machine Learning techniques also hold a lot of promise. These techniques are not concerned with solving physical processes but rather deal with complex, non-linear ways of find potentially hidden relationships between variables. These could either be used as independent prediction methods or be combined with more traditional deterministic methods as a post-processing correction tool. This holds true for more than just waves and could be applied to further developments of storm surge predictions, presented in Chapter 4, as well.

# Chapter 8

## *Conclusions*

---

A marine forecasting, operational platform (SWaSS) was developed as a significant component of this thesis. This system provides coupled water level and wave predications for the whole South African coastline. SWaSS represents a “first of its kind” for South Africa, with regional extents, resolutions and dynamics not operationally deployed before. The chapters presented here are the result of the operational system developed for South African users. SWaSS was conceptualized and built as part of the present study. Each chapter in this study was then published or submitted to an international peer reviewed journal. This approach was taken to ensure transparency regarding the methodology and accuracies underpinning SWASS. The overarching aim of the present thesis was the validation of all the components of the operational system presented in Figure 1-2 and Figure 1-3. Both the numerical modelling methodologies and validation techniques has been successful. The latter revealed accuracies within the bounds of internationally accepted margins. The peer review process also confirmed that the numerical models were appropriate for the aims of each subcomponent.

Chapter 3 validated the tidal component of SWaSS. All validation results were done with regards to the total tidal water level signal together with the harmonic components (tidal constituents). A full tidal characterisation was also added to this chapter by means of tidal constituent amplitude and phase lag analysis. These results are presented for nine *in situ* measurement locations. Regional, two-dimensional analysis was also performed. These results, together with the Form Factor confirmed the semi-diurnal tidal dominance around southern Africa. Semi-diurnal tidal resonance was also identified and confirmed over the shallower continental shelf areas of the Agulhas and Namaqua Banks. A 3-h lag was observed between the free surface water levels and tidal currents, with the strongest tidal currents observed over the continental shelves. The novelty of this chapter may be found in the first full characterisation of the South African tides and the validation of the numerical model used. The tidal current over the continental shelves are also presented for the first time. The tide propagates from the west to the east with  $M_2$  and  $S_2$  contributing approximately 75% of the total amplitude signal. The two primary semi-diurnal

constituents are thus the most important for astronomic tide prediction around South Africa. Coastal, semi-diurnal resonance is identified and quantified and has not been noted in literature before. This novelty led to this paper being featured as the cover page for the Journal of Deep Sea Research 1, volume 150. This numerical tidal model underpinned all the other models presented in the present thesis.

Chapter 4 validated the storm surge model developed in the present study. This depth-averaged water level model was driven by both atmospheric pressure and winds. The atmospheric component of the operational system was not developed as part of the current thesis. Validation was performed at six *in situ* measurement locations. The model was coupled with the SWAN wave model component of SWaSS. This implied that wave set-up was also considered in the model validation process. The various drivers of storm surge around the South African coastline was also investigated. Surprisingly, the wave set-up contributed ~20 % of the total surge signal in the southwest, with wind set-ups contributing ~55 %. The importance of the continental shelves set-ups was also elucidated and discussed. The novelty in this chapter may be found in the operational system (now providing storm surge forecasts), the storm surge validation and the quantification of the various driving influences on storm surge for South Africa.

Chapter 5 investigated the final component of the SWaSS model. Wave validation was performed at eight *in situ* measurement locations. Regional, two-dimensional validation was performed using the co-location of available satellite altimetry measurements. This component of SWaSS is now also available operationally and is online coupled with the models described in Chapters 3 and 4. This implies that the wave forecasts will respond to storm tidal water levels. Validation of the wave predictions were successfully completed with both *in situ* and remotely sensed, regional validation, producing acceptable error margins. Various commonly used methods of describing spectral boundary conditions to a coastal and regional spectral wave model were also investigated. Fully spectral conditions are not always available for developing countries who do not have the computational resources to produce their own global WW3 spectral wave predictions. Often, developing countries do not have the financial capacities to buy such output products. Thus, it was essential to know what error margins various reconstruction methods will result in. It was found that the reconstruction methods suggested were adequate for the model domain described in SWaSS. Whitecapping formulations were also investigated to identify the most appropriate models to use. It was found that the Van

der Westhuysen model had the best overall performance given that results did differ around the coastline. The main reason for the variability in results was the change in the relative interaction between swell waves and locally generated wind waves. Each whitecapping formulation has strengths and weaknesses in describing the different scenarios of mixed sea states. In Chapter 7 some more thoughts and suggestions are given with regards to how these ideas could possibly be developed further. The novelty of this chapter is in the operational system, the wave component validation as well as the physical description of the driving mechanisms and boundary condition sensitivities. The fully spectral wave model boundary conditions, extracted from WW3, was not developed within the scope of the present study.

In Chapter 6 a very practical aspect of any operational system is presented, the so-called benchmarking and scalability. Here, attention was only given to the wave model component of SWaSS, namely SWAN. The domains considered within the study once again corresponds to the SWaSS operational domain. All experiments were performed on a single computation node consisting of 28 computational threads. All benchmarking and scalability calculation were made in comparison with a single/ series computation on a single thread. The results of this study indicated that six threads are the most efficient configuration for executing SWAN. This efficiency should not be confused with total run time as other studies indicated that the run time turning point only occurs at approximately 16 nodes ( $16 \times 24$  threads). These results are intimately linked with the computational domain size and resolution, together with the computational node configuration. The novelty of this chapter lies in the parameters used to classify the scalability for practical implementations of SWAN. The results provide SWAN users with an easy reference document to estimate and plan computational experiments.

The establishment of the SWaSS operational marine forecasting platform enabled the continued development and improvement of the system. The latest of these include operational wave-current interactions (Barnes & Rautenbach, 2020). Because the SAWS marine research division is also driven by public good, metocean interactions with safety of life at sea has also been investigated (de Vos & Rautenbach, 2019). Several other studies concerned with the finer scale coastal dynamics and user engagements are still ongoing or under review. In general, these studies ushered in a new era for African based marine forecasting and set the scene for continued regional development within operational marine forecasting. Chapter 7 presents some of the first results using the new

ST 6 physics descriptions within SWAN. These results in themselves are novel and will be completed in due course. These results will ultimately enable southern African SWAN users to choose the optimal configuration of the prevailing physical parameterisations.

Readily available, *in situ* and remotely sensed measurements will enable SWaSS to provide nowcast validation, more detailed model optimization and potentially data assimilation in the future. These include machine learnt, post-processing corrections.

## References

---

- Aijaz, S., Rogers, W. E., & Babanin, A. V. (2016). Wave spectral response to sudden changes in wind direction in finite-depth waters. *Ocean Modelling*, 103, 98–117. <https://doi.org/10.1016/j.ocemod.2015.11.006>
- Alves, J. H. G. M., & Banner, M. L. (2003). Performance of a Saturation-Based Dissipation-Rate Source Term in Modeling the Fetch-Limited Evolution of Wind Waves. *Journal of Physical Oceanography*, 33(6), 1274–1298. [https://doi.org/10.1175/1520-0485\(2003\)033<1274:POASDS>2.0.CO;2](https://doi.org/10.1175/1520-0485(2003)033<1274:POASDS>2.0.CO;2)
- Barnes, M. A., & Rautenbach, C. (2020). Toward Operational Wave-Current Interactions Over the Agulhas Current System. *Journal of Geophysical Research: Oceans*, 125(7), 1–21. <https://doi.org/10.1029/2020JC016321>
- Cavaleri, L., Abdalla, S., Benetazzo, A., Bertotti, L., Bidlot, J. R., Breivik, ... van der Westhuysen, A. J. (2018). Wave modelling in coastal and inner seas. *Progress in Oceanography*, 167(September 2017), 164–233. <https://doi.org/10.1016/j.pocean.2018.03.010>
- Collins, J. I. (1972). Prediction of shallow-water spectra. *Journal of Geophysical Research*, 77(15), 2693–2707. <https://doi.org/10.1029/JC077i015p02693>
- Coppin, R., Rautenbach, C., Ponton, T. J., & Smit, A. J. (2020). Investigating Waves and Temperature as Drivers of Kelp Morphology. *Frontiers in Marine Science*, 7(July), 1–21. <https://doi.org/10.3389/fmars.2020.00567>
- de Vos, M., & Rautenbach, C. (2019). Investigating the connection between metocean conditions and coastal user safety: An analysis of search and rescue data. *Safety Science*, 117, 217–228. <https://doi.org/10.1016/j.ssci.2019.03.029>
- Erick Rogers, W., Babanin, A. V., & Wang, D. W. (2012). Observation-consistent input and whitecapping dissipation in a model for wind-generated surface waves: Description and simple calculations. *Journal of Atmospheric and Oceanic Technology*, 29(9), 1329–1346. <https://doi.org/10.1175/JTECH-D-11-00092.1>
- Fan, Y., & Rogers, W. E. (2016). Drag coefficient comparisons between observed and model simulated directional wave spectra under hurricane conditions. *Ocean Modelling*, 102, 1–13. <https://doi.org/10.1016/j.ocemod.2016.04.004>
- Harris, C. (2018). Coupled Atmosphere-Ocean Modelling. In *New Frontiers in Operational Oceanography*. GODAE OceanView. <https://doi.org/10.17125/gov2018.ch16>
- Hwang, P. A. (2011). A Note on the Ocean Surface Roughness Spectrum\*. *Journal of Atmospheric and Oceanic Technology*, 28(3), 436–443. <https://doi.org/10.1175/2010JTECHO812.1>
- Komen, G. J., Hasselmann, K., & Hasselmann, K. (1984). On the Existence of a Fully Developed Wind-Sea Spectrum. *Journal of Physical Oceanography*, 14(8), 1271–1285. [https://doi.org/10.1175/1520-0485\(1984\)014<1271:OTEOAF>2.0.CO;2](https://doi.org/10.1175/1520-0485(1984)014<1271:OTEOAF>2.0.CO;2)
- Morim, J., Hemer, M., Wang, X. L., Cartwright, N., Trenham, C., Semedo, A., ... Andutta,



- F. (2019). Robustness and uncertainties in global multivariate wind-wave climate projections. *Nature Climate Change*, 9(9), 711–718. <https://doi.org/10.1038/s41558-019-0542-5>
- Muthige, M. S., Malherbe, J., Englebrecht, F. A., Grab, S., Beraki, A., Maisha, T. R., & Van der Merwe, J. (2018). Projected changes in tropical cyclones over the South West Indian Ocean under different extents of global warming. *Environmental Research Letters*, 13(6), 065019. <https://doi.org/10.1088/1748-9326/aabc60>
- Niehuser, S., Dangendorf, S., Arns, A., & Jensen, J. (2018). A NOVEL HIGH-RESOLUTION STORM SURGE FORECAST FOR THE GERMAN BIGHT. *Coastal Engineering Proceedings*, (36), 80. <https://doi.org/10.9753/icce.v36.currents.80>
- Rautenbach, C., Barnes, M. A., & de Vos, M. (2019). Tidal characteristics of South Africa. *Deep Sea Research Part I: Oceanographic Research Papers*, 150, 103079. <https://doi.org/10.1016/j.dsr.2019.103079>
- Rautenbach, C., Daniels, T., de Vos, M., & Barnes, M. A. (2020). A coupled wave, tide and storm surge operational forecasting system for South Africa: validation and physical description. *Natural Hazards*. <https://doi.org/10.1007/s11069-020-04042-4>
- Rautenbach, C., & Theron, A. (2018). Study of the Durban Bight shoreline evolution under schematized climate change and sand bypassing scenarios. *SAICE*, 60(4).
- Tadesse, M., Wahl, T., & Cid, A. (2020). Data-Driven Modeling of Global Storm Surges. *Frontiers in Marine Science*, 7(April), 1–19. <https://doi.org/10.3389/fmars.2020.00260>
- van der Westhuysen, A. J., Zijlema, M., & Battjes, J. A. (2007). Nonlinear saturation-based whitecapping dissipation in SWAN for deep and shallow water. *Coastal Engineering*, 54(2), 151–170. <https://doi.org/10.1016/j.coastaleng.2006.08.006>
- Veitch, J., Rautenbach, C., Hermes, J., & Reason, C. (2019). The Cape Point wave record, extreme events and the role of large-scale modes of climate variability. *Journal of Marine Systems*, 198, 103185. <https://doi.org/10.1016/j.jmarsys.2019.103185>
- Vos, M. De, & Rautenbach, C. (2017). Investigating the connection between metocean conditions and coastal user safety: an analysis of search and rescue data. *Safety Science*, 117, 217–228. <https://doi.org/10.1016/J.SSCI.2019.03.029>

*I found my home in the house of the Lord*